Integrated Seismic Study of the Sudbury Structure and Surrounding Area

by

Xiao Gui Miao

A Thesis
Submitted to the Faculty of
Graduate Studies in Partial Fulfillment of
the Requirements for the Degree of

DOCTOR OF PHILOSOPHY

Geophysics, Department of Geological Sciences
The University of Manitoba
Winnipeg, Manitoba

INTEGRATED SEISMIC STUDY OF THE SUDBURY STRUCTURE AND SURROUNDING AREA

BY

XIAO GUI MIAO

A Thesis submitted to the Faculty of Graduate Studies of the University of Manitoba in partial fulfillment of the requirements of the degree of

DOCTOR OF PHILOSOPHY

致中和

天地位焉

萬物育焉

父

茵妻生題

I hereby declare that I am the sole author of this thesis.

I authorize the University of Manitoba to lend this thesis to other institutions or individuals for the purpose of scholarly research.

I further authorize the University of Manitoba to reproduce this thesis by photocopying or by other means, in total or in part, at the request of other institutions or individuals for the purpose of scholarly research.

Abstract

The integrated seismic approach, which has traditionally been utilized in a more qualitative fashion for hydrocarbon exploration, is now becoming increasingly popular in both lithospheric probing and resource exploration in crystalline rock terranes.

Since the discovery of extensive massive sulfide deposits in the Sudbury Basin in the late 1800's, considerable effort has been expended to determine the origin and structural configuration of this unique geological structure. A series of carefully planned seismic experiments and other non-seismic geophysical surveys have been carried out since 1990 in the Sudbury area as a part of the LITHOPROBE Abitibi-Grenville, Sudbury sub-transect project. In this thesis research, high resolution seismic refraction, regional and high resolution seismic reflection, and the multi-offset 3-component VSP (Vertical Seismic Profiling) experiments were utilized to investigate the geologically unique Sudbury Structure and the surrounding area.

A multi-offset 3-component VSP experiment was carried out to study the shallow seismic velocity structure in the center of the Sudbury Basin. In addition to obtaining realistic $P-$ and $S-$waves velocity models through travel time inversion and WKBJ synthetic seismic modeling, the VSP experiment provides us with an independent estimation for the dip of the contact between the Chelmsford and Onwatin formations. The velocity values are also in good agreement with laboratory measurements from the drill core samples. The VSP-CDP transformed section and corridor stacked section correlate well with the high-resolution surface reflection data. The results indicate that the multi-offset three-component VSP experiment provides important constraints and auxiliary information for shallow crustal seismic studies.

The LITHOPROBE seismic regional reflection line 42 was reprocessed in this thesis research to image the subsurface structure northwest of the Sudbury Basin. Carefully designed traditional processing steps combined with time varying cross-dip correction and the wavelet transform for removal of the ground roll noise have dramatically enhanced the seismic reflection image, in contrast to the preliminarily processed data. The reprocessed LITHOPROBE Sudbury regional reflection line 42 data has successfully extended the reflection profile of the Sudbury area to approximately an additional 20 km northwest, and has revealed the subsurface structure in the Levack Gneiss Complex and surrounding area. The newly discovered cross section of the Levack Gneiss Complex adds new constraints to the regional tectonic structures. The result also provides invaluable information for the understanding of the uplift of the Levack Gneiss Complex, which probably plays an important role in resolving the origin of the Sudbury Structure. A major fault or shear zone imaged in the reprocessed section in the northwest of the LGC suggests extended structural deformation in the northwest of the Sudbury Structure and supports a larger dimension of the original impact crater proposed by Grieve et al. (1991).

Two advanced data processing techniques were investigated theoretically and numerically implemented in this thesis. The time varying cross-dip correction algorithm developed for crooked line data processing has proved to be very effective for focusing reflection energy and imaging complex dipping structures with inconsistent cross-dips. The algorithm has also provided important information for cross-dip attitudes of the reflectors. The wavelet transform is a new digital signal processing technique which has an advantage of analyzing and localizing signals in both time and frequency domains simultaneously. In this thesis, a non-orthogonal wavelet transform algorithm

was developed for seismic application and programmed for implementation of removing ground roll noise. The results indicate that the new approach is very effective and superior to the conventional f-k filtering method. The wavelet transform was also applied to detect the reflection signals in a low S/N ratio situation with encouraging results.

The high resolution refraction experiment explores a cross-array of two profiles with an approximate 285 km long line in the NW-SE direction and a 164 km long line in the W-E direction across the Abitibi Subprovince in the Superior Province, the Sudbury Structure, the Grenville Front Tectonic Zone, and the Britt Domain in the Grenville Province. The preliminary processed seismic refraction sections were interpreted by using the Červený 's two point dynamic ray tracing and modeling algorithm. The computed travel times match well with the observed data for most phases including both head waves and wide-angle reflections. The results outline the major crustal and upper mantle structures for the study area.

Even through the seismic experiments investigated in this thesis research do not provide a complete picture of the Sudbury area, the results provide new information on the configuration of the Sudbury Structure which can add new constrains and clues for us to understand the origin of the structure.

Acknowledgements

I deeply thank my supervisor, Dr. Wooil M. Moon for invaluable guidance, encouragement, and constant support throughout this program.

I wish to thank Drs. G. Clark, D. H. Hall, I. Ferguson, and G. C. Tabisz for serving on my committee and providing constructive criticism.

I would also like to thank Dr. B. Milkereit at Geological Survey of Canada for invaluable advice throughout most of this program.

Sincere appreciation is also extended to K.E. Louden at Dalhousie University, the external examiner, for meticulous and constructive review.

I would like to acknowledge my sincere appreciation for the assistance received from Drs. K. Vasudevan and R. Maier of the LSPF (LITHOPROBE Seismic Processing Facility) located at the University of Calgary on the LITHOPROBE remote site computer and processing facilities, and Mr. J. Wenham at the University of Manitoba for the technique support during various stages of the field work.

During the preparation of the thesis research, I have greatly benefited from my friends and colleagues Drs. J. Kim, P. An, and J. Won.

I express many thanks to all my family, especially my husband (Shan Ying Duan), my daughter (Yue Duan), and my parents (Chun Sheng Miao and Quan Hui Yiao), and my sister and brothers for their continuing love and support.

Contents

List of Tables

List of Figures

Table of Symbols and Abbreviations

A	Coefficient matrix in least-square travel time inversion, or frame bound
a	Dilation parameter
a_0	Dilation step
AGC	Automatic gain control
AGT	Abitibi Grenville Transect
AGU	American Geophysical Union
B	Frame bound
$B_\epsilon(T, \Omega_0, \Omega_1)$	A finite 2D integral subset in the time and frequency space
b	Shift parameter
b_0	Shift step
CCF	Cameron Creek fault
CDP	Common depth point
CF	Creighton fault
C_h	Integral constant in Wavelet Transform
CMP	Common mid-point
DMO	Dip moveout
dt/dz, dT/dz	Derivative of traveltime with respect to depth
dT^i_{cal}/dv_j	Derivative of calculated travel time w.r.t. velocity at layer j
EM	Electromagnetic
ERS-1	Earth Resource Satellite-1 launched by the European Space Agency
eTh	Equivalent Thorium
eU	Equivalent Uranium
f	Frequency
$f-k$	Frequency-wavenumber
$F(\omega)$	Fourier Transform of a function $f(t)$
FLF	Fairbank Lake fault
FT	Fourier Transform
GFTZ	Grenville Front Tectonic Zone
GLIMPCE	Great Lake International Multidisciplinary Program on Crustal Evolution
GPS	Global Positioning System
GSC	Geological Survey of Canada
h	Depth of reflector

$h^{(a,b)}$	Wavelet function with dilation a and shift b
$h_{m,n}(t)$	Discrete wavelet function at lattice m and n
$h(t)$	Wavelet basis function
$\hat{h}(\omega)$	Fourier transform of the wavelet basis function $h(t)$
I	Identity matrix
i_b	Angle between the vertical and reflected ray at station b in the VSP experiment
IETS	Inco Exploration and Technical Services
$IT\&A$	Inverse Theory & Application Inc
k	CDP index
K	Potassium
L_2	2D algebraical space
LGC	Levack Gneiss Complex
LSPF	LITHOPROBE Seismic Processing Facility
m	Octave band
max	maximum
MF	Murray fault
MT	Magnetotelluric method
N	Number of voice
NMO	Normal Move-out
OGS	Ontario Geological Survey
PCA	Principal component analysis
P-wave	Primary wave or compressional wave
p	Ray parameter
PRS1	Portable Refraction Seismograph (vertical component)
PRS4	Portable Refraction Seismograph (three components)
$Prod(p_2p_3p_4)$	Product of p_2, p_3, and p_4
SAR	Synthetic Aperture Radar
SEG	Society of Exploration Geophysicists
SEG-Y	Society of Exploration Geophysicists data record tape format Y
SGR	Seismic Group Recorder
SIC	Sudbury Igenous Complex
SRSZ	South Range Shear Zone
SS	Sudbury Structure
S/N ratio	Signal to Noise ratio
$s(t), S(t)$	a time series function
STFT	Short Time Fouier Transform
SU	Structural Uplift
S-wave	Shear wave

t, T	Two-way travel time or time range
$\tau - p$	Intercept time τ - ray parameter p
$T(z)$	Two-way travel time at geophone depth z
δT^i	Computed and observed travel time difference at station i
Δt_i	Moveout correction at station i
t_0	Zero offset two-way travel time
t_b	Zero offset one-way travel time between borehole geophone and surface
Th	Thorium
U	Uranium
USGS	The United State Geological Survey
UTM	Universal Transverse Mercator (a map projection)
$u(t, z)$	Displacement of seismic wave
$U(\tau, p)$	Radon transform of $u(t, z)$
v, V	Velocity
VLF	Very Low Frequency; Vermilion Lake Fault
VSP	Vertical Seismic Profiling
VSP-CDP	Vertical Seismic Profiling-Common Depth Point
VV	Vertical-vertical polarization
$W_s(a, b)$	Wavelet transform of a function s(t) at dilation a and shift b
WT	Wavelet Transform
X	Column vector of residual velocity δv_j, in-line offset distance coordinate
x	Offset distance between shot point and receiver
x_i	Offset distance at the receiver station i
$x_{i,j}$	Offset between the ith shot and jth receiver
x_{source}	Surface offset between source and borehole
Y	Column vector of time difference δT^i, cross-line transverse offset distance coordinate
$y_{i,j}$	Transverse offset between the CDP and the CMP point of the ray trace from shot i to receiver j
z, Z	Depth, or Depth of borehole geophone
$z - t$	Depth-twoway travel time
$z - x$	Depth-offset distance

Ω	Frequency range
Ω_0, Ω_1	Frequency range
ϕ	Real dip angle of the reflector
ϕ_b	Apparent dip of the reflector for receiver station b
α_k	Cross-dip angle at the CDP index k
λ	Damping parameter
ω	Angular frequency
η	Parameter in the source time function
γ	Parameter in the source time function
θ	Angle subtended by the lines from receiver to wellhead and receiver to shot point in the VSP experiment
ξ	In-line dip of the reflector
$*$	Convolution
#	Location number (CDP number, station number etc.)
3-C	Three components

Chapter 1

Introduction

The continental lithosphere is the foundation on which the earth's biosphere exists, and the repository of our mineral and energy resources. The crust, which is 30 to 50 km thick, forms much of the outer most part of the continental lithosphere. Study of the chemical composition and geometrical configuration of the geological blocks and their relationships to various geological processes in the Earth is essential for an accurate understanding of our planet Earth. This knowledge, in turn, is crucial for exploration of buried mineral and fossil fuel resources, and for providing a key to the understanding of nature, origin and history of plate tectonics.

Our knowledge of the lithosphere may be gained directly from surface mapping and deep drill core observations or gained indirectly from a variety of geophysical surveys which record geophysical signatures that reflect the subsurface attributes and geometry of the rock units at depth. The physical property anomalies and the key geological signatures can thus be traced to the surface by means of geophysical profiles or extraction of well log data from depth.

Among many available geophysical methods, seismic techniques play a key role in

deep lithospheric exploration, because the seismic signal can penetrate deeper into the Earth with greater resolution than most other geophysical signals. The seismic reflection method can most effectively image geological boundaries between lithological units and associated geological structures in the subsurface. A combination of regional and high resolution reflection techniques provides us both short wavelength and high resolution seismic energy which images the shallow subsurface structures with great detail and long wavelength seismic energy which penetrates to the crustal depth. Rapidly developing data processing techniques along with increasing computer power make the reflection method more effective than any other sounding techniques. Seismic refraction surveys play an essentially complimentary role to the deep reflection techniques. In contrast to the near-vertical incident seismic reflection surveys, seismic refraction surveys make use of the arrival time and amplitude of refracted seismic waves traveling through the crustal interfaces. A vertical seismic profiling (VSP) technique makes use of the boreholes and records seismic signals directly at depth up to a few kilometers deep. By correlating and linking the characteristics of the seismic response with geological well-log information, the VSP technique bridges the observation gap between the surface observed reflection profiles and the borehole sonic logs. It thus provides invaluable information for structural, stratigraphic, and lithological investigation in complex geological areas.

Integration of various above seismic techniques along with other auxiliary geophysical techniques greatly extends the capabilities of seismic techniques. Integrated seismic study has already proven to be a very powerful technique in petroleum exploration, and it has also become a very successful approach in lithospheric exploration. During the past a few decades, a number of such integrated seismic investigation

for scientific purposes have been carried out throughout the world. They constitute the central cores of several national collaborative, multidisciplinary earth science research programs such as LITHOPROBE in Canada, ACORP in Australia, and ECORS in France (Barazangi and Brown, 1986, Meissner et al., 1991). In this thesis research, multi-offset three component VSP, surface reflection, and high resolution refraction techniques were utilized to study the complicated Sudbury Structure and surrounding area. The seismic surveys investigated are a part of the LITHOPROBE Abitibi-Grenville Transect (AGT) (Sudbury sub-transect) projects. The participants of the LITHOPROBE AGT Sudbury sub-transect include École Polytechnique, Laval University, University of Manitoba, University of Montreal, University of West Ontario; Geological Survey of Canada, Ontario Geological Survey (OGS), US Geological Survey (USGS); Inco Exploration and Technical Service (IETS), Falconbridge Ltd. and other local mineral industry participants.

1.1 Study Area and Objectives of the Research

The study area is the Sudbury Structure and surrounding area in northern Ontario, which is well known for its unique geological structure and the great economic value of the area's mineral deposits. It was chosen as a LITHOPROBE AGT Sudbury sub-transect as well as a multi-sensor geophysical survey site (1989) by the Geological Survey of Canada. For similar reasons, the Sudbury area was also chosen as one of the scientific verification sites for the Earth Resource Satellite (ERS-1) (1991) by the European Space Agency. A vast number of research activities were carried out in the past and the trend is expected to continue in the future. Table 1.1 lists some of the

geophysical and geological data sets available for this thesis research in the area.

The first reflection seismic survey in the Sudbury Basin was carried out in 1965 by a Calgary contractor GSI Inc. for IETS. The dynamite survey data, covering about 6 km across the North Range near Welsner township, were of very poor quality and the usefulness for mineral exploration was marginal. In 1985, the geophysics group at the University of Manitoba planned and contracted out a high resolution reflection seismic survey across the North Range (Moon et al., 1989). The survey was designed as a shallow high resolution reflection survey with a total line length of approximately 5 km along an abandoned power line. A high speed explosive source was used in drilled shot holes. The final processed section imaged at least two south dipping reflection zones, one of which appeared to represent the granitic gneiss wall rock.

The LITHOPROBE Sudbury sub-transect experiments were planned for investigation of the true three-dimensional geometry of the Sudbury Structure, the Sudbury Igneous Complex (SIC) and associated major faults, the geometry of the mid and lower crust beneath the Sudbury Basin, and the geometry and geological relationship with the Grenville Front boundary (Clowes, 1989).

Table 1.1: Geological and geophysical data sets available in the Sudbury area

Lithoprobe Seismic Data

- Reflection data (both regional and high resolution)(Oct., 1990, 1993)
- VSP data (Vertical Seismic Profiling) (Oct., 1990)
- High resolution refraction data (July, 1992)
- Well-log data (Summer, 1991)

Multiple Sensor Geophysical Data

- Airborne C-SAR data (C-band synthetic aperture radar) (1989)
- Landsat TM (thermatic mapper data, 1988)
- Ground gravity data (1988)
- Ground and airborne magnetic data (1988, 1989)
- Gamma ray spectrometer data (1989):
  - exposure rate
  - potassium equivalent uranium
  - equivalent thorium
  - eU/eTh ratio
  - eU/K ratio
  - Th/K ratio
- Airborne VLF-EM total field data (1989)
- Airborne VLF-EM quadrature data (1989)
- Ground EM and MT data (1991)
- ERS-1 (Earth Resource Satellite) SAR data (launched in 1991)

Geological Maps

- OGS (Ontario Geological Survey) compilation map (1984, 1990)
- Limited local mining company maps

The seismic data obtained from the LITHOPROBE seismic surveys, including the regional and high resolution seismic reflection (1990), three component multi-offset VSP (1990), and high resolution refraction data (1992), have been processed and interpreted in this thesis. The scientific objectives include:

- Design of an effective data processing sequence and estimation of optimal processing parameters for seismic reflection data acquired in crystalline rock terranes such as the Sudbury area, and imaging of the subsurface structures associated with the Levack Gneiss Complex in northwest of the Sudbury Structure.

- Application of the 3-Component (3-C) multi-offset VSP data processing and interpretation techniques to explore shallow structures in the Sudbury Basin and and correlation of the VSP data with the high resolution reflection data to resolve the relationships between the sedimentary layers within the basin.

- Development of new seismic data processing techniques for both VSP and reflection seismic data to image complex structural features such as dipping geological discontinuities and to improve the S/N ratio of the data from low acoustic impedance contrast media of the Sudbury region.

- Provision of a preliminary image of the major crustal features in the vicinity of the Sudbury Structure by combination of the results from the reflection and the high resolution refraction data.

- Interpretation of the seismic data together with auxiliary airborne and satellite-borne geophysical data to resolve and clarify the geologically significant seismic features.

- While seismic exploration techniques have become the primary exploration tool of the petroleum industry, these techniques have seen little application by the mineral industry in the past. However, both major types of the ore bodies found in the Sudbury area are coincident with pronounced stratigraphic reflectors such as the sediment-hosted sulfides lying along the Onwatin shale/Onaping tuff contact and the massive sulfides occurring at the Norite/Footwall contact. Thus an integrated seismic study is also expected to provide valuable information for base metal exploration in the Sudbury area.

With the above objectives, this thesis research was developed in two directions. Each individual seismic data set was investigated in detail, and interpretation was carried out among various of seismic results and other geophysical images interactively. Chapter 1 introduces and describes the background and objectives of the research. Chapter 2 describes the geological setting of the study area, the Sudbury Structure. It includes the current geological and planetological hypotheses on the origin, formations, and associated tectonic history of the Sudbury Structure. In Chapter 3, previous seismic and other geophysical studies carried out in the Sudbury area and related to this thesis research are briefly reviewed. Chapter 4 describes various features of seismic data acquisition such as field survey lines, recording parameters, seismic sources in the VSP, high resolution and regional seismic reflection, and high resolution refractions surveys. In the following three chapters, Chapter 5, 6, and 7, the seismic data processing steps and technique developments conducted in this thesis research are discussed in detail. Chapter 5 focuses the multi-offset 3-C VSP study, which involves data processing techniques utilized and developed for the VSP data sets, such

as travel time inversion, wavefield separation, VSP-CDP transform, and shear wave analysis techniques, and the VSP data interpretation techniques, for instance, the development of a particle motion hodogram analysis approach for estimation of true dip of reflectors, and correlation of the results with surface high resolution reflection data. In Chapter 6, the seismic reflection data processing techniques particularly designed for the regional reflection line 42 are discussed. Two newly developed data processing techniques, the time-varying cross-dip correction and removing of ground roll noise using the wavelet transform technique, are highlighted. An important result in this chapter is the successfully imaged subsurface structure in the vicinity of the Levack Gneiss Complex, the northwest of the Sudbury Structure, which is a key area for resolving the enigma on the origin of the Sudbury Structure. The integrated interpretation of the seismic results with other geophysical data sets, such as the ERS-1 SAR data and other remote sensing data, is also discussed in Chapter 6. In Chapter 7, the wavelet transform is discussed in detail. The advantages of this new technique over the conventional methods, its mathematical properties, and the effectiveness of the new approach to seismic data processing are investigated. Two examples are included to demonstrate the application of the wavelet transform. Finally the overall results of this thesis research are evaluated and discussed in chapter 8. The final conclusion and recommendation for future research are summarized in Chapter 9.

Chapter 2

Geological and Geophysical Setting of the Study Area

2.1 Geology setting of the Sudbury Structure

The Sudbury Structure (SS) is located at the 'junction' of the Superior, Southern, and Grenville structural provinces of the Canadian Precambrian shield (Card et al., 1984). The Superior Province to the north consists of Late Archean supracrustal, plutonic and gneissic rocks. The Southern Province to the southwest consists of Proterozoic sedimentary, volcanic, and mafic and felsic plutonic rocks. The Grenville Front, which is the northwestern boundary of the Grenville Province, bounds of the Sudbury Structure at about 15 km southeast. The Front is a major northeast trending structural discontinuity and is well defined in the regional potential field map at the crustal scale (Clowes, 1989). The Sudbury Structure is also located at the intersection of several major fault systems, even though the ages of these faults are younger than the Sudbury Structure itself (Peredery and Morrison, 1984). Figure 2.1 shows the regional geological setting of the Sudbury Structure.

The major geological units identified in the Sudbury area consist of (Dressler, 1984b):

- the Proterozoic mafic and felsic intrusive rocks of the Sudbury Igneous Complex (SIC), which grades from the outer ring of norite through a transition zone of gabbro to an inner ring of granophyre (see Figure 2.2),
- the Whitewater group within the SIC envelope, consists of the Chelmsford greywacke, Onwatin shale, and Onaping formations, including Onaping suevite (black and gray members of breccias) and Onaping basal member (see Figure 2.2),
- the late Archean gneissic rocks of the Levack Gneiss Complex (LGC), which lies in the north and east-side of the outer contact of the SIC and contains pyroxene granulite and amphibolite facies rocks,
- breccias in the Archean and Proterozoic Footwall rocks of the SIC,
- the quartz diorite offset dikes within the surrounding footwall rocks, which extend either radially away from, or strike parallel to, the SIC, and
- the post-igneous complex mafic dike rocks, found mainly in the South Range of the SIC and South Range Footwall rocks, include middle Proterozoic olivine diabase dikes intruded into all the forgoing rocks.

The so-called Sudbury Structure is made up of extensive regions of brecciated country rock, the SIC, and the enclosed Whitewater group. The often used terminology of the "North Range", "East Range", and "South Range" is depicted in Figure 2.2.

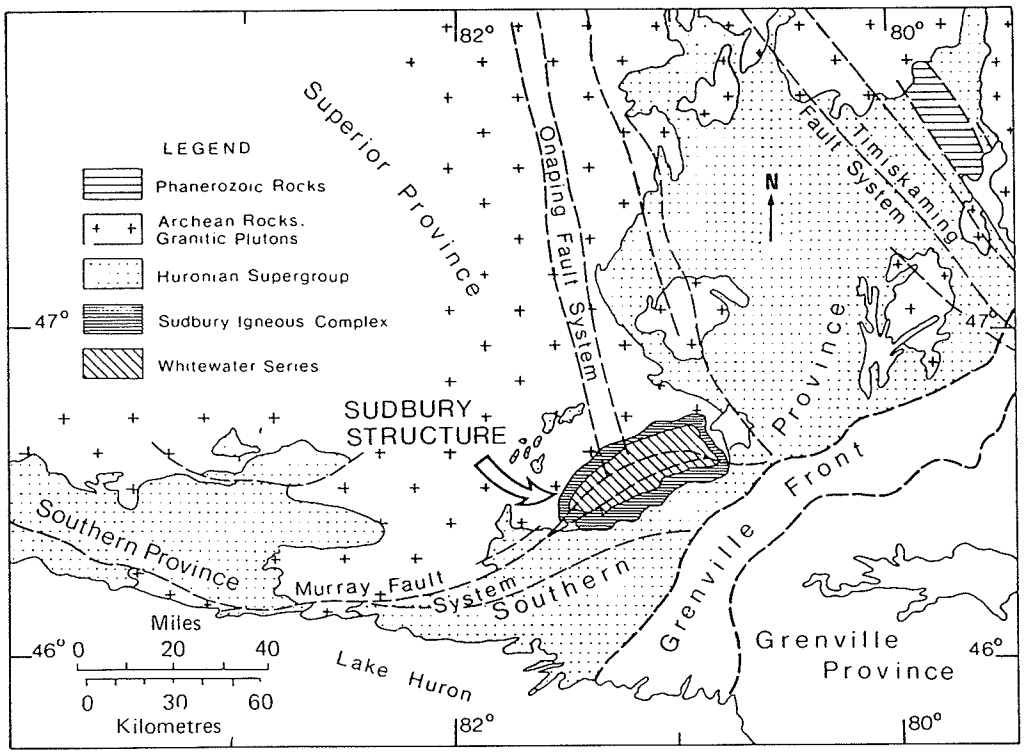

Figure 2.1: Regional geological setting of the Sudbury Structure (Card et al., 1984).

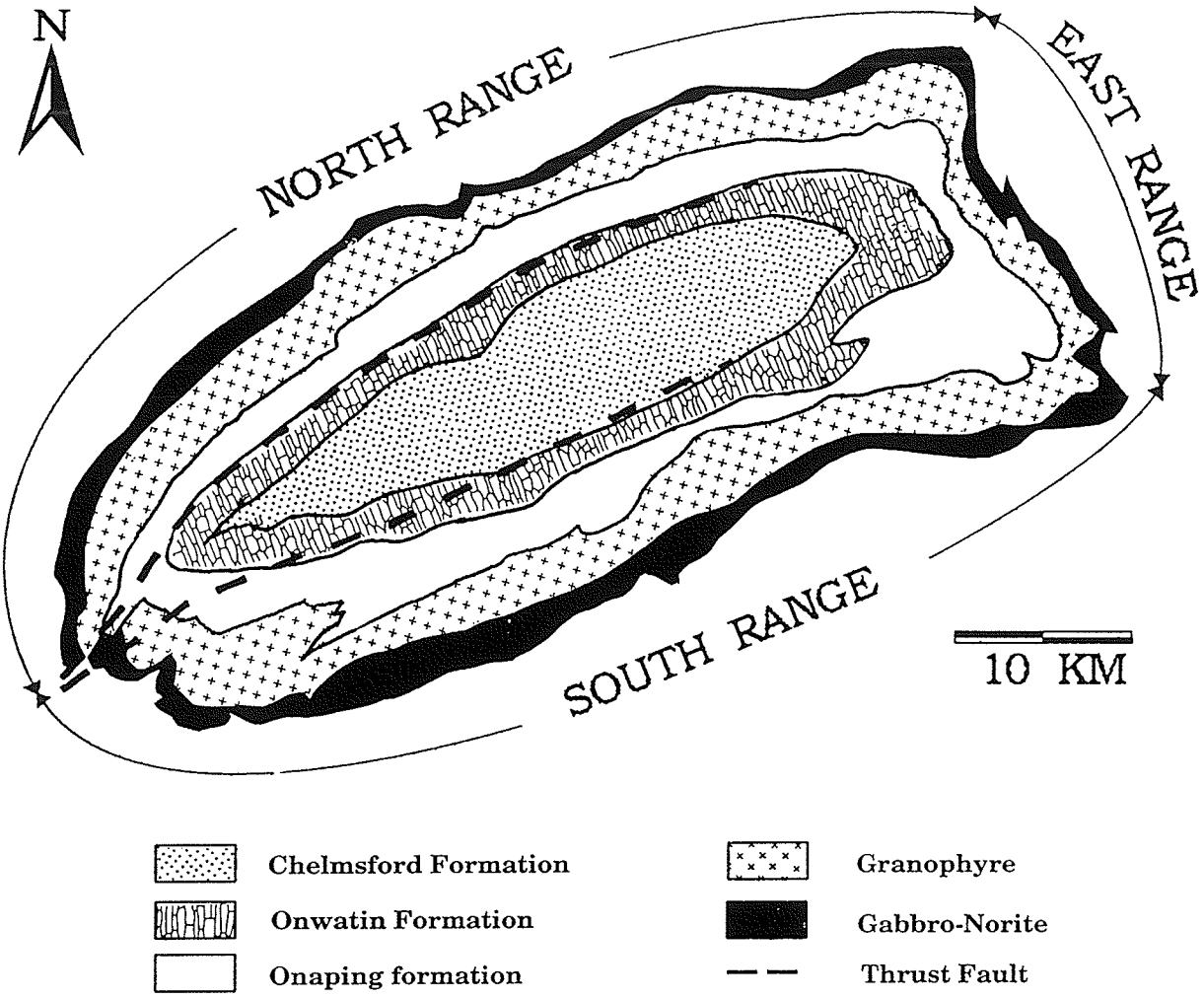

Figure 2.2: Simplified geological map showing geological formations in the Sudbury area including the Whitewater group (Chelmsford, Onwatin, and Onaping formations) and the Sudbury Igneous Complex (SIC) (Granophyre, Gabbro and Norite rock units). Modified from Wu et al., 1994.

On the gravity map (Gupta, 1984), the Sudbury Structure is situated within a large, SW-NE striking elliptical gravity high of about 30 mgal. It is part of a positive gravity anomaly extending over about 350 km from Elliot Lake to Englehart, Ontario. The anomaly itself is much broader than the Sudbury Structure. The airborne total field magnetic map of the area is characterized by a semicontinuous elliptical ring anomaly coincident with the SIC. The gabbros and associated ultramafic rocks in the SIC may be responsible for this anomaly. A linear anomaly of moderate amplitudes close to the contact between the Onaping and Onwatin Formations on the south side of the basin, and a broad positive anomaly close to North Range extending northwest to the LGC are also noticeable in the aeromagnetic map (Gupta, 1984).

2.1.1 Origin of the Sudbury Structure

There are at present two main hypotheses for the origin of the Sudbury Structure: the volcanic explosion theory and the meteorite impact theory.

(a) **Early explosive volcanism theory.** It is believed that the Sudbury Structure might have originated from a volcanic explosion 1850 Ma ago or from other possible endogenic processes. Most characteristic geological features of the Sudbury Structure can readily be explained through endogenic processes. The Sudbury Structure is, in various degrees, related to crustal features such as: the Great Lakes Tectonic Zone - Murray Fault Zone; the Grenville Front Boundary Fault; a large scale curvilinear positive gravity anomaly; large elongate positive magnetic anomalies, and the Wanapitei structure (the convex shape of the East Range, if assuming it is a cryptoexplosion). One or more large intrusions underlying the Sudbury Structure were

invoked to interpret the positive gravity anomaly. The Sudbury Structure is also genetically associated with large volumes of volcanic rocks present in the Onaping formation, and plutonic rocks present as the SIC. The setting in time and space of the Sudbury Structure indicates that it is more likely to be of endogenic origin rather than the product of meteorite impact (Card et al., 1972; Stevenson, 1980). The precise mechanisms that resulted in endogenic shock metamorphism, however, remain to be explained in detail.

(b) **Meteorite impact theory.** It was proposed that the original Sudbury Structure may have been produced by meteorite impact about 1850 Ma ago, accompanied by shock compression and excavation of a transient crater, and ejection of melt. Brecciated country rocks were thrown radially out of the crater followed by elastic rebound and isostatic adjustment to form a modified crater. The norite and granophyre magma uplift and intrusion, and subsequent collapse formed the present setting of the Sudbury Structure (Dressler, 1984a).

The impact theory was first proposed by Dietz (1964) and further evidence of shock-induced magmatism and tectonism was reported later in the country rocks surrounding the Sudbury Structure. Comparison of the Sudbury Structure with well documented meteorite impact sites indicates that the features discovered in Sudbury are of typical large impact sites (Head 1977). These include an original polygonal outline, large troughs at the apices of the polygon, terraced walls, the original relatively shallow inward dipping floor of the structures, and intense and extensive brecciation of footwall rocks. There also appears to be direct link between brecciation and shock metamorphism. The convex shape of the East Range (the Wanapitei structure) may be yet another late meteorite impact (37 Ma) superimposed on the original Sudbury

Structure.

As more impact related evidence is discovered, a majority of scientists regard Sudbury as a meteorite impact site (astrobleme), even though the origin is still debated. The dimensions and shape of the original Sudbury Structure are believed to be critical to understand the origin of the Sudbury Structure (Boerner and Milkereit, 1994). Since many observed large impact sites are circular, the present 60 × 30 km elliptical shape of the Sudbury Structure has been argued for many years. If the original diameter of the Sudbury Structure is 60 km, the energy release is not sufficient to have generated the estimated volume of the SIC as an impact melt (Boerner and Milkereit, 1994). Some people think that the postulated size of the original crater appears to require a component of internally generated magmatism to account for the volume of the SIC and associated lithologies (Peredery and Morrison, 1984). However, recent isotopic, geochemical, and petrographic studies have demonstrated that rocks and ores of the SIC were derived largely from the Archean crust and Early Proterozoic cover rocks with only subordinate contributions (if any) from mantle magmatism (Faggart et al., 1985; Naldrett et al., 1986; Walker et al., 1991; Grieve et al., 1991). This result supports the impact origin.

The recent LITHOPROBE seismic high resolution reflection survey revealed a mainly southern dipping subsurface geometry across the Sudbury Structure, which suggested a prominent shortening along the NW direction and implied a much larger size of the original diameter of the Sudbury Structure (at least twice of the present size). A dense mafic mass is no longer required to interpret the observed gravity anomaly above the Sudbury Structure based on the geometry defined by the recent high resolution seismic result (MacGrath, 1994).

Considering the NW compression of the Sudbury Structure, Roest and Pilkington (1994) studied the deformation by using an inferred horizontal strain pattern to 'decompress' the potential field data and recovered a nearly circular shape of the potential field anomalies. Roest and Pilkington (1994) also suggested that the original diameter of the present exposure of the SIC could have been at least 65 km. However, by analogy of the Sudbury Structure to lunar maria, Lowman (1993) still favors an original impact structure of elliptical shape and only slightly larger size than the present outcrop of the SIC. In reviewing the recent results from the LITHOPROBE Sudbury project and other studies, Deutsch and Grieve (1994) concluded that the present non-circular shape of the SIC is caused by the post-impact ductile deformation and northwest directed compression, thus the original diameter of the final crater could be up to 280 km.

Based on the recent LITHOPROBE seismic results, lithologic analysis of the geochemical components of the Sudbury formations, and geological observation, a recent impact model was presented by Avermann et al. (1994) to illustrate the impact history and to explain the original size and volume of the melt bodies. The model described a sequence of the impact event for the formation of the Sudbury Structure (see Figure 2.3), and also suggested a peak-ring or multi-ring structure for the Sudbury Structure with original rim diameter on the order of 200 to 250 km.

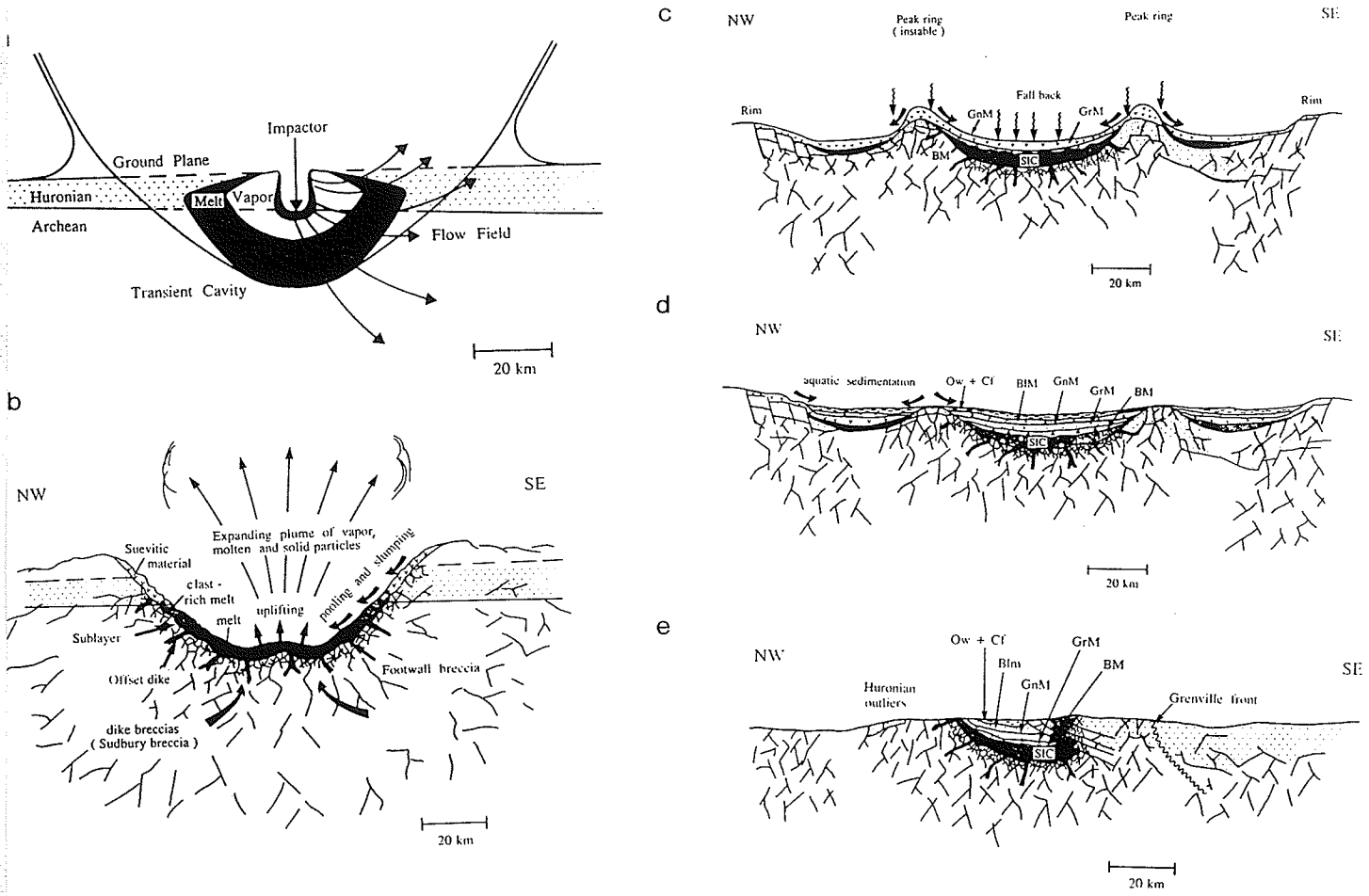

Figure 2.3: An impact model presented by Avermann et al. (1994) to represent various phases of the Sudbury impact crater formation with vertical scale exaggerated: (a) Geometer of the melt and vapor zones superimposed upon transient cavity; (b) Formations of the Sudbury breccia, Sublayer and offset dikes, and distribution of melt; (c) final stage of the transient cavity collapse with formation of peak ring and terraced rim, emplacement of melt sheet; (d) modification of the final crater by deposition of sediments; (e) the present Sudbury Structure after deformation during Penokean orogeny, regional metamorphism, and erosion. (after Avermann et al., 1994).

However, the impact related structural features in the basement of the crater, north and northwest of the SIC where the LGC is located, are relatively unknown. This increases the importance of discovering the subsurface structure in the northwest of the SIC.

In the following two subsections, two local geological units, the Whitewater group where the VSP borehole located, and the LGC the reflection line 42 crosses, will be discussed in detail to provide further geological background for seismic data interpretation in the later chapters.

2.1.2 The Whitewater Group

The Whitewater group sediments constist of argillite (Onwatin Formation) and turbidite units (Chelmsford Formation) over the Onaping breccia (Figure 2.2). Argillite units at the base of the Onwatin formation are the host of hydrothermal sedex Cu-Zn-Pb deposits (Davies et al., 1991). Structurally the Whitewater group lies above the SIC and is contained in the central depression of the Sudbury Structure known as the Sudbury Basin (Dressler et al., 1992). However the relationship between the Whitewater group and the SIC which extends to as deep as 2700 m along the footwall contact of the Sudbury Structure (Roussell, 1984) is relatively unknown. Throughout the Sudbury Basin, geological units in the Whitewater group are poorly exposed, and little is known about the timing and rate of deposition, and subsequent deformation. Where exposed, the contacts between the Onaping, Onwatin and Chelmsford formation, are described as gradational (Roussell, 1984).

2.1.3 The Levack Gneiss Complex

In the outer northwestern rim of the Sudbury Structure, there is a north to south progression from the Archean granite-greenstone rocks through massive felsic and intermediate granitic plutons to the high-grade gneissic terrain, the Levack Gneiss Complex (LGC). The LGC which forms a 5-8 km wide zone along the Sudbury Structure wraps around the North and East Ranges of the SIC (James and Dressler, 1992). To the north, it contacts with massive granites of the Cartier Batholith. The contacts on both sides of the LGC, however, are discordant (Card, 1994).

The LGC was intruded and extensively retrograded by the Cartier Batholith, post-tectonic Algoman granites, late Archean to Middle Proterozoic mafic dikes, and veins and irregular masses of the Sudbury Breccia (Pye et al., 1984). It is mostly composed of migmatitic tonalitic gneisses which contain lower crustal rocks of pyroxene granulite facies near the SIC and amphibolite facies to the north, indicating an original depth range of 21 to 28 km (6-8 kbar) assuming the underground temperature ranges from $750 - 800^{o}$C (James and Dressler, 1992). It appears to be subjected to shock metamorphism related to the Sudbury Event (the tectonic event which created the original Sudbury Structure) and contact metamorphism related to the intrusion of the SIC. The uplift of the LGC has many similarities to the Kapuskasing Structural zone, which is a prominent uplifting of a high-grade gneissic terrain in the center of the Superior Province. The relationship between the structural uplift (SU) and the size of the Sudbury Structure suggests that the maximum uplift is of the order of 15-20 km (Grieve et al., 1991). The LGC is also considered to probably contribute significantly to the formation of the SIC and its ores (Card, 1994). The Huronian sedimentary and

igneous rocks and the Nipissing mafic intrusion (2200 Ma) bound the South Range, some of which even intruded in the west of Sudbury Structure about 10 km west from the regional seismic survey line 42 (Figure 4.1). Even though the deformation in the northwest of Sudbury is relatively weak compared with the South Range, similar deformation zones probably exist north of the Sudbury Structure (Card, 1994).

The gravity and magnetic anomalies show that the LGC is situated on the edges of a large linear positive gravity anomaly zone and an elliptical positive magnetic anomaly zone. The gravity low in the northwest of the Sudbury Structure characterizes the Archean plutonic rocks. Airborne γ-ray spectrometry data outlines a wider rim of potassium anomaly in the northwest surrounding the North Range of Sudbury Structure (Singh et al., 1993). Whether the γ-ray spectrometer anomalies are related to the outer boundary of the LGC or not remains to be answered.

2.2 Tectonic History of the Study Area

The Sudbury Event (SE), which formed the original Sudbury Structure, occurred in the Early Proterozoic at about 1850 Ma. During the Sudbury Event, the SIC was emplaced and immediately followed by deposition of Whitewater group sediments. The tectonic event closely linked to the Sudbury Structure is the Penokean Orogeny, a tectonic metamorphic and thermal event which occurred in the Huronian strata of the Southern Province during 1800 Ma to 1900 Ma (Zolnai et al., 1984). The initial ductile deformation of the Huronian strata during the Penokean Orogeny appeared to be transported northward and resulted from continental-continental collision and depression of the Huronian wedge to the middle crustal level. The Sudbury basin was

then shortened by a tectonic push towards the northwest, which resulted in structural deformations including foliations, lineations, cleavages, folds, faults, and joints. The deformation in the area thus can be represented as two phases, the pre 1850 Ma ductile deformation and the post 1850 Ma brittle deformation (Zolnai et al., 1984). The intensity of deformation appears to decrease toward the northwest.

Two interpretations for the timing of the crustal uplift of the LGC were proposed based on the geological and geochemical studies (James and Dressler, 1992). One interpretation suggests that the the gneisses were tectonically uplifted prior to the Sudbury Event (possibly during the intrusion of the Cartier Batholith). The other interpretation is that the gneisses were raised to epizonal levels as a result of meteorite impact at 1850 Ma. More study is needed to determine when the LGC was uplifted, and how the distribution of the LGC is related to the SIC.

Chapter 3

Review of Geophysical Studies on the Sudbury Structure

In this chapter, the previous geophysical research conducted on the Sudbury Structure and related to the processed seismic data in this thesis is briefly reviewed.

Prior to the LITHOPROBE Abitibi-Grenville Transect experiments, geophysical studies on the Sudbury Structure were mostly focused on gravity, magnetic and electromagnetic survey. Gravity and magnetic modeling of the deep crustal structure was attempted by Gupta et al. (1984) to interpret the observed gravity and magnetic anomaly. After the late 1980's, a large number of geophysical surveys have taken place in the Sudbury area (see Table 1.1), providing high quality data sets for geophysical studies and geological interpretations. Among them the results of the seismic reflection surveys were one of the most significant achievements, revealing deep subsurface geological structures previously unknown in the Sudbury area.

3.1 Results from Previous Seismic Studies

One of the first convincing subsurface deep structural models was proposed by Milkereit et al. (1992) based on the LITHOPROBE seismic reflection survey results. The seismic reflection data (Lines 40, 41, and 42) were processed by a contractor, after which several reprocessing were carried out. Preliminary results of these seismic profiles except the line 42 profile were interpreted by Milkereit et al. (1992).

The high resolution seismic section across the North Range (line 40-1) releaved the boundary between the layered LGC and SIC with a clear change from high to low levels of reflectivity and marked by quasicontinuous reflection event E in Figure 3.1 (Milkereit et al., 1992). The LGC is represented by the prominent horizontal to south-dipping reflections beneath boundary E. The profile also marks the boundary within the SIC (granophyre to gabbro and norite sublayer). The transition of mafic rock to granophyre produces the pronounced reflection event.

An interpreted geological model of the Sudbury Structure from the lines 40 and 41 data was presented by Milkereit et al. (1992) in Figure 3.2. A conspicuous feature of the seismic section is the marked change in structural style across the center of the Chelmsford Formation at times < 2.0 s. To the north, the reflection zones (B,C,D,E in Figure 3.2b) describe slightly south dipping lithological contacts which can be traced in borehole observations (see Figure 3.2a). To the south of the section, the data are dominated by broad zones of intense reflections (P, Q, and R). The reflection events A and B represent the boundaries of units within the Whitewater group (the Chelmsford to Onwatin Formations and the Onwatin to Onaping Formations). The strong reflection events P and Q are interpreted as major faults or shear zones, projected to

the surface (R1 and R2 in Figure 3.2b) north of the mapped shear zone. In the center of the basin, the reflections are truncated by a steep south dipping fault marked by S, which interrupts the layers of the Whitewater group and granophyre.

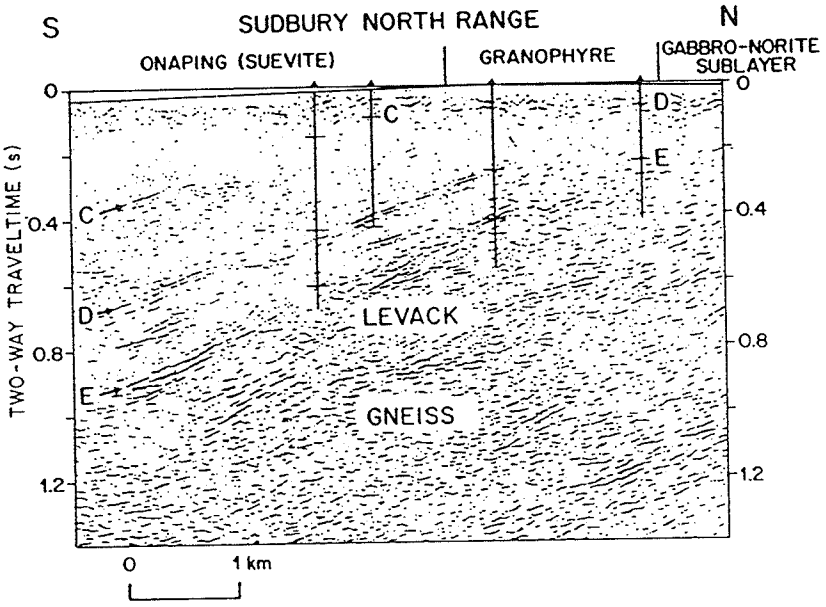

Figure 3.1: The high resolution reflection section (line 40-1) in the North Range, Sudbury (Milkereit et al. 1992).

Based on these seismic results Milkereit et al. (1992) suggested that the original dimension of the major axis of the basin structure was at least twice of the present one. The recent seismic survey results are also in agreement with the South Range Shear Zone model proposed by Shanks and Schwerdtner (1991a) from structural geology studies.

Nevertheless, the subsurface structure beyond the North Range across LGC was not investigated seismically until now mainly due to the very poor quality of preliminarily processed result of line 42. Several problems are waiting to be resolved; one of the outstanding problems is the uplift of the LGC, mentioned by Boerner and Milkereit (1994) in the special section of LITHOPROBE Sudbury project:

"The highly reflective footwall complex to the SIC, the Levack gneiss, is prominent geophysically and may represent uplifted continental crust. Theses rocks have variable properties and appear to have a more dense and more magnetic phase near the contact of the SIC. Levack gneiss exhumation history and its relation to the time of formation of the SIC is crucial."

The data from line 42 which acrosses the LGC were reprocessed in this thesis research with the objectives of resolving some of the questions related to the LGC. The details will be discussed in Chapters 6 and 7.

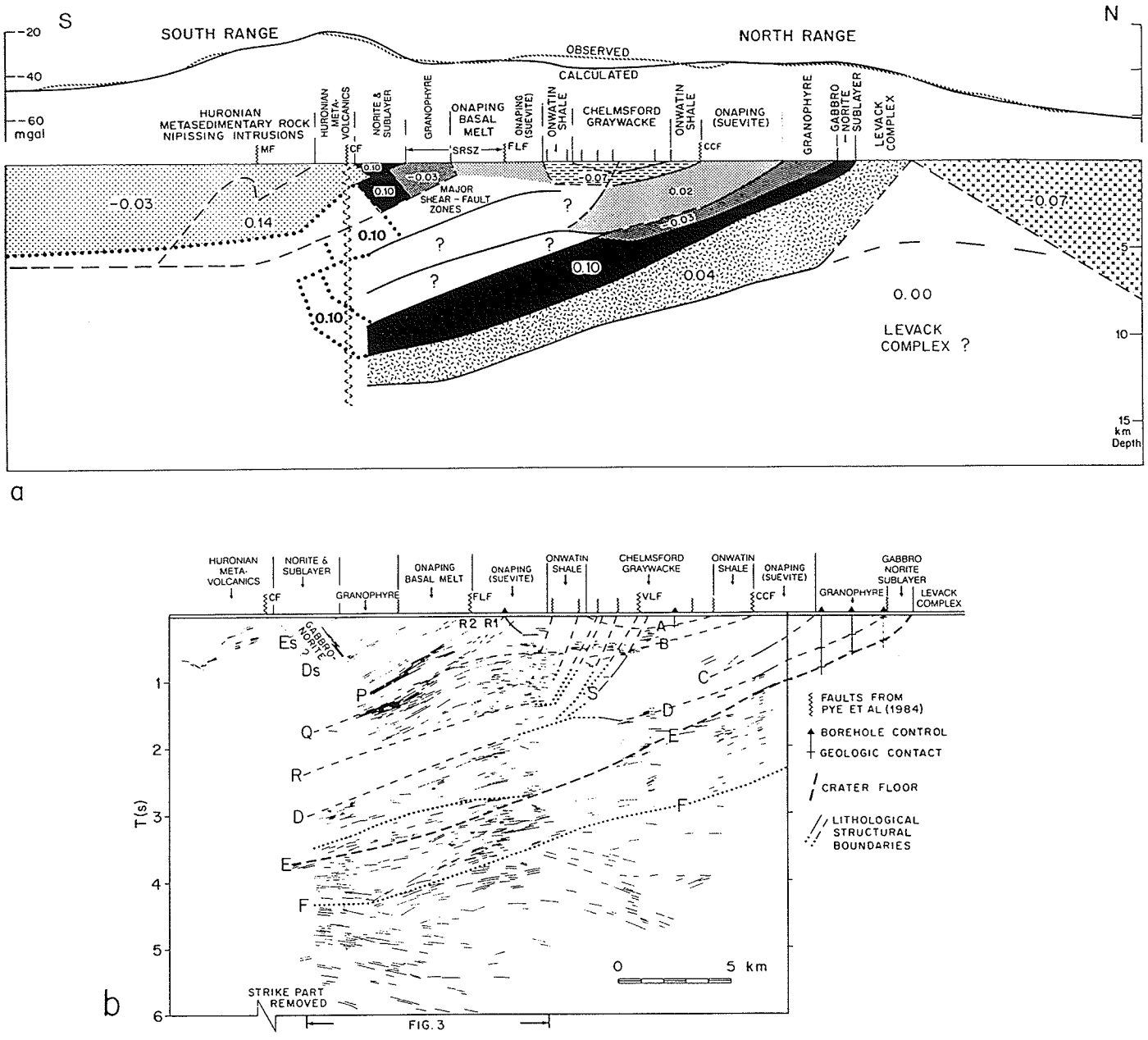

Figure 3.2: (a) Interpreted and proposed deep geometry of the Sudbury Structure. Most model boundaries are determined by seismic reflection data. Back ground density is taken to be $2.73 g/cm^3$. Relative densities are based on Sudbury rock samples. (b) Composite sketch of reflection patterns based on various stack and migrated seismic images of the lines 40 and 41. Boreholes are shown by triangles and inclined and vertical lines. Abbreviations are the same as in the Table of Symbols (e.g. VLF=Vermilion Lake Fault). (Milkereit et al. 1992).

3.2 Review of Other Geophysical and Remote Sensing Studies

3.2.1 Previous Potential Field Studies

Previous geological models of the Sudbury Structure based on gravity data (Gupta et al., 1984) were constrained by surface geology and by density measurements of surface and borehole rock samples. In general, the regional gravity lows in the Sudbury area are related to large masses of granitic rocks, whereas regional gravity highs are probably correlated to the gabbro-anorthositic rocks of limited surface exposure, but which may be much more extensive at depth (Popelar, 1977). Lack of a strong positive gravity anomaly associated with the Sudbury Structure implies a weak positive density contrast ($< 0.1\ g/cm^3$) between the Sudbury Structure and surrounding country rocks (Popelar, 1977).

To interpret the observed regional positive Bouguer gravity anomaly, Gupta et al. (1984) suggested a massive mafic layer was hidden beneath the Sudbury Structure in the depth range of 5 to 8 km with a density of approximately 3.0 g/cm^3 (Figure 3.3), and extended laterally to the west and northeast beyond the present surface expression of the Sudbury Structure.

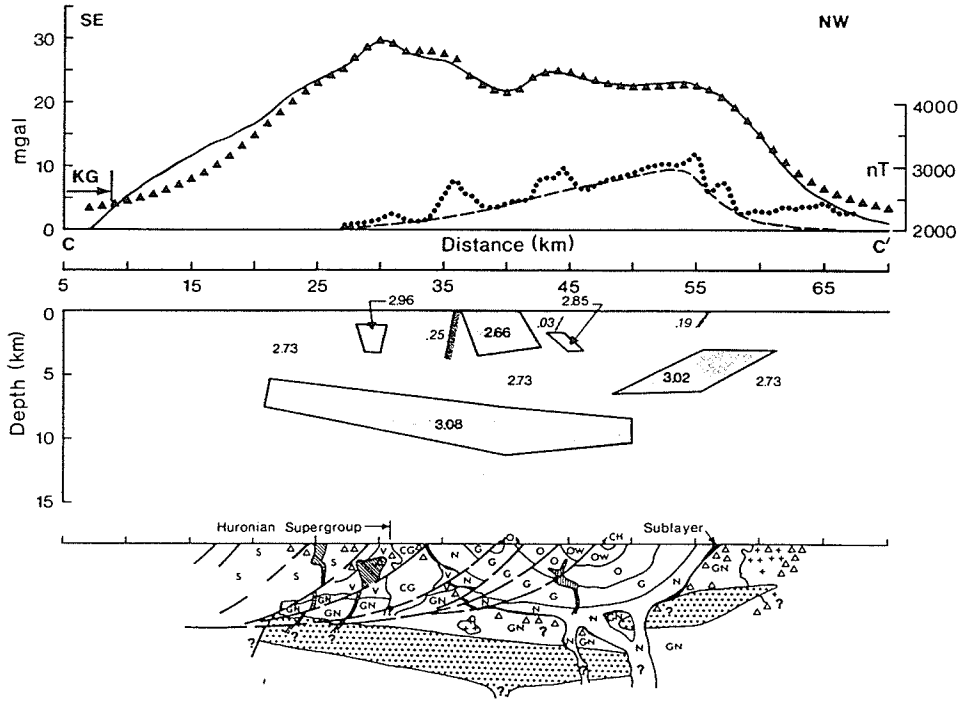

PRECAMBRIAN
Southern Province (Early Proterozoic)

SUDBURY STRUCTURE
Gabbroic rocks (from Geophysics)

SUDBURY IGNEOUS COMPLEX
Sublayer (marginal sublayer and offsets)
G Upper Zone (granophyre and plagioclase-rich granophyre) and Middle Zone (quartz gabbro)
N Lower Zone (norite)

WHITEWATER GROUP
CH Chelmsford Formation (wacke)
OW Onwatin Formation (mudstone)
O Onaping Formation (heterolithic and minor monolithic breccia)

FOOTWALL BRECCIA AND SUDBURY BRECCIA
Sudbury Breccia (pseudotachylite)

GABBROIC INTRUSIVE ROCKS
Nipissing Gabbro (from Geophysics)

FELSIC INTRUSIVE ROCKS
CG,MG Proterozoic granitic rocks
Creighton Pluton, Murray Pluton

HURONIAN SUPERGROUP
S Arenites, wackes, conglomerates
V Metavolcanics

Superior Province (Archean)
+ Granitic rocks
Gn Granulite and amphibolite facies gneisses
Mafic to ultramafic intrusive rocks (Archean or Proterozoic, from Geophysics)

Anomalous Bouguer Gravity
Calculated Gravity
296 Gravity Model, Density in g/cm^3
Observed Total Magnetic Field
Assumed Regional Magnetic Field
Computed Regional Magnetic Field
.25 Magnetic Model, Susceptibility in SI
(25) Magnetic Model, Susceptibility in SI assuming Remanent Magnetization
$\mathcal{L}$ Thickness in km
KG Killarney Granite

Figure 3.3: The gravity models proposed by Gupta et al. (1984).

Based on the new deep geometry of the Sudbury Basin outlined by high resolution reflection data, a new modeling and interpretation were made on the gravity data along the LITHOPROBE transect (Figure 3.4) by McGrath and Broomes (1994). The key difference between the Gupta et al.'s and McGrath and Broomes's models is that in the Gupta et al.'s model a base level Bouguer gravity value of -58 mGal was assumed (Gupta et al., 1984), which actually should correspond to a background density of $2.67 g/cm^3$ of granitic rocks (even though 2.73 g/km^3 was used by them). But in the McGrath and Broomes's model a base level value of -42 mGal was used, corresponding to a background density of $2.73 g/cm^3$ of the Levack gneisses. Therefore a large dense mass underlying the Sudbury Structure is no longer necessary to interpret the observed regional positive Bouguer gravity anomaly. A new gravity model compatible with the LITHOPROBE seismic results (Figure 3.5) was presented. However, one of the suggestions related to the LGC in their model is:

"the large, ramplike, gravity anomaly, parallel but largely external to, the northwest margin of the Sudbury Structure is an expression of a moderatedly northward dipping boundary within the Archean terrain between the LGC and Cartier granite."

The above interpretations show that the boundary between the LGC and Cartier granite is dipping north and the dense LGC layer (density=$2.77 g/cm^3$) is separated from the Cartier granite by an additional layer of the LGC with density of $2.73 g/cm^3$ in the northern part of the profile (Figure 3.5). At the time of the McGrath and Broomes (1994)'s study, the subsurface structure beyond the LGC was not available. Reprocessing of the Sudbury regional seismic reflection line 42 becomes important in clarifying the subsurface geological structure of this region.

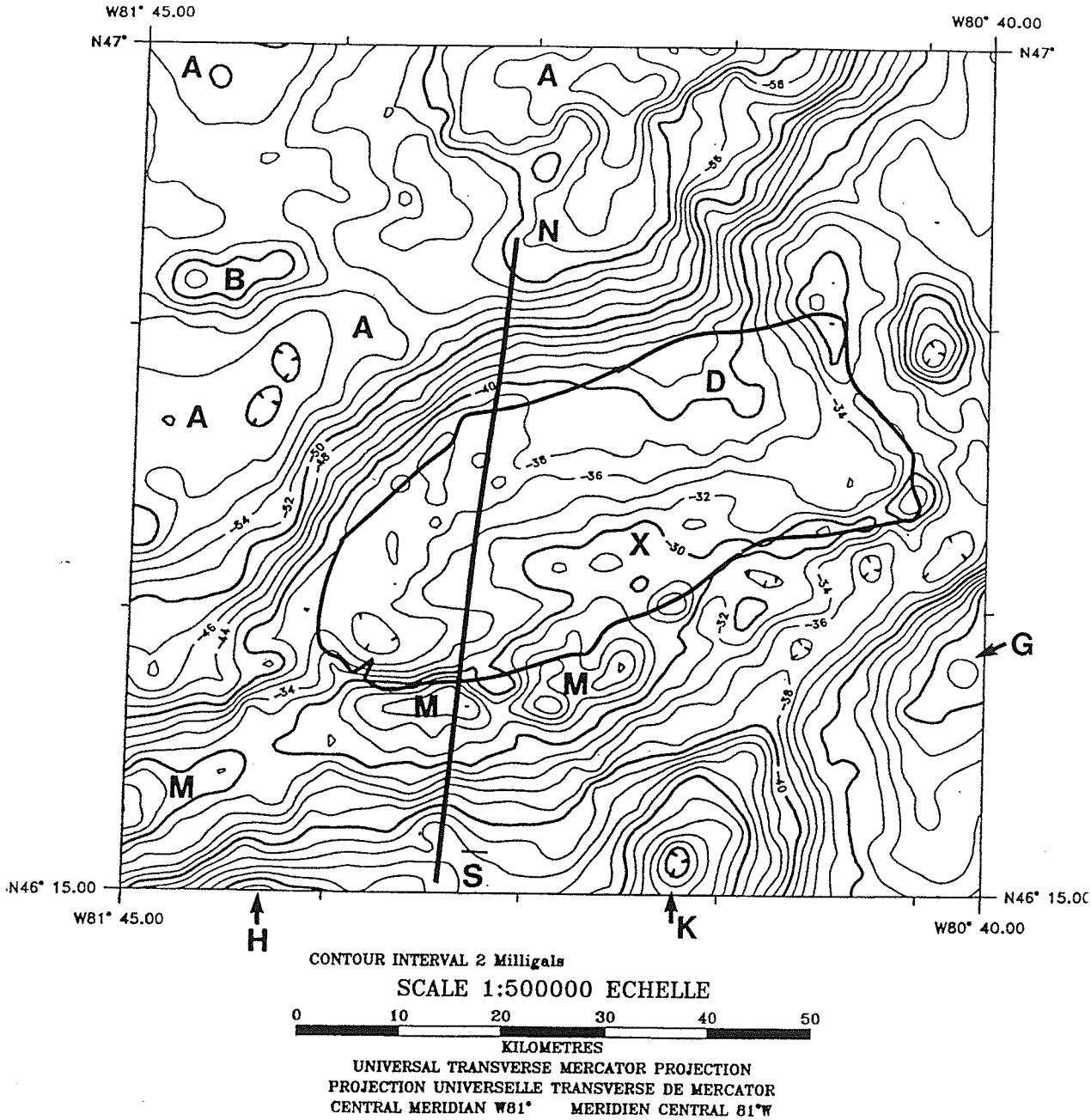

Figure 3.4: The new Bouguer gravity map of the Sudbury area. The contour interval is 2 mGal. The Sudbury Structure is located in the zone of high regional gravity. Interpretation of the profile, N-S, is illustrated in Figure 3.5 (McGrath and Broomes, 1994).

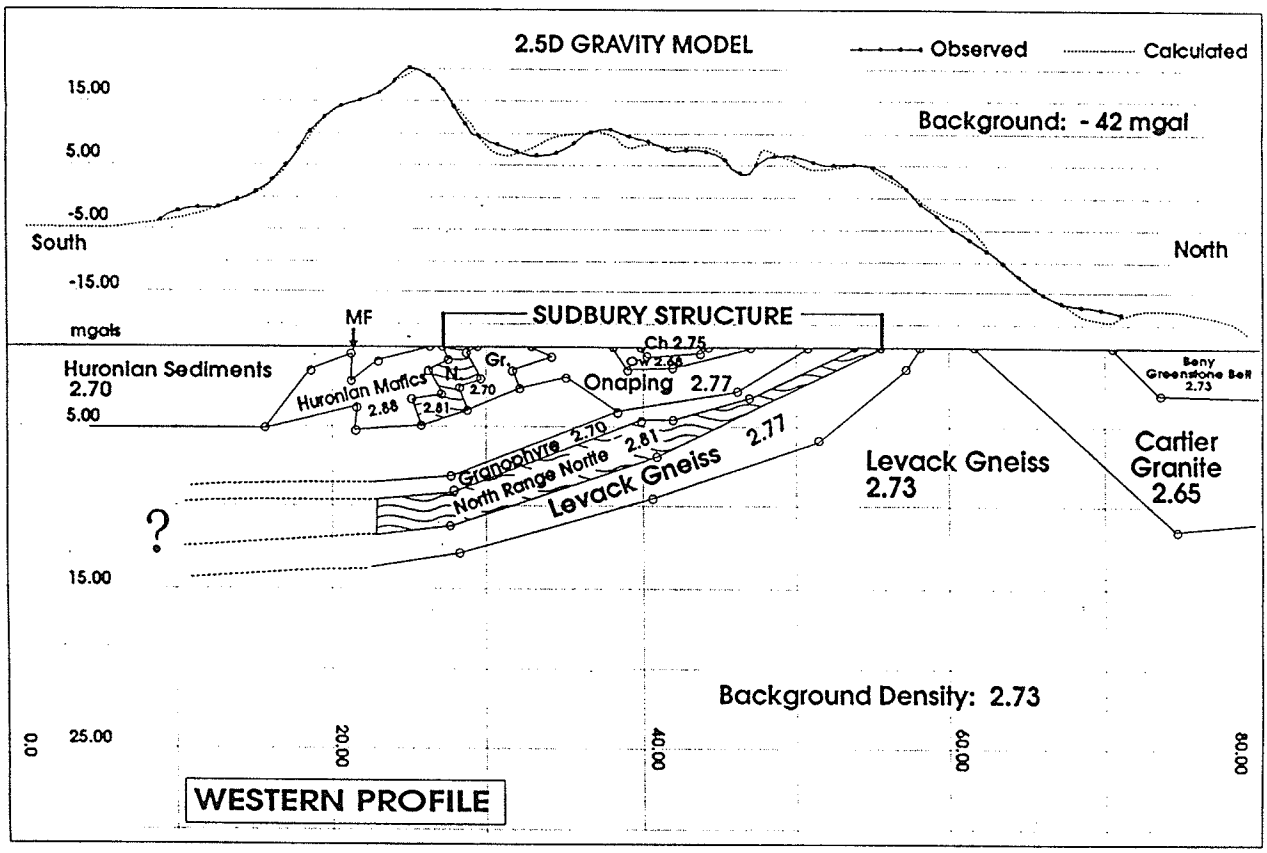

Figure 3.5: Gravity model of the Sudbury Structure along the profile N-S shown in Figure 3.4 after McGrath and Broomes (1994), where N-South Range norite, Gr-granophyre, Ow-Onwatin Formation, and Ch-Chelmsford Formations, MF-Murray Fault. Density boundaries to the north and south of the Sudbury Structure were not imaged in the seismic data.

Magnetic modeling study was also undertaken on the restrains of subsurface geometry provided by the LITHOPROBE high resolution reflection data recently (Hearst, et al., 1994). Unlike the gravity modeling, the initial magnetic modeling performed by rigidly adapting the geometry defined by seismic data did not give a good match to the observed magnetic data due to complication involved in the magnetic properties of the rock units in the SS. Further attempts were carried out by incorporating the results of new remanent magnetisation (NRM) and susceptibility measurements collected along the seismic profile line 41 and detailed magnetic structures within the broad geometric framework of the seismic and gravity model.

A new magnetic model was then obtained by Hearst, et al. with certain differences in detailed features from the gravity model (see Figure 3.6). In the magnetic model (Figure 3.6), the high magnetic anomaly was attributed to the LGC subjacent to the base of SIC. The Levack gneiss was divided into three groups, the dense Levack gneiss with susceptibility of 550×10^{-4} SI, Levack gneiss with susceptibility of 470×10^{-4} SI intruded by a couple of diabase dikes of very high susceptibility, and depleted Levack gneiss with susceptibility of 200×10^{-4} SI, to interpret the observed high magnetic anomaly above the LGC. The Cartier granite was represented as low magnetic anomaly with susceptibility of 375×10^{-4} SI. The high magnetic anomaly diabase dikes can be traced to the surface from their measurement. However, there was no observed evidence of high magnetisation zone at the surface where the LGC is located. The genesis of the enhanced magnetisation and higher density associated with the LGC, thus, was believed to be problematic geologically. (Figure 3.6) (Hearst, et al., 1994).

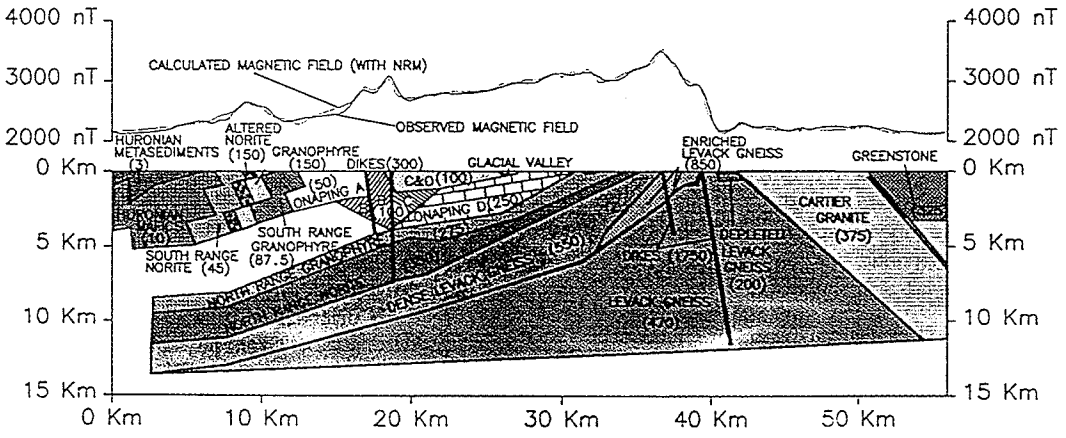

Figure 3.6: A new magnetic model along the profile N-S shown in Figure 3.4, obtained by Hearst et al., 1994 (The unit of susceptibility is 10^{-4} SI).

3.2.2 Results of Other Studies

The airborne multi-sensor geophysical data collected in 1989 by the Geological Survey of Canada (GSC) were one of the good quality data and were preliminarily studied by Singh et al. (1993). In addition to the traditional processing steps, principal component analysis (PCA) was applied to the airborne γ-ray spectrometry data to evaluate relative lithological information contents. It was concluded that the com-

posite radioelement image (produced by combination of three separate radioelement images) and the composite PCA image reflect large scale lithological difference in the near surface materials. A notable point in the airborne γ-ray spectrometry data was a broad rim of potassium anomaly in the northwest surrounding the North Range of Sudbury Structure (Figure 3.7). The felsic plutonic rocks, which may be associated the Cartier granite, are generally rich in potash-feldspar, and thus contain a high concentration of potassium. Whether the anomaly is related to the outer boundary of the LGC or not is still remain to be answered.

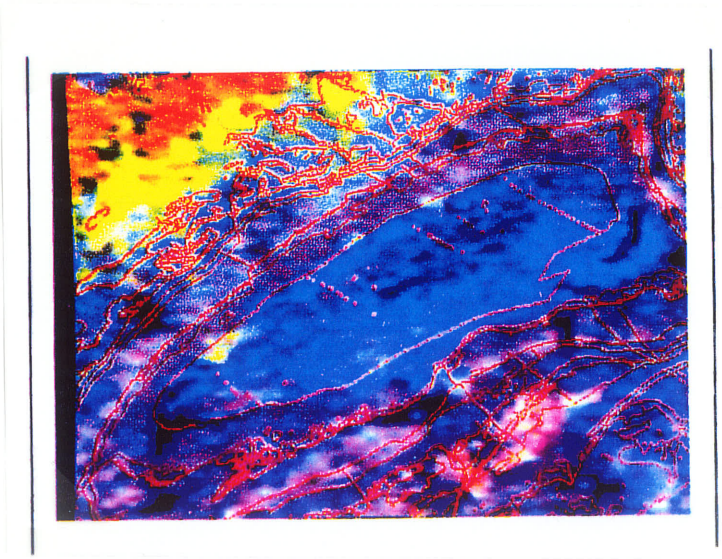

Figure 3.7: Combined potassium image of the Sudbury area (Singh et al., 1993), with the geological formation boundary overlaid shown with red lines. Colors used to create the final image are: K - red; K/eU - green; and K/eTh - blue.

Chapter 4

Seismic Data Acquisition

4.1 Introduction

In October of 1990, the regional and high resolution reflection seismic surveys were carried out as part of the LITHOPROBE AGT Sudbury sub-transect. Three regional survey lines, line 40, 41 and 42 with approximate total lengths of 10 km, 42 km and 22 km (Figure 4.1) respectively, and two coincident high resolution lines, line 40-1 and 41-1 partially overlying the regional lines, were shot. Line 40 across the North Range was designed for exploring the SIC structure which exposed in the North Range area. Line 41 which traverses the Sudbury Basin and the South Range was aimed at profiling the Whitewater group sediments, the SIC within the basin, and the South Range structure. Line 42 across the LGC to the northwest of the Sudbury Structure was designed to examine the structure of the LGC uplift and the structural relationship between the LGC and the Cartier granites. The coincident high resolution survey lines were expected to image the near surface structures in detail.

At the same time as the reflection surveys, multi-offset 3-C VSP experiments were carried out using the same recording system and Vibrators as used in the high resolution reflection surveys, in addition to a number of dynamite sources used. The VSP borehole sites were chosen in Chelmsford, North Range, and Crean Hill where the high resolution reflection lines 41-1 and 40-1 passed through (Figure 4.1) with the objectives of exploration of the shallow structures of the Whitewater sediments in Chelmsford, and the SIC in North Range, and subsequent correlation of the VSP data with the surface high resolution reflection data.

The reflection line planning and scouting were conducted by the Geological Survey of Canada and the University of Manitoba with logistic support from INCO Exploration and Technical Services and Falconbridge Ltd.. Actual data acquisition was contracted to JRS Exploration Co. (Calgary). The field data acquisition for the 3-C multi-offset VSP experiment was planned and conducted by the University of Manitoba geophysical group.

The high resolution refraction experiments were also conducted across the Sudbury Structure in 1992 to explore the crustal structure in the Sudbury area.

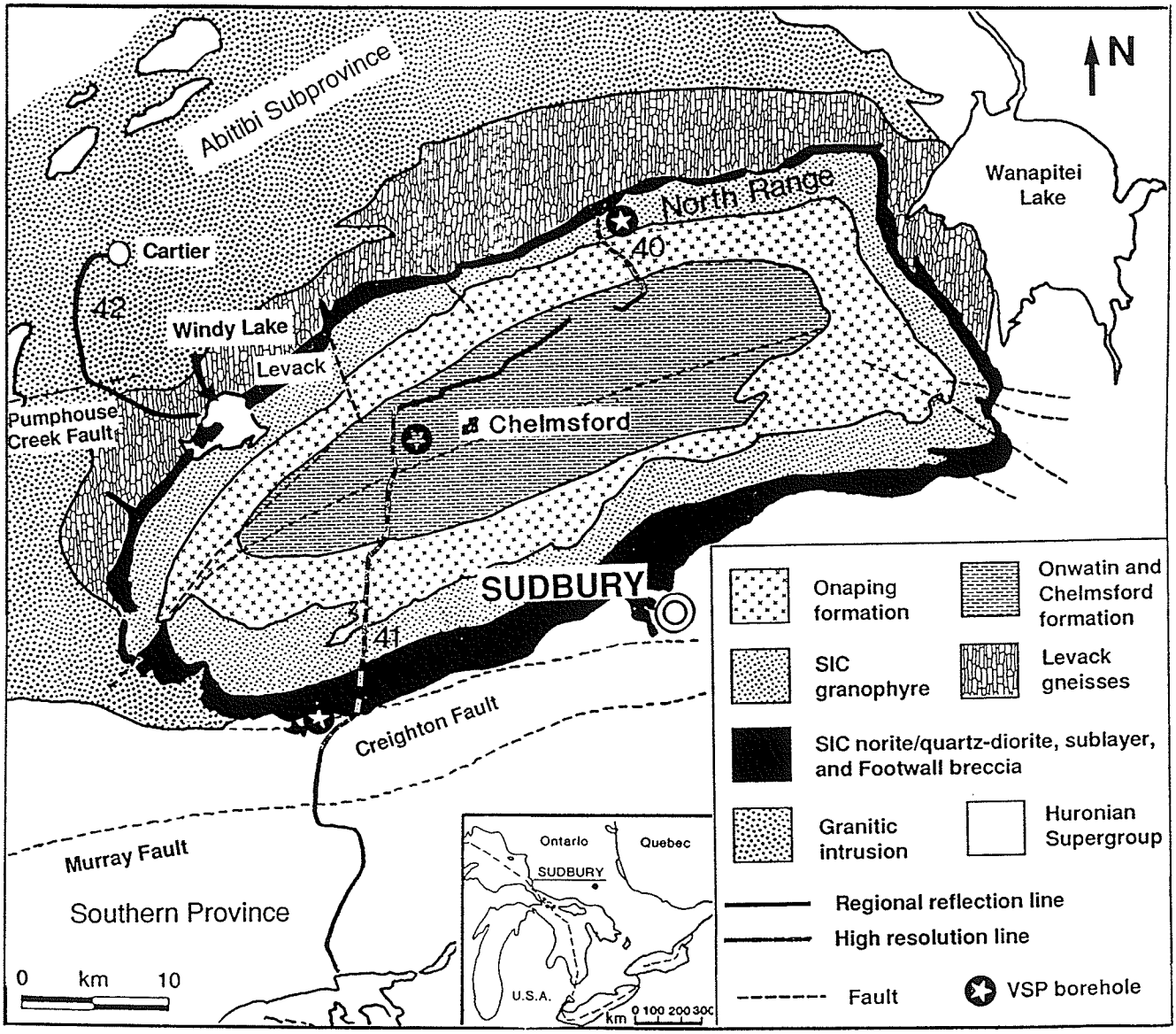

Figure 4.1: Geology map of Sudbury region showing locations of the seismic reflection survey lines and the VSP borehole sites. Dashed lines - coincident high resolution lines.

4.2 VSP Field Survey and Data Acquisition

A multi-offset three component VSP survey was carried out at the Chelmsford borehole. Information about the Chelmsford borehole, provided by Falconbridge Ltd., indicates that the total depth of the borehole is 447.1 m. It is vertical at the surface but slightly deviates at depth. At the depth of 400 m, the maximum deviation from vertical is 10^o. To avoid aliasing problem, the depth sampling constraint was set at

$$\Delta z \leq v_{min}/2f_{max}. \tag{4.1}$$

The maximum frequency of the recorded signal, f_{max}, observed during the experiment was approximately 110 Hz, and the minimum velocity of media, v_{min}, was estimated to be about 4500 m/s. Thus Δz is chosen as 10 m and 20 m. The VSP data were recorded between 0-400 m depth intervals (Figure 4.2) with surface shots at offsets of 150 m, 200 m, 250 m, and 300 m. Based on the surface geological map pattern, the multi-offset survey was planned along a dip-line that ran northwest from the borehole (Figure 4.3) towards the high resolution seismic survey line 41. Both high speed dynamite and vibrators were used as energy sources. For the vibrator experiment, the LITHOPROBE contractor JRS Exploration Co. (Calgary, Canada) recorded the data using a 240 channel SERCEL digital system. The three-component VSP data were collected by means of a GEOSOURCE three-component borehole geophone tool (one vertical and two horizontal components). The three sensors installed inside the caliper tool are close enough that the location error can be ignored. In addition to the borehole tool, two surface geophones were also deployed. Due to limited time and budget, the geophone tool was not oriented in the borehole at each depth. However,

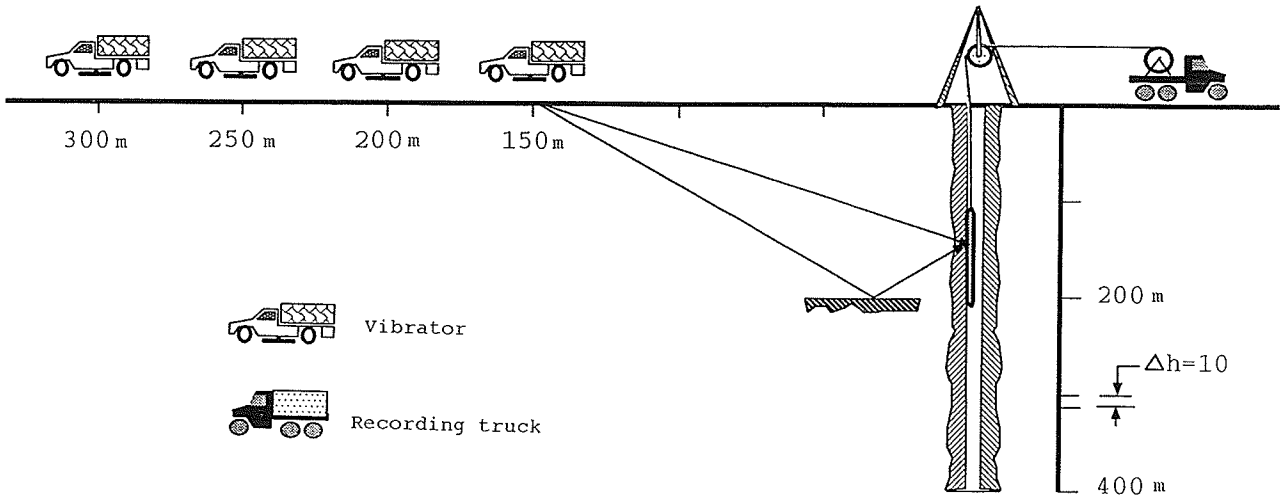

Figure 4.2: Schematic diagram of the Chelmsford multi-offset VSP experiment.

the vertical component should not deviate much from vertical since the borehole is almost vertical and the size of the borehole is small. Detailed instrument and field parameters are listed in Table 4.1.

The Vibroseis VSP data were also collected in the North Range borehole with source offsets of approximately 54.5 m approximately west of the borehole and 116.7 m northeast of the borehole (Figure 4.4). Although the depth of the borehole was 957.0 m, the borehole geophone was only deployed to the maximum depth of 600 m with a depth interval of 20 m due to limited time. The field and instrument parameters were the same as those employed in the Chelmsford experiment. Data quality, however, is not as good as that from the Chelmsford experiment. There were high level background noises and also a number of dead traces in the North Range data.

At Crean Hill, only dynamite data were recorded at the depths of 5, 10, 20, 50, 100 m respectively in order to assist picking of the first breaks for the Vibroseis data.

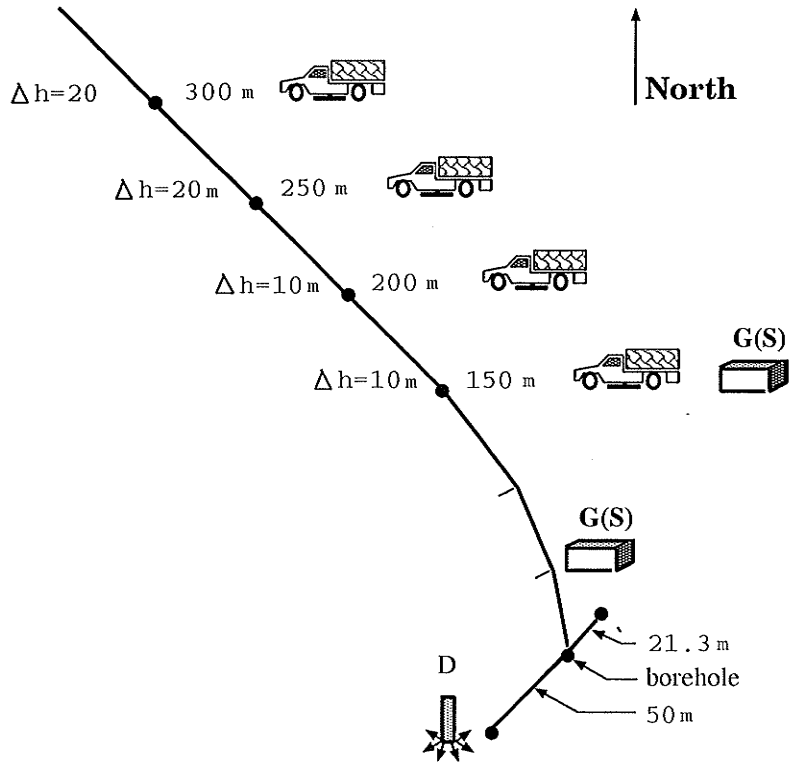

Figure 4.3: Surface layout of the 3-C multi-offset VSP experiment in Chelmsford, Sudbury.

These data sets were also used for verifying shallow near surface seismic velocity estimations.

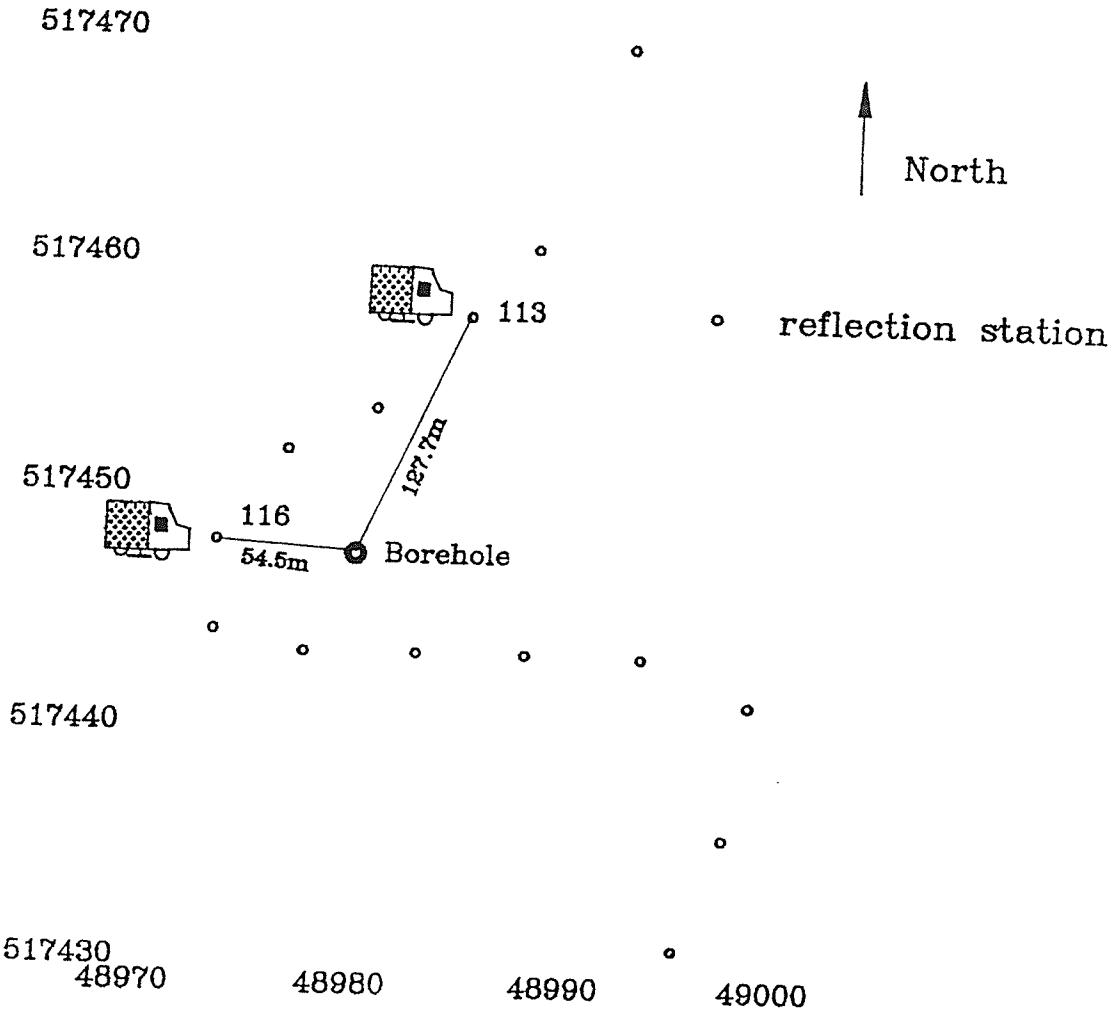

Figure 4.4: Surface layout of the 3-C multi-offset VSP experiment in North Range, Sudbury. The small circle represents the receiver station of the reflection line 40.

Table 4.1: Equipment and field parameters of the Sudbury VSP experiment

Source:	Vibroseis		
Client:	Lithoprobe	Borehole site:	Chelmsford
Borehole tool:	T42 geophone tool	Resonant freq:	14 Hz
Instrument:	SERCEL,368,SN135	Alias filter:	178 Hz/72 dB/oct
Sweep type:	Linear	No. sweeps:	4
Sweep length:	12 s	Sweep frequency:	30-140 Hz
No. channels:	5 (2H,1V,2 Surface)	Sample interval:	2 ms
Deepest receiver:	400 m	Record length:	4 s
Depth intervals:	10-20 m	Offsets:	150,200,250,300 m
Source:	Dynamite		
Shot depths:	2-3 m in water	Shot size:	250 g
Record length:	4 s	Sample interval:	2 ms
Receiver depths:	20,50,100,200,400 m	Offsets:	55,100 m

4.3 Regional and High Resolution Seismic Reflection Data Acquisition

The LITHOPROBE regional and high resolution reflection data acquisition were carried out on behalf of LITHOPROBE by a contractor, JRS Exploration Co., using a SERCEL 240 channel digital system. Four synchronized Vibrators were employed as the energy source. For the high resolution experiment, the vibrator sweep frequency is 30-140 Hz. The data were recorded with 20 m source and 20 m receiver spacings, 2 ms sampling interval and 4 s record length, and a fold coverage of 1200% (see Table 4.2). For the regional survey configuration, the sweep frequency was 10-56 Hz with 100 m source and 50 m receiver spacings. A 14 s vibrator sweep time and 18 s listening time generated 18 s records of raw data with a sampling rate of 4 ms, corresponding to a maximum image depth of approximately 54 km. The coverage was 600% (60-fold). The field survey parameters are listed in Table 4.3.

The Sudbury sub-transect line 40 profiled the North Range igneous complex and Onaping Formation. Line 41 extended from the North Range to the South Range before crossing Huronian rocks and Nipissing intrusions (Figure 4.1). The regional reflection line 42 is the only LITHOPROBE reflection line that traverses the LGC through the Cartier Batholith to the Abitibi subprovince greenstone belts (see Figure 4.1). This line was designed to probe the subsurface geological structures in the northwest of the Sudbury Structure and to resolve the persisting questions associated with the LGC. It is a crooked line and starts at Cartier (Hart Township), the north end of the line, turns sharply to the east near the Pumphouse Creek, turns to south again and ends at the north shore of Windy Lake (Figure 4.1). In this thesis research,

reprocessing effort was focused on the line 42 regional data set.

Table 4.2: High resolution reflection seismic field survey parameters

Contractor	J. R. S. Exploration Company LTD.		
Source			
Source type :	Vibrator	No. of sweeps:	4
No. of Vibrators:	2	Sweep type:	Linear
Source spacing:	20 m	Sweep frequency:	30-140 Hz
		Sweep length:	12 s
Receivers			
Geophone frequency:	30 Hz	Field Instrument:	Sercel 368, SN135
Group length:	20 m	No. of channels :	240
No. per group & base:	9, spike	Field filters:	178 Hz./72 dB/OCT.
Station interval:	20 m	Sampling interval:	2 ms
Spread configuration:	160/80	Record length:	4 s

Table 4.3: Regional reflection seismic field survey parameters

Contractor	J. R. S. Exploration Company LTD.		
Source			
Source type :	Vibrator	No. of sweeps:	8
No. of Vibrators:	4	Sweep type:	Linear
Source spacing:	100 m	Sweep frequency:	10-56 Hz
		Sweep length:	14 s
Receivers			
Geophone frequency:	14 Hz	Field Instrument:	Sercel 368, SN135
Group length:	50 m	No. of channels :	240
No. per group & base:	9, spike	Field filters:	89 Hz/72 dB/oct high cut
Station interval:	50 m	Sampling interval:	4 ms
Spread configuration:	80/160	Record length:	18 s

4.4 Refraction Field Survey and Data Acquisition

The planning and scouting of the LITHOPROBE AGT refraction survey lines were started in the summer of 1991. During the summer of 1992, the survey lines and the shot sites were flagged and precisely positioned by Global Positioning System (GPS) survey receivers. Five Canadian universities including the University of Manitoba, University of West Ontario, University of Laval, Ecole Polytechnique and Dalhousie University; LITHOPROBE; the Geological Survey of Canada (GSC) and the United State Geological Survey (USGS) participated and cooperated for this experiment. Two high resolution refraction lines, the lines AB and XY, were deployed across the Sudbury Structure (Figure 4.5).

The Sudbury refraction line AB, approximately 285 km long, starts at Parry Sound in the Grenville Province, runs northwest perpendicular to the Grenville front, crosses the Sudbury Basin, and ends in the Superior Province (Figure 4.5). The line XY is oriented northeast with a total length of about 170 km. It crosses the Sudbury Structure and Wanapitei Lake (Figures 4.5), and forms a cross-array with the line AB.

A GPS survey was carried out first to position the shot and receiver sites precisely. The positioning system utilized was the GPS PATHFINDER. It records user positions, static or dynamic, at a user-selected rate of up to 1 position per second, with an autonomous accuracy of 25 m. When two GPS PATHFINDER systems are used in a differential positioning mode, the horizontal position accuracy can be increased to 5 m after differential post-processing corrections. For the Sudbury survey, the base

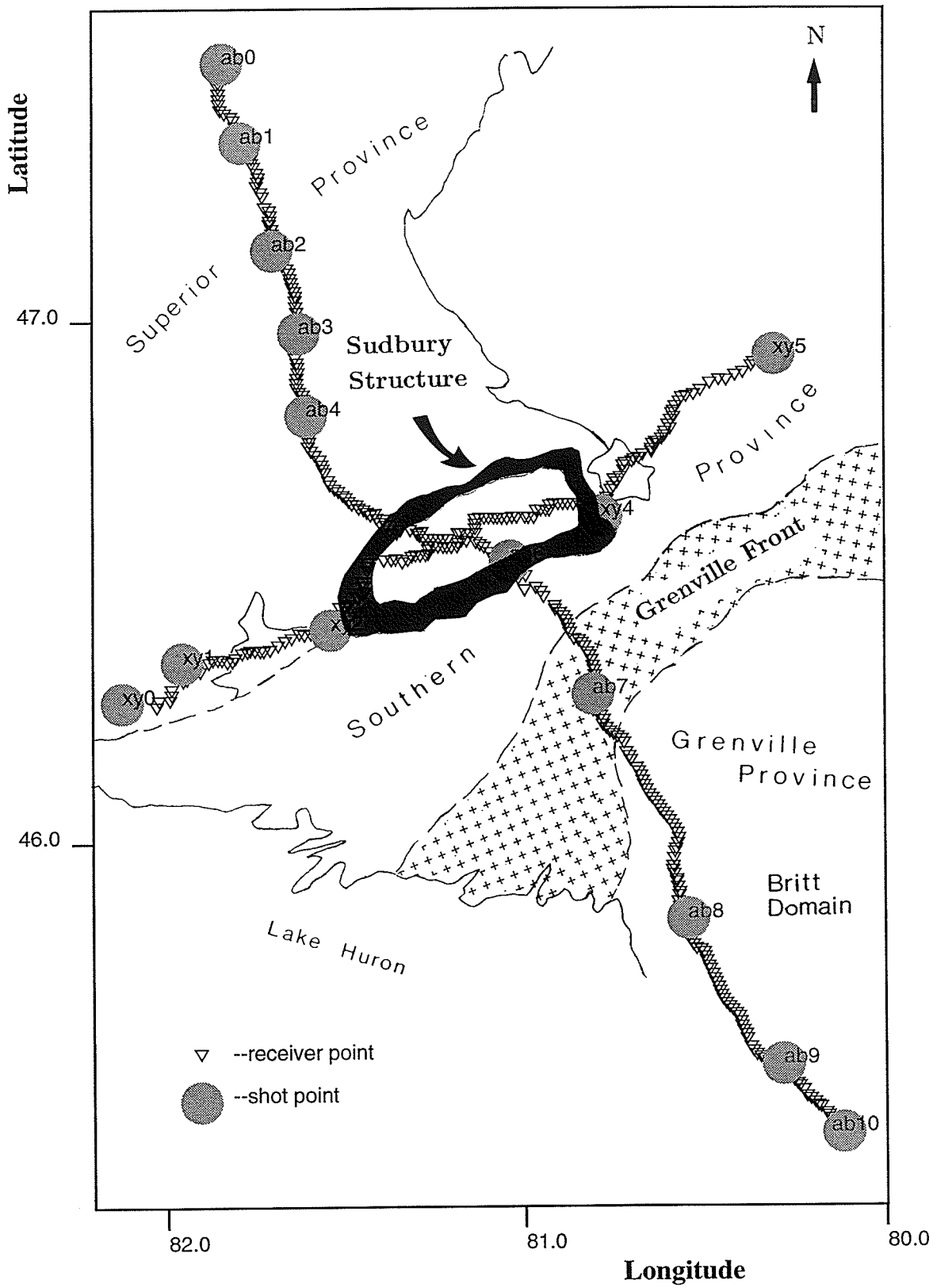

Figure 4.5: Locations of the 1992 Sudbury high resolution refraction lines, line AB and XY. Grey circles represent the shot points and triangles represent the receiver stations.

station was set up at the roof of the INCO Exploration and Technical Services building, and the differential post-processing correction was applied to each position data to assure good positioning accuracy. Depending on the satellites available during the survey, some stations' positions were 2-D fixed, and others were 3-D fixed. The ones with a 3-D fix can have not only horizontal position, but also determine the elevation with good accuracy.

A total of fifteen shot holes were drilled along line AB and line XY (Figure 4.5). The coincident shot holes ab5 and xy3 were planned and drilled, but were canceled due to safety considerations. Seismic energy generated from 200 to 1600 kg dynamite charges detonated in each drilled shot hole (approximately 40 m in depth and 20 cm in diameter) was recorded by single vertical component seismographs and shorter spreads of three component instruments deployed at station spacings of 1 to 1.5 km (see table 4.4, and Figure 4.5). The three component PRS4 instruments were deployed across the Grenville Front Tectonic Zone with objectives of studying the 3-D geological structure of the Grenville Front (Figure 4.5).

Four types of seismic recording systems were used in this experiment (Irving et al., 1992). The GSC (Geological Survey of Canada) instruments included 185 vertical component Portable Refraction Seismograph (PRS1) and 47 three-component portable Refraction Seismograph (PRS4) systems. Geophones used with the GSC instruments were 2 Hz Mark Products L4A for all vertical and horizontal components except for the 300 series PRS4 which used the L28LBH-4.5 Hz detectors (see Table 4.5). The PRS4 horizontal component instruments were aligned in the magnetic N-S and E-W directions. Eight COMPAQ model 286, 386, and 486 personal computer were used as Field Service Units (FSU) to download the shot windows into the PRS's

before each deployment and to upload the recorded data afterwards. The PRS's stored field data in their internal memory at a sampling rate of 120 samples per second, and were managed by the LithoSEIS field software system (Asudeh et al., 1993).

The USGS (U.S. Geological Survey) instruments included 140 vertical component single geophone Seismic Group Recorder (SGR) with 2 Hz geophones and 50 vertical component systems with strings of 8 Hz geophones. The SGR instruments recorded vertical component data, which were stored on digital cartridge tapes within the units. Prior to the deployment, instrument turn-on times were entered into laptop computers and these times were downloaded into each SGR unit. After the instruments were retrieved from the field, the digital data were read directly into an Everex System 1800 microcomputer system from field tapes and were sorted by shot and station numbers. Record section plots were then made. Finally the USGS data were written to nine-track tapes in SEGY format. The SGR records at a fixed sampling rate of 500 samples per second. During playback, the data were decimated by a factor of four, resulting in a sampling rate of 125 samples per second (see table 4.5).

The data recorded using the USGS instruments were resampled and scaled, and then merged with the GSC data. The refraction data were then all written into SEGY format and sorted by shots.

Since there is already a large amount of research work involved in this thesis, only preliminary processing and forward modeling were conducted for the high resolution refraction data. Details about the processing and interpretation of the refraction data are described in the Appendix B.

Table 4.4: Refraction survey field logistic and timing system parameters

Contractor:	GPR Geophysics International Inc.		
Shot information:			
No. of shot holes:	15	Dynamite type:	Hydromex T3
Depth of holes:	35 - 43 m	Detonation velocity:	5400 m/s
Diameter of holes:	20 cm (average)	Size of charges:	400 kg (35 m hole), 800 kg (43 m hole)
Average shot spacing:	30 km		
Average receiver spacing:	1 - 1.5 km		
Time service system:			
Absolute time source:	GOES (Geocentric Earth Satellite) clock.		

Table 4.5: Refraction data recording instrument parameters

GSC instruments:

Seiemograph:

Name of seismograph	PRS1	Name of seismograph	PRS3
No. of Channels	1 (vertical)	No. of Channels	3 (1 vertical, 2 horizontals)
Memory size	1 MB	Memory size	4 MB
Sampling rate	120 pre second	Sampling rate	120 pre second
recording length	120 S	recording length	120 S

Geophone type: 2 Hz Mark Products L4A (for vertical components)
4.5 Hz L28LBH (for 300 series PRS4)

Computer for uploading and downloading: COMPAQ model 286, 386 and personal 486

Software for management of PRS1 and PRS4: LithoSEIS

USGS instruments:

Seismograph:

Name of seismograph:	SGR	Sampling rate :	125 per second
No. of Channels:	1 (vertical)	recording length:	60 S

Geophone type: 2 Hz L4C and 8 Hz strings geophone

Computer for uploading and downloading: Everex System 1800 computer

Software for management: SGR play back software

Chapter 5

Multioffset 3-Component VSP Investigation

5.1 Background and Objectives

In a VSP experiment, downgoing waves, propagated in either a straight or curved ray path, are recorded directly by borehole geophones in the subsurface (see Figure 4.3). The VSP experiment thus provides direct information about velocity structures and layering of the subsurface medium and also makes measurement of interlayer velocity more easily than in surface seismic surveys. On the other hand, reflected waves from a reflector below the geophone have an opposite sign of ray parameter p from the downgoing waves, allowing a wavefield separation. The VSP experiment thus has a special merit in the exploration of shallow structure because of these particular properties.

Correlation of the seismic wavefields from both surface and subsurface survey configurations provides additional valuable information for structural, stratigraphic and lithological interpretation of seismic data. Recently, several such integrated studies

including both VSP and surface reflection survey have been carried out. They have proved to be very effective in the lithospheric exploration for calibrating surface reflection data and mapping detailed seismic velocity structures (Rector, 1988; Lűschen et al., 1991). The VSP technique is also used in determination of polarization of the seismic wavefield (Li and Crampin, 1993).

The multi-offset 3-component VSP experiments in Sudbury were designed to develop an integrated seismic study approach using both the VSP and high-resolution surface reflection techniques. The geological objectives include exploration of the shallow velocity structure of the Whitewater group sediments, mapping of shallow reflectors below the boreholes logged, and in-situ correlation of the VSP results with rock properties and surface reflection seismic data. These experiments were also aimed at helping local mining industries in future exploration for new ore deposits.

In this chapter the VSP data processing techniques utilized and/or developed in this thesis research are described. These techniques include horizontal component rotation, the least squares traveltime inversion for interval velocity analysis, the Radon transform for wavefield separation, shear wave analysis, and VSP-CDP transformation. The VSP data interpretation approaches are also investigated, which involve comparison of the VSP-CDP transformed section and the corridor stack with high resolution surface reflection data, WKBJ synthetic seismogram modeling, and particle motion polarization and hodogram analysis to estimate the dip of a reflector. The results of this study provide independent and valuable information for interpretations of the surface reflection data and rock properties in the vicinity of the boreholes studied (Miao et al., 1994a).

5.2 VSP Data Processing

A flow chart describing the VSP data processing sequence is shown in Figure 5.1. The main processing steps include horizontal component rotation, velocity analysis, wavefield separation, shear wave analysis, and VSP-CDP transform. An example of three component (horizontal 1, horizontal 2, and vertical) raw field data recorded at the offset of 150 m, Chelmsford, is plotted in Figure 5.2. Most of the three-component Vibroseis data are of excellent quality, and show strong downgoing transmission P- and S-waves (Figure 5.2) but weaker upgoing primary reflection which can hardly be identified directly in the raw data plots. Signal demultiplexing was carried out first, and followed by noise eliminations including bandpass filtering to remove high frequency noise and notch filtering to eliminate 62 Hz generator noise.

5.2.1 Horizontal Component Rotation

For the horizontal component data there was evidence of seismic sensor rotation at the shallow depths. Thus a coordinate transform was performed to rotate the horizontal components based on the polarization analysis of the compressional wave (DiSiena, 1981). Since the horizontal projection of the direct arrival particle velocity has the same direction as the ray's surface projection from the wellhead towards the source, the direction of this polarized particle velocity can be used as the fixed reference frame. After rotation, the horizontal components are actually decomposed into the radial component with SV polarization, and the transverse component with SH polarization. Figure 5.3 shows the successfully reoriented horizontal components. In the radial component plots, the rotation operation reconstructs the direct $P-$ wave

arrivals and enhances the SV energy which allows more accurate velocity estimations. In the transverse component, only particle motions in a direction which is normal to the SV and P polarizations remain. The energy of the direct $P-$wave thus almost disappears and the SH component dominates (see Figure 5.3).

5.2.2 Velocity Analysis and Travel Time Inversion

In order to pick the first break time accurately a minimum phase transform was applied to transform the two sided zero-phase Vibroseis data to the minimum phase. The first break times were mostly picked from Vibroseis data for velocity analysis, while the dynamite data were used only for reference and verification of picking the first break times accurately. The Vibroseis data are of much better quality than the dynamite data in this experiment due to the old recording system used for dynamite data collection.

Velocity analysis proceeded with a slanted-straight ray method and a least squares inversion (Stewart, 1984). The slanted-straight ray method was used at first to estimate the initial average and interval velocity models averaging over multiple offsets for both P- and S-wave data sets. The interval and average velocities are given by

$$\Delta v = \Delta z/(\Delta t/cos\theta), \tag{5.1}$$

$$\overline{v_n} = (\sum_{j}^{n} \Delta v_j)/n, \tag{5.2}$$

where θ is the angle subtended by the lines from receiver to wellhead and receiver to shot point, and Δz and Δt are respectively the depth and travel time intervals between stations. Surface velocity (at z=0) was determined by vertical component

records of the borehole geophone and two surface geophones together. Figure 5.4 and 5.5 display the initial velocity models of both P- and S- waves as grey dotted lines for the Chelmsford and the North Range boreholes respectively. The north Range data were interpolated using the Radon transform to compensate some dead traces before the velocity analysis.

Subsequently a linear least squares traveltime inversion algorithm was programmed and performed to obtain more accurate interval velocity estimation by using the above results as the starting models. The least squares inversion is composed of two steps. The first step involves ray-tracing based on the formula given in Grant and West (1965):

$$T(z) = \int_0^z \{1 - v^2(h)[\frac{1}{v^2(z)} - (\frac{dt}{dh})_z^2]\}^{-1/2} \frac{dh}{v(h)} \tag{5.3}$$

where $T(z)$ is the traveltime and its derivative is $(dt/dh)_z$, both of which can be obtained from the field data. The computed ray-tracing traveltimes are compared with the observed times. The difference between calculated and observed times is assumed to be linearly related to the correction terms and applied to update the velocity model. The correction terms may be estimated as

$$\Delta T_{cal}^i = \sum_{j=1}^{n} \frac{dT_{cal}^i}{dv_j} \Delta v_j \tag{5.4}$$

and formulated as a matrix expression of

$$Y = AX \tag{5.5},$$

where Y is a column vector of ΔT_{cal}^i (the difference between the calculated and observed times), X is a column vector Δv_j (the correction term for velocity), A is the matrix of partial derivatives dT_{cal}^i/dv_j.

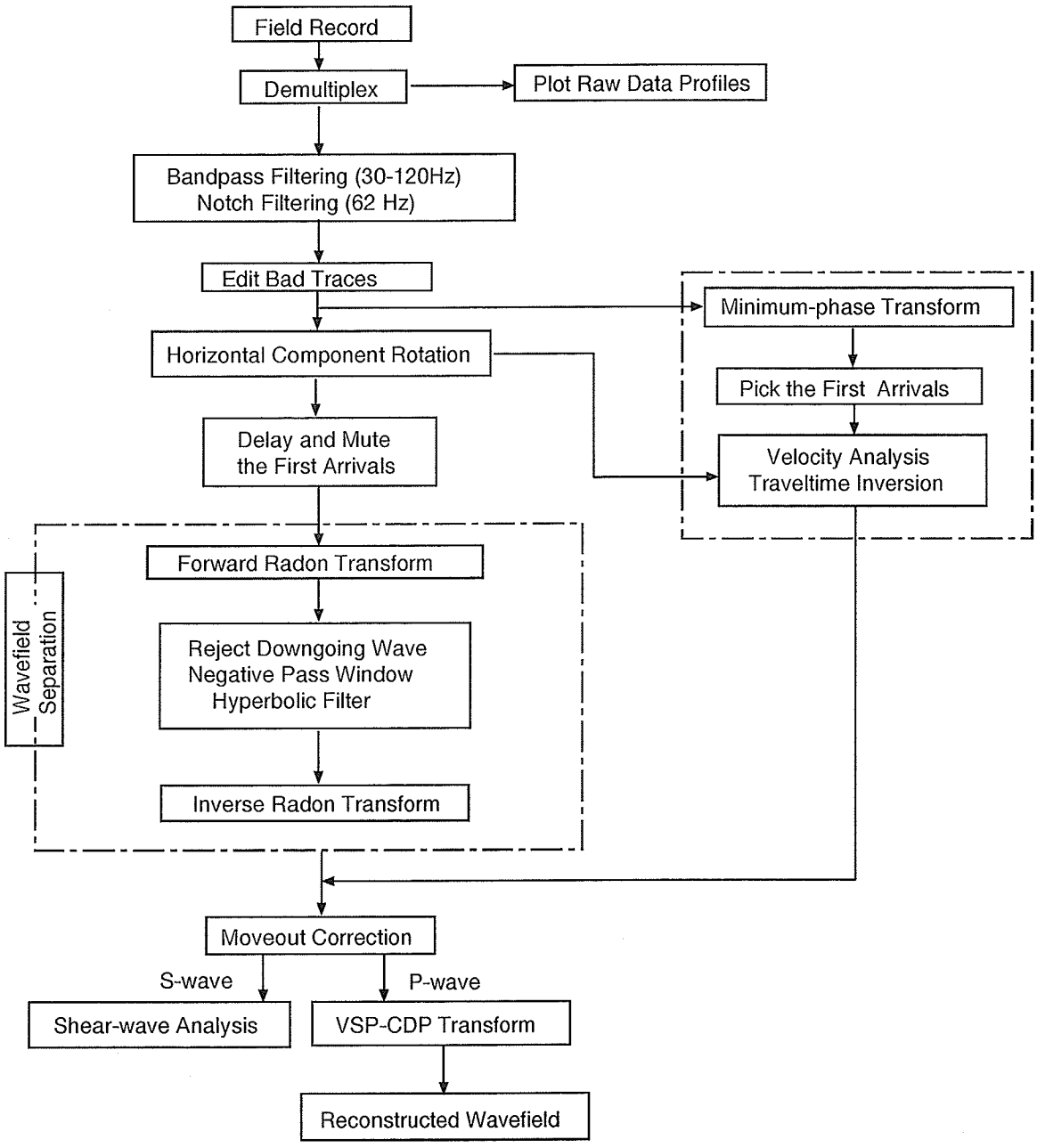

Figure 5.1: Flowchart of the VSP Data Processing

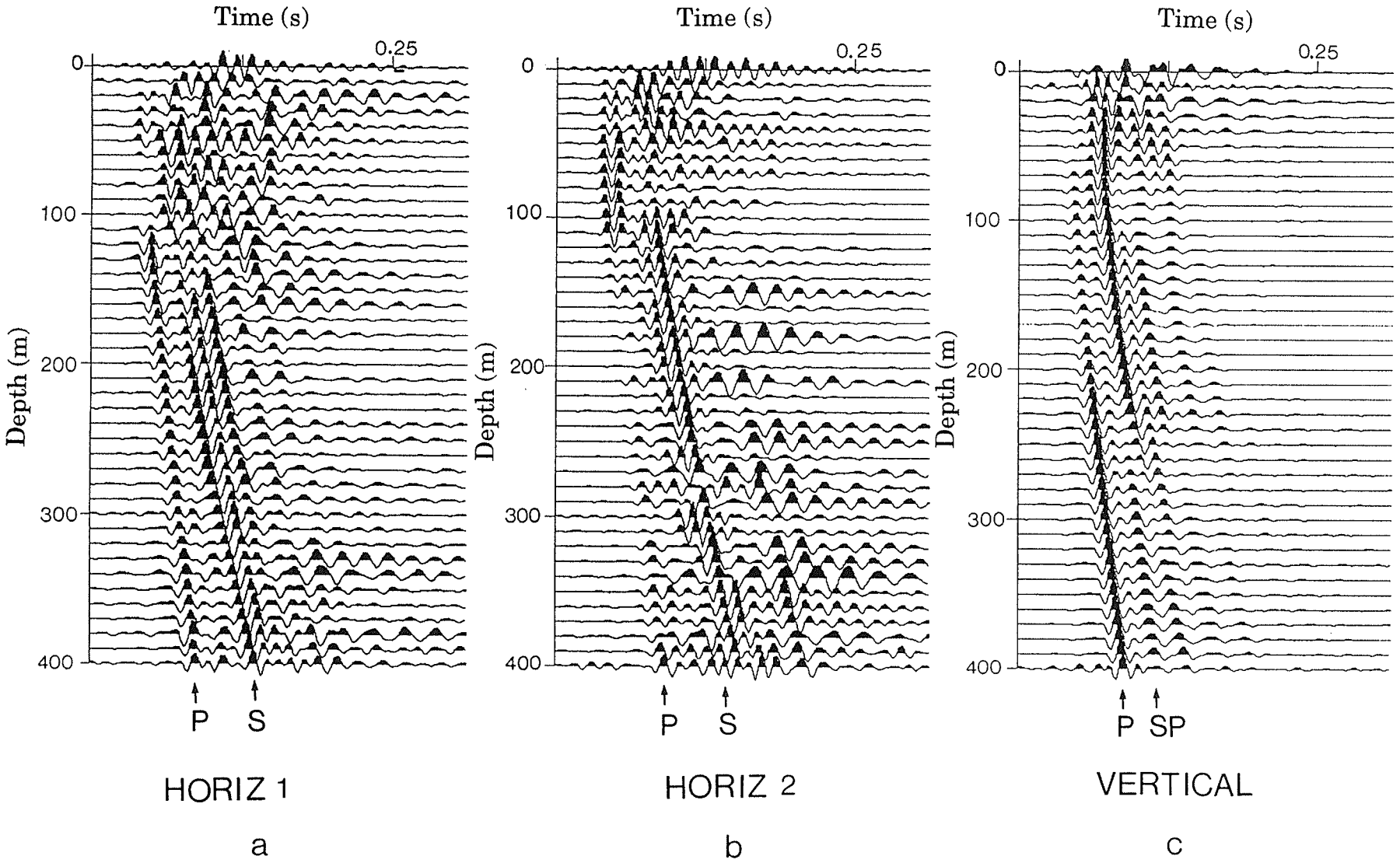

Figure 5.2: Unprocessed three-component Vibroseis VSP data at the 150 m offset (Chelmsford borehole, Sudbury). (a) Horizontal component 1; (b) Horizontal component 2; and (c) Vertical component (no processing applied) with compressional (p), shear (s) and converted (sp) waves highlighted.

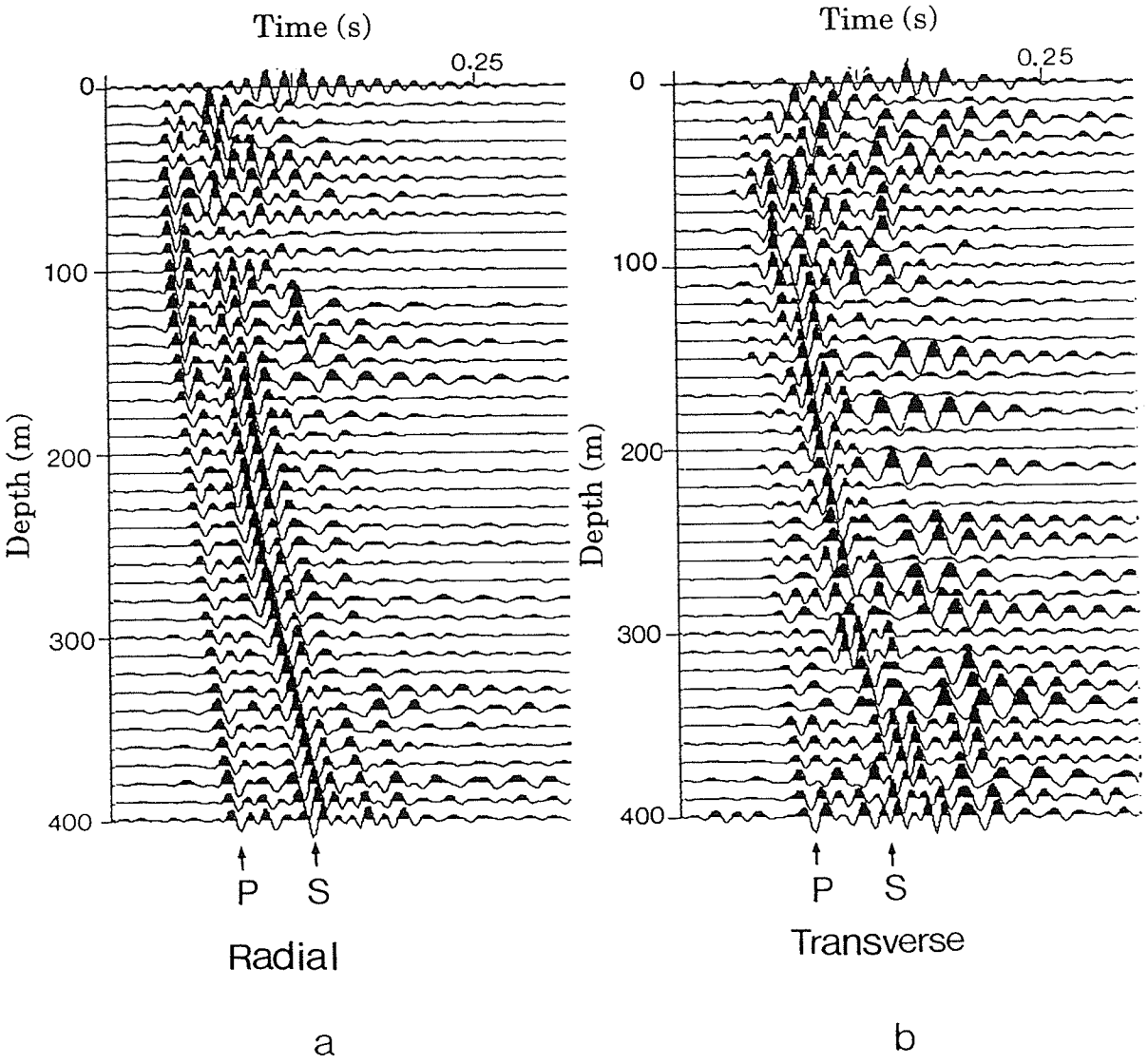

Figure 5.3: An example of the rotated horizontal component of the VSP data recorded at the 150 m offset using the particle motion polarization. (a) Radial component data with SV polarization; (b) transverse component data with SH polarization.

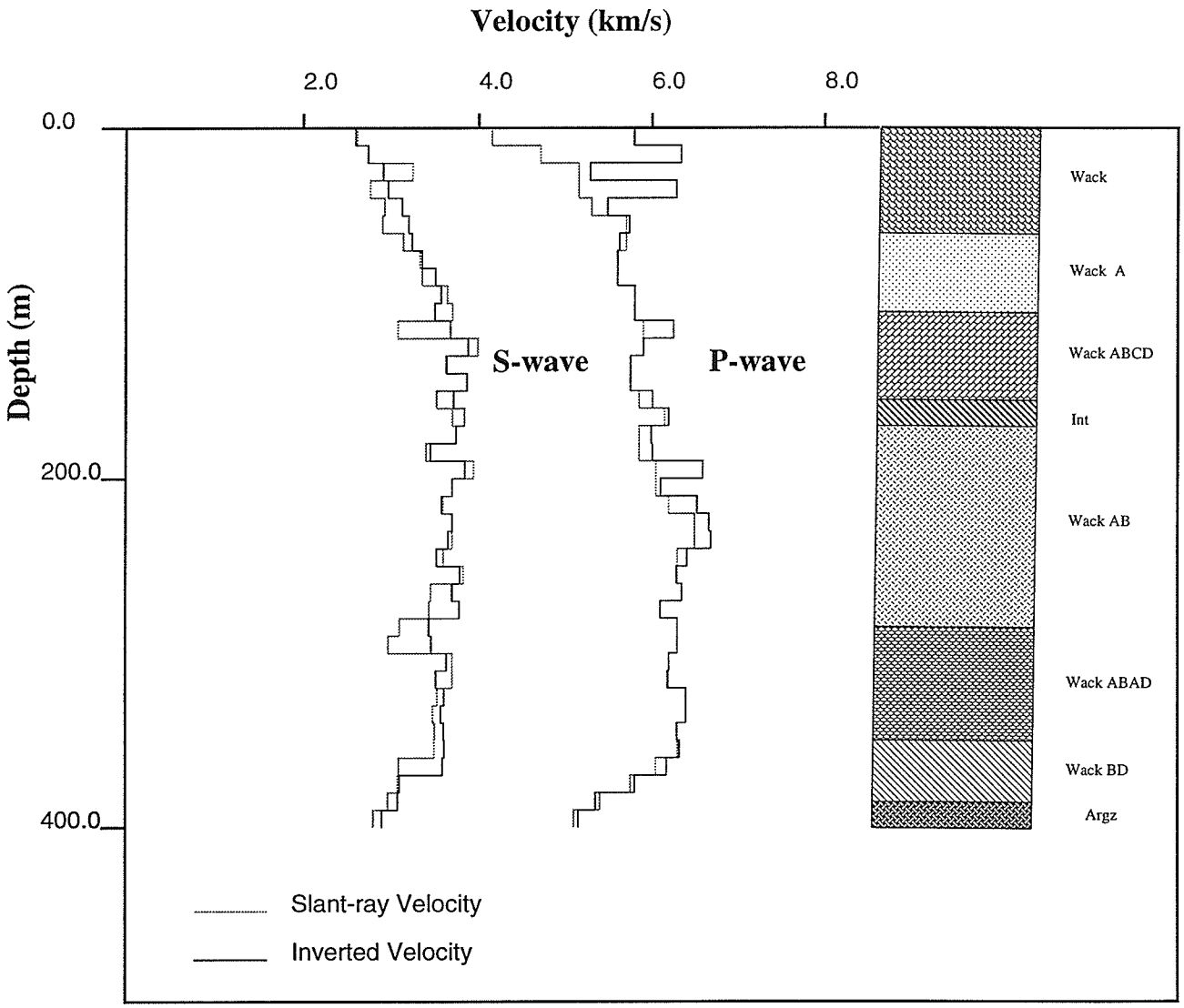

Figure 5.4: Inverted velocity models of the P- and S- wave data for the Chelmsford borehole. The grey dotted line is the initial P-wave interval velocity estimated using the slanted-straight ray average, and the dark solid line is the interval velocity estimated using the least squares inversion. The stratigraphic terms are named by Falconbridge Ltd..

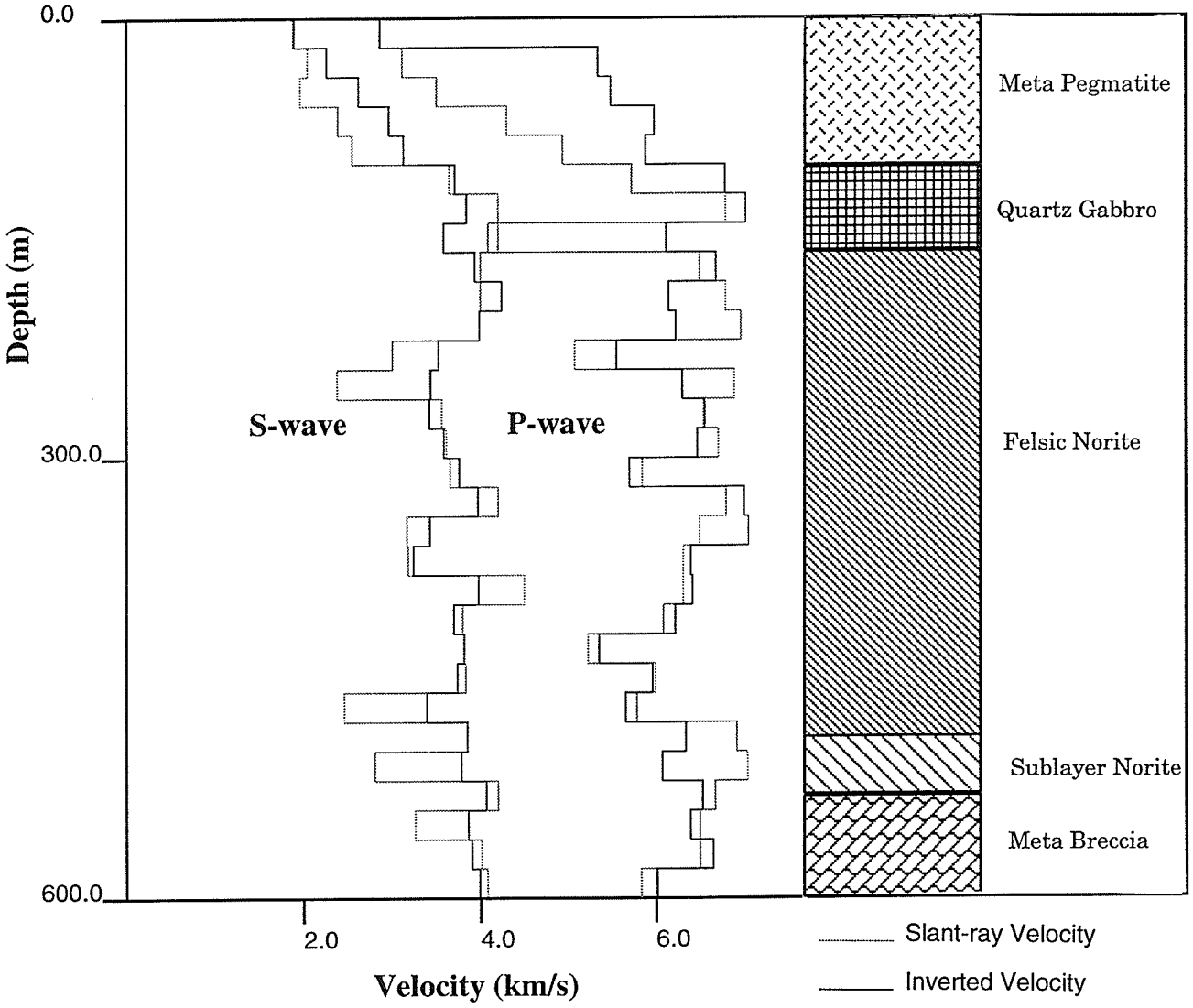

Figure 5.5: Inverted velocity models of the P- and S- wave data for the North Range borehole (the dead traces in the data were interpolated using the Radon transform, the result only intents to provide an approximate estimation). The grey dotted line is the initial P-wave interval velocity estimated using the slanted-straight ray average, and the dark solid line is the interval velocity estimated using the least squares inversion. The stratigraphic terms are named by IETS.

The second step is the damped least squares inversion procedure for refinement of the initial model and can be formulated as:

$$X = (A^T A + \lambda^2 I)^{-1} A^T Y, \tag{5.6}$$

where λ is the damping parameter, and I is the identity matrix. This iteration is repeated until either the difference between the calculated and observed travel times within the experimental error or the interval velocity parameters converge to a set limit. The interval velocity models computed using the above inversion process for both P- wave and S- wave are displayed respectively in Figure 5.4 and 5.5 as dark solid lines. The final traveltime residuals are used to evaluate the solution. In this experiment the maximum traveltime residuals are respectively 11 ms for P- wave and 16 ms for S-wave data. Errors in the velocity estimation are relatively larger at shallow depths.

5.2.3 Velocity Comparison with Results from Drill Core Samples

Seismic velocity and rock properties provide important correlation between the interpretation results of various seismic surveys and the actual geology of the study area. For this reason, this section reviews and summarizes the recent results from both seismic study and laboratory measurements.

The average $P-$ and $S-$ wave velocity values of rock types were estimated from the multi-offset VSP velocity models and were compared with velocity measurement from the drill core samples in the laboratory (Table 5.1). Measurement of the $P-$ and S-wave velocities from the drill core samples were made using a pulsed oscillator

with a frequency of 820 kHz at five different pressures, ranging from 3.5 MPa to 44.2 MPa (Messfin and Moon, 1984). The highest pressure, 44.2 MPa, corresponds to approximately 2 km in depth. The results of the laboratory measurement have, in general, higher values than the VSP results. The Sudbury norite sublayer and the meta-gabbro-norite complex have unusually high P-wave velocities and can be used as a key reflection horizon in the future seismic experiments if they involve these lithological formations. According to Messfin and Moon (1984), a massive sulfide layer can produce very large acoustic impedance contrast resulting in strong reflections. The boreholes used in this study, however, did not encounter massive sulfides so neither in-site seismic velocity estimation nor observation of seismic reflections could be made.

Additional velocity and density measurement of the drill core samples have also been made by Salisbury et al. (1994) recently (see Figure 5.6). The measurement was carried out under hydrostatic confining pressure ranging from 0-600 MPa for 120 drill core samples representing all major lithologies exposed in the Sudbury area, including samples from the Chelmsford and North Range boreholes. Their results show that the velocity for Chelmsford greywackes is 5.91 km/s and for Onwatin shale is 5.2 km/s. Compared with the VSP results, the average velocities are 5.99 km/s for Chelmsford greywackes and 5.43 km/s for Onwatin argillite. For the North Range borehole, the velocities from the laboratory measurement are 6.20 km/s for granophyre and 6.47 km/s for norite. These results are close to the velocity estimated from the VSP data, which shows an average velocity of 6.27 km/s for felsic norite and 6.35 km/s for sublayer norite (Figures 5.4 and 5.5). The detailed velocity values are listed in Table 5.2.

Table 5.1: P- and S-wave velocity for typical rock types in the Study area (The numbers in the bracket for Messfin and Moon(1984) represent the number of samples).

Rock Types	P-wave Velocity Lab. Measurement (km/s) (Messfin & Moon, 1984)	P-wave Velocity from VSP (km/s) (This Study)	S-wave Velocity Lab. Measurement (km/s) (Messfin & Moon, 1984)	S-wave Velovity from VSP (km/s) (This Study)	Comments
Felsic Norite	5.555-6.412 (3)	5.837-6.790*#	3.333-3.562 (3)	2.838-3.896*	*- North Range
Mafic Norite	5.912-6.480 (3)		3.428-3.540 (3)		#- includes
Sublayer Norite		6.67 -6.90*		3.317-3.960*	White et al. (1994)
Micropegmatite	5.791-6.371 (6)	4.50 -5.712*	3.444-3.600 (6)	2.424-3.640*	
Quartz Gabbro	6.310-6.721 (3)	4.08 -6.791*#	3.638-3.912 (3)	3.401-4.451*	#- includes
Granite Breccia	5.647-6.317 (4)		3.187-3.581 (4)		White et al. (1994)
Granite Gneiss	5.568-6.141 (2)		2.946-3.524 (2)		
Mafic Gneiss	5.741-6.850 (4)		3.342-3.752 (4)		
Massive Sulfide	4.914-5.209 (1)		2.763-2.845 (1)		
Sudbury Breccia	5.845-6.176 (1)	4.75 -5.52***	3.479-3.564 (1)		***- Crean Hill
Meta-Gabbro-Norite Complex		6.41 -6.821*		3.263-3.935*	*- North Range
Olivine Diabase	6.335-6.702 (1)		3.466-3.551 (1)		
Grey Onaping		4.700-5.425~			~ Moon et al. (1989)
Black Onaping		5.252-5.475~			
Onaping	6.133-6.363 (2)		3.620-3.686 (2)		
Greywacke(Chelmsford)		4.38 -6.51**		2.95 -3.74**	** includes
Argillite (Onwatin)		5.11 -5.75**		2.87 -3.08**	Moon et al. (1989)

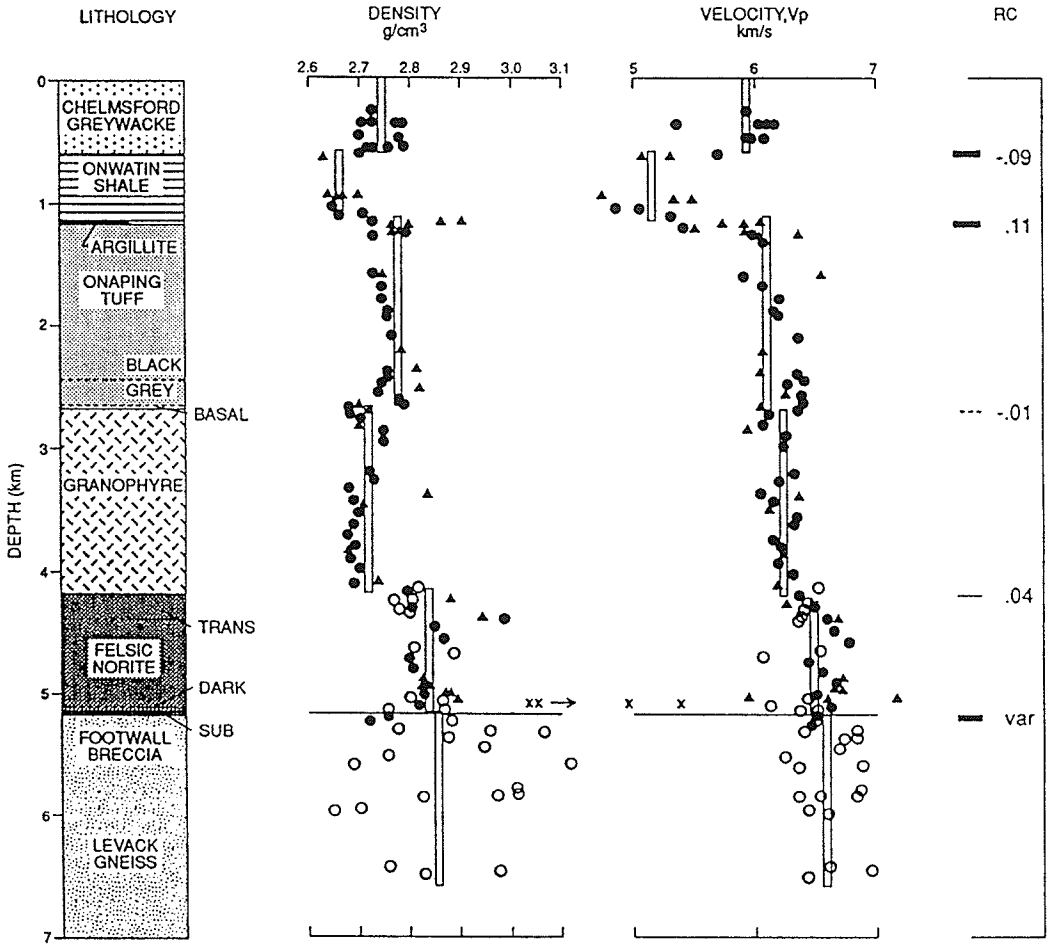

Figure 5.6: Velocity and Density measurement of the recent drill core samples from the study area. RC=reflection coefficients (Salisbury et al., 1994).

Table 5.2: The P- and S-wave velocities from the VSP experiment and from the recent drill core samples (Salisbury et al., 1994).

Rock Type	Velocity from VSP (km/s)		Velocity from core sample (km/s)*
	Vp	Vs	Vp
Chelmsford greywacke	5.99 ± 0.54	3.49 ± 0.38	5.91± 0.18
Onwatin shale			5.16 ± 0.30
Onwatin Argillite	5.43 ± 0.28	3.02 ± 0.10	
Onaping tuff			6.09 ± 0.25
Meta pegmatite	5.61 ± 0.33	2.61 ± 0.35	
Granophyre			6.20 ± 0.13
Quartz gabbro	6.56 ± 0.52	3.56 ± 0.37	
Norite			6.47 ± 0.24
Felsic norite	6.27 ± 0.47	3.34 ± 0.63	
Sublayer norite	6.35 ± 0.18	3.89 ± 0.14	
Levack gneiss			6.57 ± 0.20

* Results from Salisbury et al. (1994)

5.2.4 Wavefield Separation

The downgoing direct waves which arrive first have much stronger energy than other waves, and the later arrivals with small amplitudes are difficult to identify in the original records. The purpose of wavefield separation is to suppress the downgoing waves and enhance the upgoing waves. Of the VSP data processing steps, the wavefield separation is the most crucial step, because it determines whether the reflection events can be used or not. The nature of the wavefield separation problem leads to the concept of velocity filtering, a multichannel processing method introduced by Embree et al. (1963). This method suppresses undesired signals with apparent velocities which are significantly different from those of the desired signals.

In recent years, several wavefield separation techniques have been published which include 2D $f-k$ filtering (frequency-wavenumber domain) (Hardage, 1983), the Radon transform (Moon et al., 1985; 1989), multi-level median filtering (Hardage, 1983) and optimum array filtering (Seeman, 1983). The $f-k$ velocity filtering technique utilizes different signatures of apparent velocities between the downgoing waves and the upgoing waves. Due to employment of the FFT algorithm, it requires a constant sampling rate. Median filtering is actually a first break muting procedure which depends on the statistical characteristics of the data. Optimum array filtering is a kind of autocorrelation processing procedure. Although it makes no assumption as to the spacing of geophones, the method requires some knowledge of the impedance structure and well-posed data for a VSP section in which the reconstructed wavefield is properly placed. The Radon transform has no requirement of a regular sample rate, the wavefield separation in the research was thus carried out using the Radon

transform separation technique.

Radon Transform

The theory of the Radon transform was first introduced to seismology by Chapman (1981). Mathematically the Radon transform is a linear invertible integral transformation from the $z-t$ (receiver depth - traveltime) reference plane to a reference plane of $\tau-p$ (intercept time - ray parameter), where $\tau=t-pz$ and ray parameter p is defined by $p=\frac{sini}{v}$, i is ray incident angle and v is velocity.

The 2-D Radon transform, under the assumption of a line source, of seismic data $u(z,t)$ to U(p,τ) in the $\tau-p$ plane is defined by

$$U(p,\tau)=\int_{-\infty}^{\infty}u(z,pz+\tau)dz. \tag{5.7}$$

It can be numerically implemented by two steps. First, a linear moveout is applied to the data through a coordinate transform (Claerbout, 1978)

$$\tau=t-pz.$$

Next, the amplitudes are summed along the ray parameters over the offset axis. With application of the equation (5.7) to the VSP data, the upgoing and downgoing waves which have p values with opposite signs are separated and mapped into different quadrants of the $\tau-p$ plane (see Figure 5.7) respectively.

To avoid aliasing during the $\tau-p$ transform, the sampling rate for the ray parameter p must be chosen to satisfy the aliasing criteria (Moon et al., 1986). If f_{max} is the maximum frequency of propagating wavelets, the sampling constraint is given by

$$\Delta p\leq 1/(2\pi f_{max}z_{max}) \tag{5.8}$$

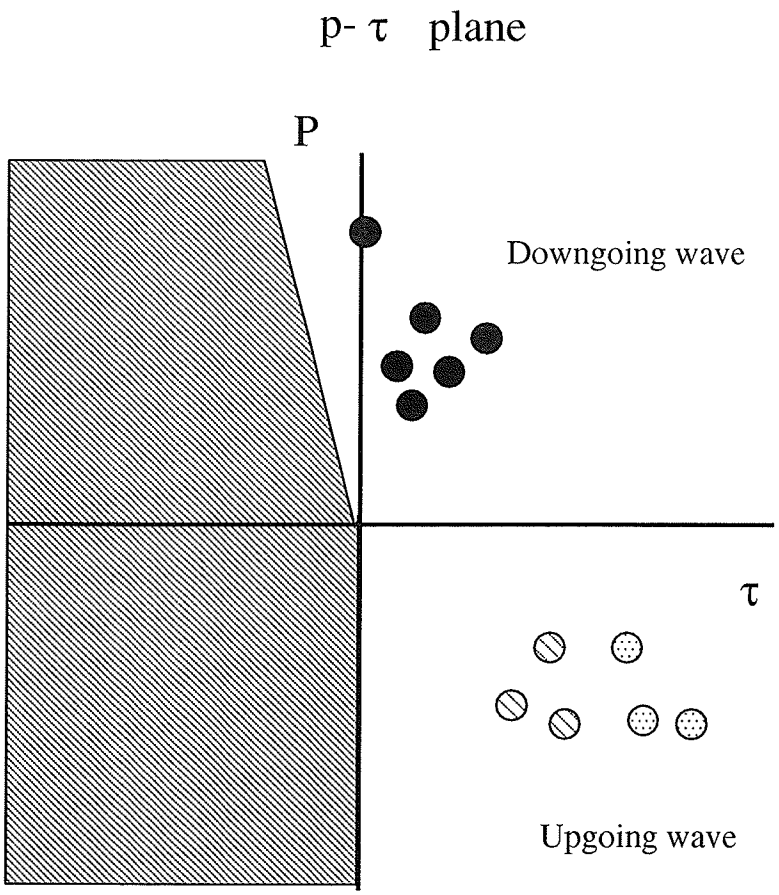

Figure 5.7: A schematic plot of the theoretical $\tau - p$ plane information produced by Radon transform. The upgoing and downgoing waves, which have opposite signs of p, are separated and mapped into different quadrants in the $\tau - p$ plane.

where z_{max} is the maximum spatial length of the data. For the Chelmsford data with $z_{max} = 0.4$ km, $f_{max} = 110$ Hz, Δp should be less than 0.0036, thus $\Delta P = 0.002$ was chosen as the p sampling interval.

For the North Range data, there was clearly a violation of the Nyquist sampling constraint in the depth sampling interval (see equation 3.1) due to several dead traces in the records. The data sets were less useful and excluded from the subsequent processing.

The inverse Radon transform that images seismic energy from the $\tau - p$ plane back to the $z - t$ plane is defined as (Chapman 1981)

$$u(z,t) = \int_{-\infty}^{\infty} \frac{d}{dt} H[U(p, t - pz)]dp, \tag{5.9}$$

where H represents the Hilbert transform. It is implemented as a three-step procedure. The first and second steps involve application of the Hilbert transform and then computation of the time derivative. Reconstruction of the wavefield separated seismogram in the $z - t$ plane is completed by integrating the resulting function along different lines of $\tau = t - pz$. To reconstruct upgoing wavefield, a negative-pass window or filter is imposed on the $\tau - p$ plane so that the output plane retains only the desired upgoing waves. Despite the fact that the basic idea of wavefield separation in the $\tau - p$ plane is similar to the $f - k$ filtering, the Radon transform method is more flexible due to its capability to accommodate an unequal sampling interval along the depth axis.

In principle, application of a negative pass window in the $\tau - p$ plane can reject the undesired downgoing wave in reconstructed wavefield. But it is often not easy to obtain an optimum separation, energy smearing between the downgoing and upgoing

waves in the $\tau - p$ domain sometimes occurs, especially in the region of small ray parameters. The effectiveness of separation becomes poorer as the ray parameter approaches small values or far offsets (see Figure 5.8 for explanation).

This may be attributed to the following points: low acoustic impedance contrast in a crystalline rock environment producing less clear reflection events, dip of reflectors and undesirable artifacts in the $\tau - p$ transform. The Chelmsford formation consists of different sequences of graywacke, across which acoustic impedance contrasts are very low. The Onwatin formation which underlies the Chelmsford formation has, in general, lower seismic velocities. In addition to the lithology, dip of the reflectors can also affect the arrival times of reflection events. If a reflector dips toward the borehole, it will result in advanced arrivals of the reflected energy, which can interfere with the downgoing waves. Some of the numerical artifacts associated with the $\tau - p$ transform introduced by the line source approximation can also be a cause of less satisfactory performance of the wavefield separation process, especially near the region of small ray parameters (far offset) where energy smearing occurs (Brysk and McCowan 1986). Since the energy of the downgoing waves is at least several times larger than that of the upgoing waves, a little energy smearing during the wavefield separation can cause appreciable energy of the downgoing waves to be retained in the reconstructed wavefield.

This problem was also reported by Kappus et al. (1990). By comparing the performance of five different methods of the Radon transform on marine multichannel data and similar synthetic profiles, they found out that at small ray parameters, on fully sampled synthetic profiles, only the methods that assume a three-dimensional (3-D) nature of the point source provide correct amplitude and phase information,

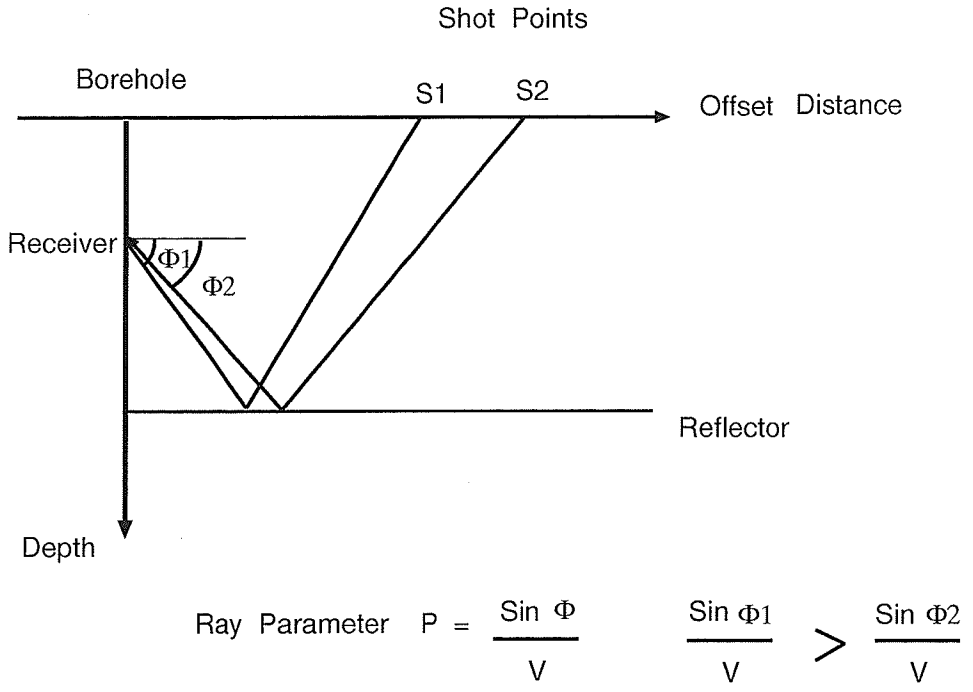

Figure 5.8: A schematic plot demonstrating decrease of the ray parameter p as offsets increase.

whereas 2-D linear source and asymptotic approximation of point source methods do not. Thus a hyperbolic filter was designed in this research. It was applied together with the Radon transform for wavefield separation.

Hyperbolic Filtering

The hyperbolic filter applied to a data set in the $\tau-p$ plane actually acts as a muting process along two hyperbolic curves in the $\tau - p$ domain. The Radon transform of each individual trace is muted along the curves depending on the velocity limits. This technique was discussed by Kelamis et al. (1989) for surface reflection data. For the VSP configuration, some modifications were made. The basic principles of hyperbolic filtering are summarized as follow.

For a transmitted (downgoing) wave, the travel time is given by

$$t^2 = (z^2 + x_{source}^2)/v^2. \tag{5.10}$$

Differentiating t with respect to z and substituting $t = \tau + pz$ into equation (5.10), the ray parameter of the downgoing wave is obtained as a function of τ:

$$p_{down} = -\frac{\tau}{2z} \pm \sqrt{(\frac{\tau^2}{2z})^2 + 1/v^2}. \tag{5.11}$$

For a reflected (upgoing) wave, the travel time equation becomes (see ray paths in Figure 5.9):

$$t^2 = (x_{source}^2 + (2h - z)^2)/v \tag{5.12}$$

where h and z are depths of reflector and receiver respectively, x_{source} is offset distance, and v is velocity. The ray parameter p then is

$$p_{up} = -\frac{\tau}{2z} \pm \sqrt{\frac{\tau^2}{2z} - (\frac{2h}{z} - 1)/v^2} \tag{5.13}$$

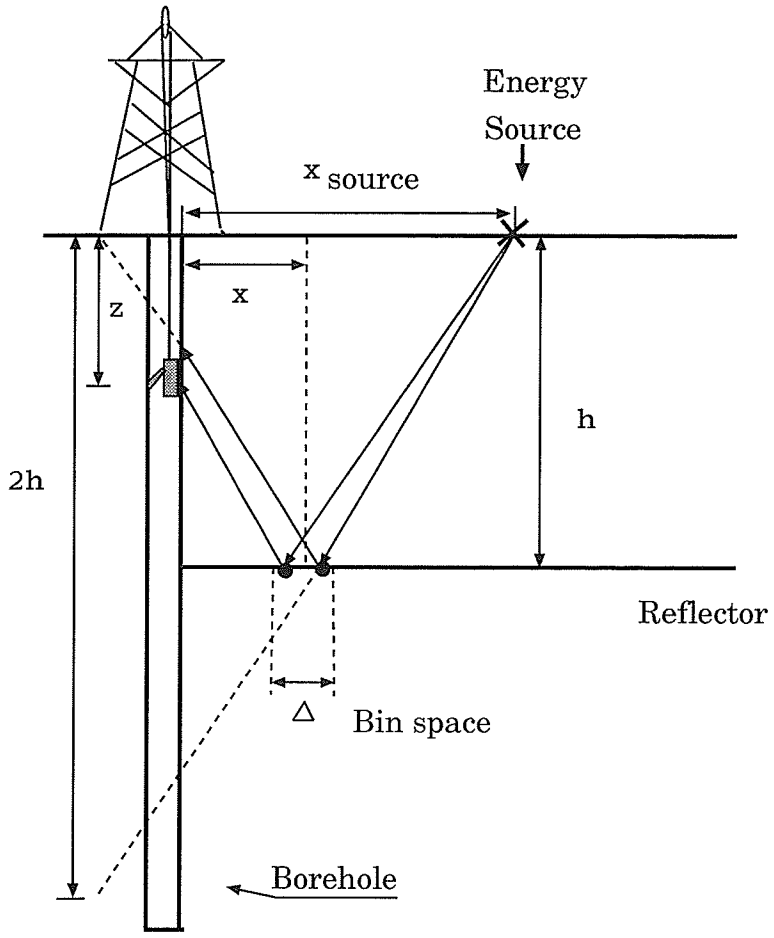

Figure 5.9: Geometric depiction of the downgoing and upgoing ray pathes in a VSP experiment.

which is a hyperbolic curve equation. Since the term $(\frac{2h}{z} - 1)/v^2$ is always larger than zero, the p_{up} always has a negative sign, which is opposite to the p_{down}.

Therefore, the range of the ray parameter p for the upgoing waves is given by:

$$-\frac{\tau}{2z} - \sqrt{(\frac{\tau}{2z})^2 - \frac{1}{v_{max}^2}(\frac{2h}{z} - 1)} \leq p_{up} \leq -\frac{\tau}{2z} + \sqrt{(\frac{\tau}{2z})^2 - \frac{1}{v_{max}^2}(\frac{2h}{z} - 1)} \quad (5.14)$$

where v_{max} is the maximum velocity in the media. The p_{down} will lie in the different part of the $\tau - p$ domain.

If one restricts signals to within these two hyperbolic curves (Figure 5.10) in equation (5.14), the desired image of upgoing waves will be obtained. Application of a hyperbolic filter to real data, by specifying v_{max} as 6.5 km/s in this study, has enhanced the reflected energy after wavefield separation.

The results of wavefield separation turned out to be satisfactory, especially for near offset data (offset = 150 m and 200 m). Figure 5.11 shows an example of the wavefield separated data. At the 150 m offset, the downgoing waves were almost completely rejected after separation. The upgoing waves, which were hardly recognizable in the original section, were clearly identified in all of the three-component data.

Figure 5.12 shows the flattened upgoing wavefield of the vertical component data for P-wave at offset of 150 m, which was obtained after separation of the wavefield and converted to the two-way traveltime by the moveout correction. The information was then plotted with the velocity, density (the density data were provided by J. Mwenifumbo of the GSC, and reflectivity coefficient. At three depth levels (160 m, 280 m, and 380 m) where the velocity and density produced an anomalous reflective coefficient, the corresponding reflection signals are shown in the processed P-wave section (Figure 5.12d). Especially at the depth of 380 m where obvious decrease occurs in both density and velocity, a strong reflection event is seen.

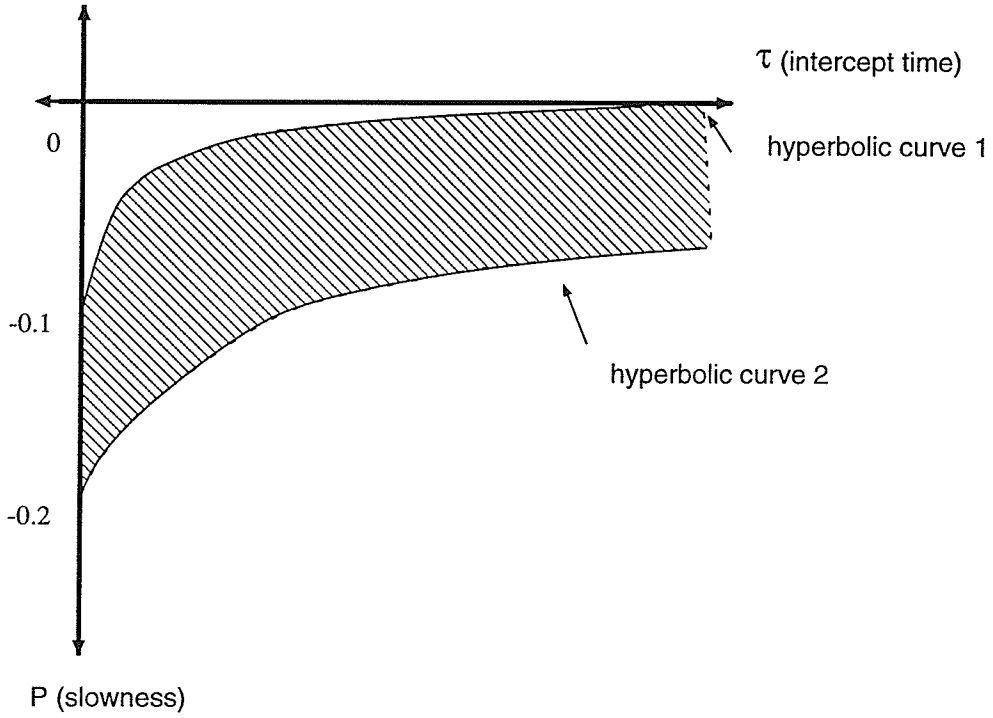

Figure 5.10: Schematic plot of the pass band in the hyperbolic filtering. Seismic energy outside the two hyperbolic curves is muted during the filtering.

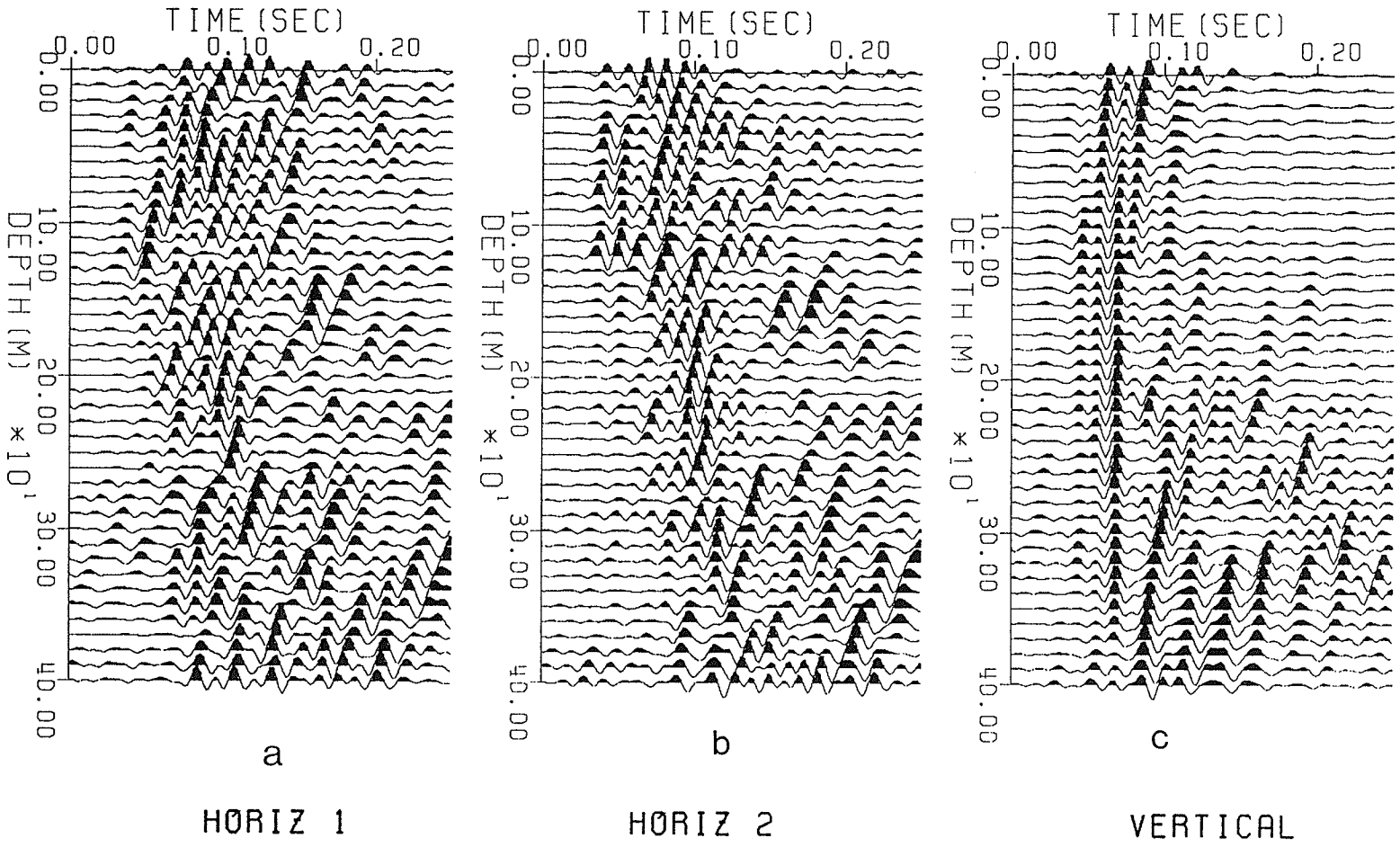

Figure 5.11: Separated wavefield of the VSP data recorded at the 150 m offset, Chelmsford, after Radon transform and hyperbolic filtering. HORIZ 1=horizontal component 1; HORIZ 2=horizontal component 2; and VERTICAL=vertical component.

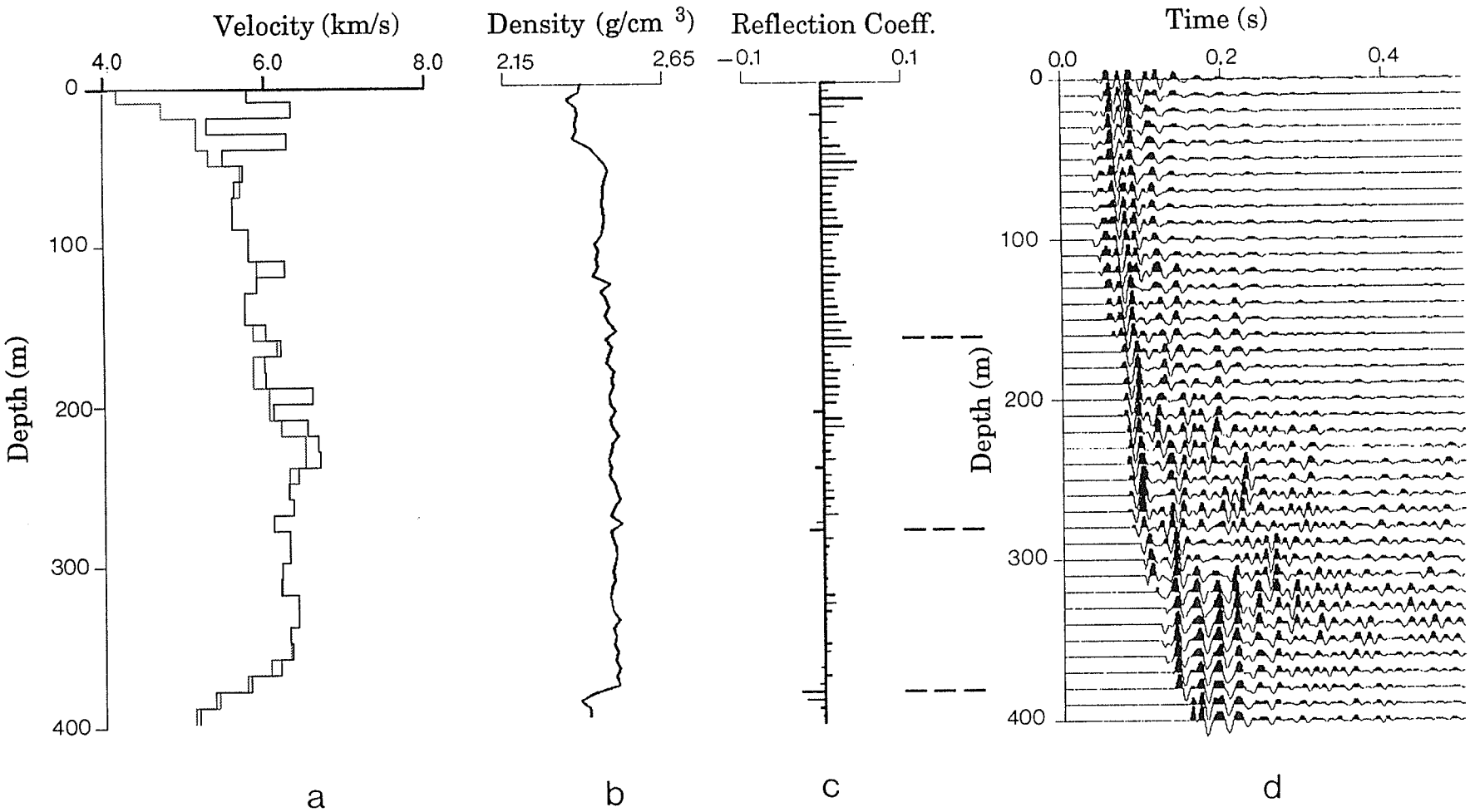

Figure 5.12: The P-wave flattened upgoing wavefield of the VSP data at the 150 m offset, Chelmsford, with density and velocity information. (a) Velocity estimation from VSP; the dotted line is the initial S-wave interval velocity estimated by slanted-straight ray average, and solid line is the interval velocity estimated by a least-squares inverse; (b) the density data from well-log; (c) the reflective coefficients computed from the density log and the P-wave interval velocity (a result from a least square inversion); and (d) the P-wave VSP flattened upgoing wavefield.

5.2.5 Shear Wave Analysis

The reoriented horizontal component data were processed for shear wave analysis. The wavefield separation results were better for the horizontal component data than for the vertical component data (Figure 5.11b and c). One possible reason is that energy of the downgoing direct P-wave, which contaminates the upgoing P-waves, is weaker in the horizontal component data. Several reflection events can be traced in the separated wavefields of the horizontal components even though there appears to be some P-wave and converted wave energy. Comparison with the P-wave data indicates that the S-wave data are more sensitive to geological interfaces probably due to its shorter wavelength. Discontinuities associated with each known interfaces can also be observed in the flattened upgoing wavefields (Figure 5.13d).

In the original records arrival times of the downgoing S-wave can be clearly seen (Figure 5.2) except at very shallow depth. The arrival times of the downgoing S-wave were picked through an interactive procedure with both the original data records and the flattened upgoing wavefields. If the reflectors were flat and the arrival times were correctly picked, the primary reflections should align in an approximately straight line after delaying of the first arrival times. The S-wave interval velocity model was obtained using the same traveltime inversion approach as discussed in the previous section, which was used later to flatten the S-wave upgoing wavefield. Figure 5.13d shows the flattened upgoing wavefield recorded with a source at the 150 m offset. Primary reflection events from the depths of approximately 120m, 160 m, 280 m, and 380 m are clearly observable. They also correlate closely with the reflection coefficients computed using the well-log density data and the S-wave velocity model.

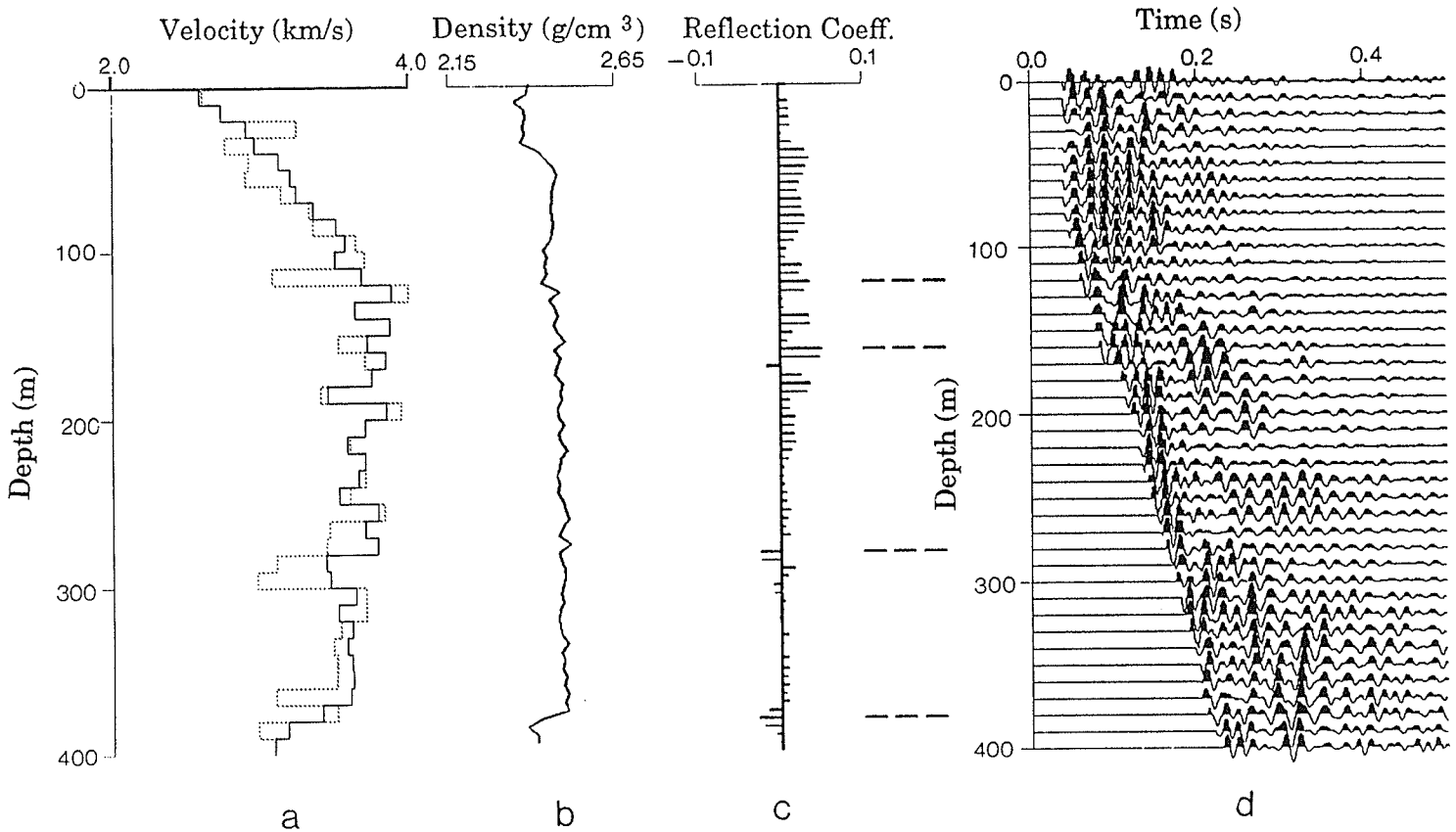

Figure 5.13: The S-wave flattened upgoing wavefield of the VSP data at the 150 m offset, Chelmsford, with density and velocity information. (a)Velocity estimation from VSP; the dotted line is the initial S-wave interval velocity estimated by slanted-straight ray average, and solid line is the interval velocity estimated by a least-squares inverse; (b) the density data from well-log; (c) the reflective coefficients computed from the density log and the S-wave interval velocity (a result from a least square inversion); and (d) the S-wave VSP flattened upgoing wavefield.

The reflection event at the depth of 380 m coincidences with significant decreases in both density and S-wave velocity. This in turn corresponds to the geological contact between the Chelmsford and Onwatin formations.

5.2.6 VSP-CDP transform

The wavefield separated P-wave sections were VSP-CDP transformed to correlate the VSP data with the surface reflection data. The algorithm, based on Moeckel (1986), pertains to upgoing wavefields only, which assumes that separation of wavefields has been achieved and all the reflectors are horizontal. Since there are dipping reflectors involved, the method is an approximation and was used to test geological correlation. In this transformation, amplitudes of a single VSP trace are mapped onto several traces in the $x - t_0$ plane as illustrated in Figure 5.14, where x is the lateral distance from reflection point to the borehole and t_0 is the twoway travel time. The resulting $x - t_0$ section consists of traces similar to the traces of a migrated zero-offset section.

The VSP-CDP transform consists of three steps: binning, moveout correction, and stack. As shown in Figure 5.9, a VSP experiment carried out with a source at x_{source} on the surface has a reflection point at x on the reflector. The reflection loci located within the range of $x \pm \Delta/2$ are sorted into the same binning gather.

Inspection of Figure 5.9 indicates the relation

$$x = \frac{(h - z)x_{source}}{(2h - z)}. \tag{5.15}$$

Let t_0 represent the twoway traveltime from the surface to a reflector and back to the surface, and t_b represent the one-way vertical first-break time from geophone to

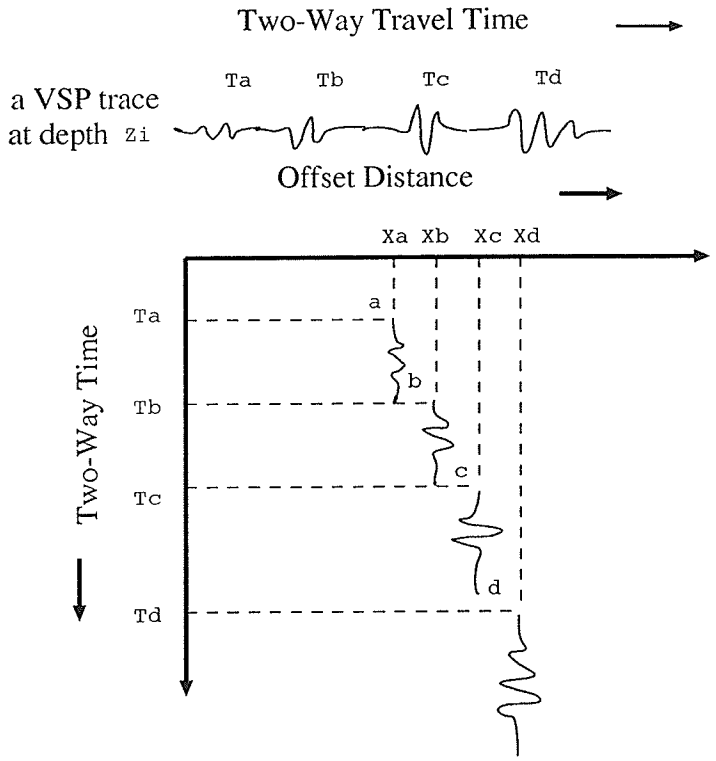

Figure 5.14: Schematic diagram of the VSP-CDP transform and horizontal stack of the VSP data. The top is a VSP trace recorded at depth z_i and converted to the two-way vertical travel time. The lower part of the diagram shows the four reflection events in a twoway time and offset plane. (Modified from Hardage (1983)).

surface. Replacing h by $t_0/2$, and z by t_b in equation (5.15) results in

$$x = \frac{(t_0 - 2t_b)x_{source}}{2(t_0 - t_b)}. \tag{5.16}$$

Rewrite it, one has

$$t_0 = \frac{2t_b(x_{source} - x)}{(x_{source} - 2x)} \tag{5.17}$$

The equation (5.17) is the bin relation equation, and is valid only when x lies within the range of $0 \leq x \leq x_{source}$.

The formula for moveout correction is given by

$$\Delta t_i = t_i - t_0, \tag{5.18}$$

where

$$t_i = t_0\sqrt{1 + \frac{x_{source}^2}{(t_0 - t_b)^2 v^2(t_0)}} - t_b\sqrt{1 + \frac{x_{source}^2}{(t_0 - t_b)^2 v^2(t_b)}}. \tag{5.19}$$

The VSP-CDP transformation proceeds according to the following steps:

(1) x_{source} is evenly divided into x_1, x_2 ....., x_i ....., x_n with interval of Δ. The interval Δ is data dependent. If Δ is very small, little data will be collected in a bin, whereas more data will be collected in a bin if Δ is very large, however, reflection energy smearing may happen. The data in a bin are called common reflection point data.

(2) each trace reflected at x is sorted according to the bin equation (5.17), and t_i can be derived from equation (5.19). Then the data set in a bin is generated as follows:

$$u(i, x_{source}, z, t) = 0, \qquad \text{if} \quad t \notin [t(i, x_{source}, z), t(i+1, x_{source}, z)]$$

$$u(i, x_{source}, z, t) = u(x_{source}, z, t), \quad \text{if} \quad \text{t} \in [t(i, x_{source}, z), t(i+1, x_{source}, z)]. \quad (5.20)$$

Repeat the procedure for all traces.

(3) moveout corrections are applied to each set of binned data using equation (5.18) to align them in twoway travel time t_0.

(4) moveout-corrected VSP data are stacked in each bin (indexed i) and placed at bin centers:

$$x_i = x_1 + \frac{(2i+1)\Delta}{2}, for \quad \text{i} = 1, 2, ...n. \quad (5.21)$$

The final stack is then derived by the formula

$$\bar{u}(x_i, t_0) = \sum_{x_{source}, z} w_i u(i, x_{source}, z, t_0). \quad (5.22)$$

The weighting factor w_i can be determined by counting the total number of non-zero contributions to the indicated sum at time t_0 in the ith bin.

The optimum bin spacing Δ was determined by testing with the data. Because of limited offsets and receiver points, the coverage in each bin was inhomogeneous and sometimes very poor regardless of Δ, especially when the reflector was shallow. $\Delta =$ 12.25 m was judged to be a suitable bin spacing for this experiment. The Chelmsford data which have excellent wavefield separation were VSP-CDP transformation into the $x - t_0$ plane.

The final CDP $x - t_0$ sections can be compared with the surface reflection sections to determine the depths of reflectors (see Figure 5.15) if there is no serious deviation from the assumption of horizontal reflectors.

5.3 VSP Data Interpretation Techniques

The techniques used for the VSP data interpretation are mostly developed in this research, which include correlation of the VSP data with the high-resolution surface reflection, particle motion polarization hodogram analysis to estimate dips of the key reflectors, and WKBJ synthetic seismogram modeling (Chapman, 1981).

5.3.1 Correlation with Surface High Resolution Reflection

The VSP-CDP transformed section was inserted into the high-resolution surface reflection data at the borehole site. At very shallow depth level, the frequency content in the VSP data is lower due to the NMO stretch. However at greater depths, there are several reflections which match with corresponding ones in the surface reflection section. They are observed at depths of 560 m, 650 m, 1240 m, 1520 m and 2305 m respectively (Figure 5.15). That the reflection event at about 380 m in the VSP section does not match well with the high-resolution surface data events is probably due to the effects of the dip of the reflector and weaker-reflection in the high-resolution surface reflection section.

The corridor-stacked P-wave VSP section was also spliced at the approximate borehole location into the interpreted high-resolution surface reflection section for comparison (Figure 5.16). In the high-resolution reflection section two major reflections are observable (also see Milkereit et al., 1992), which correspond respectively to the lithological contacts between the Chelmsford and Onwatin formations and between the Onwatin and Onaping formations. These reflection events are also clearly shown

in the corridor-stacked VSP section at 0.21 s and 0.45 s, both of them are in very good agreement with the surface high-resolution data. Since the high-resolution surface data were obtained after datum correction and surface consistent statics, the first reflection event in the corridor-stacked VSP section actually corresponds to the reflector at the depth of 380 m at the borehole location, and the second one is at the depth of approximately 1240 m in the vicinity of the borehole.

5.3.2 Hodogram and Particle Motion Analysis

Estimation of reflector dip using hodogram analysis stems from the fact that a compressional disturbance causes rock particles to oscillate in a polarized direction normal to the $P-$wave wavefront. Thus the particle displacement created by a P-wave wavefield points to the direction from which the P-wavefront comes. This direction will be the raypath's arrival angle at the borehole. The direction of the arrival vector carries information about the dip of the geological interfaces from which the reflection occurs. Therefore, one can estimate the dip of a reflector from three-component analysis of compressional reflection events (Figure 5.17).

The principle for estimating the dip of reflector is described by Hardage (1983) for the case when the propagating vector is normal to the reflective interface and of constant velocity. Throughout the Chelmsford formation, the velocity is not constant. However the data used for the hodogram analysis were recorded in a small receiver depth range between 340m and 370m. It was assumed that within this depth range the velocity variation can be negligible. The method requires vertical component data and either one of the two horizontal component data as long as the vertical sensor

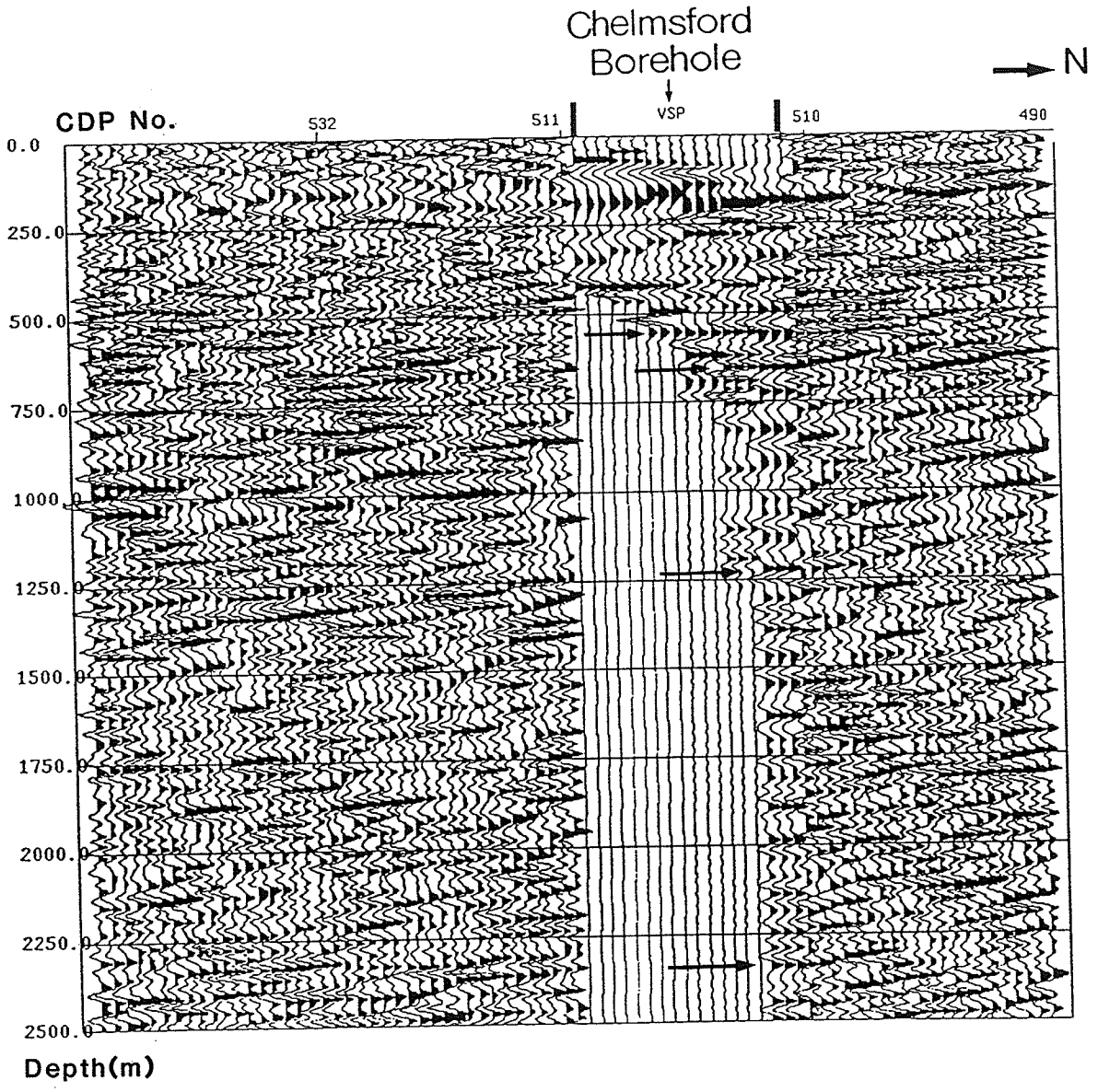

Figure 5.15: The VSP-CDP transformed P-wave section plotted and inserted into the high-resolution surface reflection section. The reflections at depths of 560 m, 650 m, 1240 m, 1520 m and 2305 m match well between the two sections.

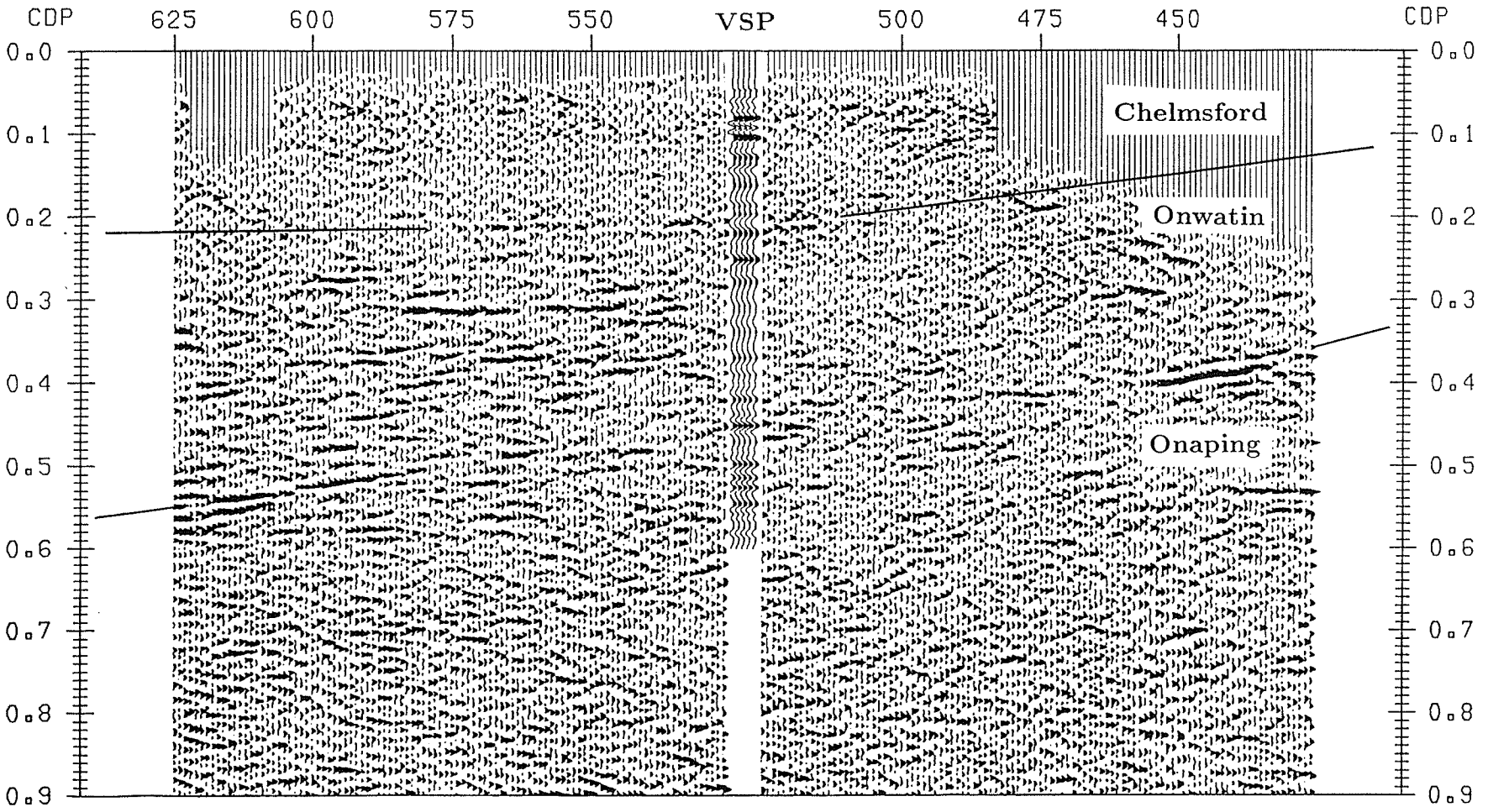

Figure 5.16: The corridor-stacked P-wave VSP data form the Chelmsford borehole is spliced into the interpreted high resolution seismic reflection data (Milkereit et al., 1992). The two major lithological contacts at 0.21 s and 0.45 s correlate well.

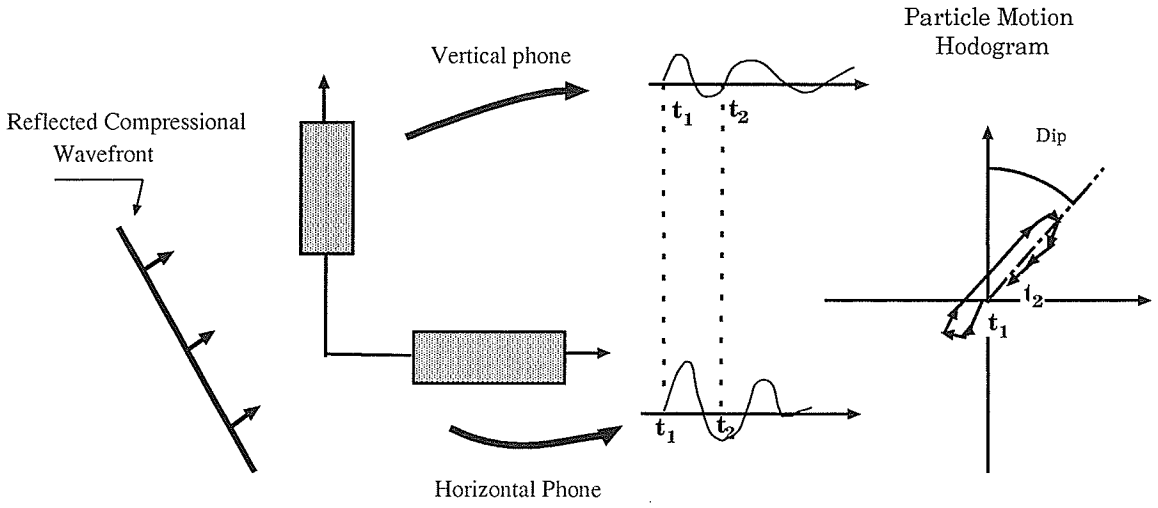

Figure 5.17: Schematic diagram depicting the basic principle of the particle motion hodogram estimating dip of reflectors.

stays vertical. In the case of the Chelmsford VSP experiment the direction of the propagation vectors was not always perpendicular to the reflectors, therefore some modifications were necessary to the method. Figure 5.18 depicts the geometry for estimating the true dip (Miao et al., 1994). When the source and reflector are on the same side of the borehole, the apparent dips obtained from the hodogram analysis which corresponds to the propagating vectors that are not perpendicular to reflector are always larger than the real dip (Miao et al., 1994b). The relationship between them is given by

$$\phi_b = \phi + i_b, \tag{5.23}$$

and

$$tan(\phi_b - \phi) = \frac{(x^2_{source} + z^2)^{1/2} cos(\theta - \phi)}{(x^2_{source} + z^2)^{1/2} sin((\theta - \phi) + 2(h - z)cos\phi)}, \tag{5.24}$$

where i_b is the reflection angle with respect to the reflector, ϕ is the real dip and ϕ_b is the apparent dip for the receiver station b, and $\theta = tan^{-1}(z/x_{source})$ (Figure 5.18).

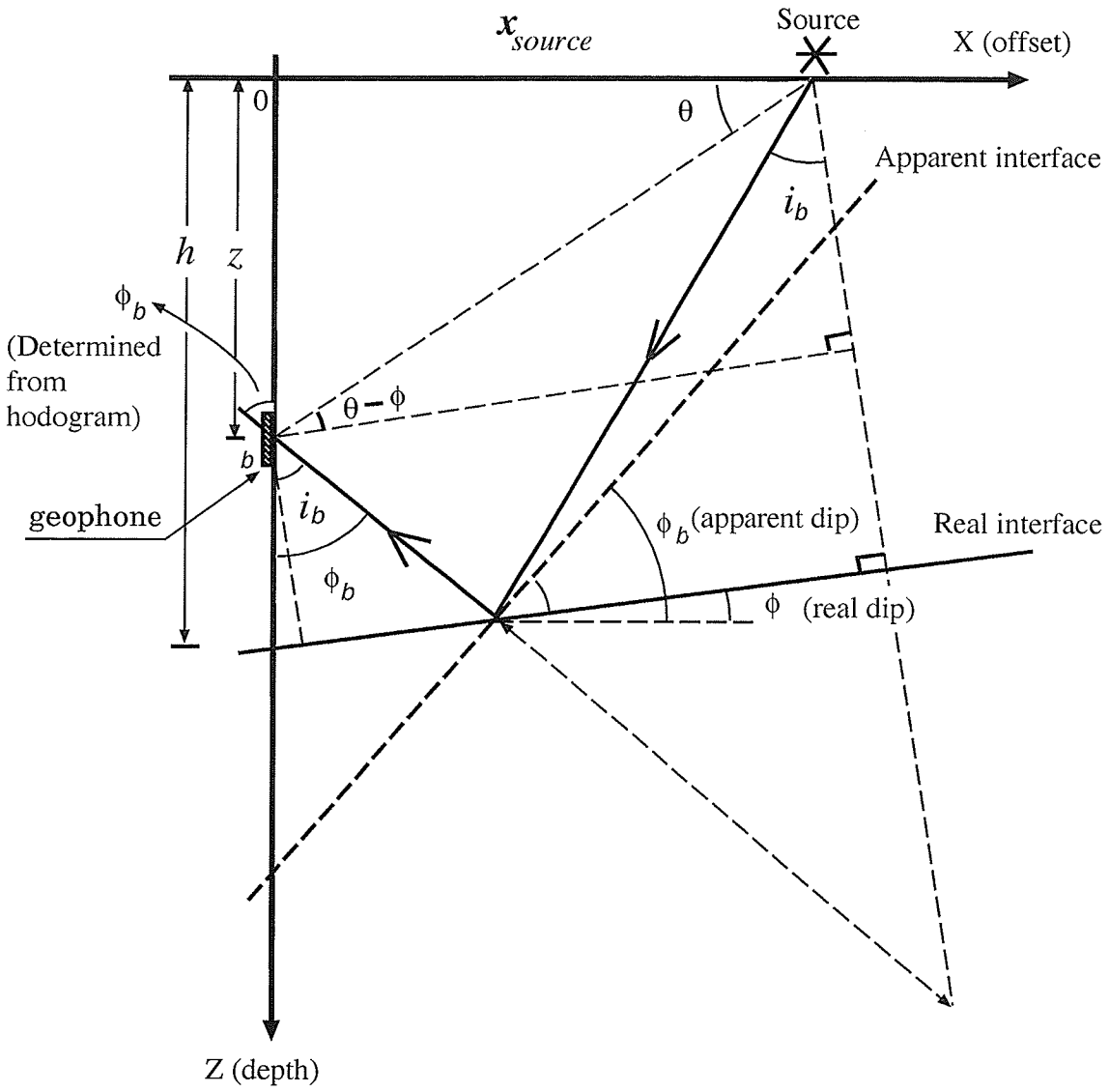

Figure 5.18: Schematic diagram depicting geometric principles for estimating the true dip from an apparent dip measured from the hodogram analysis.

Other parameters are the same as in equation (5.14). The angle ϕ_b can be estimated for each receiver depth on the basis of the hodogram analysis. Thus the only unknown in the equation (5.24) is the real dip angle, which can then be determined graphically.

Since the $P-$wave particle motions in the vertical and radial components oscillate in the same plane, which allows more accurate estimation for hodogram. Thus the vertical and the reoriented radial horizontal components were used to estimate the dip of the major reflector sequence at the depth of 380 m. This level corresponds to the contact between the Chelmsford and Onwatin formations. The computed reflection $P-$wave particle motion hodograms between the receiver depths of 340 m and 370 m are plotted in Figure 5.19. The results exhibit an almost constant orientation. The apparent dip for each receiver was obtained from the hodograms, then the real dip was estimated as shown in Figure 5.20. The intersection of the two curves (Figure 5.20) that represent the left and the right sides of the equation (5.24) respectively is the solution for each receiver depth. The real dip of a reflector sequence, thus, can be obtained as the horizontal coordinate of the solution. The values estimated in this case have an average value of approximately $10.4^o \pm 1.94^o$ for the 150 m source offset data. Since the surface reflection data indicates that the Chelmsford and Onwatin formations are dipping southeast, the result estimated from the hodogram analysis supports that the reflector really dips toward the southeast at about $10.4^o \pm 1.94^o$ (Figure 5.20).

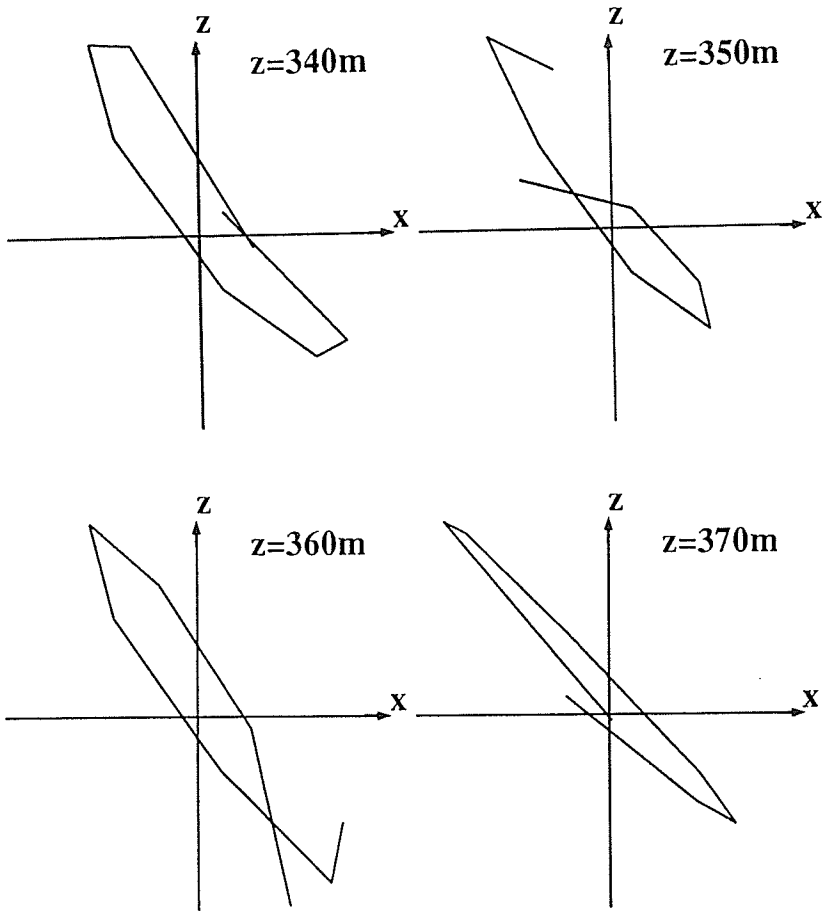

Figure 5.19: The particle motion hodograms for the P-wave reflection from the Chelmsford-Onwatin contact recorded by a three-component geophone located between 340 m and 370 m depths with the source offset of 150 m. Here the time window length is 16 ms, and Z represents the vertical component and X represents the horizontal component 2.

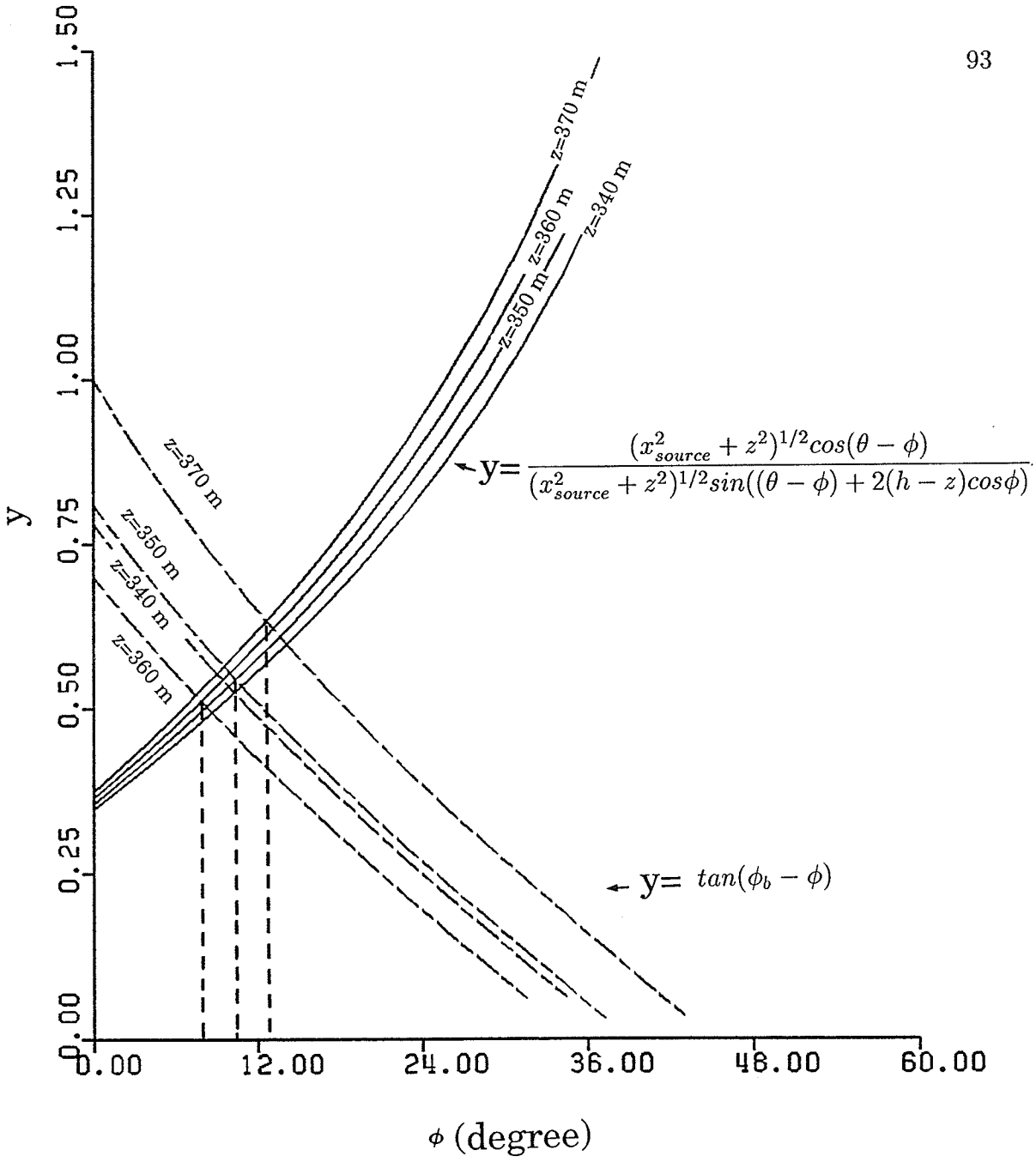

Figure 5.20: A graphic solution process for estimating the true dip ϕ of the reflector sequence at the depth level of 380 m using particle motion data recorded between the 340 m and 370 m depths. The source offset is 150 m and the parameters used here are the same as described in Figure 5.18.

5.3.3 WKBJ Seismic Modeling

In order to evaluate the estimated P- and S-wave velocity models, theoretical synthetic seismogram modeling was also carried out in this research. The synthetic seismogram algorithm used was a WKBJ method developed by Chapman (1981). It not only can handle vertically inhomogeneous media with horizontal layering, but also can compute various body wave phases of both primary reflections and any order of multiples with various source and receiver geometries. The synthetic seismogram is computed from the solution of the elastic wave equation under the WKBJ approximation, which assumes that the change in slowness functions in one wavelength must be much less than the slowness itself. In most realistic situation the WKBJ algorithm provides acceptable approximation, and it works well in generating seismograms for both shear waves and converted waves.

Independent of the algorithm, the final synthetic seismogram is programmed as a simple convolution model

$$u(t) = w(t) * e(t) \tag{5.25}$$

where $u(t)$ is the seismogram, $w(t)$ is the seismic wavelet including source signature and recorder response, and $e(t)$ is the earth's impulse response. Depending on the algorithm used, $e(t)$ can be derived by solving the wave equation with specific boundary conditions.

The initial velocity models for P- and S- wave were based on the results of VSP data analysis, and the density model was determined from the well log data (Falconbridge Co.). The final shallow velocity model derived from the WKBJ modeling produced excellent near true amplitude and arrival times for all of the four offset data. Figure

5.21b shows the synthetic section of the vertical component data for the offset of 150 m. Inspecting the original record of the vertical component data (Figure 5.21a), one observes that at shallow receiver levels the amplitudes of the downgoing P-wave are weaker. As the depth increases they become gradually stronger. In contrast, the next prominent seismic phase, which is the downgoing S-wave, shows strong amplitudes at shallow levels, while the amplitude gradually decreases with depth. This can be explained by the radiation pattern of the Vibrator source sweep signal. At shallow depths the geophones recorded stronger horizontal vibrations, and as the depth increases the recorded vertical vibrations become stronger. This feature in the raw data section is faithfully reconstructed in the synthetic seismogram section. Another feature worth pointing out is the very strong downgoing waves. Even though both primary and multiple reflections were generated at each reflection level, they were hardly observable in the raw data due to large amplitude of the downgoing waves. This is consistent with observation of the original records. Figure 5.21c is the velocity model used for computation of the synthetic seismograms plotted along with the well-log data. In general, the velocity model correlates well with the well-log lithological interfaces.

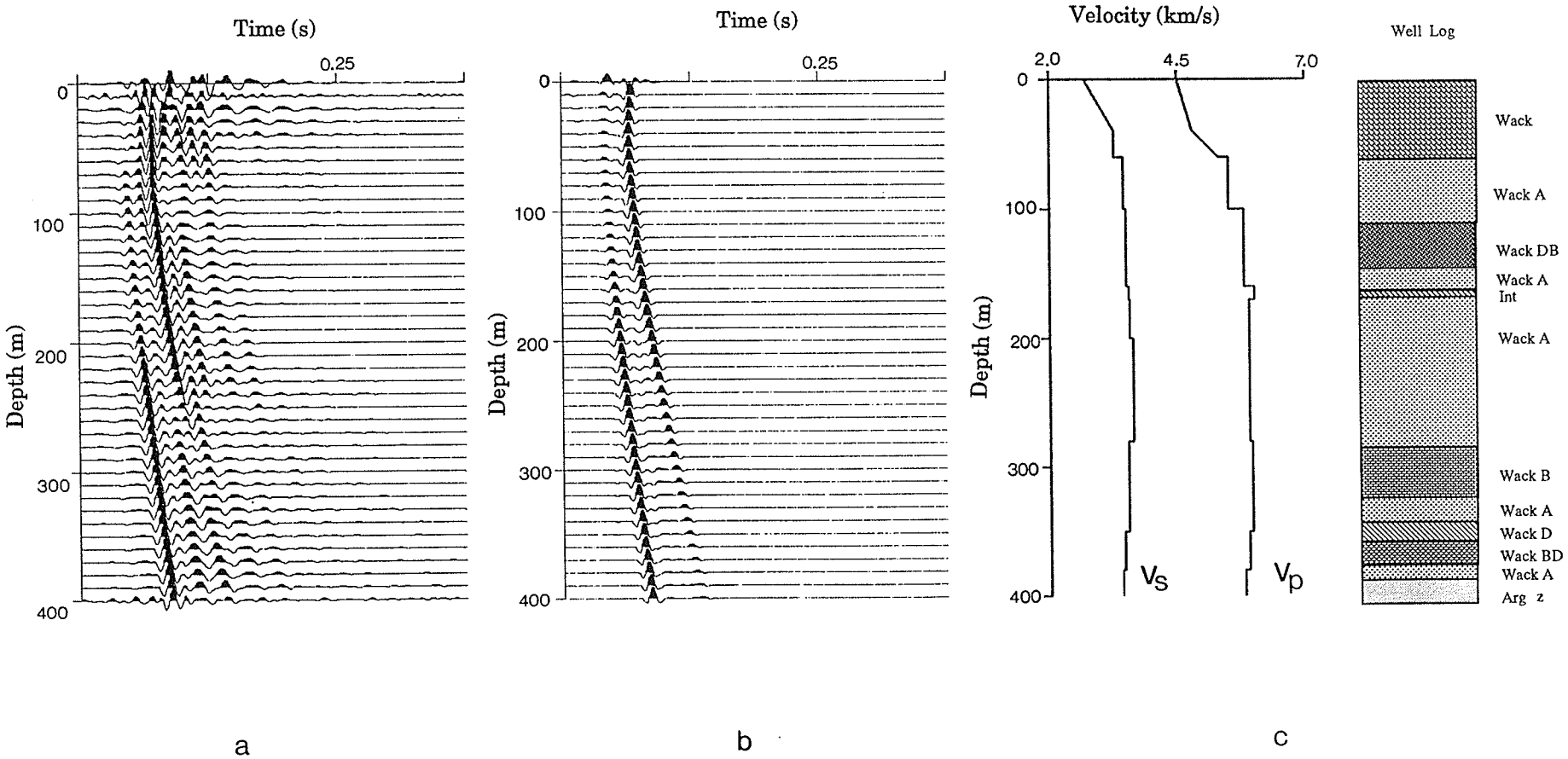

Figure 5.21: The VSP data recorded at the offset of 150 m (Chelmsford): (a) the vertical component of the original VSP record; (b) the vertical component of the WKBJ synthetic VSP seismogram; (c) the corresponding velocity model plotted with the well-log lithological data (Falconbridge Ltd..). (Arg=argillite, Wack=graywacke, and Int=intrusive).

Chapter 6

Seismic Reflection Investigation

6.1 Characteristics of Seismic Reflection in the Crystalline Rock Terrane

Upcoming seismic reflection energy is generated from subsurface contrasts in acoustic impedance. The factors which affect the acoustic impedance contrast, actually densities and seismic velocities within rock units, are diverse. Lithology is one of the most obvious factor that determines velocity and density of a rock formation. Porosity of rocks, temperature and pressure under which rocks are buried are also important factors for velocity change. The interstitial fluid in porous rocks can affect the seismic velocity and rock properties as well. In terms of the propagation of seismic waves, reflection strength is modified by geometrical spreading, anisotropy of rocks, constructive or destructive interference, and anelastic attenuation.

The physical processes of seismic reflection in a sedimentary basin is in general different from that in a crystalline rock terrane. In a sedimentary basin reflection occurs mostly at the interfaces between depositional layers, at tectonically imposed

structural boundaries, and is governed by the properties of interstitial fluids (Sheriff and Geldart, 1986). The signatures of reflections are much more pronounced than those from a crystalline terrane.

Seismic reflection data from a crystalline rock environment are usually characterized by:

- low S/N ratio - rock types are usually of igneous and metamorphic origin, and the acoustic impedance contrast between these rock units is generally low compared with that in sedimentary environment. There are often gradual changes in the physical properties even in the same rock units. The interfaces from which reflections occur are of structural or intrusive ones in most cases, and the reflectivity or reflection coefficient is commonly lower than that from a more consistent and continuous sedimentary boundary;

- lack of lateral continuity - disturbance of layering resulting from later tectonic activity, igneous intrusion, and local metamorphic reaction superimposed on older crystalline rocks, often complicate the geological environment (Dahl-Jensen, 1989, Mike, 1990), and consequently reflection horizons become discontinuous and are commonly replaced by dipping or subhorizontal events with complex attitudes;

- scattering energy from shallow inhomogeneities - shallow subvertical faults, joints, and near surface fracture zones produce energy scattering, which distorts shallow reflection images. Careful processing is required to preserve true images of shallow structures (Strahler, 1981).

- sensitive to multi-layered boundary - seismic reflections are more sensitive to multi-layered boundaries than to a single lithological contact due to the low acoustic impedance contrast in igneous and metamorphic rocks units, and also due to wavefield interferences between primary, converted and multiple reflections.

In spite of the above unfavorable factors, some strong reflections have been observed in crystalline rock terranes in recent years. Explanations for reflection process fall into five principal categories (Green et al., 1990): (1) primary unmetamorphosed depositional layering; (2) primary intrusive layering; (3) tectonically imposed layering, including shear zones of various types; (4) metamorphic layering; and (5) fluid related phenomena. These physical explanations are not exclusive of each other. Depending on local geological setting, one or more factors may play a major role for causing seismic reflection energy.

Recent study shows that in the Abitibi greenstone belt (Jackson, et al., 1990) Archean igneous layering and the tectonically high-strain zones are the most likely sources of strong seismic reflections, even though fluid-rich horizons such as fault zones, extensive zones of deformation, brittle fault zones, mylonite zones, and lithological contacts may also be responsible for the reflections. In the Kapuskasing high-grade metamorphic terrane (Green et al., 1990, Milkereit et al., 1991), where the lower crustal gneissic units containing granulite facies were uplifted to the surface, with certain similarities to the Sudbury LGC, prominent reflection zones are associated with sheared rocks along the cataclastic zone and the interlayered package of gneiss and tonalite. Shallow reflections are generated from tonalitic rocks enclosing lenses

of mafic gneisses and paragneisses. In the Grenville front tectonic zone (Green, et al., 1990), the reflections are characterized by relatively discrete bands of strong reflection bordering by the area of low reflectivity. The strong reflections are mostly generated at the mylonitic boundaries between lenticular units of less deformed or very finely layered gneissic rocks (Green et al., 1989). Intensely sheared rock is probably another one of main sources for enhanced reflectivity (Calvert and Clowes, 1990). The transparent characteristic of seismic reflection data across some high-grade metamorphic terranes may be due to very steep dips, lack of significant variation in lithology and strain, or extremely complex structures (Klemperer, 1987).

6.2 Seismic Reflection Data Processing

There were three seismic reflection profiles surveyed in 1990, and the results of two profiles (lines 40 and 41) were interpreted and published by Milkereit et al. (1992) after preliminary processing. The result of the preliminarily processed line 42 data, however, releaved almost no identifiable geological information. It was thus excluded in the published preliminary interpretation of the Sudbury reflection data (Milkereit et al., 1992). Therefore reprocessing of the Sudbury line 42 regional reflection data was planned and carried out at the University of Manitoba, and constitutes one of the major parts of this thesis research.

Preliminary processing of the line 42 data by the contractor included crooked spread geometry, datum and weathering correction, velocity analysis, CDP trim statics, stacking and spectral whitening. The quality of the stacked section turned out to be unsatisfactory, particularly in the shallow part (0-3s) where almost no significant

reflection events can be observed (Figure 6.1). The possible reasons for the poor quality are probably due to (1) low S/N ratio environment in the crystalline rock terrain, (2) discrete reflection bands, (3) complex subsurface structures, and (4) inadequate processing parameters.

Examination of the raw reflection data from Sudbury regional line 42 found out that random noise is minor. The main sources of noise appear to be ground roll and air-wave. The reflections tend to lack lateral consistency, even though they exist in many shot gathers. Reflective patterns are thus highly variable from one shot gather to another.

The strategy for reprocessing of the line 42 data emphasized improvement of the S/N ratio and focusing of the reflection energy, which include traditional approaches such as spectral balance, $f - k$ filtering, refraction statics, careful velocity analysis cascaded with residual statics, and offset limited stack. In addition, two advanced processing techniques were developed for this processing task, which include focusing of the reflection energy using the time-varying cross-dip correction and removal of ground roll by means of the wavelet transform. Figure 6.2 shows the specially designed reprocessing flow chart. The important reprocessing parameters are listed in Table 6.1, and the new programs developed in this thesis are also marked as double stars in Table 6.1.

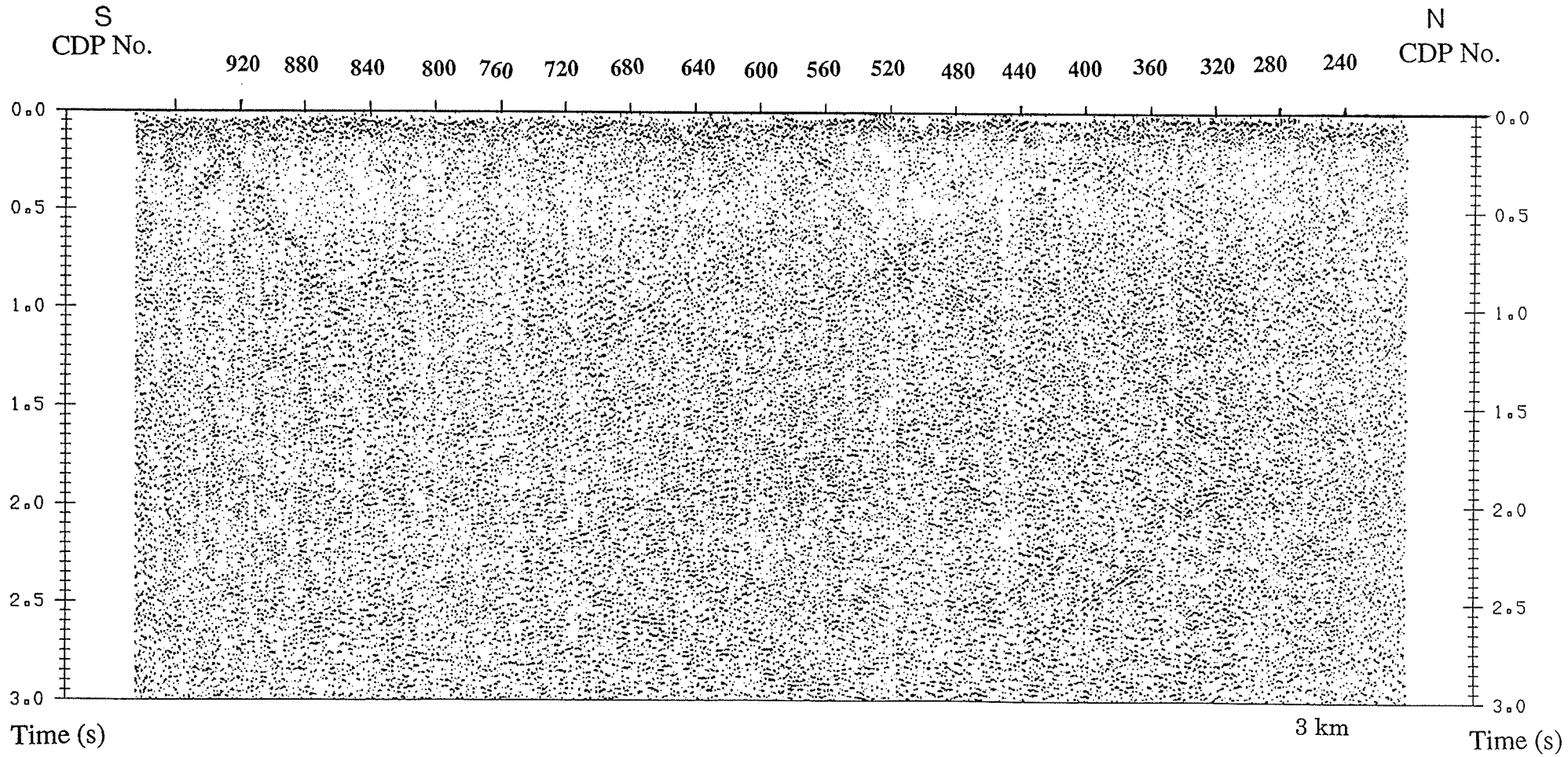

Figure 6.1: The preliminarily processed profile of the regional seismic reflection line 42 of the LITHOPROBE Sudbury Transect.

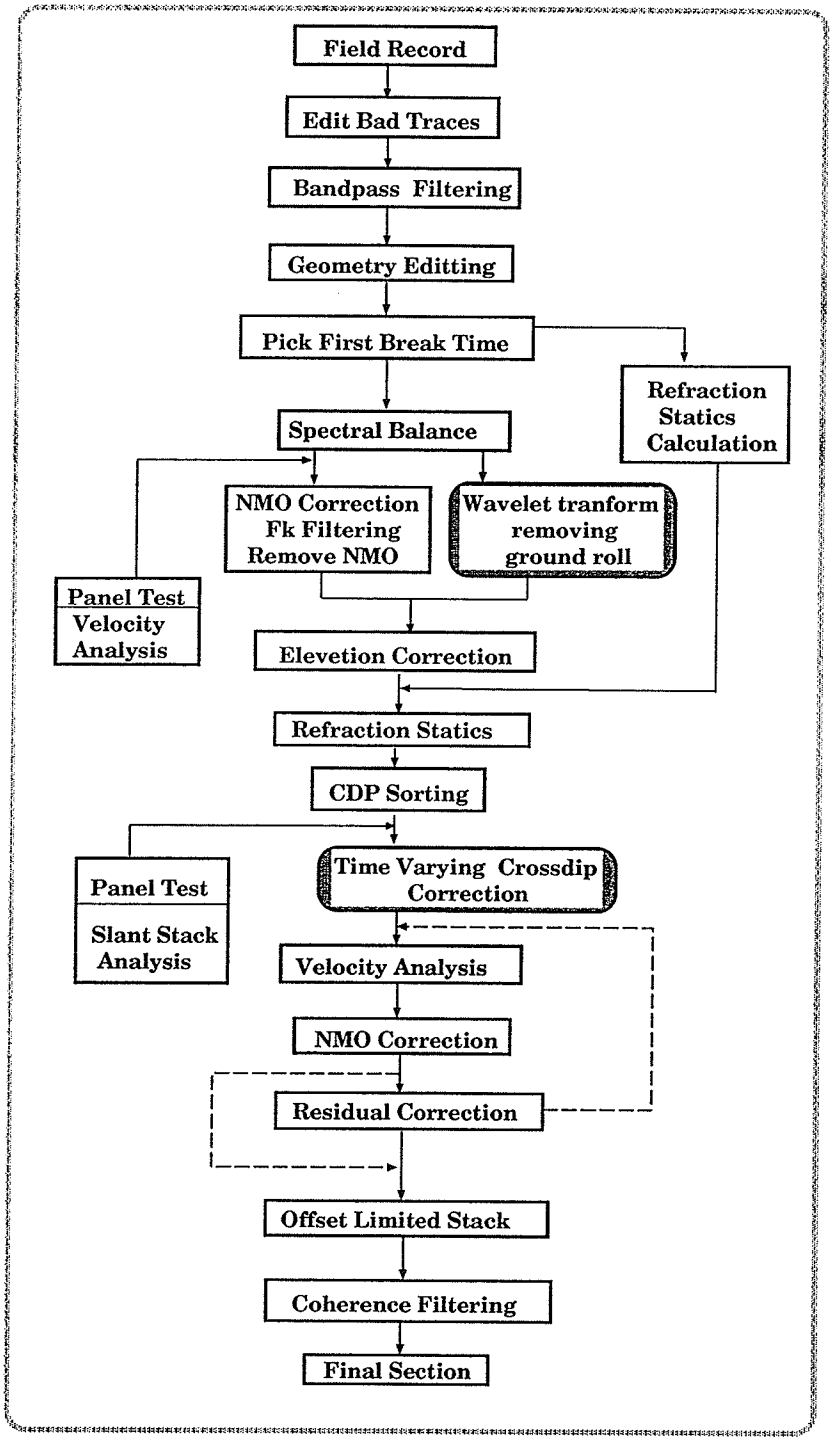

Figure 6.2: Flow chart for reprocessing of the line 42 data. The wavelet transform and time varying cross-dip correction are the two new techniques developed in this thesis research.

Table 6.1: Processing parameters and INSIGHT modules used in the line 42 data processing.

Processing task	parameters	Modules
Spectral balance	10-56 Hz, 10 Hz slide window 0.5 s AGC	EQRA *
Removal of ground roll		
f-k filter	< 4850 m/s rejected	FKS2, * FKSURG
Wavelet Transform		WT program**
Refraction statics		
First break picks	Interactive	
Datum correction	400 m, 6100 m/s	DATM *
Refraction statics		REFSTAT2*
Crooked line geometry		
Bin width	25 m	CDPBIN*
Bin height	800 - 1000 m	
Cross-dip correction		
Slant stack scan	-0.2 ms/m - 0.2 ms/m	SLNR*
Cross-dip correction		Time-varying ** crossdip correction
Velocity analyses		
Constant velocity scan		VAC2 *
Semblance analysis		VSMB*, VAN2 *
Residual statics		
Super-fold statics		SUPER_FOLD*
Maximum shift	20 ms	
Offset limited stack	5000 m	SELO, NMO2* STA2
Coherency filter		
Maximum slowness	± 10 ms/trace	SLNW *
Sliding window	11 traces	

* ---- INSIGHT module **---- in house writen program

Actual processing of the data was implemented using IT&A's INSIGHT software (Version 4.0), to which the newly developed routines for this project were interfaced. In this study the time varying cross-dip correction was applied to the data with time window of 0-3 s two-way traveltime, and the other processing steps were limited to the time window of 0-6 s.

6.2.1 Crooked Line Geometry

Since the reflection survey line 42 is a crooked line, the common depth points (CDP) for each pair of the shot and receiver no longer stay along the survey line. They are scattered around the survey line in both in-line and cross-line directions. To stack the traces in a specific CDP bin efficiently, a slalom line was chosen to replace the true survey line for the CDP binning (see Figure 6.3). This was accomplished by using the processing module CDPBIN in the INSIGHT-4.0 package. For processing without the cross-dip correction, a bin height of 800 m and a bin width of 25 m were used. For processing including the cross-dip correction, the bin height increases to 1000 m. The CDP binning strategy for cross-dip correction will be discussed in section 6.2.4 in detail. Figure 6.3 shows the survey line geometry and the CDP binning used for processing including the cross-dip correction.

6.2.2 Refraction Statics and Filtering

The raw data were first tested with bandpass filtering and automatic gain control (AGC) to gain some knowledge of the frequency ranges of the signal and noise. It was found that the reflection signals had a spectral range from 20 to 50 Hz. A

bandpass filter with the frequency band from 10 to 56 Hz was initially applied to the shot gathers and an AGC window of 0.6 s was used. Subsequently spectral balance was carried out over the frequency band from 10 to 56 Hz with a sliding bandpass filter of 5 Hz width and 5 Hz taper at both ends of the band. A 0.6 s AGC was also applied to each component trace during the spectral balance. Application of the spectral balance slightly increased the S/N ratio, but was not as effective as for high resolution data because of the limited spectral width of the regional data. Figure 6.4 shows an example of a shot gather after application of bandpass, AGC and spectral balance.

Static corrections consist of datum correction and refraction statics. Datum correction was carried out using a datum of 400 m and replace-velocity of 6100 m/s. The time-term method of Farrell and Euwema (1984) was used to solve for surface-consistent refraction statics by assuming a weathering layer of varying thickness and velocity overlaying a half-space of laterally varying velocity. In the approach, each first break time is considered to consist of three terms as follows:

$$T_{jk} = t_{sj} + t_{rk} + p \times x_{jk}, \tag{6.1}$$

where: T_{jk} is the picked traveltime for a seismic ray travelling between the shot j and the receiver k;

$t_{sj} = z_s(v_b^2 - v_w^2)^{1/2}/v_b v_w$ is the downward vertical traveltime at source location, z_s is the depth to bedrock below the receiver, v_w is the weathering layer velocity, and v_b is the bedrock velocity;

$t_{rk} = z_r(v_b^2 - v_w^2)^{1/2}/v_b v_w$ is the upward vertical traveltime at receiver locations, z_r is the depth to bedrock below the shot;

p is the ray parameter; and

x_{jk} is the offset distance between the shot j and the receiver k.

By giving an estimated half-space velocity and knowing the offset distance, the unknown terms t_{sj} for shot location and t_{rk} for receiver location can be computed by the least-square decomposition method. In the time-term method, the estimation of the weathering velocity is made by smoothing the results of a preliminary estimation.

Although many people have considered that the weathering layer in the crystalline terrane is usually very thin and refraction statics could be neglected, the result of application of the refraction statics to the line 42 data has proved its effectiveness when the first break times were carefully picked. Figure 6.5b shows a segment of the stacked section with refraction statics applied. The corresponding segment of the stacked section without application of refraction statics is shown in Figure 6.5a. After the refraction statics, the long wavelength anomaly is removed and reflection events between 4-6 s are enhanced (see Figure 6.5b).

The short wavelength anomaly, however, can not be removed by refraction based statics (Yilmaz, 1987), hence reflection based residual statics was applied in cascade. Figures 6.5c and 6.5d show the results after both refraction and reflection statics. Both long and short wavelength anomalies were removed. Further detail on the residual statics will be discussed in section 6.2.5.

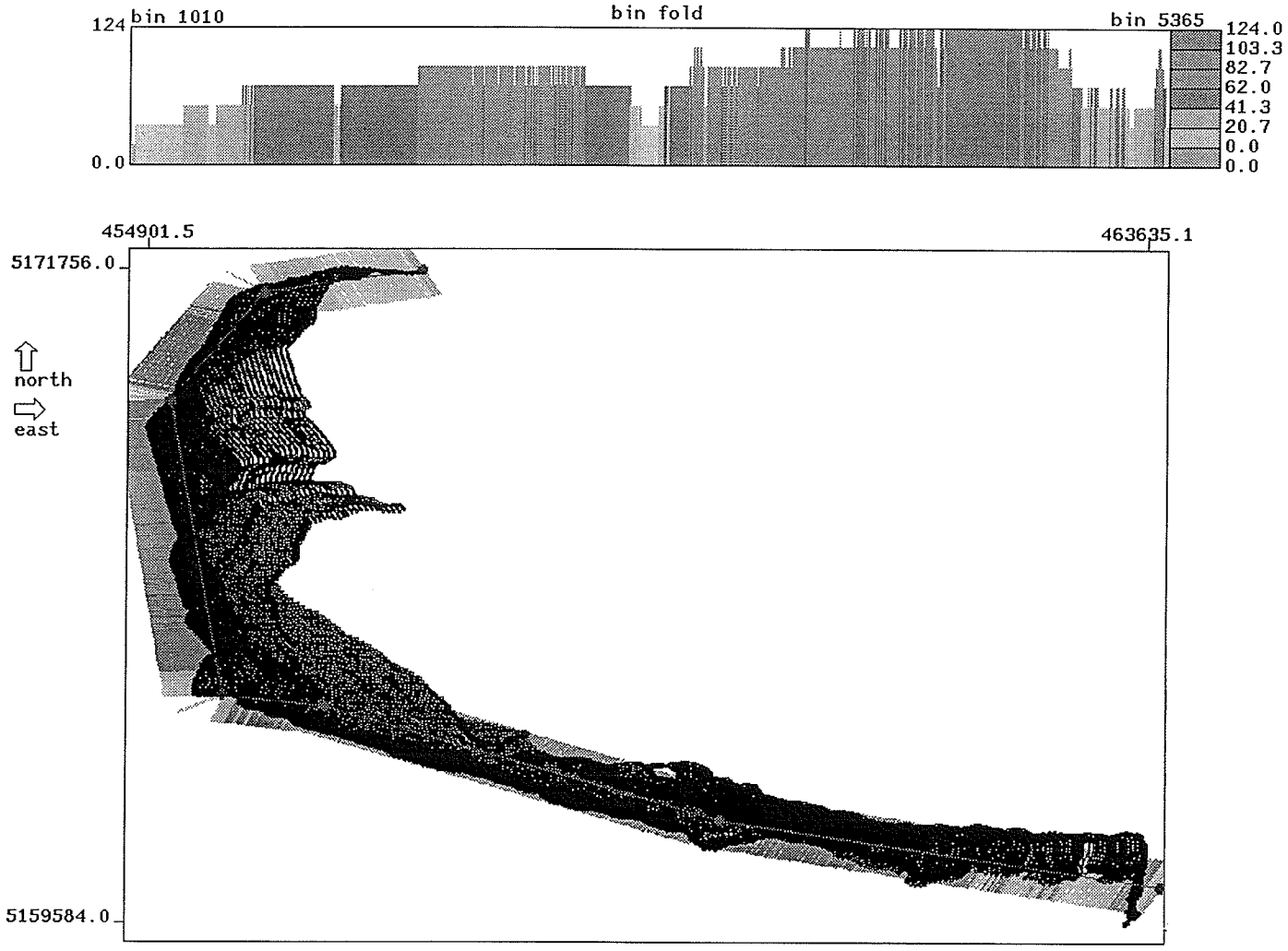

Figure 6.3: Geometry of the line 42 survey line and CDP binning: dots represent the mid-points between each receiver and shot pair. The fold coverage is shown by grey level plot at the top of the figure. The bin height is 1000 m and bin width is 25 m. The slalom line is depicted as a thin line in the middle.

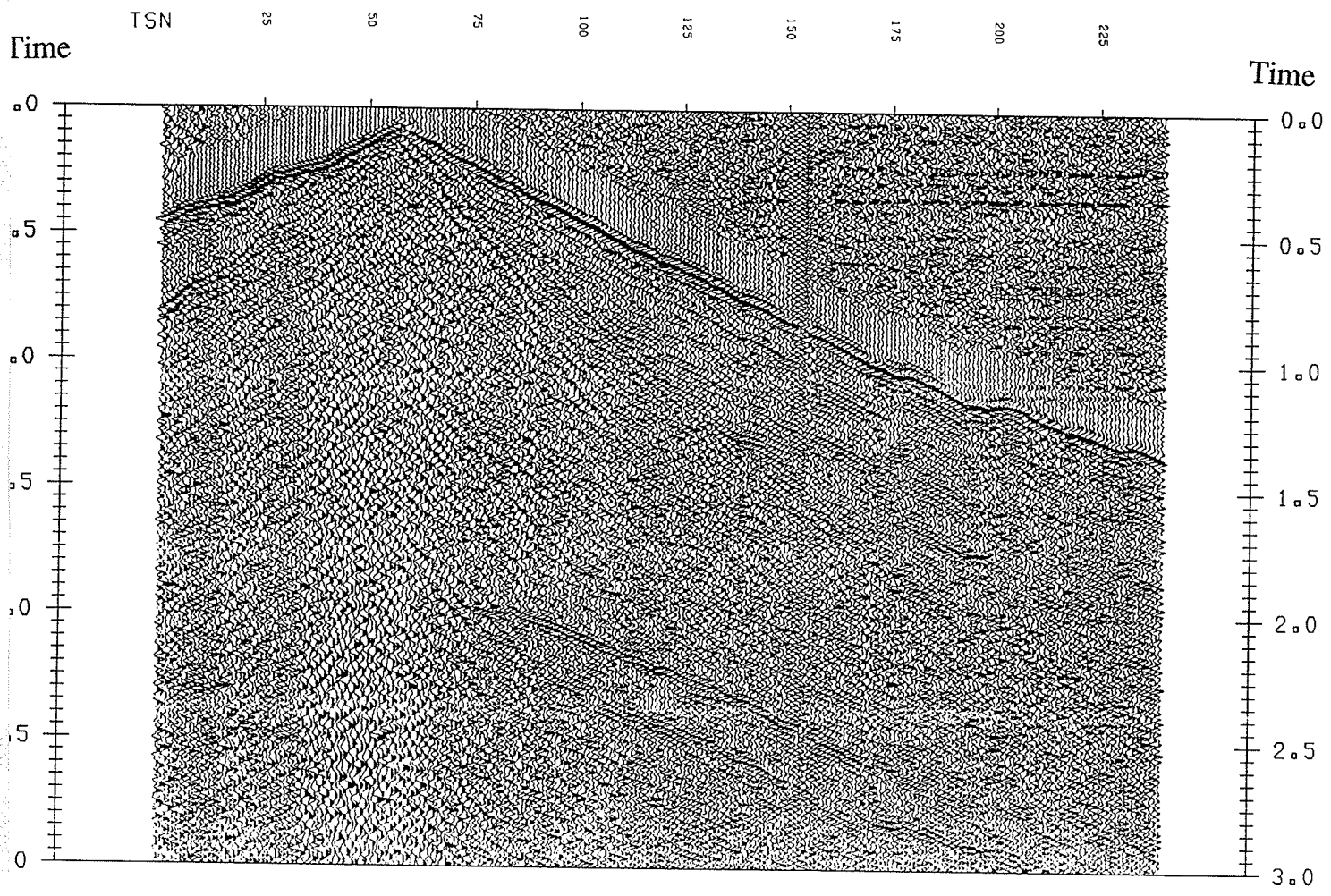

Figure 6.4: AGC and bandpass filtering: an example of the original raw shot gather after AGC and bandpass filtering.

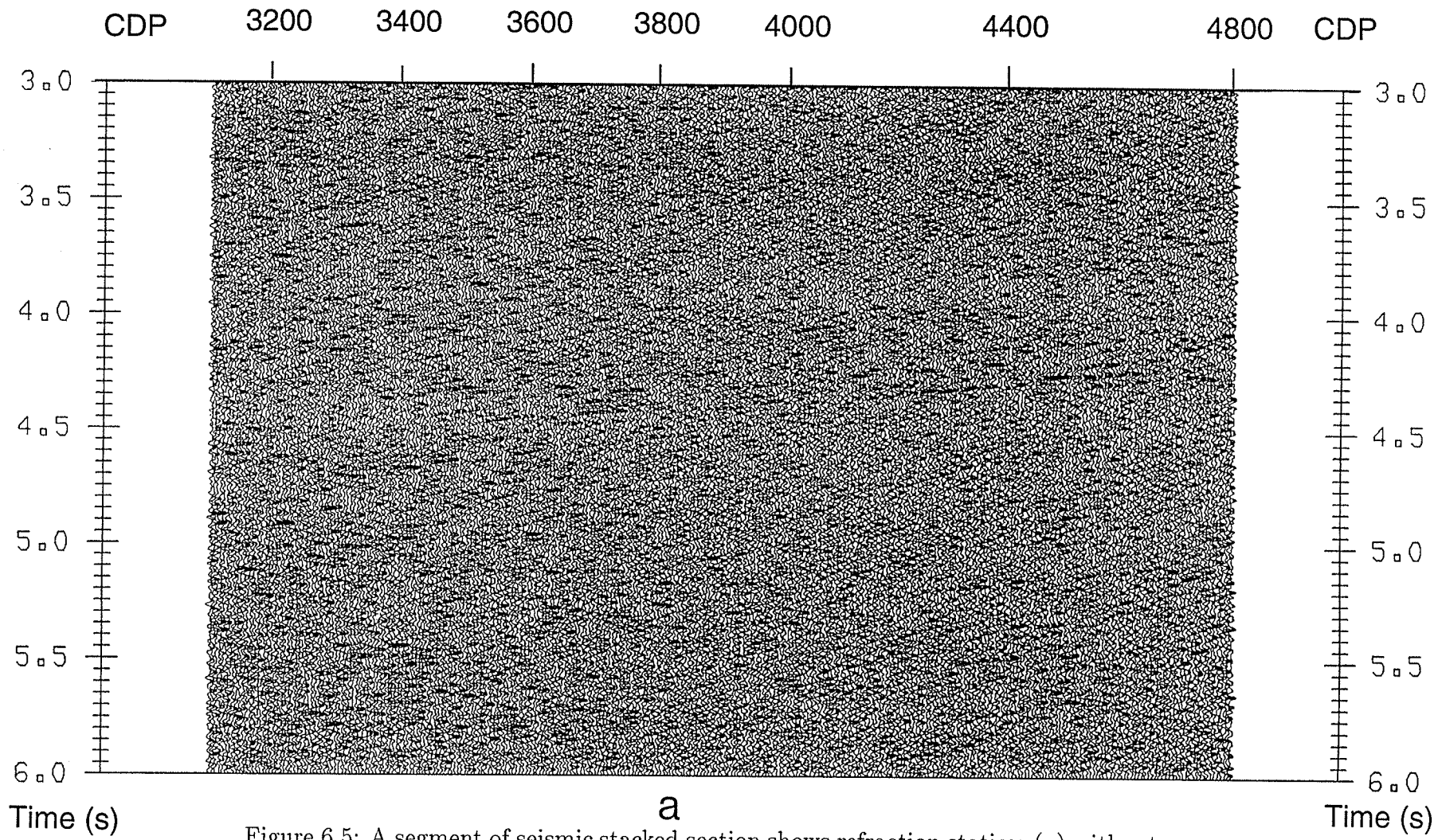

Figure 6.5: A segment of seismic stacked section shows refraction statics: (a) without refraction statics; (b) with refraction statics; (c) with both refraction and residual statics; (d) the bias plot of (c) after coherency filtering. Continue to the following pages.

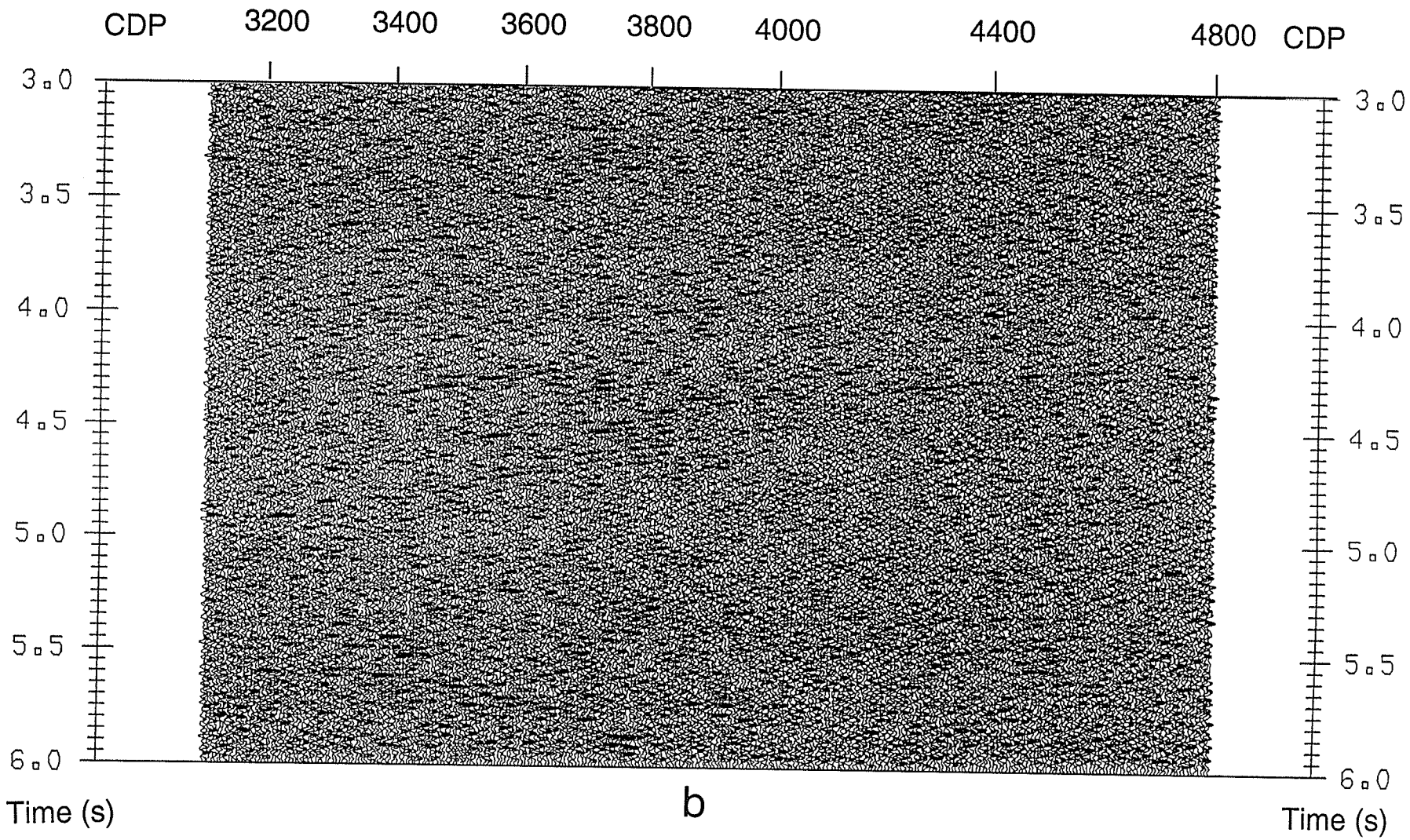
CDP
3200
3400
3600
3800
4000
4400
4800
CDP
3.0
3.5
4.0
4.5
5.0
5.5
6.0
Time (s)
b
Time (s)

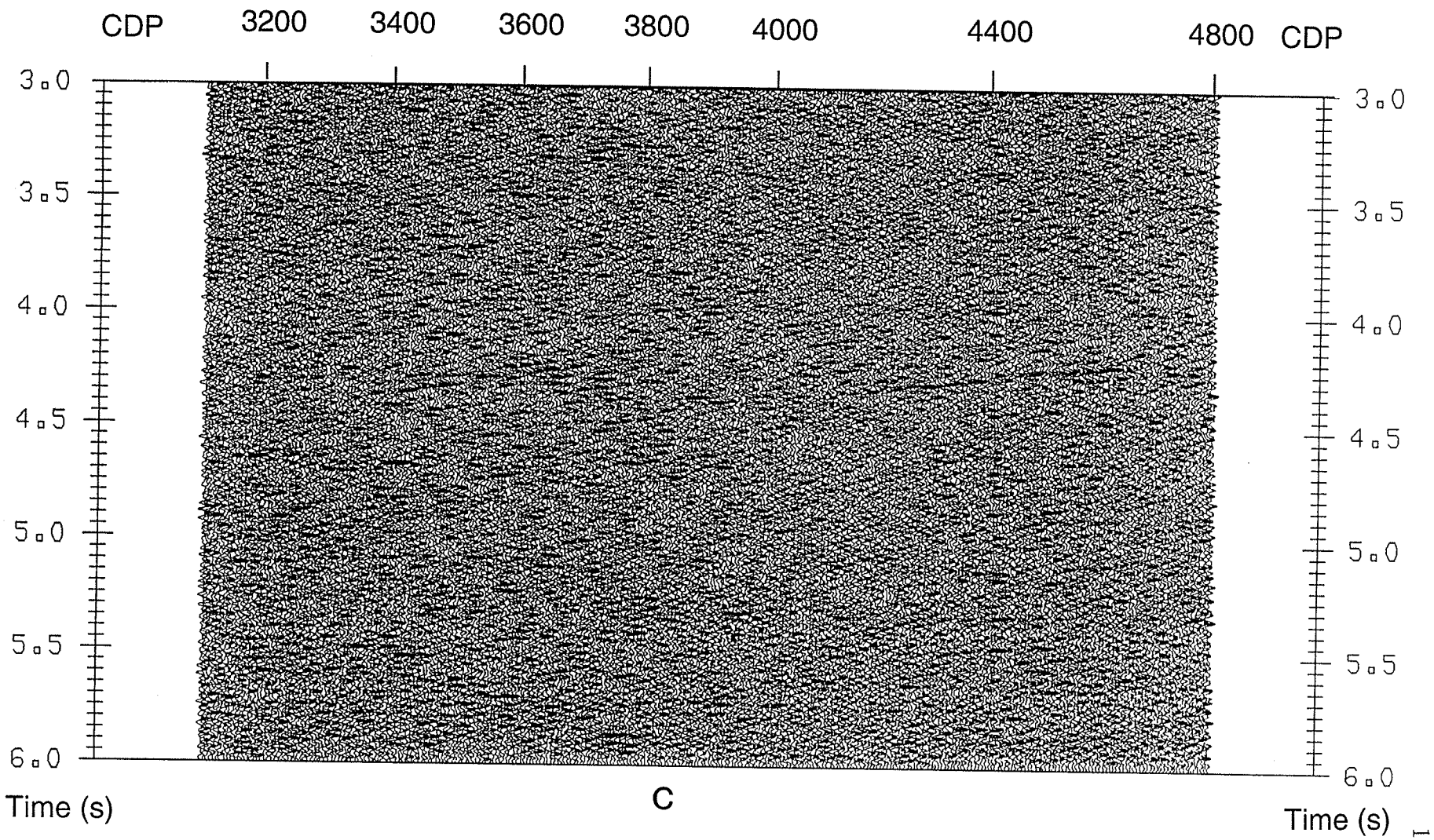
CDP
3200
3400
3600
3800
4000
4400
4800
CDP
3.0
3.5
4.0
4.5
5.0
5.5
6.0
Time (s)
C
Time (s)

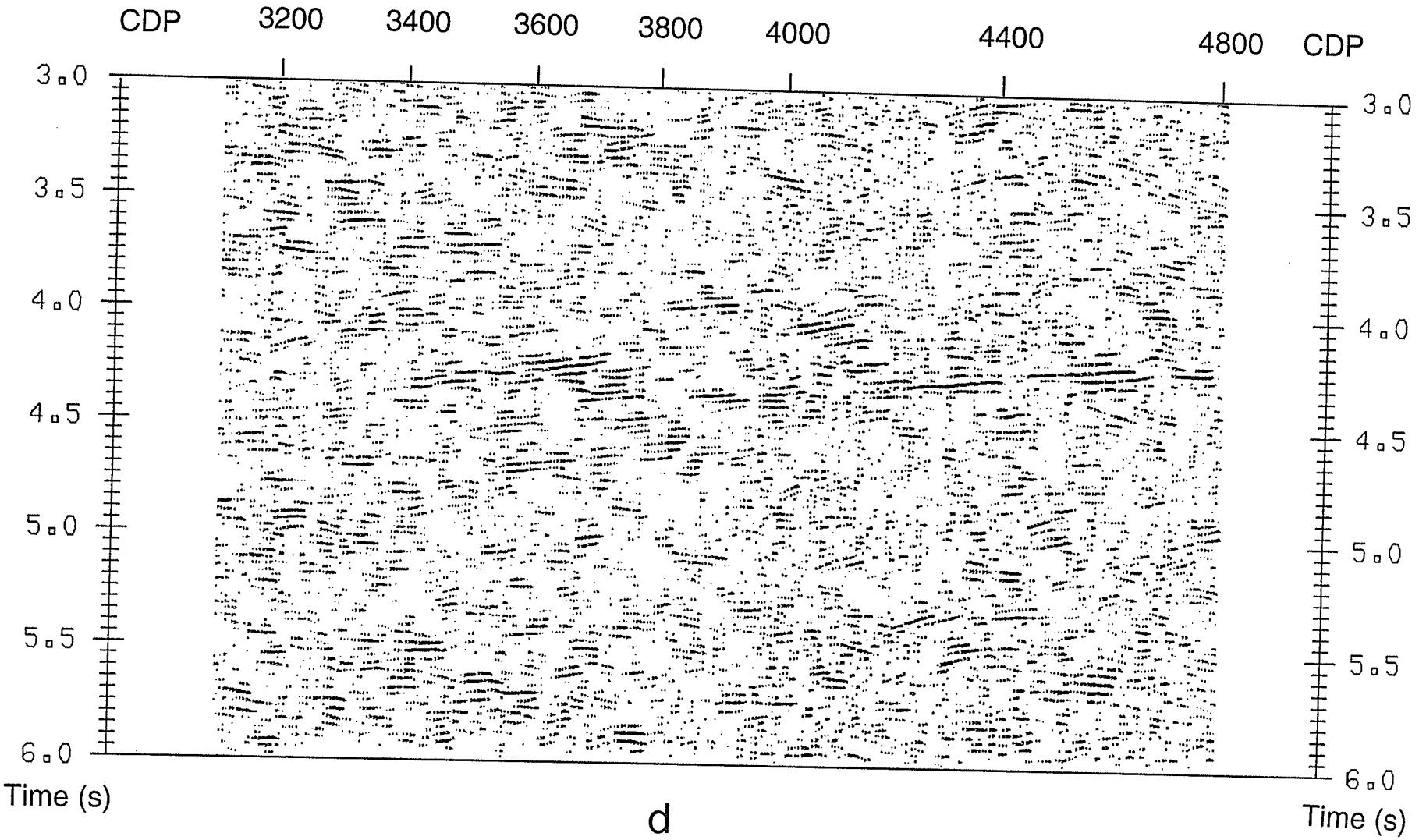
CDP
3200
3400
3600
3800
4000
4400
4800
CDP
3.0
3.5
4.0
4.5
5.0
5.5
6.0
Time (s)
Time (s)

d

6.2.3 Removal of Ground Roll Noise Using the Wavelet Transform

The $f-k$ filtering technique has been traditionally used to remove ground roll noise. Although it is generally very effective for removing coherent $f-k$ domain noise, the approach often introduces undesired artifacts. In order to minimize processing artifacts, apparent velocities used for rejection of the ground roll noise were carefully tested and selected for every 5 shot gathers. After applying the $f-k$ filter to the data, ground roll noise was effectively suppressed and shallow reflections which were originally contaminated by the ground roll noise became visible (see Figure 6.6). However, processing artifacts are clearly observable. The wavelet transform technique was thus developed and tested to remove the ground roll noise and associated coherent noises.

The wavelet transform (WT) is a new signal processing technique developed in the computer science and engineering disciplines in the recent years (Chui, 1992, Daubechies, 1990, Mallat, 1989). A special characteristic of the new approach is that it provides insight into the combined features of time and frequency domains. It also has zoom-in and zoom-out capability in signal sampling. Although the WT is a relatively new mathematical tool, it has developed rapidly because of its attractive features for the time-frequency analysis. It has gained wide application in signal processing and other transient process analysis. The detailed principles and applications of the WT will be further discussed in Chapter 7. Only the result of application of the WT for removing ground roll noise from the line 42 seismic data is discussed here.

Ground roll noise generated during the surface seismic survey is a kind of surface

wave characterized by low frequency and low apparent velocity. It becomes dispersive when the propagating medium consists of multiple layers with increasing velocity with depth (Aki and Richards, 1980). Hence the general characteristics of the wavelets of the ground roll noise vary in both traveltime and frequency. The wavelet decomposition of a seismic signal represents its time and frequency characteristics simultaneously. Coherent noise, such as ground roll noise, which has distinct features from the seismic signal in both time and frequency can then be effectively suppressed through the weighting of information content during the inverse WT.

Figure 6.7a shows a shot gather (the shot gather #29) which contains strong ground roll noise. Reflections in the shallow depth at near offsets are contaminated by the ground roll noise. Figure 7.9 in the next chapter is the WT panel for the shot gather 29. In the panel, the ground roll is separated from the desired signals by existing only in the octave range from 3 to 5. While reflections lie between the octave range of 1 to $2\frac{3}{4}$. By excluding those octave bands containing ground roll during the inverse WT, the ground roll can be rejected. Figure 6.7b shows the shot gather after removing ground roll noise by the WT. Comparison of the result with the $f-k$ filtered data in Figure 6.6b, significant improvement is clearly visible in the results produced by the new WT technique. The major reflection event at approximately 2.0 s is enhanced without significant artifacts and the outline of the reflection hyperbola is now further extended to the near offset region. This fact demonstrates that the new WT approach can remove coherent noise very effectively if its time and frequency characteristics are distinct.

Another approach for removing coherent noise is combining deconvolution and the inverse WT. From the WT panel one can easily find a band containing only the

ground roll noise. It can be chosen as a template gather of the ground roll noise, and therefore the ground roll can be removed by deconvolution of the WT panels with the template gather and followed by the inverse WT. Figure 5.7c shows the result of combination of the deconvolution and the WT methods. Although the result does not have a good quality as applying the WT method alone due to boosting of high frequency components by deconvolution, combination of other conventional filter with the WT is certainly a good method worth to try in the future research for coherence noise suppression.

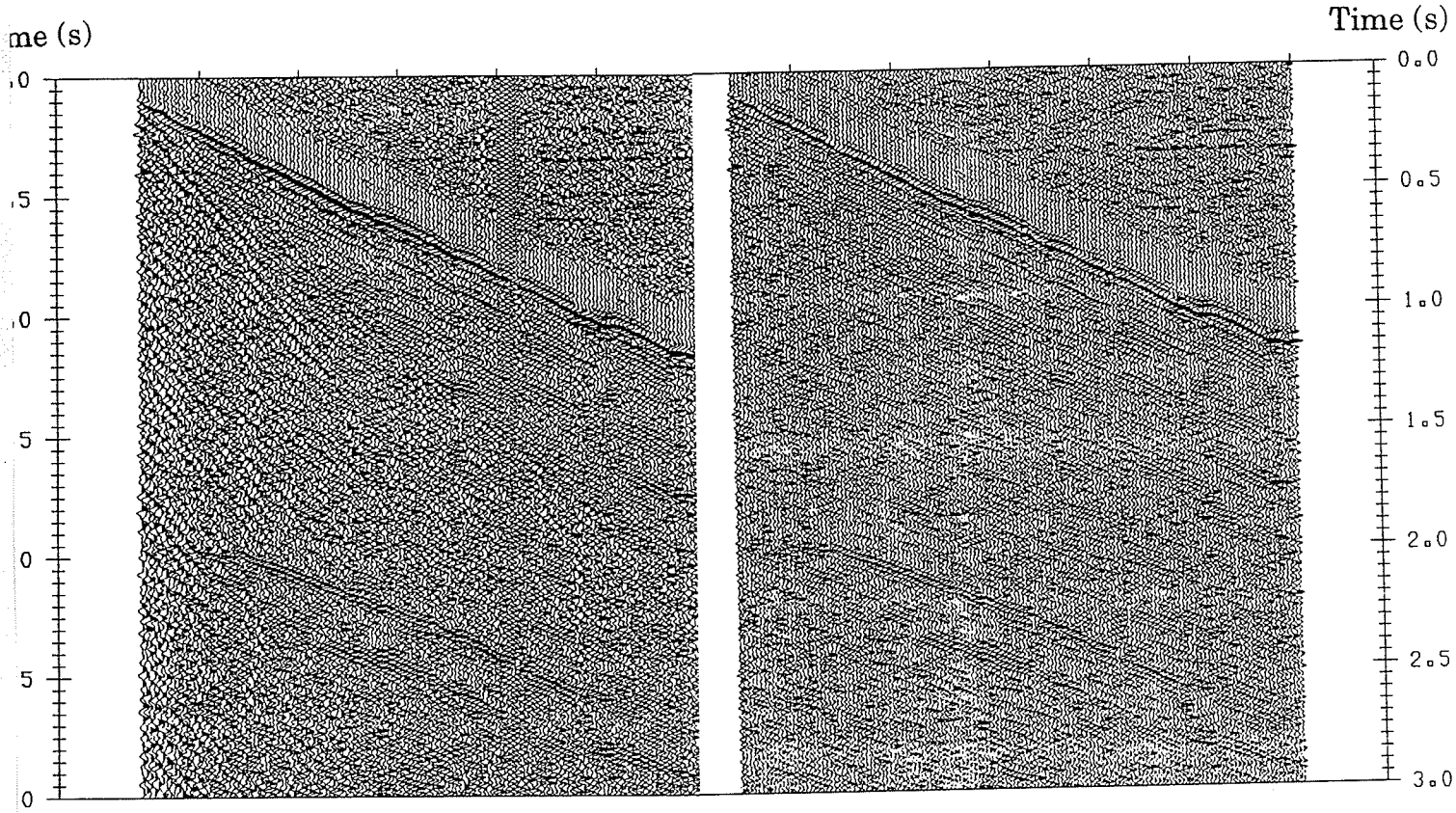

Figure 6.6: Removal of ground roll noise using the $f-k$ filtering: (a) the original shot gather, (b) the same shot gather after the $f-k$ filtering.

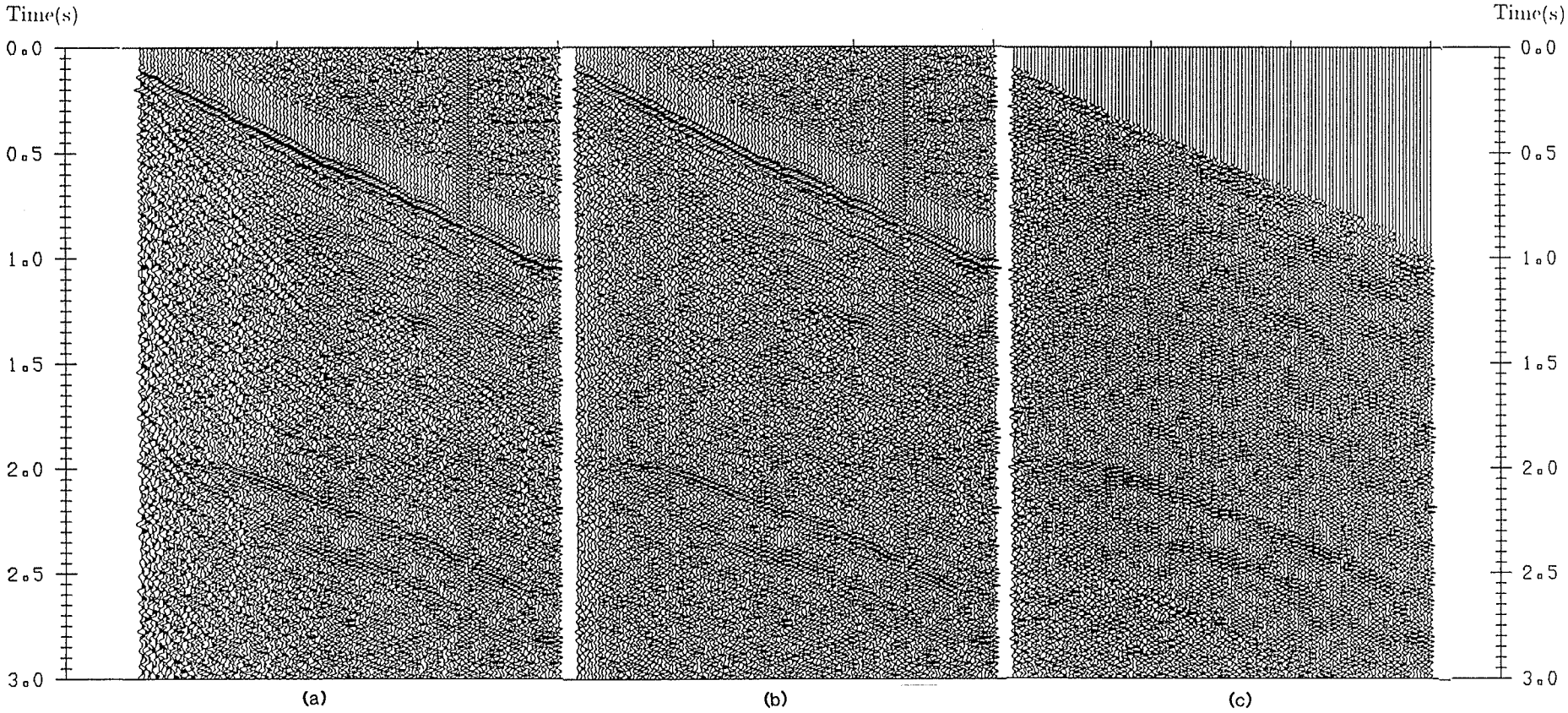

Figure 6.7: Removal of ground roll by the WT: (a) the original shot gather; (b) reconstruction of the data by the inverse WT after removal of the bands containing the ground roll; (c) removal of ground roll by combination of the deconvolution and the WT methods.

6.2.4 Time Varying Cross-Dip Correction

The method of CDP stack is based on the assumption of flat subsurface reflectors and constant velocity horizontally. If the survey line is straight, the reflective points will form a line on the reflector which lies vertically below the survey line (Figure 6.8a), so that the CDP stack after NMO correction will intensify the reflection energy. When the subsurface reflector is dipping but the survey line is straight, the CDP points lie along the survey line. There is no transverse offset (in this thesis, transverse offset is defined as the offset distance between the mid-point of a CDP bin and a true mid-point of each shot and receiver pair) (Figure 6.8b), hence only in-line dip moveout correction (DMO) may be required for focusing reflection energy. If the survey line is crooked but the reflector is flat, the reflective points will scatter in both in-line and cross line direction, but the amount of NMO correction will be the same for reflection points sorted in a CDP bin (Figure 6.8c) because of the assumption of the constant velocity horizontally. There is no additional moveout involved. However, when the reflector is dipping and the survey line is crooked, the situation becomes complicated. Reflection points are no longer located in a 2-D profile, they scatter in both in-line and cross-line directions (Figure 6.8d). The dip of subsurface reflectors in the cross-line direction, or called cross-dip, can introduce substantial reflection energy smearing associated with transverse offsets, which degrades the seismic image (Larner et al, 1979; Kim et al., 1992), because the amount of moveout associated with transverse offset is not taken into account in either NMO or DMO corrections. The cross-dip correction, thus, as a reflection energy focus technique was investigated and applied to the line 42 data.

a

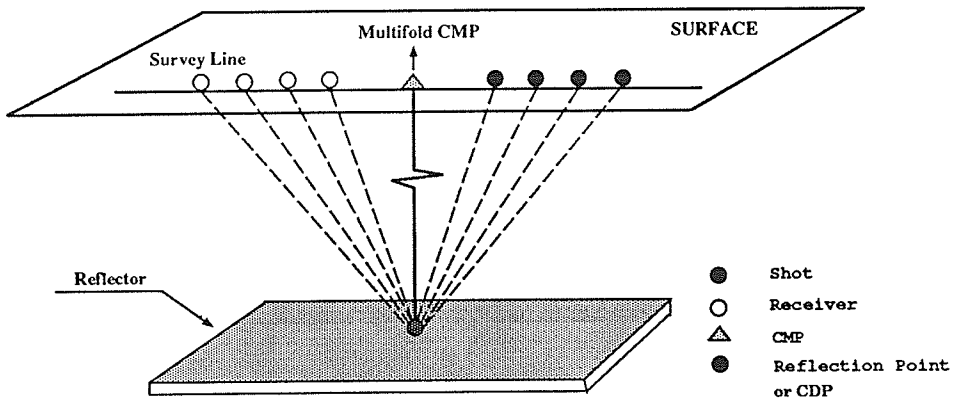

b

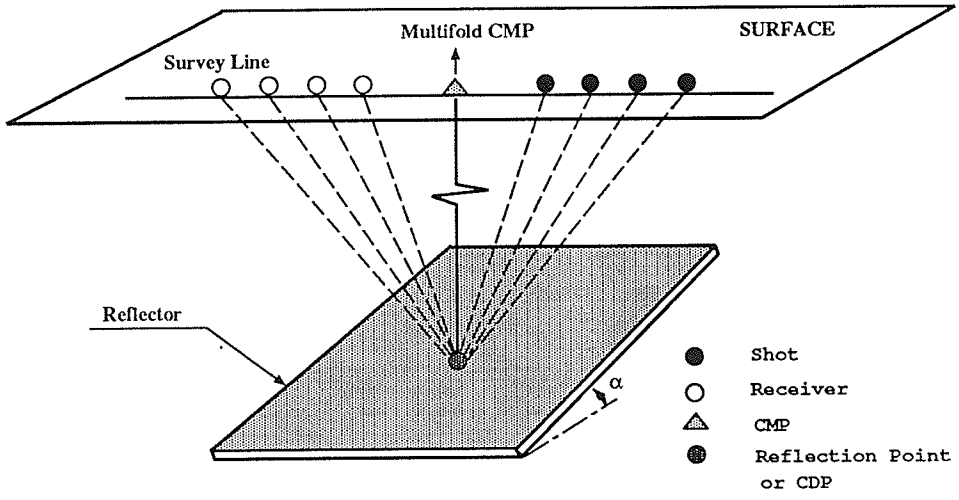

Figure 6.8: Geometry of CDP stack: (a) straight survey line and flat reflector; (b) straight survey line with a dipping reflector; (c) crooked survey line with a flat reflector; (d) crooked survey line with a dipping reflector. Continue on the following two pages.

C

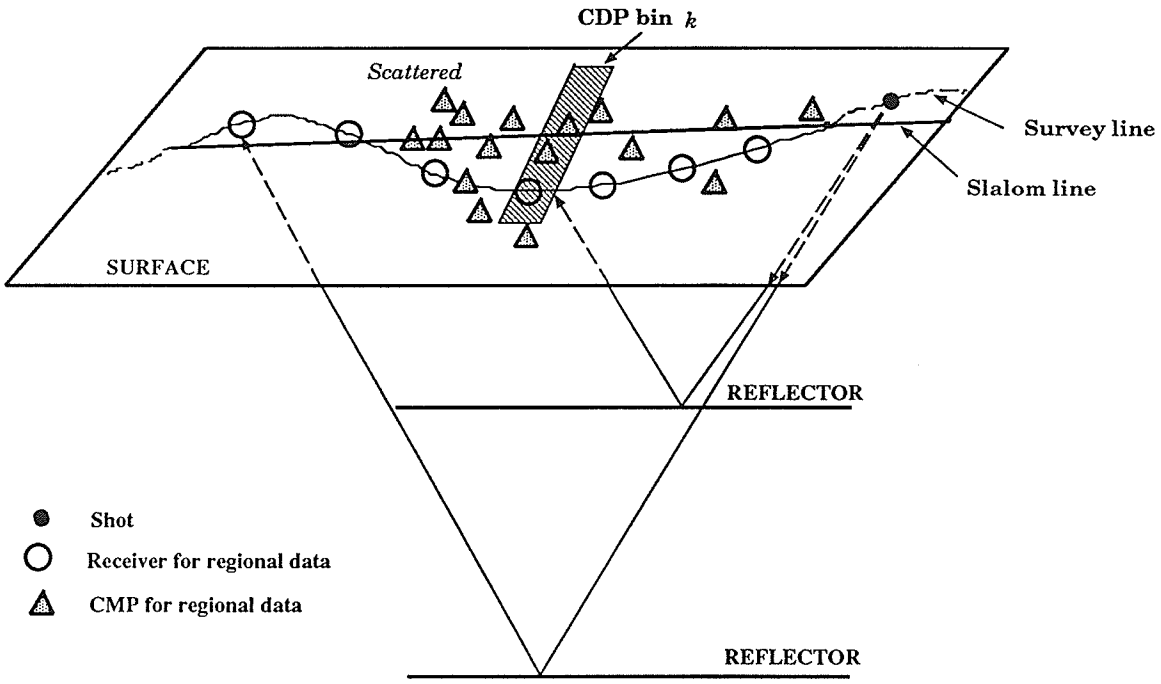
CDP bin k
Scattered
Survey line
Slalom line
SURFACE
REFLECTOR
REFLECTOR
Shot
Receiver for regional data
CMP for regional data

d

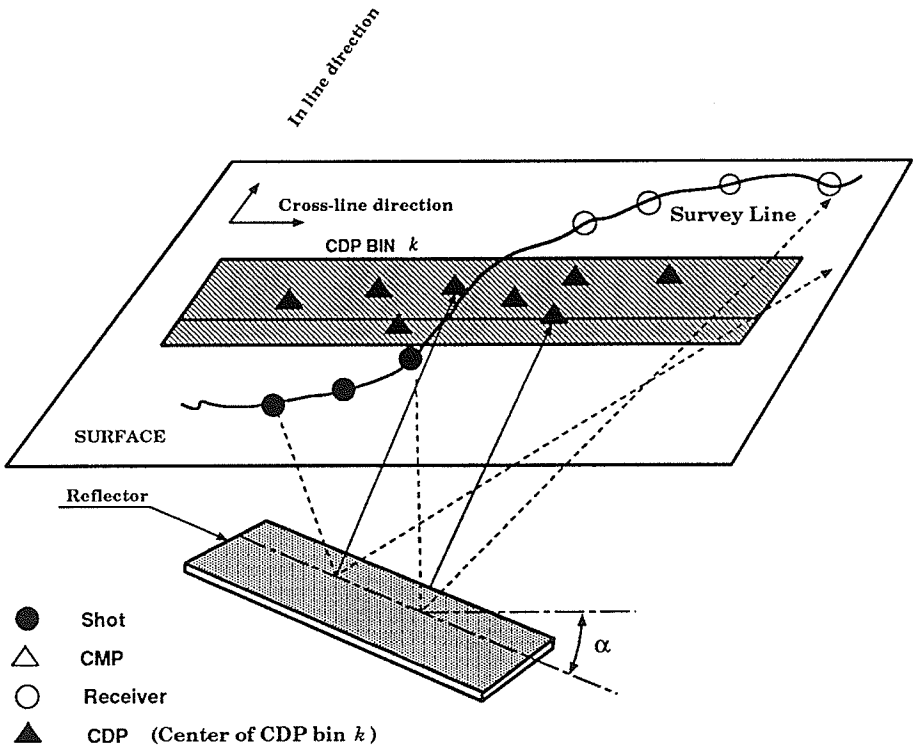
In line direction
Cross-line direction
Survey Line
CDP BIN k
SURFACE
Reflector
α
Shot
CMP
Receiver
CDP (Center of CDP bin k)

To derive the cross-dip moveout, a 3-D coordinate system has to be constructed. Let z be the depth direction, x be the in line direction and y be the cross-line direction. Since the above 3-D coordinate system is constructed with respect to the survey line and the survey line is not usually coincident with the strike of subsurface reflectors, both in-line and cross-line dip are referred to as apparent dip in the structural geological term. When the survey line travels along the strike of structures, the cross-dip angle reaches a maximum value, then the cross-dip correction may make significant improvement for focusing reflections. When the survey line travels perpendicular to the strike, the cross-dip angle approaches to a minimum value, and the amount of cross-dip moveout is negligible.

In the 3-D coordinate system, a seismic trace for the ith shot and the jth receiver reflected at the CDP bin number k has a traveltime of:

$$t_{i,j}^2 = (t_0 + CDM)^2 + \frac{x_{i,j}^2}{v^2} - \frac{x_{i,j}^2 sin^2\xi_k}{v^2}, \tag{6.2}$$

where

t_0 is zero offset two-way time at the CDP point;

$x_{i,j}$ is offset distance between shot and receiver;

ξ_k is in-line dip angle of the reflector;

CDM is the cross-dip moveout.

In equation (6.2) the second term is associated with the zero-dip normal moveout (NMO), while the third term is associated with the DMO (in-line dip moveout) since it is the moveout related to the in-line dip of reflectors.

Cross-dip moveout

To derive the term associated with cross-dip moveout, first assume there is only a single reflector with cross-dip angle of α or the reflectors underground are conformly dipping along the depth direction. Figure 6.9 illustrates the geometry of the cross-dip moveout. In a CMP gather, after NMO and DMO correction the reflection rays located in the gather should be perpendicular to the reflector. The ray path corresponding to the exact CDP point has a traveltime of t_0, which is the exact zero offset (zero in-line and cross-line offsets) two-way traveltime. The other rays whose CMP points deviate from the CDP point in the CMP gather all have two-way traveltimes either longer or shorter than the t_0 depending on the cross-dip direction of the reflector. From the diagram 6.9 the cross-dip moveout can be expressed as a simple equation:

$$\Delta t_{ij} = 2\frac{sin(\alpha_k)}{v_k} y_{ij} = 2p_k y_{ij} \tag{6.3}$$

where

Δt_{ij} is cross-dip correction associated with the shot number i and receiver number j;

v_k is velocity at the CDP bin k;

α_k is cross-dip angle at the CDP k;

y_{ij} is transverse offset between the mid-point of CDP bin and the corresponding CDP point; and

p_k is the cross-dip ray parameter at the CDP bin index k (as depicted in Figure 6.9), in the case of conformly dipping reflectors, p_k is a constant along the depth or two-way time direction.

However, in most geological cases there may be several reflectors with arbitrary dips. Time varying, or depth varying, cross-dip correction is required to focus reflection energy efficiently. To complete this the cross-dip correction term Δt_{ij} is replaced by a summation of Δt_{ijl} which represents the cross-dip moveout corresponding to each reflector, where the index l represents a index variable of two-way time. It can be calculated with a varying value of parameter p_{kl}. The equation (6.3) then is modified as

$$\Delta t_{ij} = \sum_l \Delta t_{ijl} = \sum_l 2 p_{kl} y_{ij} \tag{6.4}$$

.

To see the physical meaning of p_{kl}, a case of two reflectors with arbitrary dips is illustrated by Figure 6.10. From the diagram, the cross-dip moveout for each reflector can be derived as

$$\Delta t_{ij1} = 2\frac{sin\alpha_{k1}}{v1} y_{ij}, \tag{6.5}$$

and

$$\Delta t_{ij2} = 2\frac{sin(\alpha_{k1} \pm \alpha_{k2}) cos\alpha_{k1}}{v2} y_{ij}. \tag{6.6}$$

Therefore

$$p_{k1} = \frac{sin\alpha_{k1}}{v_1} \tag{6.7}$$

and

$$p_{k2} = \frac{sin\bar{\alpha}_{k2}}{v2}, \tag{6.8}$$

where $\bar{\alpha}_{k2} = sin^{-1}[sin(\alpha_{k1} \pm \alpha_{k2}) cos\alpha_{k1}]$, the sign of plus or minus depends on the direction of dips (if subsurface reflectors dip in the same directions, it should be minus, otherwise it is plus.).

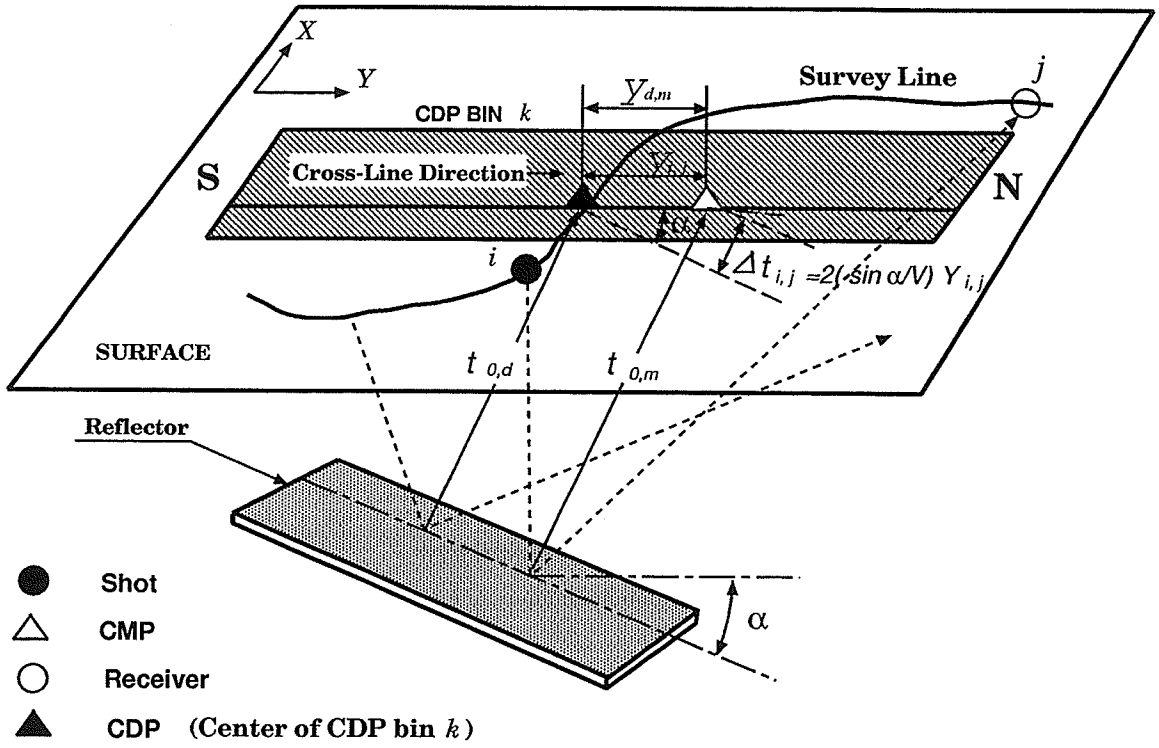

Figure 6.9: Schematic diagram for the geometry of the cross-dip correction. At the CDP bin k, Δt_{ij} is the cross-dip correction for the trace associated with the shot number i and receiver number j, v_k is the velocity at the CDP bin k, α_k is the cross-dip angle at the CDP k, y_{ij} is the transverse offset between the mid-point and the corresponding CDP point, and p is the cross-dip ray parameter.

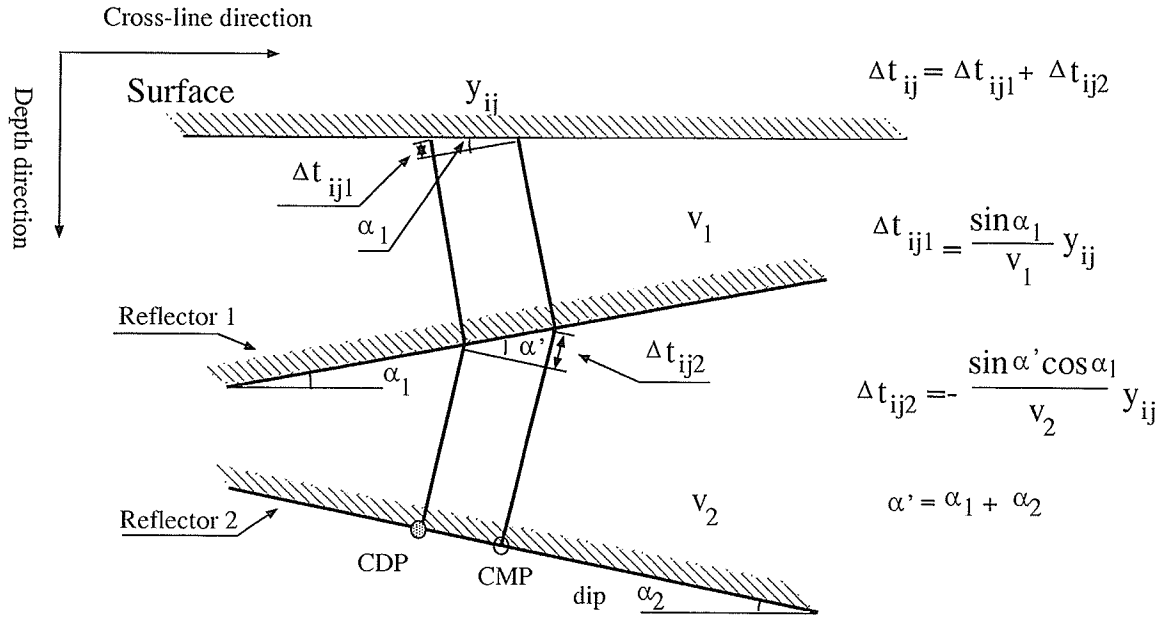

Figure 6.10: Two reflectors with arbitrary cross-dips. Δt_{ij} is the cross-dip moveout for the CMP point with the shot number i and receiver number j.

However the cross-dip of the nearest reflector to the surface can still be estimated from equation (6.7) if p_{k1} is known. The values of p_{kl} can be estimated through a slant stack scan (details will be discussed later).

Implementation of the cross-dip correction consists of three steps: crooked line geometry, a slant-stack scan to determine the cross-dip ray parameter p_{kl}, and application of cross-dip correction (see Figure 6.11 for flow chart of cross-dip correction). At first several binning strategies were examined and tested with line 42 data. The final slalom line for binning was selected based on the criterion of raising the fold coverage by using large CDP binning heights and simplifying the geological interpretation by straightening the slalom line during the binning. To exclude the data from very far offsets, which may be introduced by large binning height, the in-line source

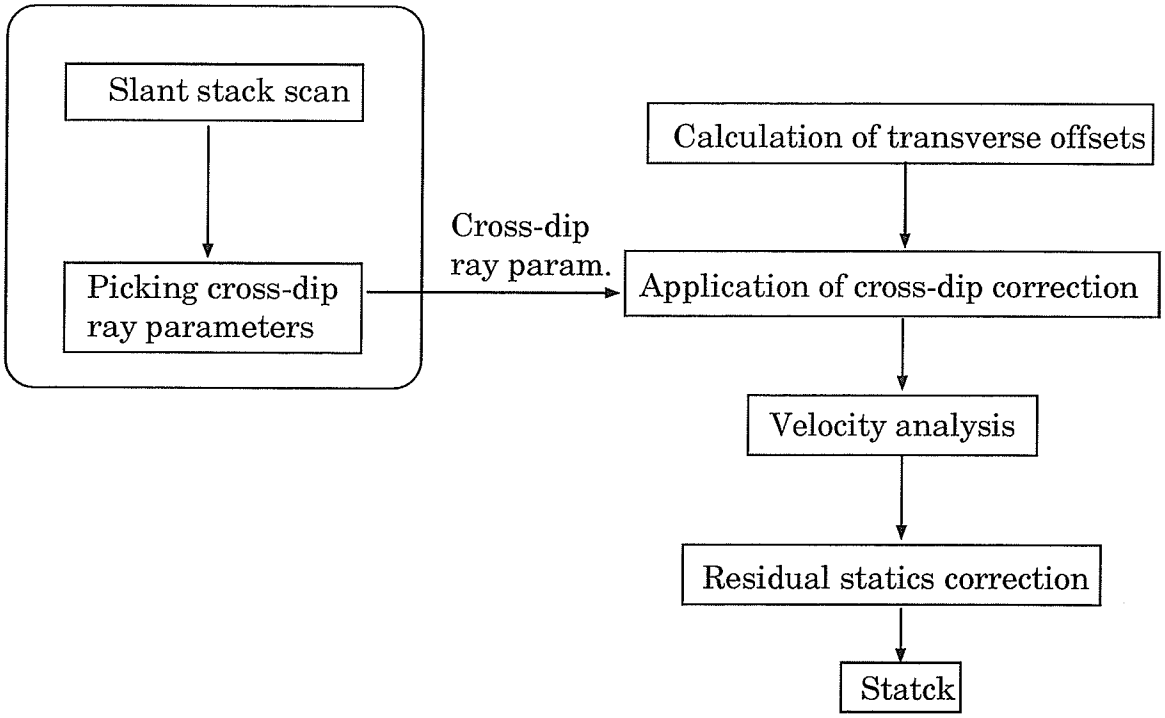

Figure 6.11: Flowchart for the cross-dip correction.

to receiver offset range was restricted in the final stacking. Thus the slalom line was straightened into mainly two parts. From the northern end (CDP number 1025) to the CDP number 3140, the line runs approximately north-south, and the rest of line runs approximately west-southeast. The CDP bin height was raised from 800 m to 1000 m to avoid poor fold coverage resulting from straightening of the slalom line in the southern end of the line, and in-line offsets were limited to 5000 m in the final stacking. Thus the fold coverage was increased and reached a maximum fold of 124. Figure 6.12 shows the west-southeast part of the CDP binning. The fold coverage is shown in the left corner of the diagram and the amounts of cross-dip near the surface derived from the slant stack scan are plotted at the top.

Slant stack scan

The slant-stack is equivalent to the Radon transform (discussed in Chapter 5). To construct slant-stack gathers, data in the time-offset coordinate are transformed into the $\tau - p$ coordinates by summing amplitudes in the offset domain along ray parameters, or slanted ray paths. The slant stack can be implemented in the CMP gather, common shot gather or poststacked sections. In the cross-dip correction case, the slant-stack transform is carried out in the CMP gathers, the offsets are replaced by the transverse offsets and p represents cross-dip ray parameter.

After the slant stack transform, the traces with same p value are sorted into a stacked section in the CMP coordinate. The stacked sections with different values of p construct the slant stack scan panel. Reflection events with a preferred alignment of special p value will generate constructive waveforms, thus the p value can be estimated in the slant stack scan without requirement of prior knowledge about dip of the structures. This is equivalent to the velocity scan to estimate stacking velocity values

for the NMO correction.

For line 42 data the slant-stack with respect to the transverse offsets was scanned from the two-way horizontal slowness of -0.2 ms/m to 0.2 ms/m with a ray parameter interval of 0.01 ms/m, and pairs of ray parameters and corresponding times were picked from the slant stack panel.

A program for time varying cross-dip correction was written in this research and inserted into the IT&A INSIGHT-4.0 version to implement the cross-dip correction in a similar way to the NMO correction. The algorithm only requires pairs of input parameters of the cross-dip ray parameter p and the corresponding time determined from the slant-stack scan. It is sufficiently flexible to deal with reflectors with arbitrary cross-dips. Figure 6.13 displays a CMP gather with and without cross-dip correction. The CMP gather was sorted into transverse offsets. The offsets with negative sign corresponds to the CMPs situated in the south of the CDP. A cross-dipping trend toward the south in the CMP gather (Figure 6.13a) is clearly observable. However, with application of the cross-dip correction, the dipping trend becomes flat (Figure 6.13b).

The velocity semblance analysis, which will be discussed in section 6.2.5, further demonstrates the significant improvement in elimination of time deviation with application of the cross-dip correction (Figure 6.14b). The reflection energy is obviously more focused after cross-dip correction. For comparison of the results with and without the cross-dip, a portion of the stacked section is shown in Figure 6.15, in which a strong southeast dipping reflection event at 2.0 s to 2.5 s was imaged clearly after the cross-dip correction (Figure 6.15b). This reflection event can not be identified in the

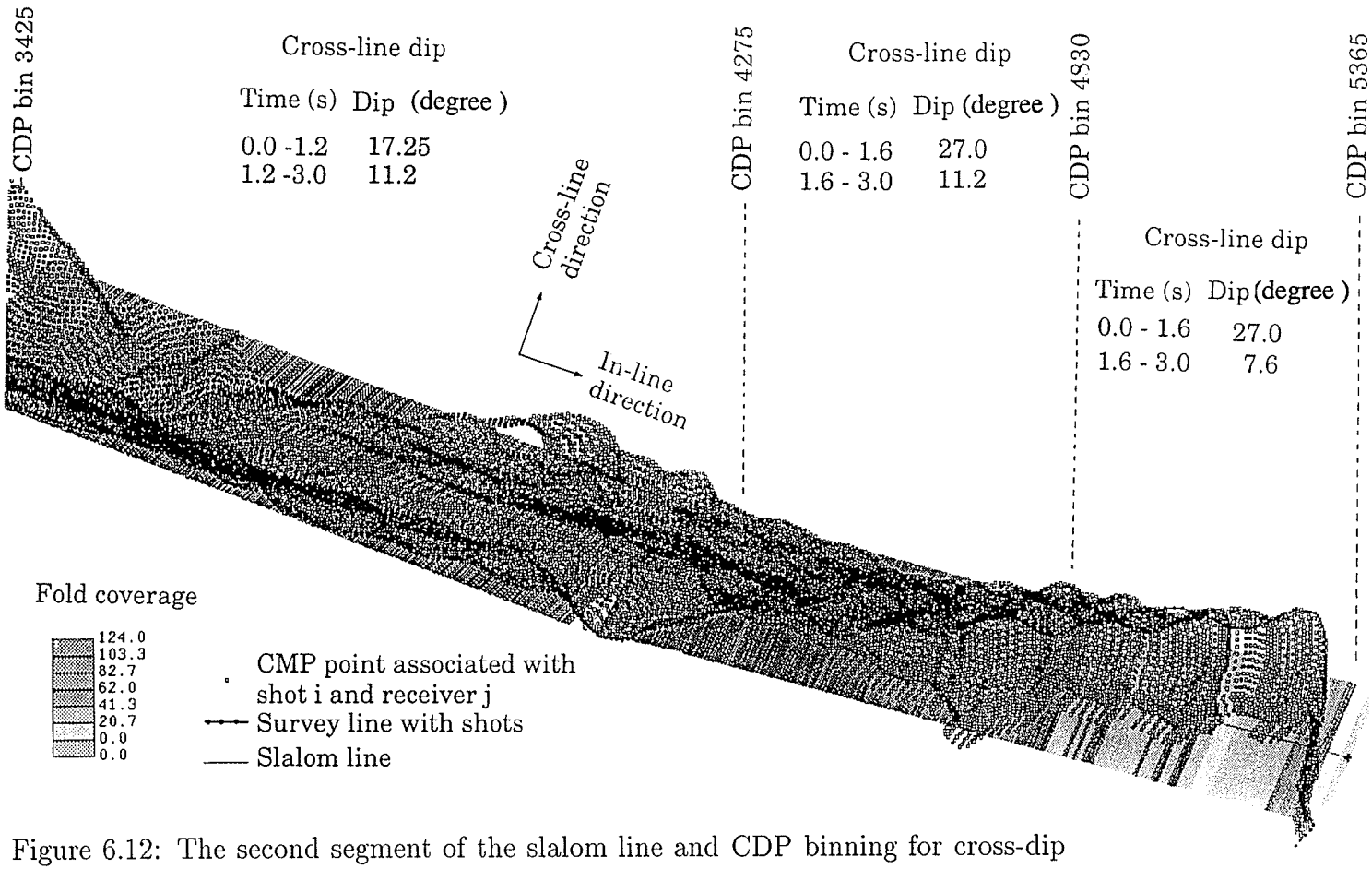

Figure 6.12: The second segment of the slalom line and CDP binning for cross-dip correction. Dots represent the mid-point between each receiver and shot. The fold coverage is shown by grey levels. The bin height is 1000 m and bin width is 25 m. The slalom line is depicted as a thin line in the middle. The corresponding amounts for the cross-line dip are tabled on the top of the diagram.

original profile (Figure 6.1), or in the profile before the cross-dip correction (Figure 6.15a).

The cross-dip correction has greatly improved focusing of the reflection energy. The amount of the cross-dip varies along the line from 5.7^o to 27^o approximately. At the southern end of the line, the cross-dip is relatively larger. From the CDP numbers of 3400 to 4265, the cross-dip is about 17.25^o between 0-1.2 s time range, but the apparent cross-dip angle decreases to 11.2^o at 1.2-3.0 s twoway time. From the CDP numbers 4275 to 5365, the cross-dip in the shallow part (0-1.6 s) is south dipping with a dip angle of approximately 27^o. At deeper parts (1.6-3.0s), the apparent cross-dip becomes more gentle (Figure 6.14).

6.2.5 Velocity Analysis and Residual Statics

Velocity analysis

The velocity analysis was carried out using both constant velocity scan and semblance analysis. To generate a constant velocity scan panel, the CMP gathers are NMO corrected over a range of velocity values and displayed side by side in a form of panel. A reflection event may be overcorrected if the velocity used is low, and it may be undercorrected if the velocity is high. A flat event corresponds to the proper stack velocity value used for NMO correction, this velocity can be picked as a stack velocity.

The velocity semblance analysis is an alternative technique for constant velocity scan. At first a velocity spectrum can be generated by applying NMO correction to a CMP gather over a range of velocity values and stacking all the traces together.

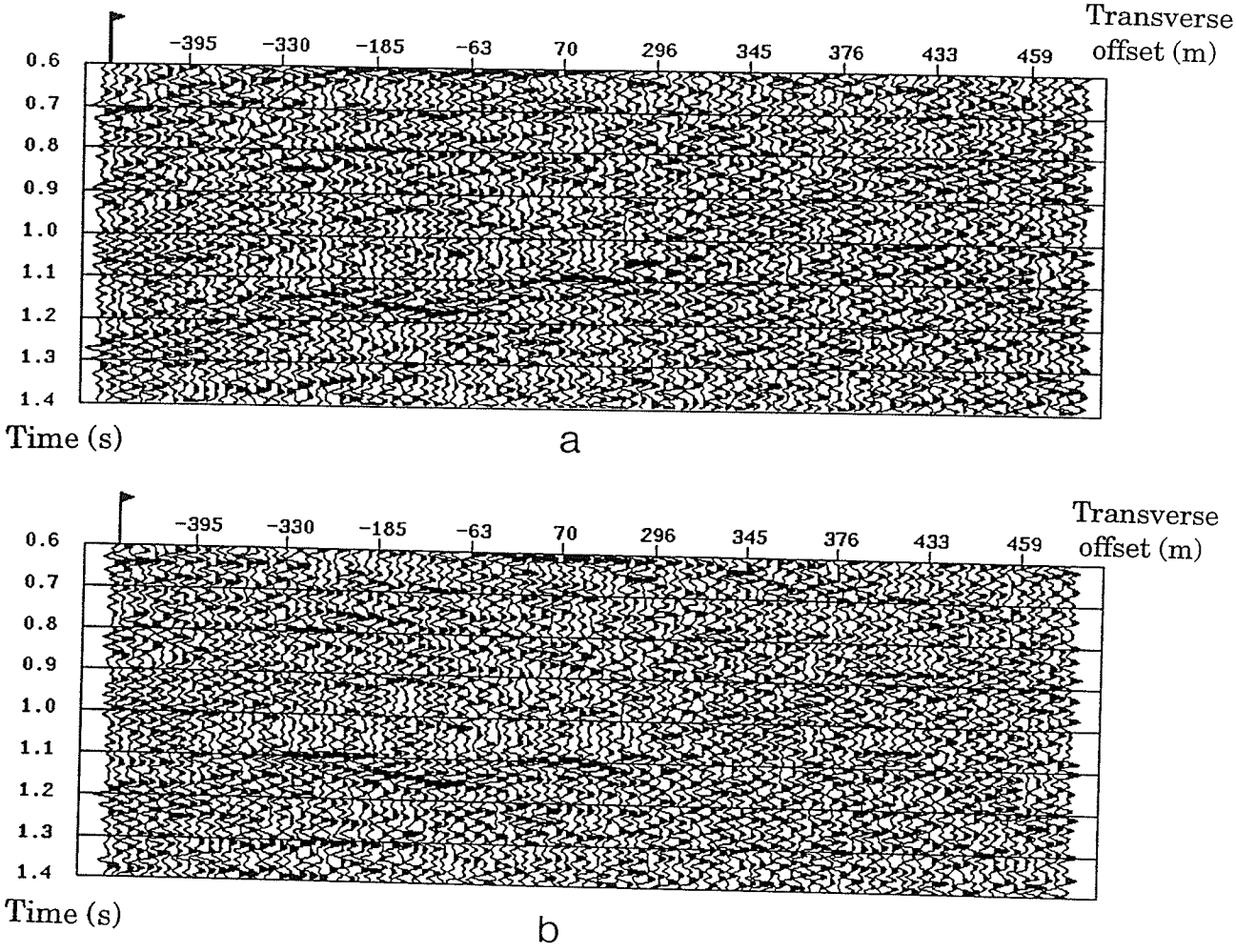

Figure 6.13: An example of the CMP gather (CMP 4150) data: (a) without cross-dip correction and (b) with cross-dip correction.

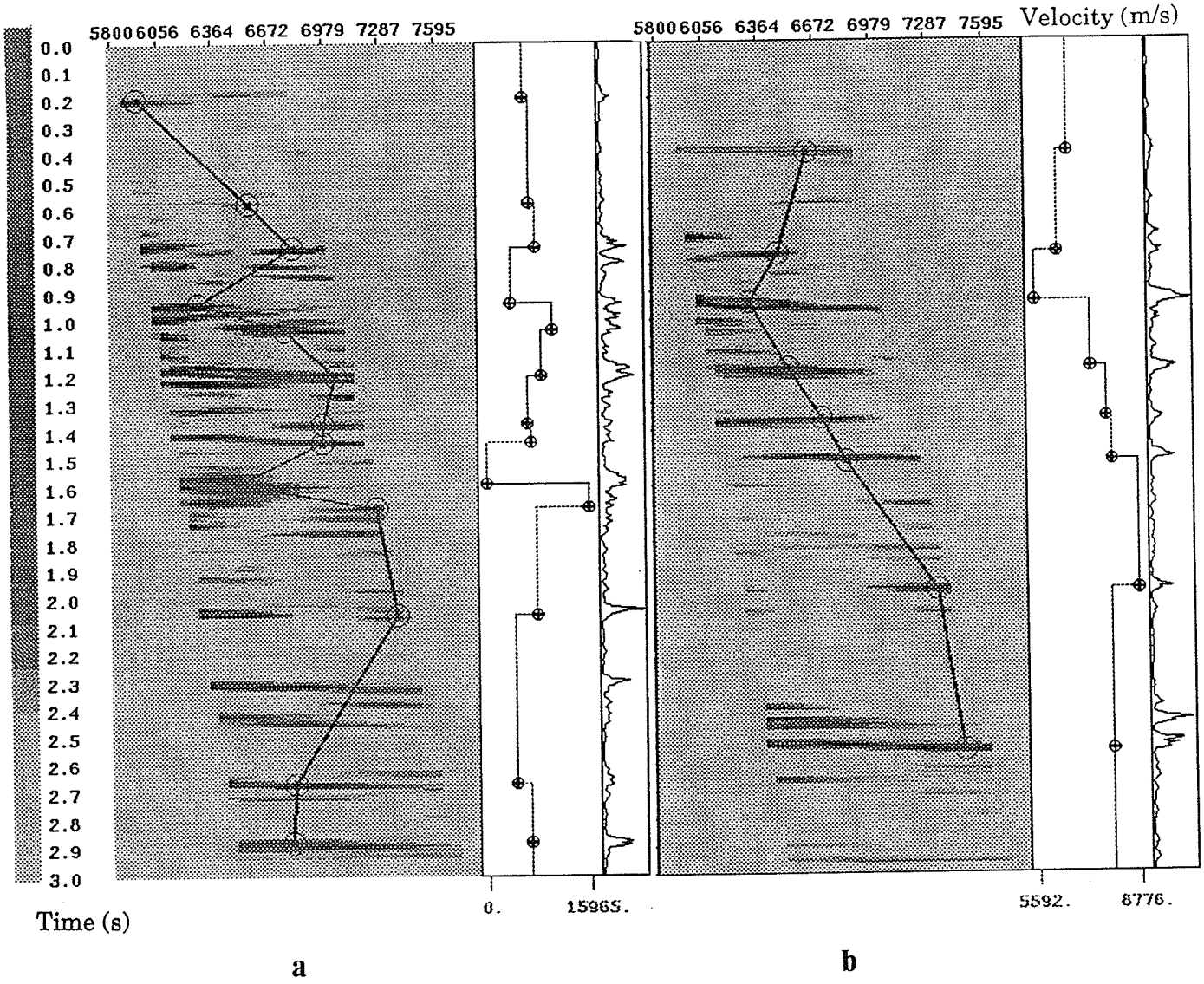

Figure 6.14: The velocity semblance plot for the CMP gather 4150: (a) without cross-dip correction and (b) with cross-dip correction.

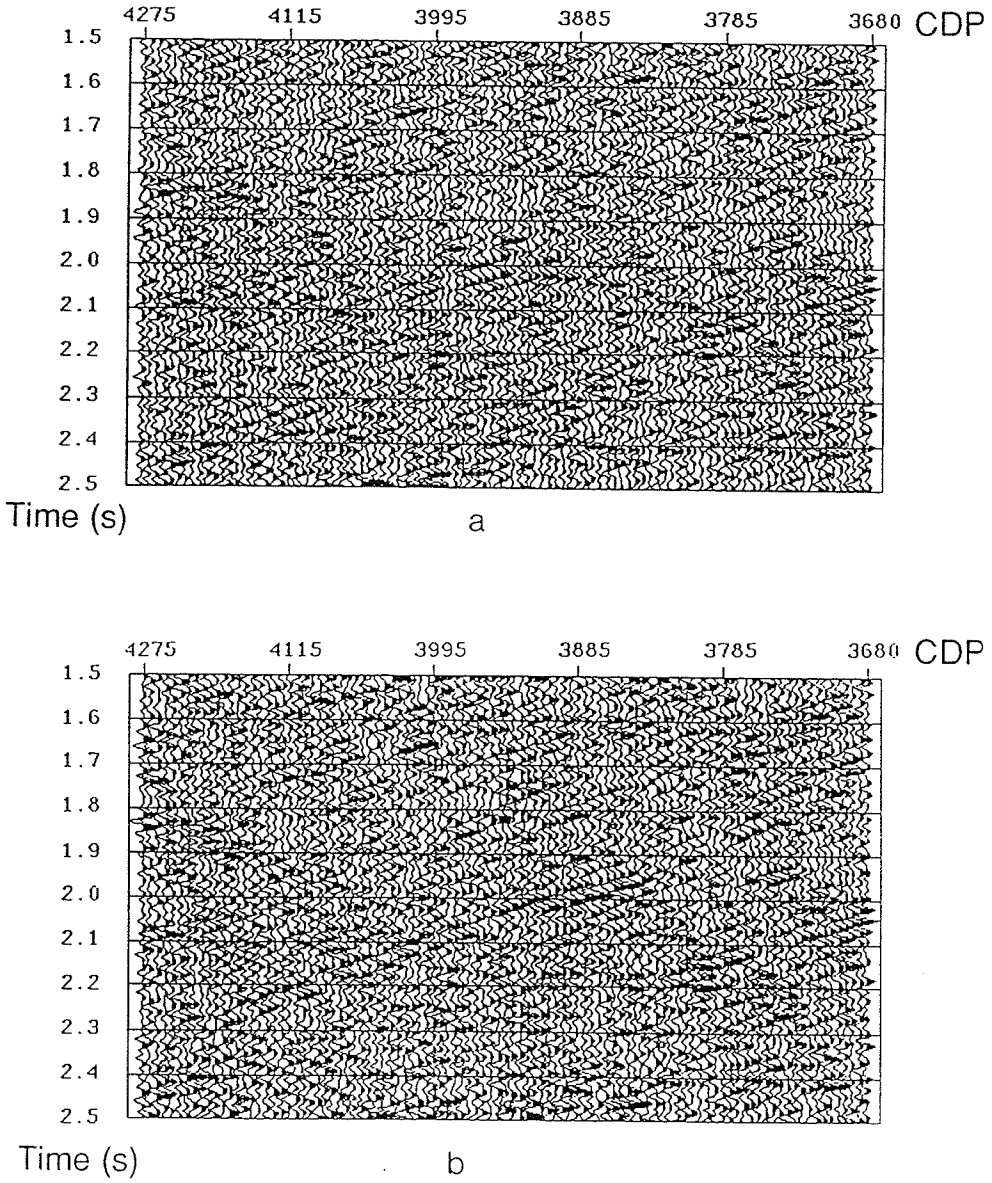

Figure 6.15: A segment of the reprocessed stacked seismic section: (a) without the cross-dip correction and (b) with the cross-dip correction.

The highest stacked amplitudes occur when the scanned velocity coincides with the velocity of a particular reflection hyperbola. Instead of simply stacking the amplitudes of the traces, a coherency technique, semblance analysis, is based on the following formula (Yilmaz, 1987):

$$NE = \frac{1}{M} \sum_{i} (\sum_{i=1}^{M} u_{i,t_i})^2 / \sum_{i} \sum_{i=1}^{M} u_{i,t_i}^2, \tag{6.7}$$

where u_{i,t_i} is the amplitude of the ith trace at the two-way time t_i, M is the number of traces in the CMP gather. The semblance NE represents the normalized output to input energy ratio. If the lateral coherency in a CMP gather is good and the output energy is high, then the value of NE is large. Stacked velocities can be picked in such a velocity semblance spectrum. In comparison with the constant velocity scan, the velocity semblance analysis is more suitable for data containing multiple reflections (because of lower coherency of the multiples than the primary reflection) and less suitable for a complex structure problem. Figure 6.14 displays an example of the velocity semblance plot for the CMP gather 4150 over the velocity range of 5800 m/s to 7400 m/s with a 100 m/s velocity interval.

After several tests with the constant velocity scan it was found that the stacked patterns in the very shallow part (0-1s) were very sensitive to velocity variation. This phenomenon is probably due to complicated shallow structures including geological variations and minor structures, which scatter the seismic reflection wavefield. Thus the shot gathers were examined again at this stage to check the true trends of reflections.

The velocity depth functions were picked for every 14 CDP gathers from semblance plots. The final stack velocities listed in Table 6.2 were determined by velocity analysis

and testing with the data. A noticeable point in the result of the velocity analysis (Table 6.2) is that in the vicinity of the CDP number 4700 and the near surface part of the CDP number 4205, which corresponds to the southern end of the line and also where the Levack Gneiss Complex (LGC) located, the velocity is much higher than in the rest of the line, especially near the surface. This result indicates that the LGC has much higher velocity values than the Cartier granitic intrusions. An example of the stack section with velocity analysis is also plotted in Figure 6.16, which shows much improved stacked reflection patterns near the surface when careful velocity analysis is applied to the data (Figure 6.16b).

Residual statics

The residual statics correction is reflection based statics. It is used to correct short wavelength anomalies associated with near surface irregularities. Based on the surface consistent model (Figure 6.17), in 3-D space the traveltime that corresponds to the jth receiver station, the ith source station, and the kth midpoint along the lth horizon can be approximately modeled as:

$$T_{ijl} = t_{si} + t_{rj} + g_{kl} + m_{kl}x_{ij} + b_{kl}y_{i,j}, \tag{6.8}$$

where

t_{si} is the traveltime from shot point i to datum;

t_{rj} is the traveltime from receiver j to datum;

g_{kl} is the normal two-way traveltime from datum to a subsurface reflector at the CDP bin k and the lth horizon. It refers to structural variations along the horizon and is called the structural term;

Table 6.2: Velocity functions picked from velocity analysis.

CDP 2825		CDP 3430		CDP 3885		CDP 4205		CDP 4700	
time	**velocity**	**time**	**velocity**	**time**	**velocity**	**time**	**velocity**	**time**	**velocity**
0.007	5900	0.010	6100	0.009	6000	0.124	5900	0.117	6400
0.227	6100	0.539	6200	0.127	6100	0.265	6100	0.204	6800
0.545	6900	1.023	6900	0.344	6700	0.425	6200	0.390	7200
0.685	7000	1.269	6900	0.777	6800	0.590	6300	0.790	6700
0.821	6900	1.481	6700	0.863	6600	0.950	6600	0.803	7100
0.922	6900	1.601	6700	1.028	6900	1.042	6700	1.065	6700
1.276	7000	2.000	7100	1.380	6600	1.521	6800	1.604	6900
1.834	6800	2.169	7100	1.586	6700	1.986	6900	1.740	7000
1.847	6600	2.620	6400	1.956	7000	2.064	7100	2.290	7200
2.315	6500	2.860	6500	2.062	6900	2.216	7000	2.640	7300
				2.293	6900	2.465	7100		

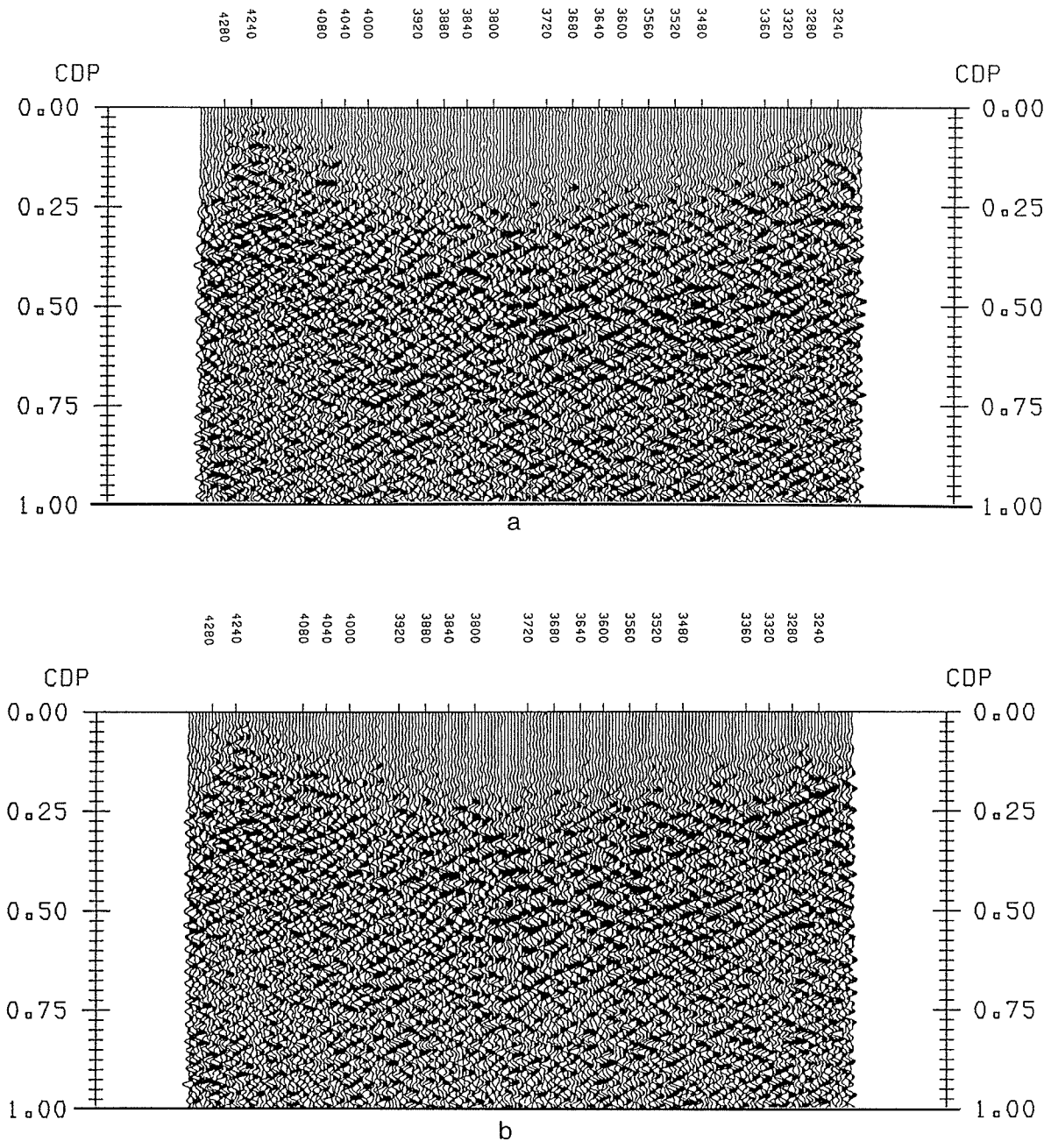

Figure 6.16: Velocity analysis: (a) a stack section with application of rough velocity analysis, and (b) the same stack section with application of careful velocity analysis.

$m_{kl}x_{ij}$ is the residual moveout that accounts for imperfect NMO moveout;

$b_{kl}y_{ij}$ is the residual moveout that accounts for cross-dip moveout.

After the cross-dip correction, the equation (6.8) can be rewritten as

$$T'_{ijl} = T_{ijl} - b_{kl}y_{i,j} = t_{si} + t_{rj} + g_{kl} + m_{kl}x_{ij}. \tag{6.9}$$

Hence the existing conventional residual statics method in the INSIGHT package can be applied directly with enhanced accuracy (Kim et al., 1994), since ambiguity associated with the cross-dip is reduced. To determine residual statics, a three step algorithm is involved: (1) picking time value T_{ijl}; (2) decomposition of T_{ijl} into its components: source and receiver terms, structural term and residual moveouts; (3) application of the derived source and receiver statics to its traveltime.

A super fold program based on the Ronen-Claerbout algorithm (Ronen and Claerbout, 1985; Dahl and Jensen, 1989) in the INSIGHT-4.0 package was used to implement residual statics. In the algorithm, the time picking is replaced by the stack power maximum method. That is, the preliminary time shift of a trace is determined by maximum cross-correlation with a preliminary supertrace, while the preliminary supertrace itself is formed by stacking the NMO corrected traces in this CMP gather. The preliminary time shifts are applied to each trace in this CMP gather, and a final supertrace is composed by stacking each trace after the preliminary time shift, and it is cross-correlated with other traces again in the gather to determine the final time shifts. A stack trace is constructed after application of the final time shifts in the CMP gather and this stack trace is used as preliminary supertrace for the next CMP gather. Subsequently the time shifts for entire data set can be calculated and they are

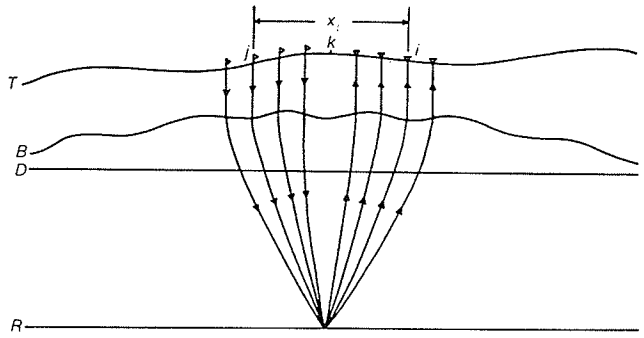

Surface-consistent statics model
Here, T = surface topography, B = base of weathering layer, D = datum to which static corrections are made, R = deep reflector, j = shot station index, i = receiver station index, k = midpoint location index, x_{ij} = offset between the shot and receiver stations.

Figure 6.17: Surface-consistent residual statics model after (Yilmaz, 1987).

then least-squares decomposed into source and receiver terms. The residual statics then can be applied to the data set.

The processing flowchart for residual statics is illustrated in Figure 6.18. First the NMO correction was applied based on estimated velocity values, and subsequently the residual statics was calculated. After these steps, the NMO was removed and residual statics was applied to the data, and the velocity analysis was carried out again. Such steps were repeated three times. The above approach was found to be very effective and produced a much improved subsurface seismic image (see Figure 6.19b).

6.2.6 Offset Limited Stack and Coherency Filtering

The final profile was obtained by stacking the data within an offset limit of 5000 m. Migration was performed, but the discontinuous nature of the reflections produced significant concave-up artifacts with this data. Thus the unmigrated reprocessed section is presented in Figure 6.19c after application of the coherency filtering for display. It shows considerable improvements compared with the preliminary processed profile in Figure 6.1.

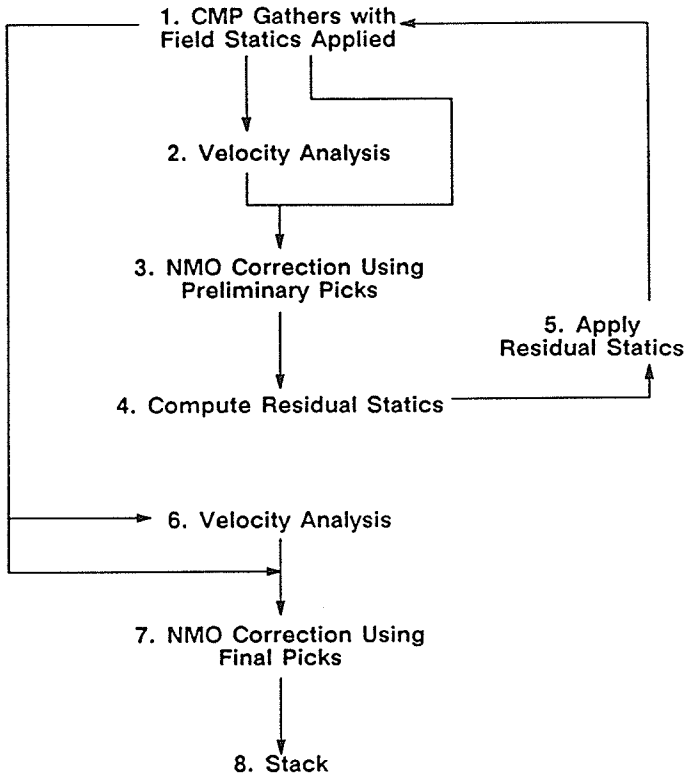

Figure 6.18: The flowchart for residual statics correction.

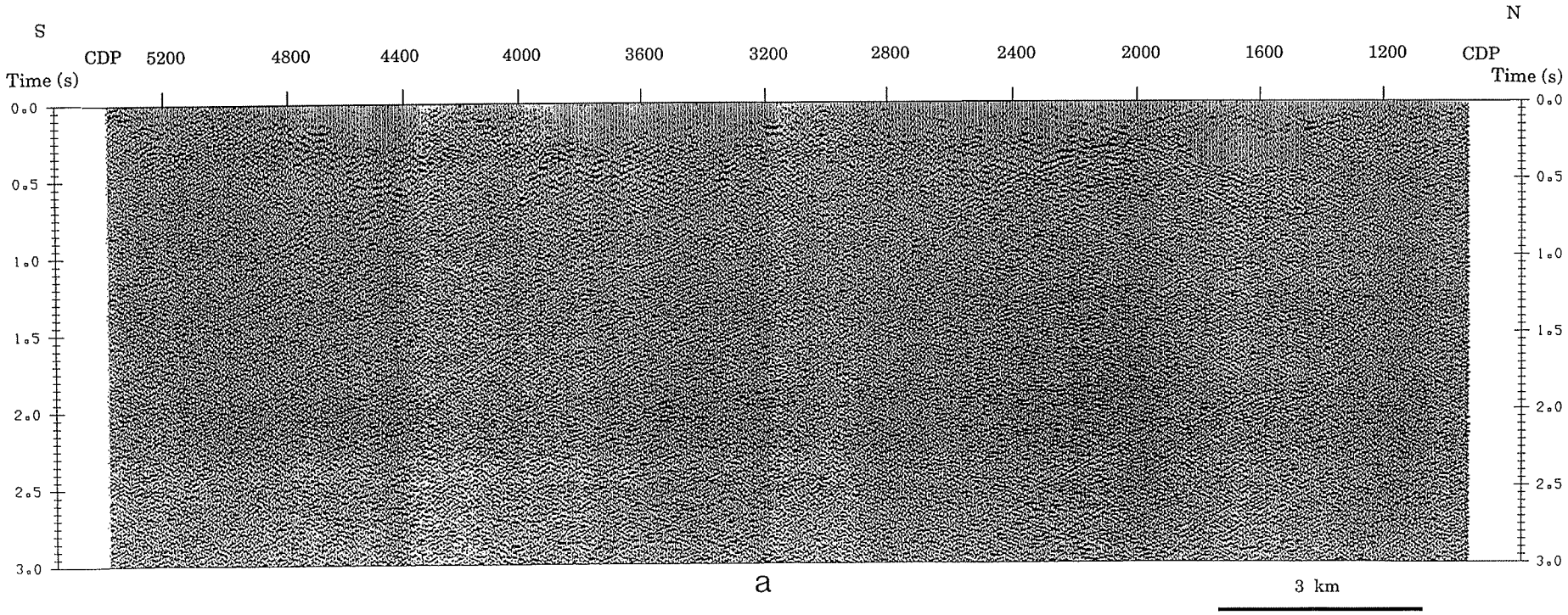

Figure 6.19: The final stack section: (a) the stack section without cross-dip correction; (b) with cross-dip correction; (c) the bias plot of final stack section after cross-dip correction, residual statics and coherent filtering. Continue on the following pages.

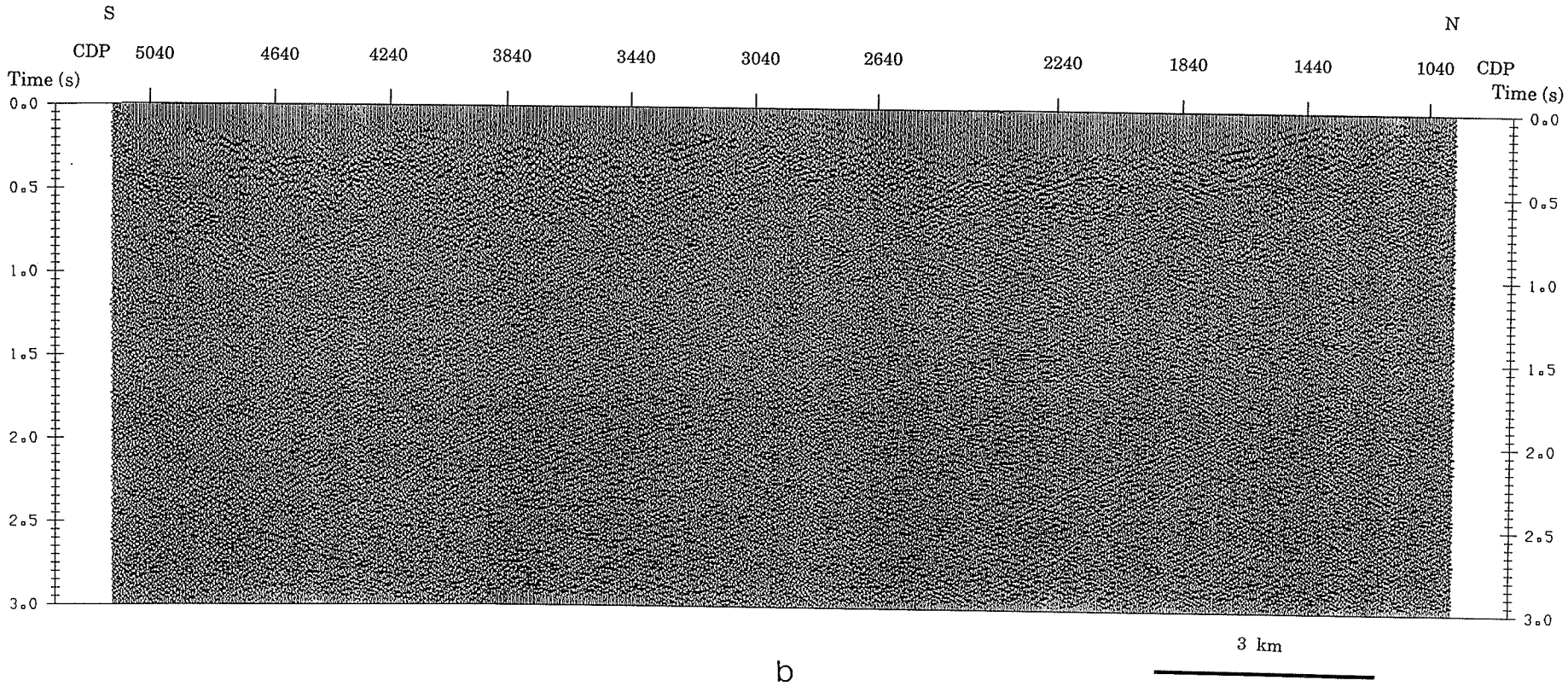
S
N
CDP
5040
4640
4240
3840
3440
3040
2640
2240
1840
1440
1040
CDP
Time (s)
Time (s)
0.0
0.5
1.0
1.5
2.0
2.5
3.0
3 km

b

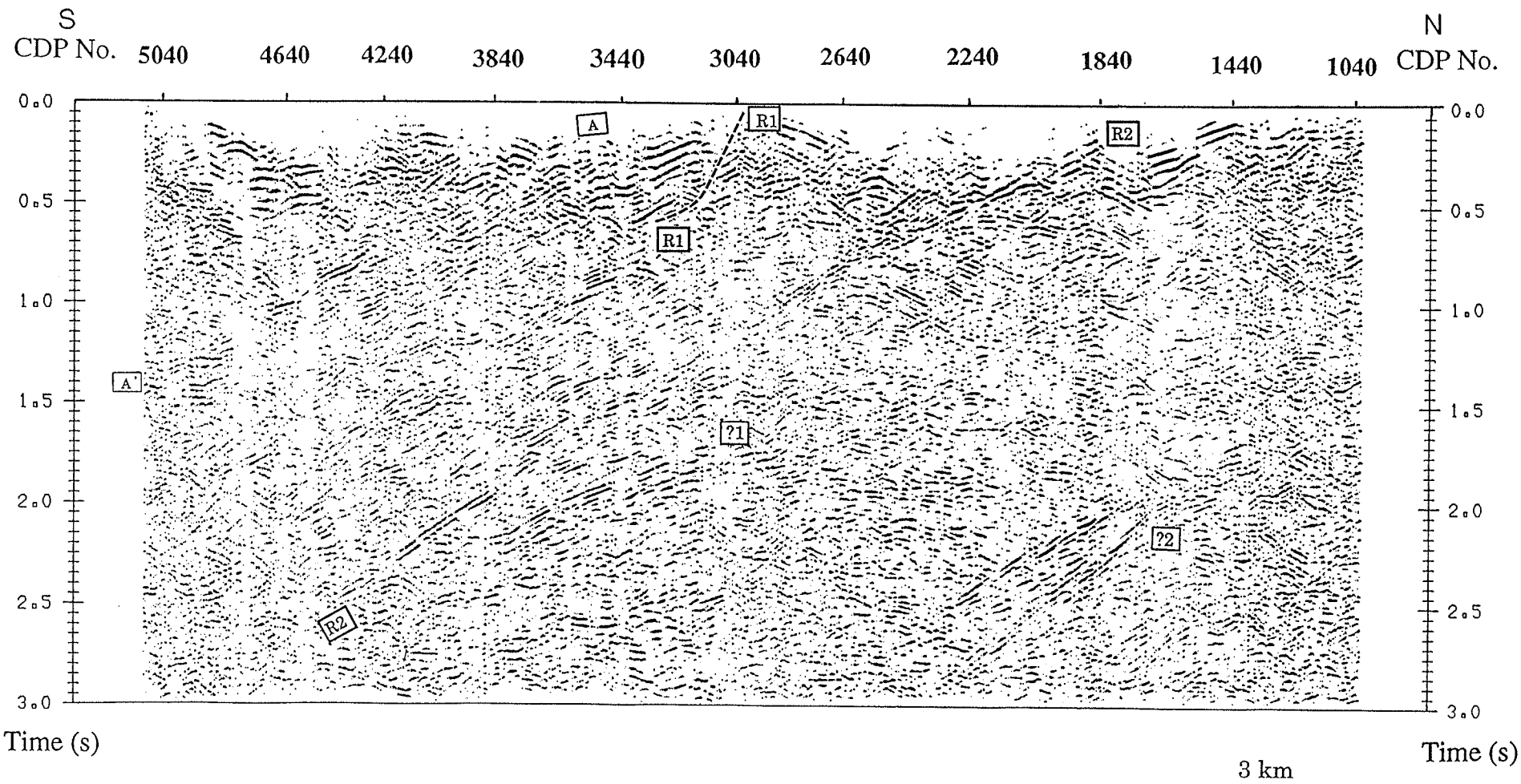
S
CDP No.
5040
4640
4240
3840
3440
3040
2640
2240
1840
1440
1040
N
CDP No.
0.0
0.5
1.0
1.5
2.0
2.5
3.0
A
A'
R1
R1
R2
R2
?1
?2
Time (s)
Time (s)
3 km

C

6.3 Results from Line 42 Seismic Reflection Data

The subsurface structure across the Levack Gneiss Complex (LGC) towards the Abitibi granite-greenstone belts is optimally imaged after the reprocessing steps described above and is shown in Figure 6.19c. The main features of the line 42 reflection section include three major reflections and a couple of uninterpreted events.

The Contact between the LGC and the Cartier Granite

The contact between the LGC and Cartier granite intrusive rocks is probably an intrusive interface and is marked in the seismic profile by an in-line east dipping event AA' (Figure 6.19c). It intersects the surface close to the CDP number 3760, which is approximately 1.5 - 2 km north from the present geological boundary on the compilation map (Dressler et al., 1984). This is, however, consistent with the field mapping carried out by Fueten et al. (1992) who reported that the LGC/Cartier granite boundary is a couple of kilometers north of its current position in the compilation map. Even though the reflections along the projected interface are not very coherent, the trend of the contact is seen clearly (Figures 6.19b and 6.19c).

The reflective patterns in the LGC generally vary from horizontal to slightly subhorizontal, and they change to east dipping on the west side of the contact. The reflected energy within the layer is probably produced by the compositionally layered gneissic rocks. By means of compressional wave velocity and density measurements to hydrostatic confining pressures of 600 Mpa for drill core samples, Salisbury et al. (1994) found that the LGC has velocity and density values as high as 6.5 km/s and $2.86 g/cm^3$ respectively and that the density value of the LGC is highly variable. Al-

though the average reflection coefficient at the norite/LGC boundary is low (-0.01), density variation in the LGC suggests that the Norite/LGC and LGC/Cartier granite contacts can be strong reflectors locally. This is consistent with the observed reflection patterns along the LGC/Cartier granite boundary. The reflections from the contact are not as coherent as from sedimentary contacts, but they are locally strong enough and the trend of the contact can be traced in the final processed profile.

Figure 6.20 shows a schematic plot of the profiles for line 42 and the related part of line 41. From the results of line 41 profile, the lower boundary of the LGC lies at approximately 2.3 s at the north end of the line 41 (Milkereit, 1992). At the south end of line 42 the base of the LGC lies at approximately 1.3 s. The travel time difference may have resulted from the geographic offset of the two lines for about ten kilometers (see Figure 4.1). The thickness of the LGC at the north end of line 41 and at the south end of line 42 appears almost unchanged. The in-line dip of the interface is approximately 32^o - 35^o southeasterly in the line 42 profile. This is steeper than that of the line 41 profile (Figure 6.20). According to the cross-dip correction, the cross-dip in the shallow part (0-1.6 s) of this portion is southwest dipping with an apparent dip angle approximately ranging from 17.25^o to 27^o as it approaches to the south end of the line.

Reflection event R2 - a major fault or shear zone?

The most distinct reflection event in the seismic profile of Line 42 is the reflection event R2 (Figure 6.20). It dips southeast extending through most of the line from the CDP number 1860 on surface towards the CDP number 4300 down to the two-way time of 2.5 s. It appears to be approximately parallel to the interface between the LGC and the Cartier granitic intrusive rocks (event AA'). The reflection patterns across

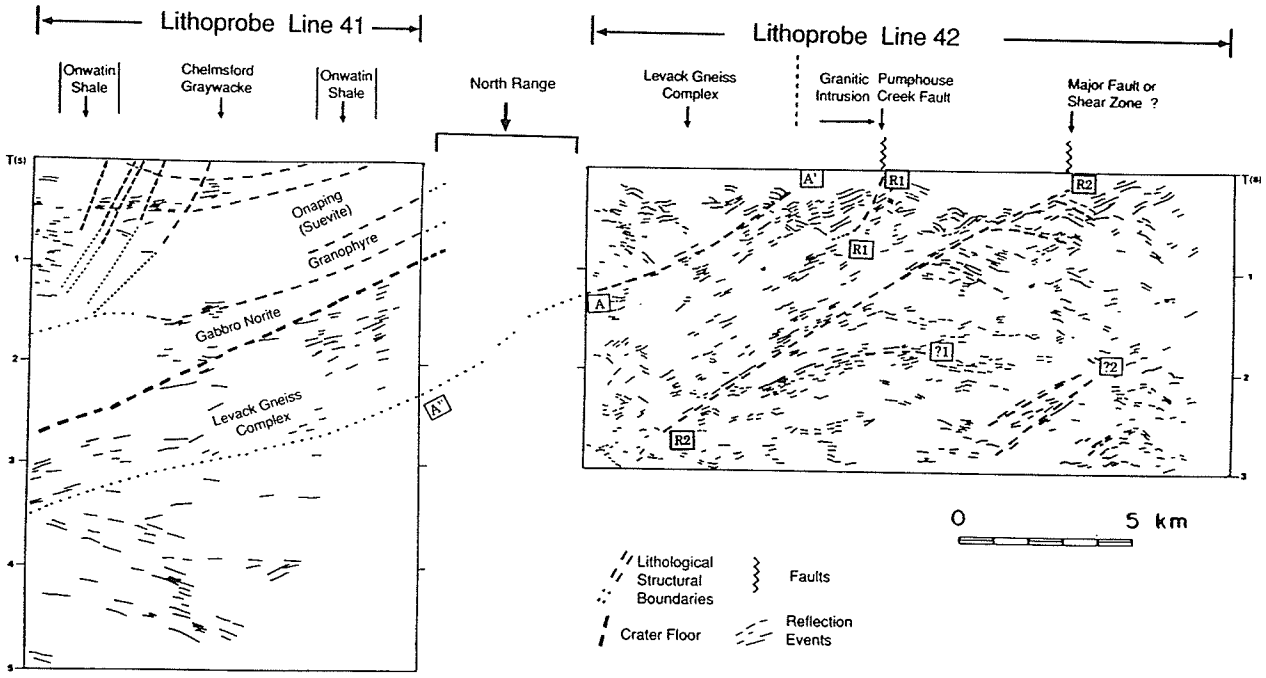

Figure 6.20: The schematic plot of the northern portion of the line 41 and line 42 profiles with preliminary interpretations (For locations of line 41 and 42 see Figure 4.1).

this event change markedly. There is a main trend of southeast dipping patterns in the hangingwall side of the R2 event, but irregular reflection patterns are displayed in the footwall side. On the geological compilation map there is no distinct fault or structural boundary in the vicinity of the CDP number 1860. Thus the interpretation is carried out with the aid of an ERS-1 (Earth Resource Satellite) SAR (Synthetic Aperture Radar) and other airborne geophysical images, which will be discussed in section 6.4.

Other events

Two uninterpretated events, reflection event ?1 below event R2 and event ?2 in the northern portion of the line at 2.0 to 3.0 s depth are prominent in the profile 42. The geophysical significance of the convex-shaped reflection event ?1 and the south dipping event ?2 is uncertain at this time. For more convincing geological interpretation of these events, further laboratory and field investigation of the geological and tectonic evolution of these rocks must be carried out.

6.4 The SAR and Airborne Geophysical Sensor Images

Since no detailed geological mapping has been carried out in the northwest portion of the Sudbury Structure at the time of interpretation of the line 42 data, the ERS-1 Synthetic Aperture Radar (SAR) image (Figure 6.21) along with airborne EM and magnetic data were processed and carefully examined in the vicinity of the line 42 to help the interpretation of the seismic data (Miao et al., 1994c). The field survey parameters and preliminarily processing of the C-band SAR image data and the multi-

parameter airborne geophysical data are described in Appendix D and E respectively .

The main linear features that are found in the SAR data include the Pumphouse creek fault (F1 in Figure 6.21) which corresponds to the event R1 in the reprocessed seismic reflection profile (Figure 6.20), three northwest striking dikes in the northeast corner of Figure 6.21 and the major north striking Fecunis Lake Fault. In addition to these, there are two other distinct linear features on the SAR image which intersect with the northern portion of the seismic line 42. One is the northwest striking linear feature F2, and the other is a less noticeable linear feature F3. This feature is oriented northeast and parallel to the North Range ring structure of the SIC. The F2 has the appearance of a major structural feature such as a major fault or shear zone based on the surface expressions. It cuts through the SIC structure implying a post-impact origin. F3 in the SAR image also may be a fault or shear zone. Both F2 and F3 have surface expressions of major subsurface structural boundaries, one of which should correspond to the major reflection event R2 in the reprocessed line 42 seismic profile. At shallow depths (0 - 1s) of the reprocessed seismic data, the reflection event R2 is mainly south dipping with a slight west dip (0^o - 5.7^o cross-dip). But as depth increases, the event becomes southeast dipping with in line dip of approximately 35^o east and cross-dip of approximately 11.2^o south. The near surface expression of the reflection event R2 seems to align with the northwest striking feature F2 in the SAR image (Figure 6.21). But at great depths, the attitude of the reflection event R2 appears correlate to the linear feature F3 in the SAR image. It is also possible that the reflection event R2 is a result of a later shallow tectonic event associated with the surface feature F2 in the SAR image superimposed on the earlier deep southeast

dipping structure which originally has a surface expression associated with F3 in the SAR image. Geological interpretation of the major events F2 and F3 requires further detailed field investigations.

Examination of the airborne magnetic and EM total field and quadrature data together with the SAR image (see Appendix D and E for the SAR and airborne image data processing) indicates that the three diabase dikes in the northeast corner of the SAR image match well with the linear anomalies in the magnetic and EM data. Events F1 and F3, however, do not coincide with any of the linear anomalies prominent in the airborne geophysical data. There is, however, a major linear anomaly with uncertain significance in the magnetic data which lies a few hundred meters northwest of the F3 with same orientation. The event F2 does not exactly coincide with a linear anomaly in the airborne data. The resolution of the airborne magnetic and EM data are much lower than that of the SAR data, which can sometimes result in broader appearances than that of real anomalies in magnetic and EM images, while the SAR images display much finer features. It is, therefore, uncertain whether the weaker linear anomalies in the airborne geophysical data do correlate with the event F2 in the SAR image. Of course not all linear features in the airborne geophysical data correspond to mafic dikes in the area. Some features shown in the EM data, for example, do not match with magnetic anomalies. They are probably noise produced by man-made structures such as power lines and railroads (see Appendix E).

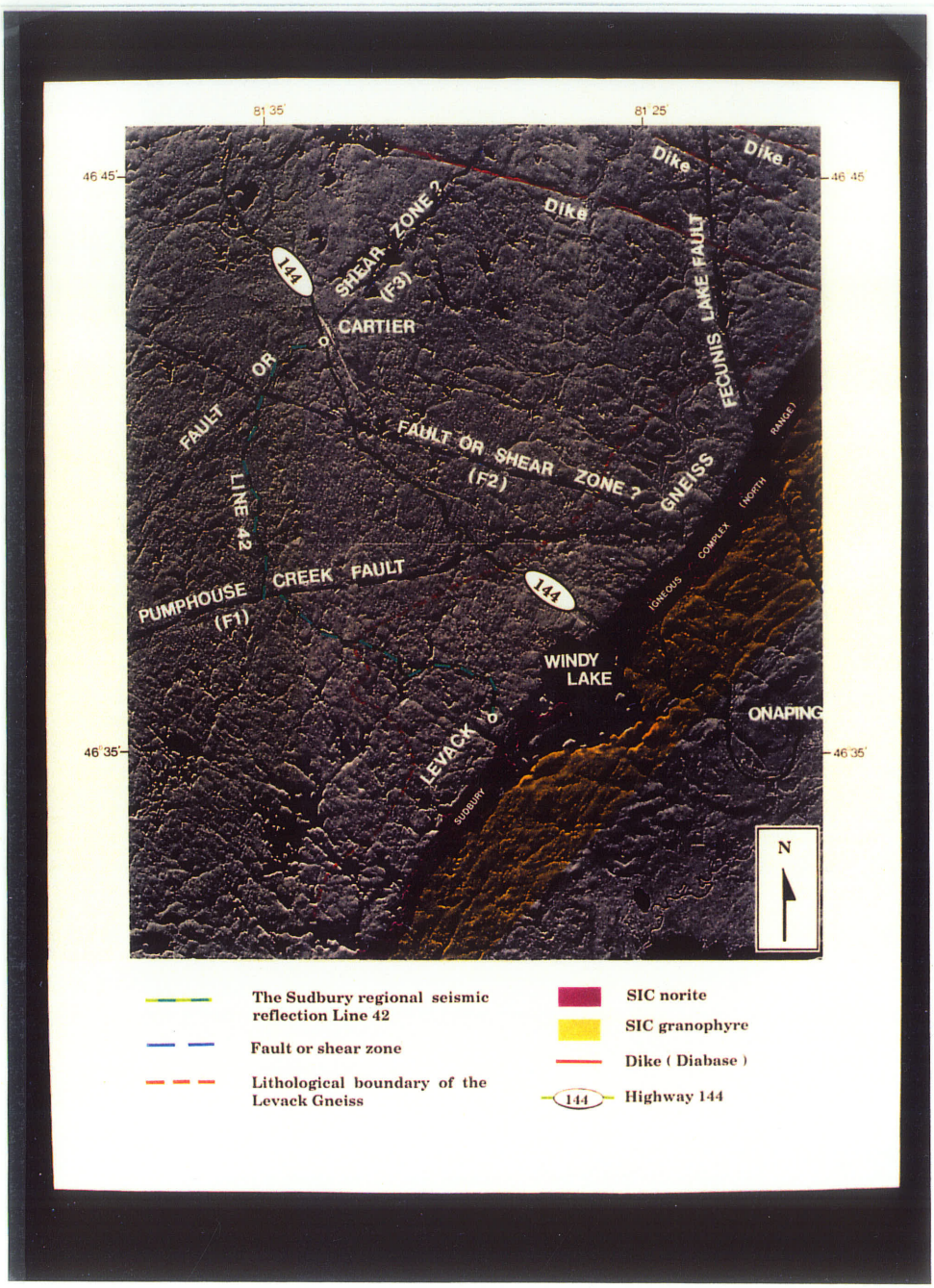

Figure 6.21: The C-SAR image in the northwest portion of the Sudbury Structure with preliminary interpretations and the location of line 42.

Chapter 7

The Wavelet Transform and Application in Seismic Data Processing

7.1 Introduction

7.1.1 Conventional Approaches for Signal Analysis

Fourier analysis.

The Fourier transform (Papoulis, 1962), which decomposes a time series into orthogonal frequency components or vice versa, has been widely used for geophysical data processing for many years. Not only is the Fourier analysis technique of fundamental importance in many areas of sciences and engineering, but it also has a significant physical interpretation. In addition, the development of the fast Fourier transform algorithm has made the Fourier analysis very attractive and useful, mainly because of the orthogonality properties of the Fourier series and of its simple expres-

sion. However, upon inspection of the Fourier transform formula:

$$F(\omega) = \int_{-\infty}^{\infty} f(t)e^{-it\omega}dt, \tag{7.1}$$

one must notice that the Fourier transform extracts periodic signals from a function $f(t)$ of infinite time duration and the frequency information can not be associated with time locally. One can only analyze and process signals in either time or frequency domain.

Short Time Fourier Transform.

To compensate for the inability of the Fourier transform to deal with time-frequency analysis of non-stationary time series, the Short Time Fourier Transform (STFT) was developed. One such typical STFT is the Gabor transform, which is defined as (Chui, 1992):

$$G_{\alpha,b}(f) = \int_{-\infty}^{\infty} f(t)e^{-it\omega}g_{\alpha}(t-b)dt, \tag{7.2}$$

where g(t) is a Gaussian function,

$$g_{\alpha}(t) = \frac{1}{2\sqrt{\pi\alpha}}e^{-t^2/4\alpha}.$$

It is also called a window function (in other forms of the STFT, the Gaussian function is replaced by other window functions). Thus the Gabor transform localizes, or windows, the Fourier transform of a signal $f(t)$ around $t = b$. The width of the window is determined by a fixed positive constant α. In all of the STFT methods there is very undesirable computational complexity when narrowing of the window is required for good localization or when widening of the window is required for producing a more global picture (Chui, 1992).

7.1.2 Wavelet Transform–A New Approach

Recently, a comprehensive foundation of the wavelet transform (WT) has been developed (Daubechies, 1990 and Chui, 1992) and has become a powerful tool in inhomogeneous fractal physics, in turbulence phase transition, as well as in transient signal and image processing disciplines. The distinct advantage of the WT over the Fourier transform is that the WT has the capability of combining the features of both time and frequency information. One feature especially worth mentioning is treatment of transient effects and events. A further advantage of the WT which distinguishes itself from any STFT is its zoom-in and zoom-out capability. Unlike the Gabor transform in which the width of the window is fixed, the WT localizes signals in a variable window governing by a dilation parameter a (which will discuss later). Hence the sampling rate is higher for high frequency components and lower for low frequency components.

Seismic signals are characterized by their traveltime, frequency characteristics, and phase information, and as well as coherent noise (Sheriff and Geldart, 1986). In seismic data processing, it is often necessary to carry out time-evolution frequency analysis for which conventional Fourier analysis is not suitable. Nonstationary properties of a seismic wavelet can be caused by dispersion, attenuation and other nonlinear processes which vary with frequency and time simultaneously. The WT is well suited for such problems and has a potentially powerful application in seismic data processing.

The algorithm for implementing the WT varies depending on whether the basis wavelet function chosen is orthogonal or non-orthogonal. For the orthogonal WT, a

fast algorithm conjuncted with the multiresolution analysis was developed and called the orthogonal multiresolution analysis (Mallat, 1989; Meyer, 1985,1896). In applications, practical implementation of the transformation is performed by using a basic filter bank ($m_0(\omega+\pi)$, $\bar{m}_0(\omega+\pi)e^{-i\omega}$), where m_0 is a low-pass transfer function and $\bar{m}_0$ is a high-pass function. They are also called quadrature filters. The wavelet function can be derived from them. However, the algorithm imposes the reconstruction condition of $|m_0(\omega)|^2 + |\bar{m}_0(\omega+\pi)|^2 = 1$. This orthogonal relation is very strict for filter designs. Furthermore, it is impossible to find a such filter $m_0(\omega)$ with finite impulse response (FIR) and linear phase at the same time (Feauveau, 1992). For the non-orthogonal WT, the algorithms are variable depending on different wavelet functions, and a fast algorithm for implementation of the non-orthogonal WT remains under investigation. Even though the WT has become very popular in the image processing field, application in seismic data processing is relatively new. Because the popularly developed wavelet functions are compactly supported orthogonal wavelets which are mostly not symmetric or anti-symmetric, such as Daubechies wavelet, their non-linear phases create distortion problems after the WT. This is undesirable when subsequent data processings are required. The non-orthogonal WT provides a better choice since it behaves like a linear phase filter.

In this chapter, the WT theory to explain the relative properties of the WT and wavelet function is introduced first, which are essential for understanding what kind of wavelet should be selected for each individual application (this is also the difference between the WT and any other transformations, in which the operators are usually unchanged). Then a non-orthogonal WT using the Morlet wavelet function for testing with seismic data is discussed. The Morlet wavelet is a continuous complex wavelet

function, however, it is compactly supported and well localized in time and frequency domains. We explore and try to provide insights into certain properties of the transform and its physical meanings in digital signal analysis. Application of the WT is studied and tested with both synthetic and real data to analyze the time-dependent frequency features of seismic data. A method of suppressing coherent noise such as ground roll is developed and applied to the Sudbury reflection line 42 as mentioned in the Chapter 6. The purpose of this study is to see how the WT can apply to seismic data processing and what kind of effects it will have.

7.2 The Wavelet Transform Theory

7.2.1 Continuous Wavelet Transform

The Forward Wavelet Transform.

The wavelet transform of a continuous signal $S(t)$ is defined as an inner product in Hilbert Space of the L^2 norm:

$$W_s(a,b) = \langle h^{(a,b)},\ S(t)\rangle = \frac{1}{\sqrt{|a|}} \int h^*(\frac{t-b}{a}) S(t)\ \mathrm{d}t, \tag{7.3}$$

where $h^{(a,b)} = |a|^{\frac{-1}{2}} h(\frac{t-b}{a})$ is a family of wavelet functions, generated from a mother wavelet through dilation, determined by the parameter a which governs frequency, and shift, controlled by the parameter b which determines position translation

$$h^{(a,b)} \underbrace{\longleftarrow}_{\text{dilation a and shift b}} h(t).$$

The family of the wavelet functions $h^{(a,b)}$ constitutes the basis functions for the WT and the WT transfers signals from a one dimensional space of t to a two dimensional space of (a,b).

The mother wavelet function $h(t)$ must be a square integrable function and satisfy:

$$C_h = \int \mathrm{d}\omega |\omega|^{-1} |\hat{h}(\omega)|^2 < \infty, \tag{7.4}$$

where $\hat{h}(\omega)$ is the Fourier transform of $h(t)$ (Daubechies, 1990). This condition requires that when the frequency approaches zero, the Fourier transform of the wavelet function must also approach zero.

The Inverse Wavelet Transform.

The inverse WT is defined as:

$$S(t) = {C_h}^{-1} \int \frac{da}{a^2} \int db\, W_s(a,\, b)\, h^{(a,b)} = {C_h}^{-1} \int \frac{da}{a^2} \int db < h^{(a,b)}, S(t) > h^{(a,b)}. \tag{7.5}$$

Thus a function $S(t)$ can be reconstructed using the inverse WT from $W_s(a, b)$. The basis functions defined in the Hilbert space are usually orthogonal. However, in the framework of the WT, the basis functions are not required to be orthogonal, and the coefficients are not always required to be independent to each other. This leads to the theory of the frame – an alternative to the orthogonal basis functions. It has been proved that even when the basis functions are not mutually orthogonal but are "overcomplete", the basis functions can be a good frame for decompositions of any signal function in the Hilbert space (Daubechies et al., 1986).

7.2.2 Discrete Wavelet Transform

In a discrete time-frequency space (the time-frequency space is also called the phase space), one can discretize the dilation parameter a as $a = a_0^m$, where a_0 is a fixed dilation step $a_0 > 1$ and m is an integer, and take b as $b = nb_0a_0^m$, where b_0 is a fixed

translation step ($b_0 > 0$) and n is an integer. The discretized basis functions of a given wavelet are then defined as

$$h_{m,n}(t) = h^{({a_0}^m, n{b_0}{a_0}^m)}(t) = {a_0}^{-m/2} h({a_0}^{-m}\, t - n b_0). \tag{7.6}$$

Usually a_0 is taken as 2, in which case m is called octave. When $m > 0$, the wavelet spreads out; when $m < 0$, the wavelet shrinks. For a finer division of the dilation parameter, the basis functions can be defined as:

$$h^j(t) = {a_0}^{-\frac{j}{N}}\, h({a_0}^{-\frac{j}{N}}\, t) \qquad\qquad j = 0, 1, 2, ... N-1 \tag{7.7}$$

where N is the number of "voices" per octave and j represents a voice. By combining equations (7.6) and (7.7), the basis functions can be written as

$${h^j}_{m,n}(t) = {a_0}^{-\frac{j}{N}}\, h_{m,n}({a_0}^{-\frac{j}{N}}\, t) = {a_0}^{-\frac{j}{N}} \cdot {a_0}^{-\frac{m}{2}}\, h({a_0}^{-(m+\frac{j}{N})}\, t - n b_0), \tag{7.8}$$

where $m = 0, \pm 1, \pm 2$, ..., and $j = 0, 1, 2, ... N-1$.

Figure 7.1 shows an example of the phase space lattice where the time and frequency relationship associated with each sampling point is explained. The vertical axis represents frequency and the horizontal axis represents time. The sampling rate in time is $\triangle b = {a_0}^m\, b_0$, and the frequency interval between neighboring octaves is $\triangle\omega = \omega_0 {a_0}^{-m}(a_0^{-1} - 1)$, where ω_0 is a constant associated with the mother wavelet function. From the schematic diagram one can observe three features of the sampling lattice corresponding to the WT approach. Unlike the conventional Fourier transform methods, the frequency is represented in a logarithmic scale. In contrast to the STFT in which the time-frequency sampling window is rigid (Chui, 1992), the time-frequency sampling window in the WT is flexible. When $m > 0$ the sampling interval

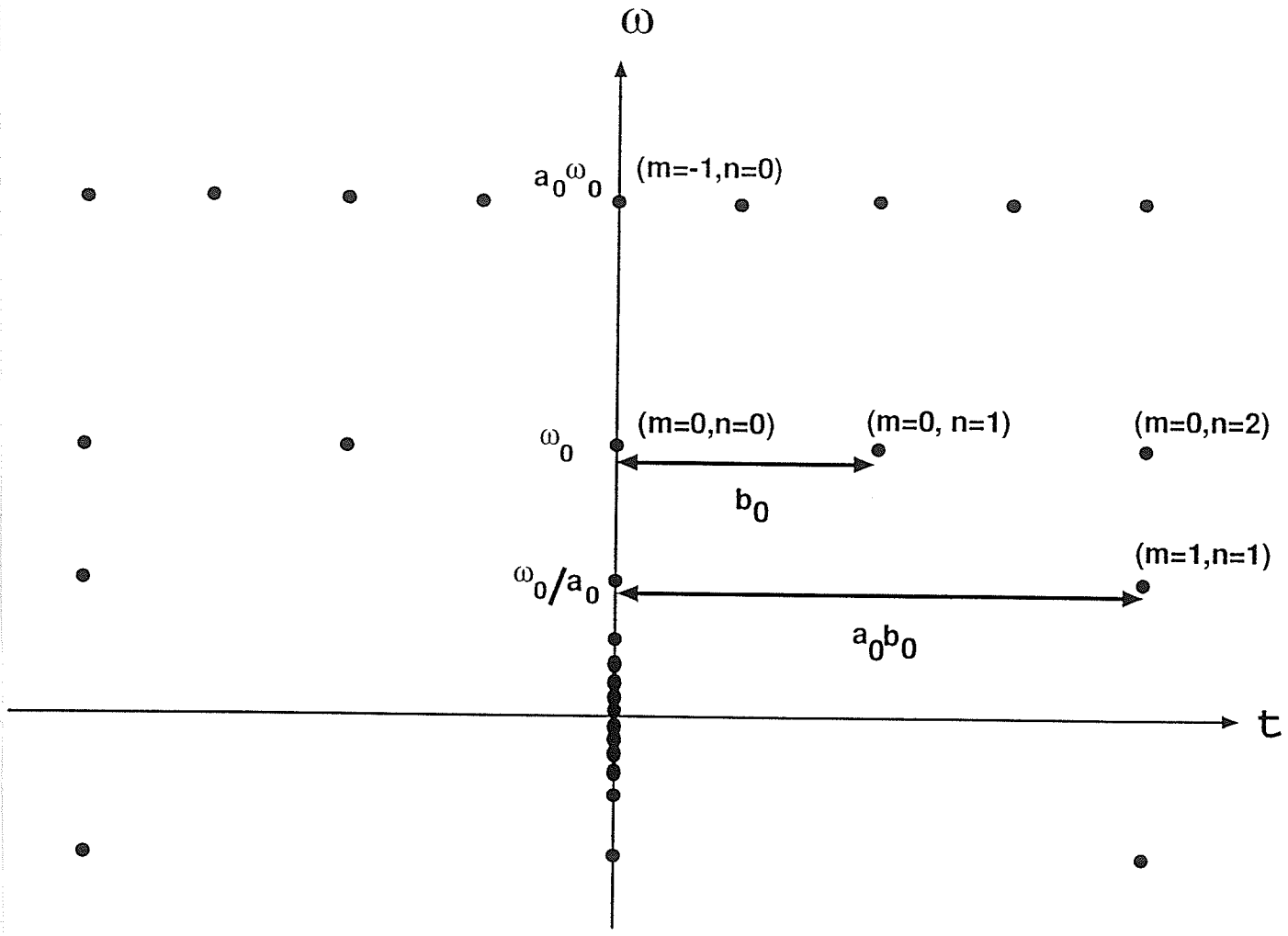

Figure 7.1: Phase space lattice corresponding to the wavelet transform. The ω_0 is a constant associated with the mother wavelet, $a_0 = 2$ and $\hat{h}$ is assumed to be even.

is coarser, and when $m < 0$, the sampling interval becomes smaller. Therefore the sampling resolution is higher for high frequency components, and it is lower for low frequency components. This is a very efficient way for information representation for any large data storage and processing tasks and for the time-frequency analysis of a signal with both high and low frequency components.

7.2.3 The Wavelet Functions and Properties

Since the basis functions are wavelet functions, the WT always depends on the selection of the mother wavelet. Understanding the properties of the wavelet functions is therefore very important for the selection of a proper wavelet for specific applications.

Localization of the WT Representation

One of the important properties of the WT is localization of the WT coefficients for signal representation. A wavelet function is called "well localized" when only those m, n for which $\{\pm {a_0}^{-m},\ n{a_0}^m b_0\}$ lies in or close to $[-\Omega,\ \Omega] \times [-T,\ T]$ play a significant role in reconstruction of the signal $S(t)$ (Daubechies 1990). Here $[-T, T]$ and $[-\Omega, \Omega]$ are time and frequency ranges respectively. A wavelet function can only be "essentially" well localized, because no one function and its Fourier transform are both compactly supported.

The conditions which make a wavelet function well localized are called decaying conditions. They are defined by the following theorem (Daubechies, 1990).

Suppose

$$h_{m,n}(t) = a_0^{-m/2} h(a_0^{-m} t - n b_0)$$

constitutes a frame with frame bounds A and B, and its dual frame $\widetilde{h_{m,n}}$ (the du-

ality between $h_{m,n}$ and $\widetilde{h_{m,n}}$ is expressed as: for any given function f and g in the Hilbert space, $\langle f, g\rangle = \sum\langle f, \widetilde{h_{m,n}}\rangle\langle h_{m,n}, g\rangle)$, then a given function $S(t) \in L^2$ can be reconstructed by its inner product with the frame $h_{m,n}$ and the dual frame $\widetilde{h_{m,n}}$ as

$$S(t) = \sum_{m,n\in Z} (\widetilde{h_{m,n}})\ \langle h_{m,n},\ S(t)\rangle, \tag{7.9}$$

where z is 1-D integer space. Assuming the Fourier transform of the mother wavelet $\hat{h}(\omega)$ satisfies:

$$|\hat{h}(\omega)| \leq c|\omega|^{\beta}(1+\omega^2)^{-(\alpha+\beta)/2} \tag{7.10}$$

where $\beta > 0$, $\alpha > 1$, and for some $\gamma > 1/2$ the mother wavelet itself $h(t)$ satisfies:

$$\int dt(1+t^2)^{\gamma}|h(t)|^2 < \infty \tag{7.11}$$

for a fixed time range $T > 0$ and a frequency range $0 < \Omega_0 < \Omega$, where Ω_0 is a constant. There then exists a finite subset $B_{\in}(T, \Omega_0, \Omega_1)$ of Z^2 (the 2-D integral space) such that, for all $S(t) \in L^2$,

$$|S(t) - \sum_{m,n\in B_{\in}(T,\Omega_0,\Omega_1)} (\widetilde{h_{m,n}})\ \langle h_{m,n},\ S(t)\rangle| \ \rightarrow \text{very small value.}$$

This is equal to the phase space localization. Equation (7.10) and (7.11) are respectively the decaying conditions for the Fourier transform of a wavelet function and the wavelet function itself. However, wavelet functions which satisfy these two conditions are often not orthogonal.

Wavelet Functions

There are several kinds of wavelet functions which are suitable for normal applications. Among the common ones are the Mexican Hat wavelet, the Meyer wavelet, the Morlet wavelet, and the Daubechies wavelet (Daubechies, 1990; Sheng and Szu,

1992). Some of these wavelet functions are orthogonal while others are not. They all have different useful properties depending on application.

(a). **The Meyer wavelet**– To derive orthonormal wavelet basis functions, Meyer constructed a wavelet function (Meyer, 1985-1986). The Fourier transform of the Meyer wavelet is defined as:

$$H(\omega) = e^{i\omega/2}\frac{1}{\sqrt{2\pi}}(U(\omega) + U(-\omega)), \tag{7.12}$$

where

$$U(\omega) = \left\{ \begin{array}{ll} 0 & \omega < \frac{2\pi}{3} \text{ or } \omega \geq \frac{8\pi}{3} \\ \sin\frac{\pi}{2}v(\frac{3\omega}{2\pi} - 1) & \frac{2\pi}{3} \leq \omega \leq \frac{4\pi}{3} \\ \cos\frac{\pi}{2}v(\frac{3\omega}{4\pi} - 1) & \frac{4\pi}{3} \leq \omega \leq \frac{8\pi}{3}, \end{array} \right\}$$

$v(\omega) = 0$ for $\omega \leq 0$, $v(\omega) = 1$ for $\omega \geq 1$, and $v(\omega) + v(1-\omega) = 1$ for $\omega \in [0, 1]$. Figure 7.2 shows the wavelet and its Fourier transform. The Meyer wavelet is a largely supported and orthonormal wavelet It is symmetric but not compactly supported, thus it is not suitable when good localization is required.

(b). **The Daubechies wavelet**– By giving a set of constraint conditions for quadrature filter, Daubechies constructed another orthonormal discrete wavelet functions (Daubechies, 1989). Figure 7.3 shows the graph of the Daubechies wavelet and the module of its Fourier transform. There are two features in the graph. First of all, it is not regular. It is found out that the support widths for wavelet functions increase linearly with their regularity. Thus highly compactly-supported wavelet functions are usually less regular. Another feature is the lack of any symmetry or antisymmetry axis for the wavelet. It is also known that there exist no compactly-supported orthogonal wavelet bases in which the wavelet function is either symmetry or antisymmetry

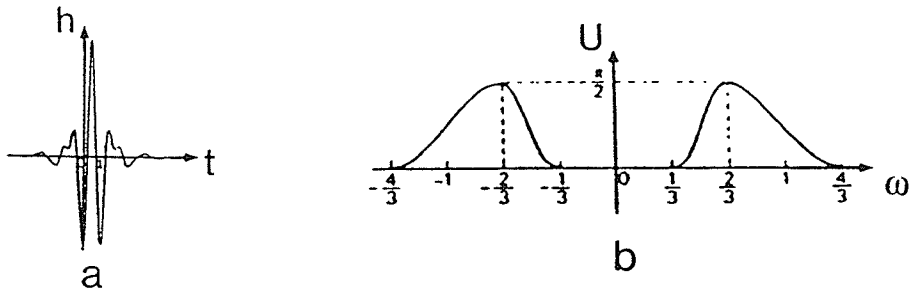

Figure 7.2: The function of the Meyer wavelet and the module of its Fourier transform. (a) The Meyer wavelet function; (b) the module of its Fourier transform.

around any axis (Daubechies, 1989). However, the Daubechies wavelet is an excellent compactly-supported and orthonormal wavelet. Based on it a fast algorithm was developed, and it is popularly used in many image processing problems as long as the non-linear phase produced by non-symmetry of the wavelet does not affect processing tasks.

(c). **The Morlet wavelet**– One of the useful non-orthogonal wavelet functions is the Morlet wavelet (Morlet, 1982). It is a continuous and complex wavelet. The definition of the Morlet wavelet and its Fourier transform are:

$$h(t) = \pi^{\frac{-1}{4}}(e^{ik_0 t} - e^{-\frac{k_0^2}{2}})e^{-\frac{t^2}{2}}, \tag{7.13}$$

$$H(\omega) = \pi^{\frac{-1}{4}}(e^{\frac{-(\omega-k_0)^2}{2}} - e^{-\frac{{k_0}^2}{2}}e^{-\frac{\omega^2}{2}}), \tag{7.14}$$

where $k_0 = \pi\,(\frac{2}{\ln 2})^{\frac{1}{2}}$.

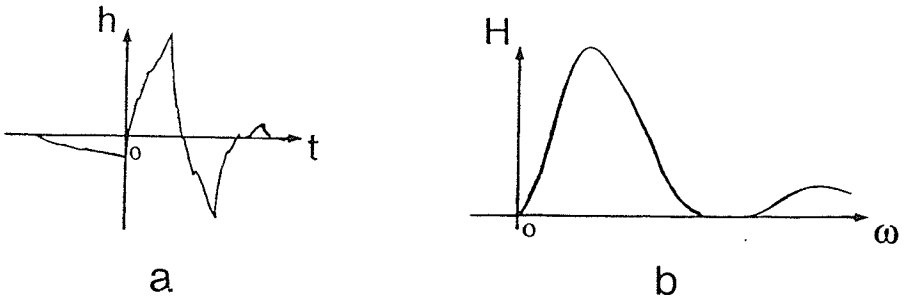

Figure 7.3: The function of the Daubechies wavelet and the module of its Fourier transform. (a) The Daubechies wavelet function; (b) the module of its Fourier transform.

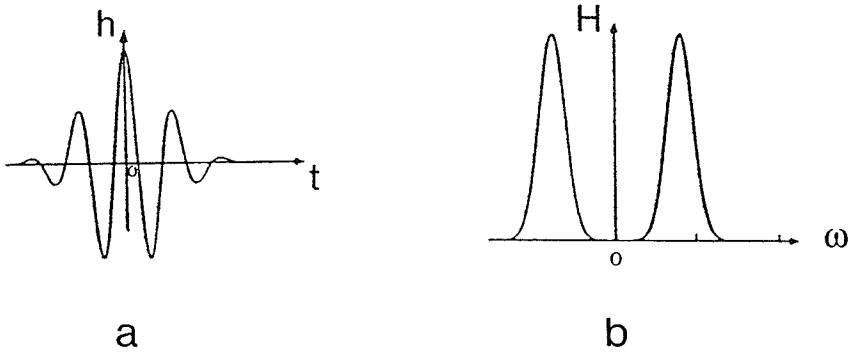

Figure 7.4: The real part of the Morlet wavelet and its Fourier transform. (a) The real part of the Morlet wavelet function; (b) its Fourier transform.

The graph of Morlet wavelet is shown in Figure 7.4. The negative terms in equations (7.13) and (7.14) assure that the spectrum decays to zero when the frequency approaches zero. This wavelet is not orthogonal but compactly supported in Hilbert Space. The ratio of the frame bounds for the Morlet wavelet is close to 1 when proper parameters of N and b_0 are chosen (Daubechies 1990). Thus, even though the Morlet wavelet is not orthogonal, it is an excellent alternative for the orthogonal basis. It is also noticed that the Fourier transform of the Morlet wavelet has no imaginary part, hence there is no phase distortion introduced during the WT.

7.3 Application of the Wavelet Transform

7.3.1 Non-orthogonal Wavelet Approximation Algorithm

The Morlet wavelet function was selected as the basis function for testing of the WT with real seismic data. The selection was made after careful consideration of its properties of compact support, lack of phase distortion, and localization in both time and frequency space. The WT integral is approximated by the Runge-Kutta algorithm, and the inverse WT is based on an approximation formula derived by Daubechies (1990) as following:

$$S_{approx} = \frac{2}{A+B} \sum_{m,n} h_{m,n} < h_{m,n}, S >, \tag{7.15}$$

where $< h_{m,n}, S >$ is the inner product of the wavelet function $h_{m,n}$ with the signal S (it is also the WT of the signal S), and A and B are the frame bounds of the wavelet function. If the parameters b_0=0.5, a_0=2, and N=4 are chosen (see equation (7.8) for detail), the ratio of A to B for the Morlet wavelet is equal to 1.0006 (Daubechies,

1990). Thus the formula (7.15) becomes a good approximation for the reconstruction equation (7.5) (Daubechies, 1990).

The family of wavelets used as the operators of the WT is shown in Figure 7.5. Figure 7.6 shows the decomposition of a seismic trace into different bands using the WT. The original signal is shown in the middle of the plot. The 33 traces in the upper half of the figure show 33 octave bands of the wavelet transformed data of the original signal. The original trace is shown in the middle of the figure. For display purposes, the traces are normalized. Since a_0 is 2, different values of m represent different octaves as described by the definition in equation (7.4) and each octave is divided into a number of voices with a physical meaning similar to the one in music. In this example, the octave m ranges from 0 to 8 and the number of voices is 4. The trace with octave $m = 0$ has the finest resolution and the one with octave $m = 8$ has the coarsest resolution, which also has the lowest frequency. The trace at the bottom of the figure is the reconstructed one using the WT.

Figure 7.7 shows comparison of the spectra of the reconstructed trace with that of the original one. Both the reconstructed trace and its spectrum are almost identical to the original trace and its spectrum in every detail. This stems from the properties of the Morlet wavelet, i.e., when proper value of b_0 and N are chosen, it serves as a good frame in the Hilbert space.

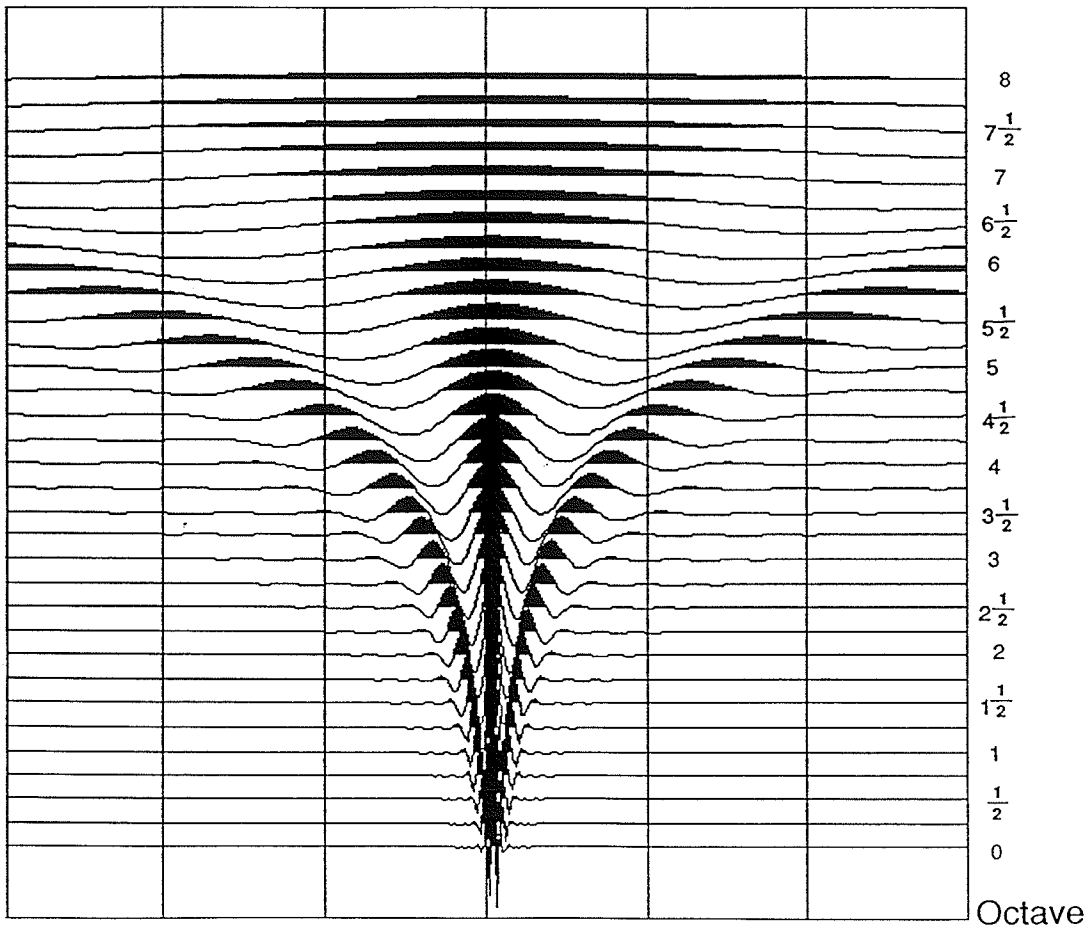

Figure 7.5: The family of the Morlet wavelet used as the operators in the WT integral. The octave ranges from 0 to 8 (m=0,1,..8) and the number of voice is 4 (N=4).

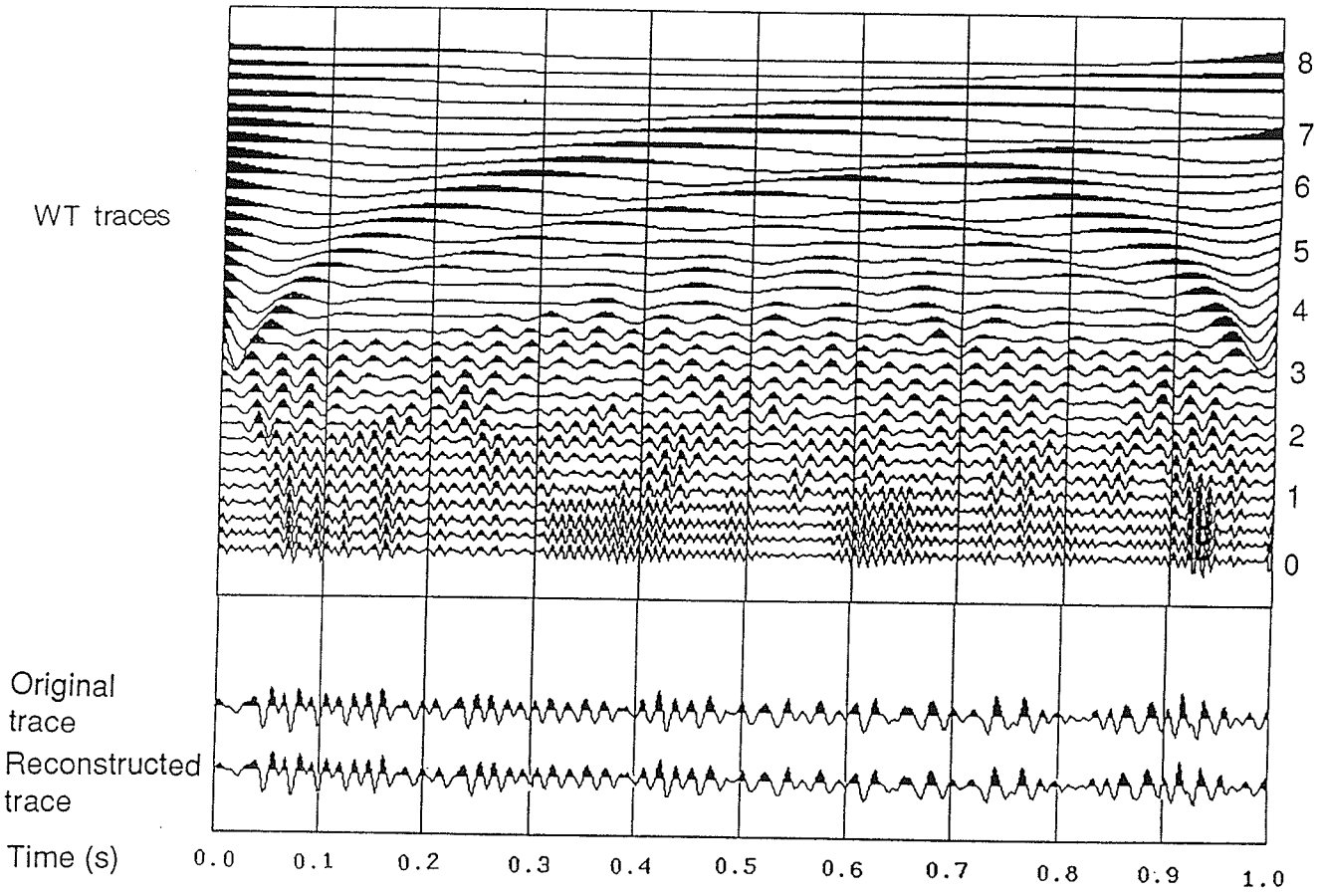

Figure 7.6: A sample seismic trace and its wavelet transform of the 33 octave bands (m=0,1,...8, N=4). The 33 traces in the upper part of the figure are the wavelet decomposed traces; the middle trace is the original seismic trace; and the bottom one is the reconstructed seismic trace.

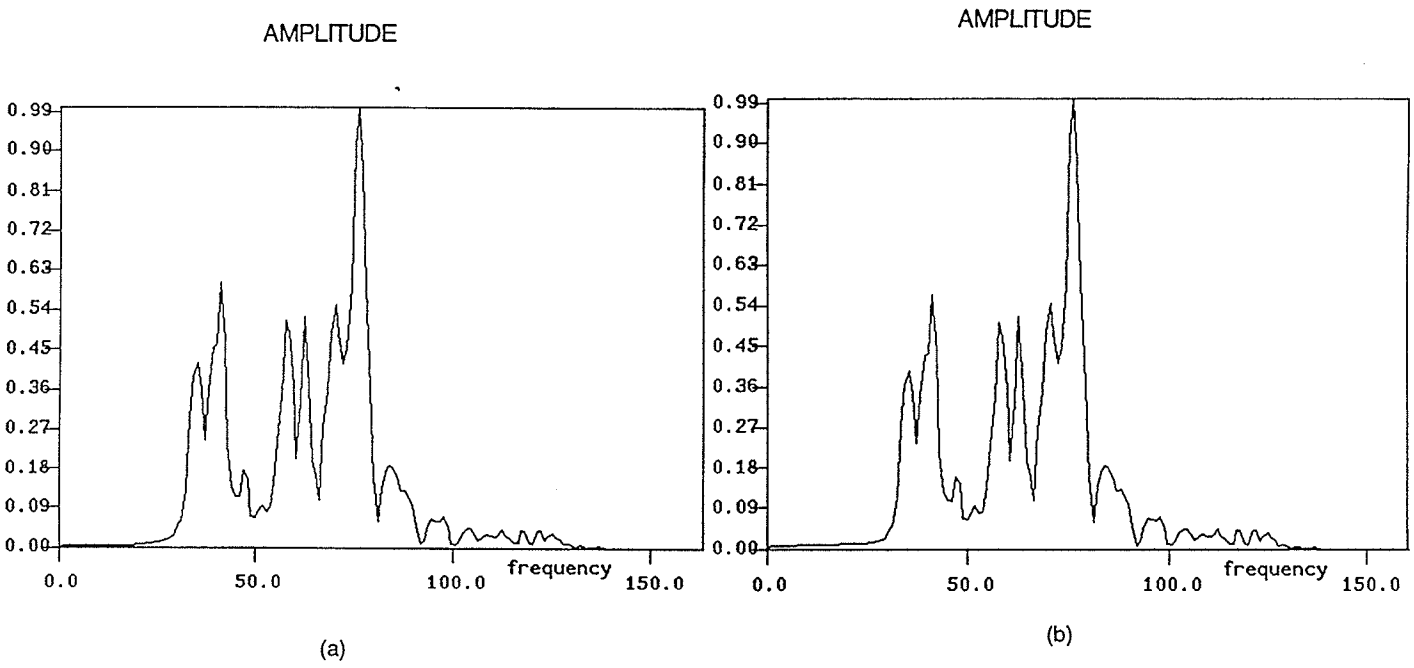

Figure 7.7: Comparison of the spectra of the reconstructed seismic signal with the original signal. (a) The spectrum of the original seismic trace (left); (b) the corresponding spectra of the reconstructed trace (right).

7.3.2 Removal of Ground Roll Noise

A reflection shot gather from the LITHOPROBE Sudbury line 42 was used to test the effectiveness of the WT in removing coherent noise. Figure 7.8 shows the original shot gather. The usual characteristics of the first break, ground roll and reflections are all included in the data.

Figure 7.9 shows decomposition of the original shot gather using the WT. In this example the same octave range (m: 0–8) and the number of voices (N=4) as in the previous example are used. Altogether there are 33 octave bands decomposed and plotted. For convenience of display, only every 4 bands are shown in the Figure 7.9, which correspond to m=0, 1, 2, 3, 4, 5, 6, 7, and 8 and N=0. The octave band 1 (m=0) has the finest resolution. The wavelet transformed data in octave 1 and 2 have relatively higher frequencies and the reflections are dominated. In both octave bands there is no any significant indication of the ground roll. The first break is relatively weak also. In the octave 3, the first break become stronger as the dominant frequency approaches that of the true first arrival waves. As the octave bands increase, ground roll appears and it becomes the strongest in octave 4. Reflections are completely invisible in these low frequency bands. In the higher octave bands, low frequency components become dominant. From the WT panels, one can identify reflections, ground roll, the first breaks and other coherent events. An important fact is that when m changes, even in a very narrow bandwidth, signals still maintain their time positions.

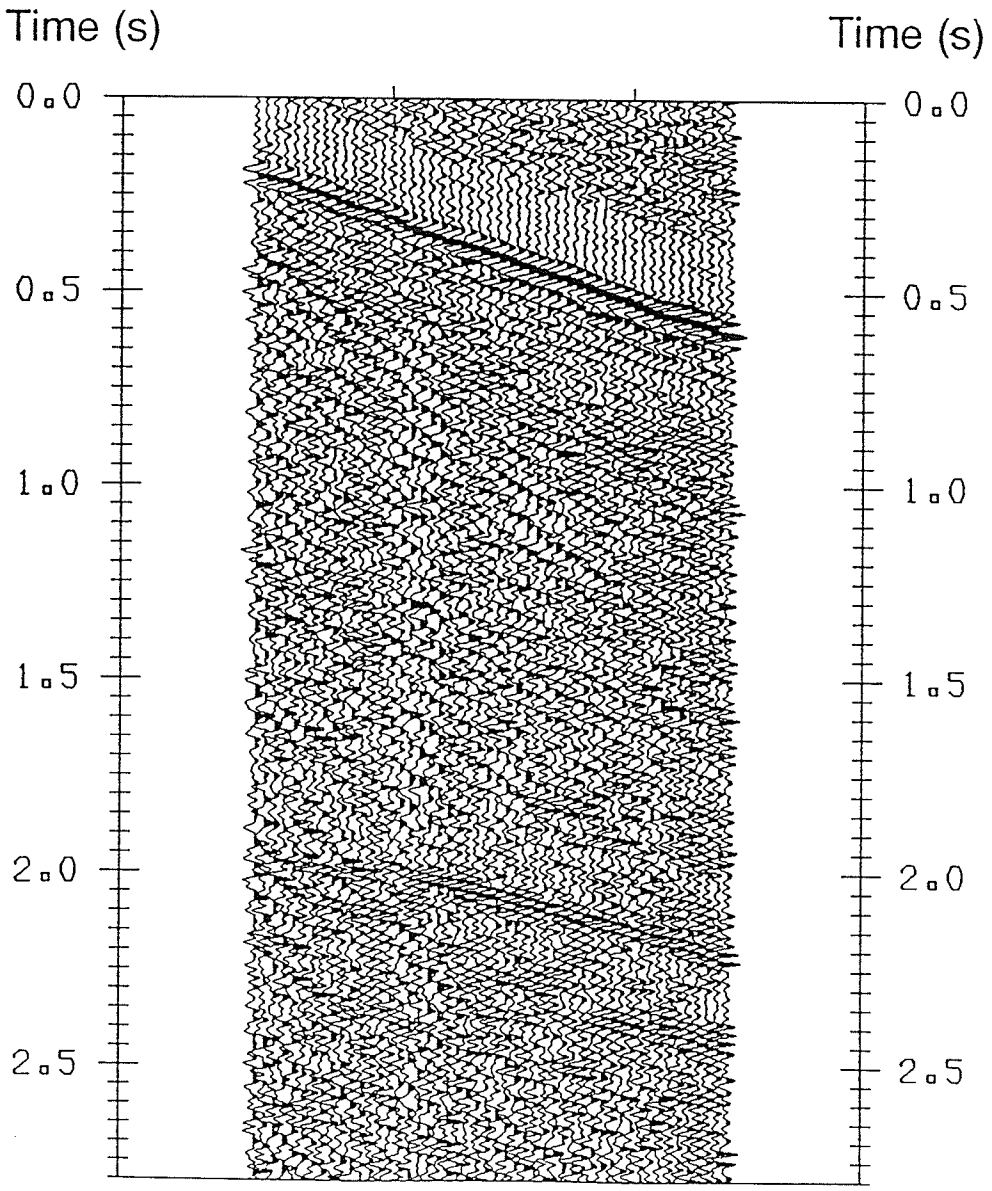

Figure 7.8: An original seismic shot gather from the Sudbury Line 42 regional reflection data.

Figure 7.10 shows the corresponding spectra of the WT panels (Figure 7.9). In the octave band 1, which has the highest resolution, the spectral band is broader and it contains the highest frequency components. As the octave bands increase, the highest peaks of the spectra shift to lower frequency and the bandwidth becomes narrower because of the tight localization of the signal information. In octave band 1 and 2, the reflection signals are dominant. Ground roll noise starts to appear in band 3 and become dominant in band 4. In band 4 the ground roll noise has a dominant frequency of approximately 11.0 Hz. The other WT panels appear to contain signal information of low frequency components.

The characteristics of the WT panels shown above are very useful for removal of specific coherent noise. Figure 7.11a shows the reconstructed shot gather using the Inverse WT. The reconstruction was performed by simply excluding the bands containing the ground roll noise. They are the bands 11 to 15 . One can see that the ground roll is almost completely removed and the reflection events are enhanced compared to the original shot gather (Figure 7.8).

The Fourier spectrum of the reconstructed gather (Figure 7.12b) obtained from the inverse WT is examined and compared with the spectrum of the original shot gather (Figure 7.12a). It can be seen that ground roll which has the peak of frequency at about 11 Hz is effectively suppressed. This fact further demonstrates that the new WT approach can remove coherent noise very effectively if their time and frequency characteristics are distinct.

A bandpass filter can not be compared to the WT in coherent noise suppression. Because in most cases signal and noise are mixed in the same frequency range. In

the WT method, both time and frequency features of the data are utilized and also a spatial filter can be applied to the octave bands which contain both noise and signal. The inverse WT, thus, can reconstruct the signal with noise suppressed. While a bandpass filter can not achieve such a result. The computation speed with the present version of the wavelet transform algorithm is not as fast as the conventional FFT algorithms. However, a fast wavelet transform algorithm (Mallat and Zhong, 1992) can be adapted to increase the computation speed for this application.

The above results (Figure 7.11a) are also compared with the f-k filtered data (Figure 7.11b). Significant improvement is clearly visible in the results produced by the new WT approach. The major reflection event at approximately 2.0 s is enhanced without significant artifacts and the outline of the reflection hyperbola is now further extended to the near offset region. The results of the WT processed shot gather is obviously superior to the f-k filtered one. The f-k filtered shot gather exhibits processing artifacts. Another point worth mentioning is that suppression of the ground roll using the WT is not limited by the geometry of field survey lines. Data from very crooked survey lines is not suitable for the f-k filtering approach to remove ground roll, however, it can be accepted by the WT approach.

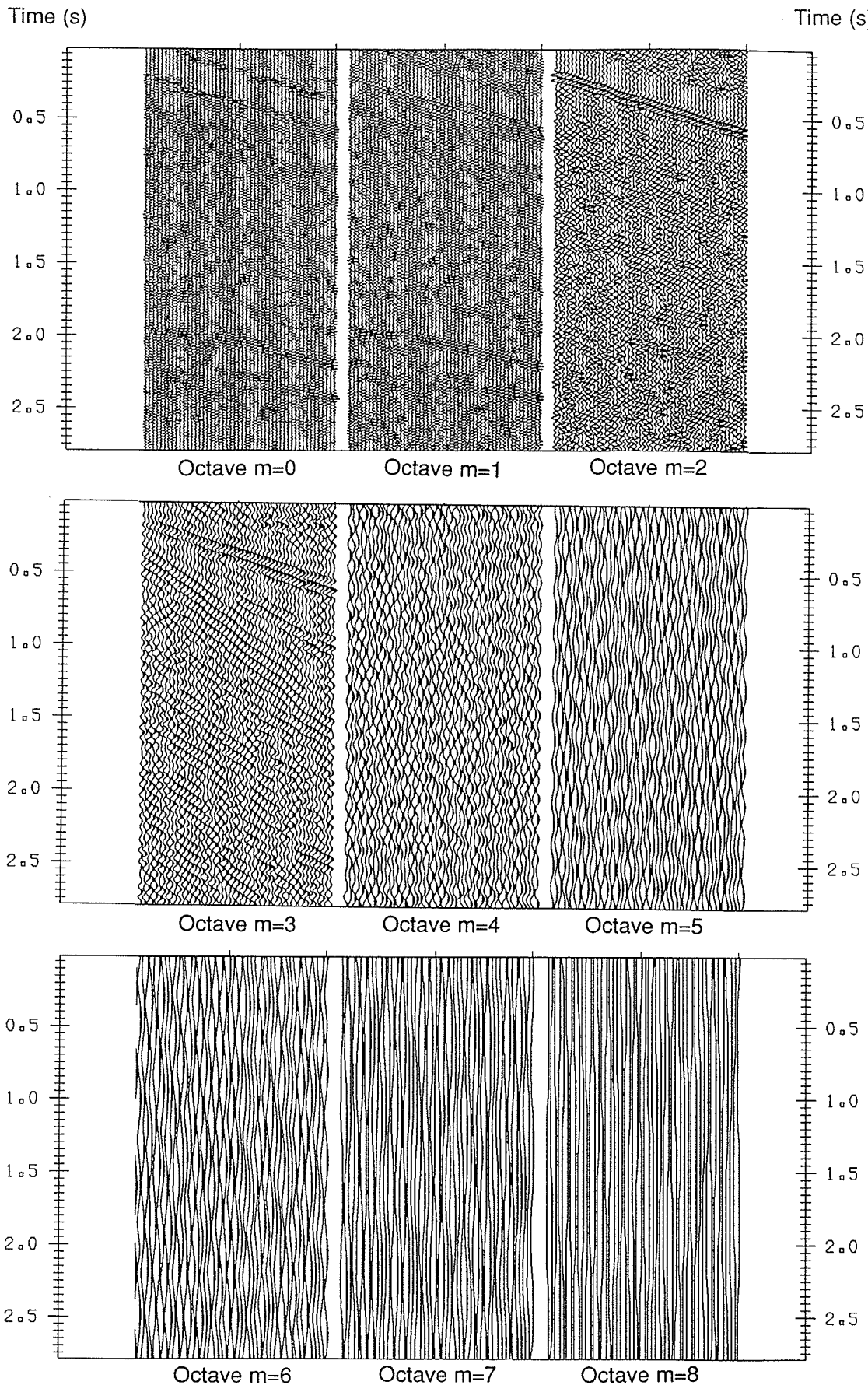

Figure 7.9: The wavelet transformed panels of the test shot gather shown in Figure 7.8. Every 4 octave bands are shown which correspond to m=0, 1, 2,...8 and N=0.

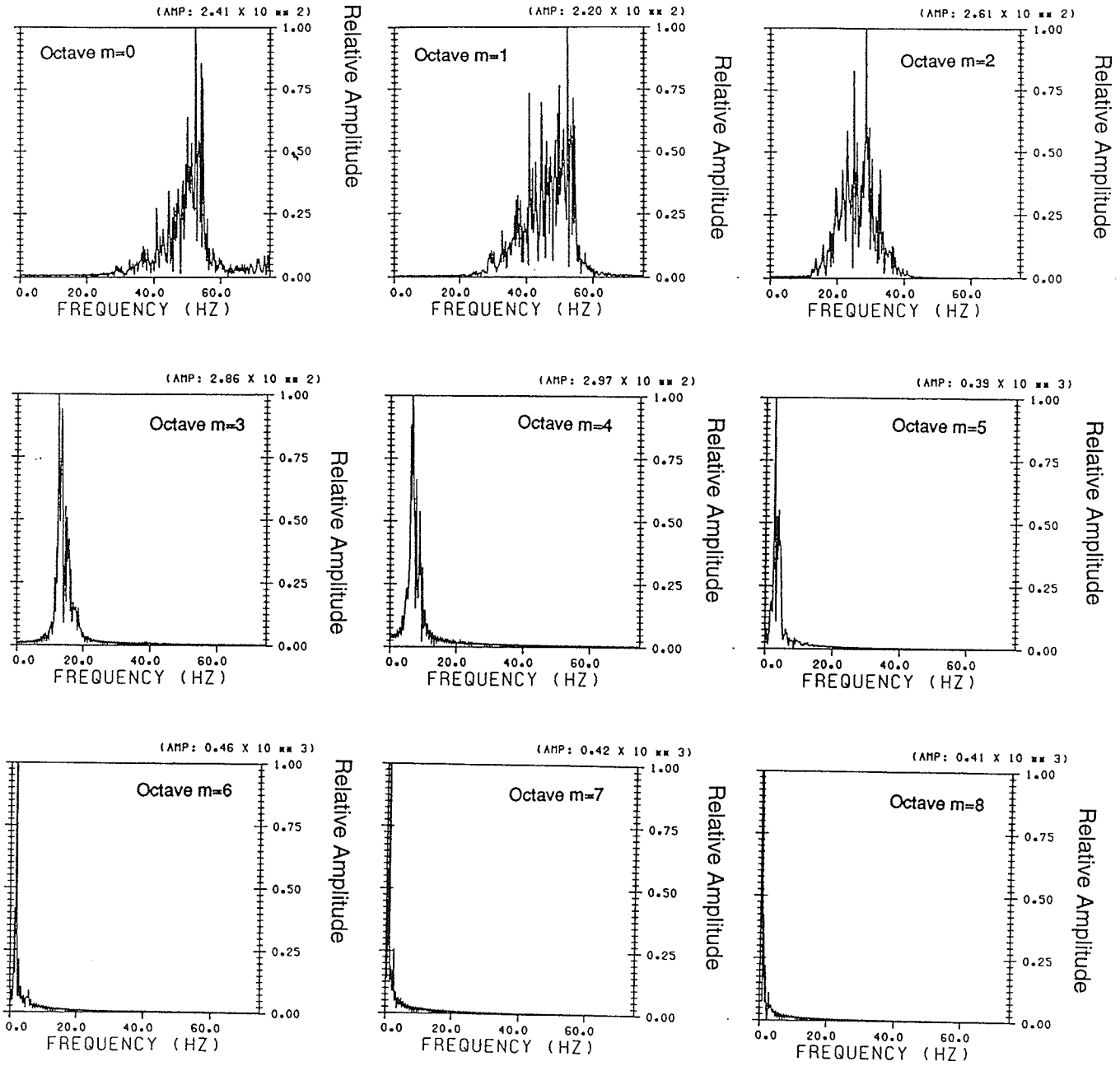

Figure 7.10: The corresponding Fourier spectra of the wavelet transformed panels shown in Figure 7.9.

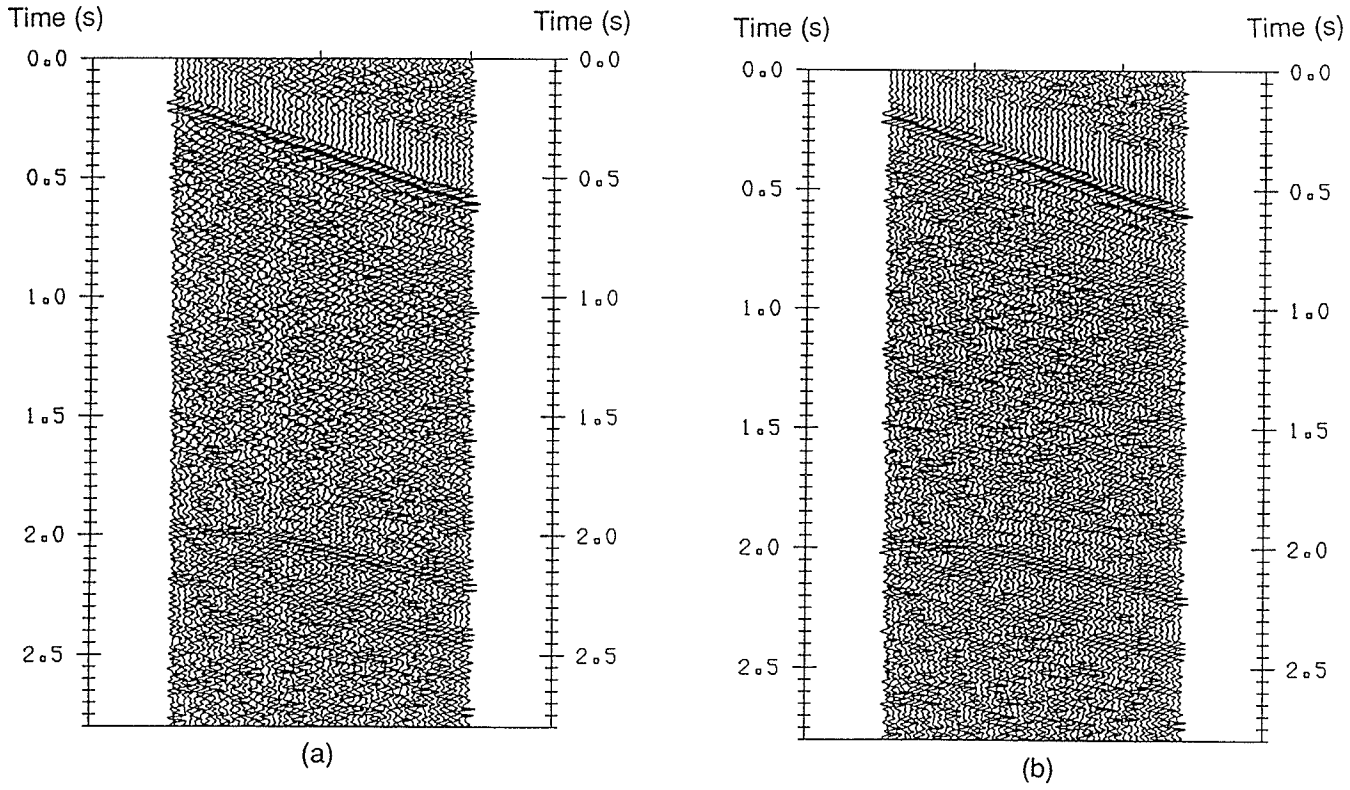

Figure 7.11: (a) Reconstruction of the shot gather by the inverse wavelet transform after removal of the bands containing the ground roll noise; (b) removal of ground roll noise using the f-k filtering technique.

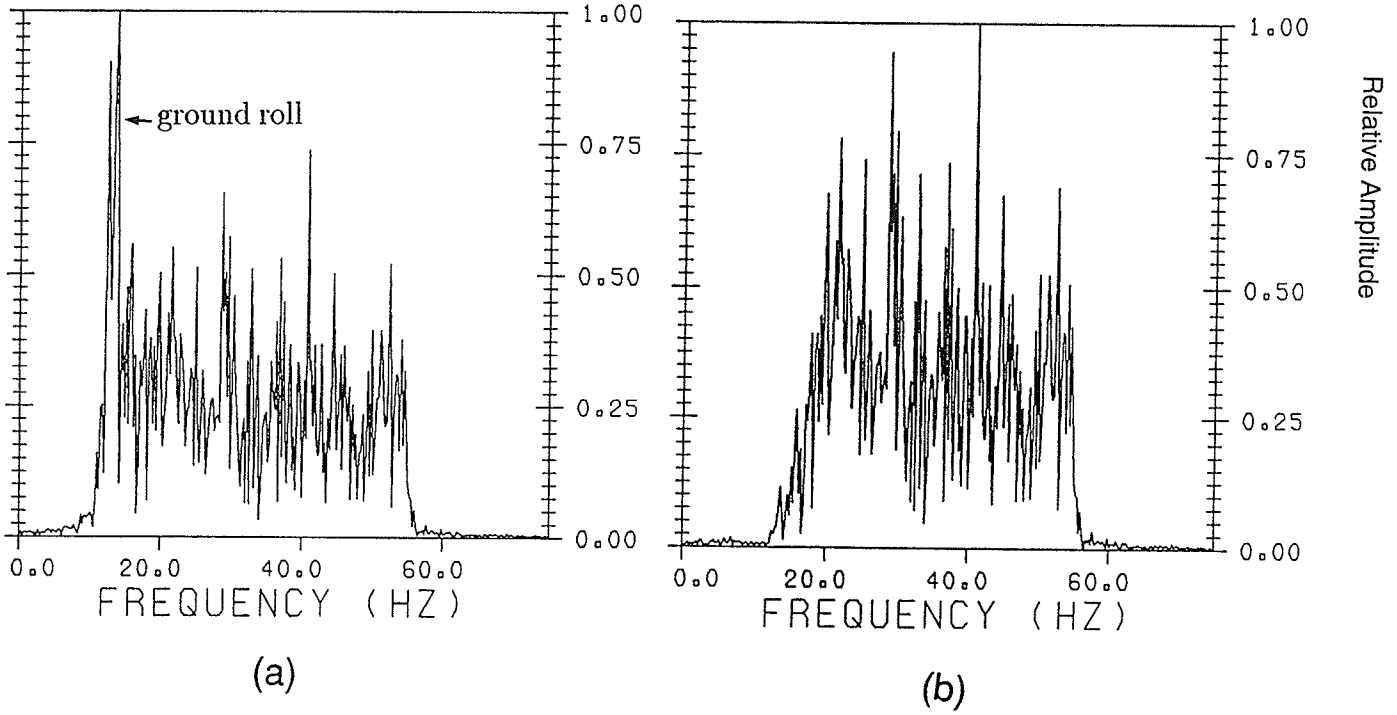

Figure 7.12: Spectrum of the reconstructed data using the inverse wavelet transform compared with the spectrum of the original data. (a) The spectrum of the original data; (b) the spectrum of reconstructed data having ground roll noise removed during the inverse wavelet transform.

7.3.3 Detection of Reflection Events

The characteristic of simultanuous time and frequency localization allows the WT technique used for detecting amplitude and phase discontinuity of a signal. The initial test was carried out with simple sinusoid waves. Figure 7.13a shows two decaying sinusoid waves s1(t), s2(t), and their summation s(t). The s1(t) and s2(t) have frequencies of 48 Hz and 55 Hz respectively. The s1(t) starts at 0.078 ms and ends at 0.924 ms, and the s2(t) starts at 0.098 ms and ends at 0.902 ms (Figure 7.13a). After summation, it is difficult to see when the signal s2(t) starts and it ends. The WT was tested to detect the arrival and ending times of the signals s1(t) and s2(t). Figure 7.13b shows the wavelet transformed result of the signal s(t). Four peaks in the Figure (7.13b) clearly mark the arrival and ending times of the original signal s1(t) and s2(t).

Further test was carried out with a synthetic seismogram modeling. The model is a two horizontal layers with a limited extent thin layer inserted between them. The velocities of the two layers are respectively 3550 m/s and and 3850 m/s, and the velocity of the thin layer is 3680 m/s, and the thickness is 8 m as shown in Figure 7.14a. A Ricker wavelet was used as the source wavelet and the receiver interval was 25 m. Seismic modeling was carried out using the modules in ITA INSIGHT 4.0 seismic processing software, and the synthetic traces are displayed in Figure 7.14b. From the data shown in Figure 7.14b, the effect of the thin layer across the section can be hardly identified and it is impossible to tell where the thin layer starts, pinch-out, or how thick the thin layer is. To detect the thin layer, the WT approach was tested. Figure 7.15 shows a corresponding wavelet transformed section of the synthetic

data in Figure 7.14b at octave band m=0. It is the the octave band having highest resolution. In this band, short wavelength discontinuities in the signal are detected. The starting and pinch-out points of the thin high velocity trapezoid can be easily identified. The corresponding four velocity discontinuity points are respectively at the offsets of -400m, -200m, 200m and 400m. With enlarged vertical scale, the two amplitude peaks corresponding to the reflections from upper and lower boundaries of the thin layer trapezoid can also be distinguished. This result suggests that the wavelet transform provides a powerful tool for multi-resolution analysis. The short wavelength discontinuities can be effectively detected in the high resolution octave band, while the long wavelength variations can be characterized in the low resolution octave band. The above tests suggest that the WT method can find wide applications in raising resolution for thin layer and fine structure exploration in the oil and gas field, even though more tests are certainly required to overcome the noise problem in real applications.

7.4 Summary

The WT can localize information in both time and frequency space simultaneously. It thus provides a potentially powerful technique for seismic data analysis and processing. Based on the preliminary analyses and tests with real seismic data, the following points can be summarized:

1. The WT provides an efficient sampling method, which has a higher sampling rate for high frequency information and lower sampling rate for low frequency components.

2. The WT critically depends on selection of the mother wavelet function. Cer-

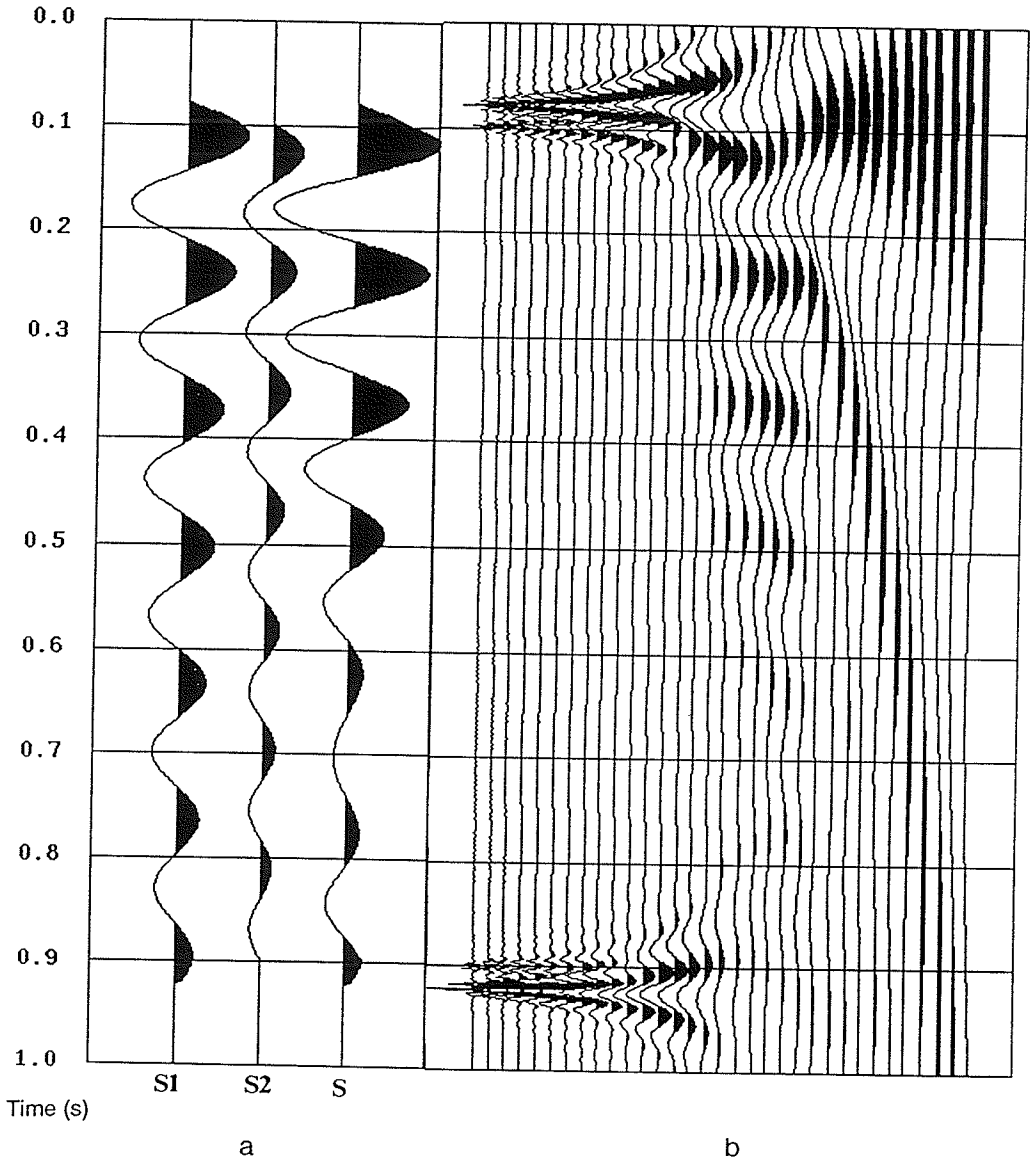

Figure 7.13: A test example showing detection of discontinuities using the wavelet transform: (a). decaying sinusoidal waves s1(t), s2(t) and their summation trace s(t); (b) the wavelet transform of the signal s(t).

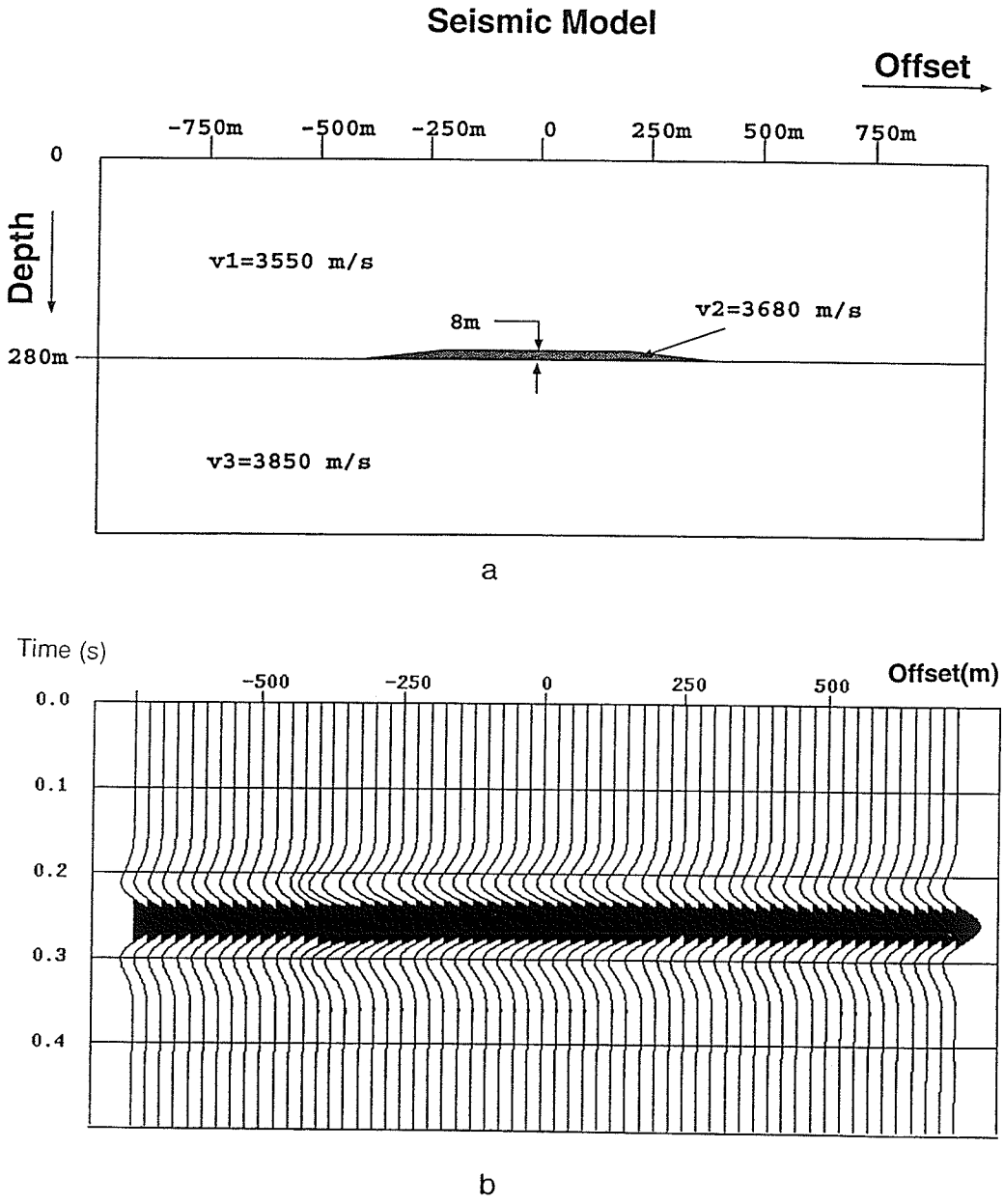

Figure 7.14: A synthetic seismic section and the geological model used for generating synthetic seismograms: (a) the velocity model; and (b) the synthetic seismic section.

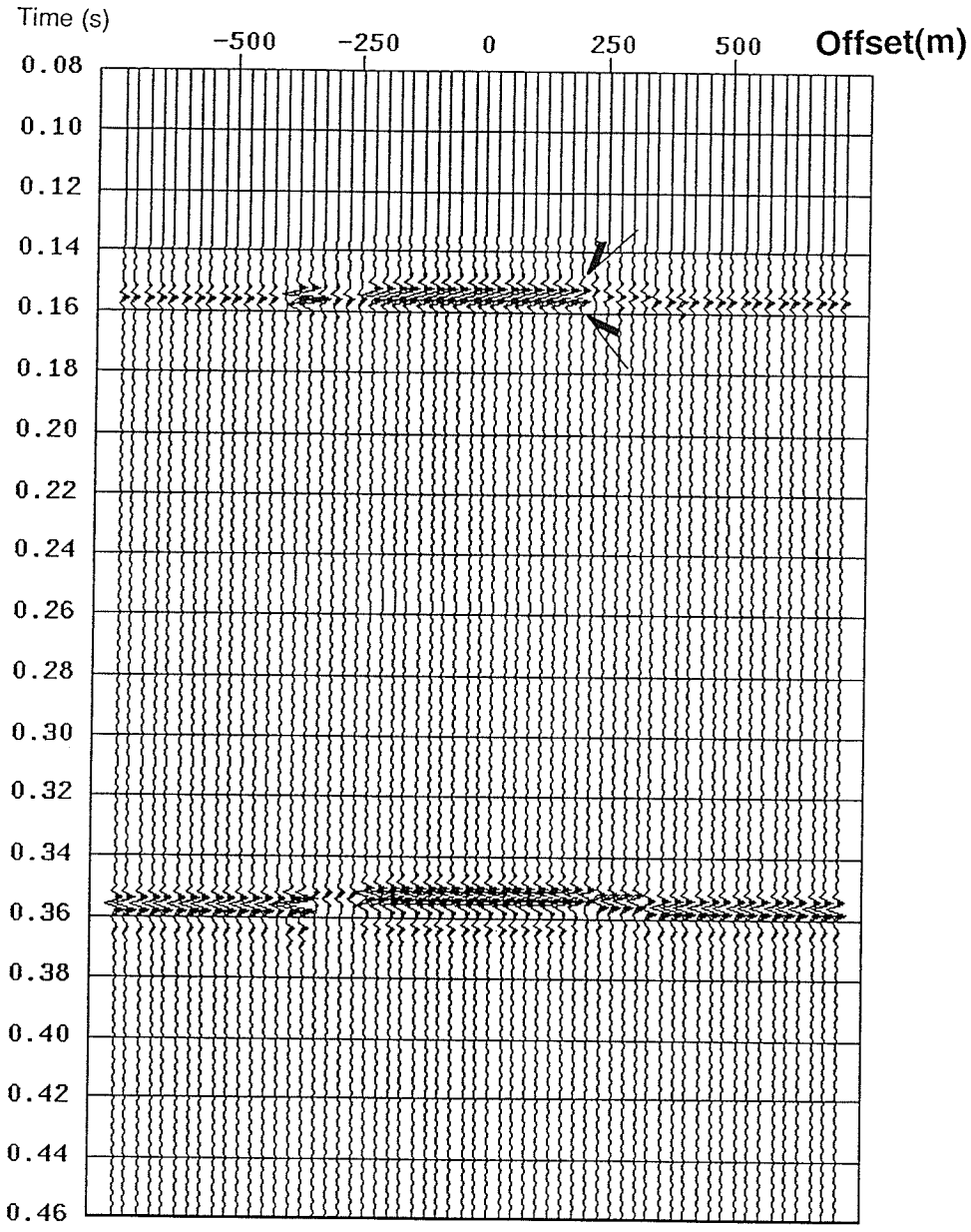

Figure 7.15: The highest octave band of the wavelet transformed data of the synthetic seismic section shown in Figure 7.14b.

tain wavelet functions which are compactly supported and well localized may not be orthogonal, whereas certain wavelet functions which are orthogonal may not be compactly supported. However, there exist wavelet functions that have both properties. For seismic application, the non-orthogonal Morlet wavelet provides a better choice due to its properties of good localization in the time and frequency space and lack of phase distortion, which, however, exists in the compactly supported orthonormal WT.

3. By representing and localizing signals in both time and frequency space simultaneously, the WT provides a new approach for time-dependent frequency analysis, which can make significant contributions in seismic data analysis, and detection and enhancement of reflection events.

4. After decomposition of seismic data by the WT, coherent signals, such as seismic reflections, refractions, air wave, and ground roll, can be identified in the time and frequency space panels, and unwanted coherent noise can be removed during the inverse WT. Both the direct WT and the WT - deconvolution methods tested in this paper were very effective in removing the ground roll noise without significant artifacts. The results are superior to the conventional $f - k$ filtering technique.

5. Application of the WT approach for detecting discontinuity shows that the WT provides a powerful technique for high resolution analysis which can be used for detecting short wavelength discontinuity effectively.

Even though the test results with seismic data are superior to other popular processing application results, further investigation will certainly broaden the theory and and application of the WT techniques in seismic data processing.

Chapter 8

Results, Interpretations and Discussions

The subsurface structures of Sudbury and the surrounding area were investigated in this thesis research by means of the seismic reflection, refraction, and VSP techniques. Considerable efforts were devoted and significantly new and interesting results were obtained. In the following sections, the overall results from each experiment are summarized.

8.1 Results of the Multi-offset VSP Experiment

The VSP technique provides specially valuable and detailed information on velocity structure and stratification of rocks and directly links the velocity information to lithology when well log information is available. The multi-offset three component VSP experiments carried out in Sudbury represents one of the first such experiment for crustal seismology research and the results can be summarized as follows:

(1) The $P-$ and S- wave interval velocity models obtained using the least squares

inversion approach provide the basic velocity information for the Chelmsford borehole, and correlate well with the well-log data. The horizontal component rotation processing has improved the accuracy of velocity estimation for the $S-$ wave. Based on the VSP data, the average $P-$ wave velocities are 5.99 km/s for the Chelmsford greywacke and 5.34 km/s for the Onwatin argillite, which are close to the laboratory measurements (Salisbury et al., 1994) of 5.91 km/s for the Chelmsford greywacke and 5.16 km/s for the Onwatin shale. The results of the VSP also indicate that the seismic velocity contrasts between different lithological unit are significant enough that the seismic technique can be very useful for both direct and indirect mineral exploration applications.

(2) The Radon transform wavefield separation technique has proved to be very effective for separating the upgoing wave from the downgoing wave. Application of a hyperbolic filter further improved the wavefield separation, and the vertical resolution of the primary reflection data was increased, especially for the near offset data. As the offset increases, which corresponds to the ray parameter diminishing, energy smearing between the upgoing and downgoing wave may happen. This is partially caused by the linear source approximation in the Radon transform implementation. Low and irregular acoustic impedance contrasts in the crystalline rock environment with complex geological structures and advanced reflection arrivals from reflectors dipping toward the borehole are also responsible for this energy smearing.

(3) From the flattened upgoing wavefields of P-wave and S-wave data, three reflection events from the depth levels at 160 m, 280 m and 380 m can be clearly identified. They are in close agreement with the lithological information obtained from the well log data. The reflector at the 160 m depth corresponds to an intrusion

(Figure 5.9c), which is probably a local feature near the borehole. The reflector at 280 m corresponds to the interface between different wack sequences in the Chelmsford formation, and the reflector at 380 m represents the lithological interface between the Chelmsford and Onwatin formations.

(4) The effectiveness of the CDP stack after VSP-CDP transform depends crucially on the preceding wavefield separation. In Chelmsford the VSP-CDP transformed VSP section has good correlation with the high-resolution surface reflection data at several deep horizons.

(5) The corridor-stacked P-wave VSP section is in excellent agreement with the interpreted surface high-resolution reflection data for the two major lithological contacts (Figure 5.16). The reflections from these two contacts can be consistently identified in both sections. They are located at the depths of about 380 m and 1240 m respectively and correspond to the lithological interfaces between the Chelmsford and Onwatin formations and between the Onwatin and Onaping formations.

(6) The hodogram analysis results based on the reflection events from the contact between the Chelmsford and Onwatin formations at an approximate depth of 380 m indicates that the geological contact dips toward southeast with an estimated true dip angle of 10.4^o.

(7) The WKBJ synthetic seismograms computed with the velocity models obtained in this experiment demonstrate remarkable similarities with the original VSP field records. This indicates that the velocity models obtained in this study represent near true subsurface velocity structure at the survey site, and has demonstrated that the synthetic seismogram modeling technique can provide an effective tool for true

amplitude wavelet analysis when the dip of the reflector is not too steep.

8.2 Results and Interpretation from Seismic Reflection Line 42

In contrast to the refraction, the seismic reflection technique images subsurface structures in greater detail due to its higher spatial resolution. Reprocessed line 42 reflection data using traditional and novel seismic data processing techniques has successfully imaged the quasi 3-D subsurface geological structures in the northwest of the Sudbury Basin. The results can be summarized as follows.

1. Careful design and implementation of the reprocessing steps using the traditional processing techniques, such as refraction statics correction, velocity analysis, and residual statics correction, along with the newly developed techniques, such as removal of the ground roll noise using the wavelet transform and time varying cross-dip correction, are shown to be essential for imaging of the true subsurface geological structures. The reprocessing effort has resulted in a significantly improved seismic image (Figure 6.19) compared to the preliminarily processed one (Figure 6.1). The result has provided valuable new information for the structural interpretation of the northwestern portion of the Sudbury Structure.

2. From the reprocessed seismic reflection line 42, three major reflection events can be identified.

LGC/Cartier Batholith Contact.- The contact between the LGC and granitic intrusions (AA' in Figure 6.20) is approximately a few kilometers north of the present location in the geological compilation map (Dressler, 1984), and has a in-line dip of

approximately $30^o - 35^o$ southeast. This result is consistent with the field structural mapping carried out by Fueten et al. (1992), who also indicated that the true location of the boundary is approximately 2 km north of the current geological map. The contact is not as coherent seismically as that of a sedimentary boundary in a seismic section due to the density variation in the LGC. The trend of the contact, however, can be clearly seen. Strong local reflection energy can be observed, which represent local high-amplitude reflections along the contact and within the LGC. The result of velocity analysis with the reflection data (Table 6.2) shows that the velocity of the LGC is very high. At the surface the velocity reaches 6.4 km/s It is much higher than that of the northern neighbouring area, where the surface velocity is only 5.9 km/s. The velocity variation clearly marks the petrological boundary between the high velocity LGC and the low velocity Cartier Batholith. The result of this velocity analysis is in good agreement with the velocity measurements which reported an average velocity of 6.5 km/s for the LGC (Salisbury et al., 1994). It is also compatible with the recent gravity model that assumed a very dense ($2.87g/cm^3$) LGC layer immediately underlying the SIC (McGrath and Broome, 1994).

However, in order to model the gravity anomalies associated with the Sudbury Structure and the surrounding area, an additional LGC layer with a density of $2.73g/cm^3$ was assumed to follow the dense LGC layer ($2.87g/cm^3$) and has a northward dipping boundary with the northern Cartier granitic rocks (McGrath and Broome, 1994) (see Figure 3.5). This is incompatible with the result from the reprocessed seismic section. The reprocessed result shows that the contact between the dense LGC and Cartier granite is dipping southeast, and no additional layer with density of $2.73g/cm^3$ lies between them. Instead, a major shear zone or fault, dipping

southeast, marked as R2 in the line 42 reflection profile (Figure 6.20), lies adjacent to the LGC/Cartier contact on the north side. From the surface exposure, the rock type between the LGC/Cartier granite contact and the reflection event R2 is the Cartier granitic intrusive rock, which has lower values in both seismic velocity and density.

A major shear zone or fault R2.- The newly discovered major southeast dipping reflection event R2 almost extends to the surface, which probably corresponds to the surface linear features of either F2 or F3 in the ERS-1 SAR image. The ERS-1 SAR image shows that F3 strikes northwest, which should correspond to a subsurface structure with southwest dip, and the other linear feature F2 strikes northeast and corresponds to a southeast dipping structure (Figure 6.21). Based on the cross-dip correction information, the reflection event R2 has an attitude of southeast dip. Thus it appears to correspond to the surface expression of F2. It is also possible that the reflection event R2 is a result of a later shallow tectonic event associated with the surface feature F2 in the SAR image superimposed on the earlier deep southeast dipping structure which originally has a surface expression associated with F3 in the SAR image.

Pumphouse Creek fault.- The Pumphouse Creek fault, which exists in the geological compilation map and clearly shows in the SAR image, appears in the reprocessed seismic section as an almost vertical shallow fault. The depth extension appears very limited.

3. The reprocessed seismic profile for the line 42 also indicates that the structure further north of the reflection event R2 (Figure 6.20) is quite different from that of the southern side. Whether this implies that the reflection event R2 represents the

last ring structure of the original basin structure remains to be investigated in the future.

4. One of the unusual features of the line 42 reflection profile is numerous scattered low frequency reflections marked as local high amplitude reflections. Does this relate to density variation of the LGC? Or does it represent some older rock trapped by later granite intrusion (xenoliths)? A probable geological interpretation could be that the older LGC was uplifted to surface with a wider areal extent than it is now, and was then intruded by the Cartier Batholith. The layer between the LGC/Cartier contact and the major shear zone or fault R2 appears to be the margin of the intrusion, and thus contains some trapped xenoliths of the LGC, which generate locally strong reflections.

The major fault or shear zone R2 should be investigated further and verified on surface by detailed field mapping. From a recent geological study, Card (1994) reported that there were two major ductile shear zones, or deformation zones, identified to the northwest of Sudbury. Figure 8.1 shows the schematic geological map prepared by Card (1994). The Benny deformation zone is located near the Cartier Batholith - Benny Greenstone Belt, and the other is found near the contact between the LGC and Cartier Batholith and it is called the Pumphouse Creek deformation zone. However the surface expression of R2 is a few kilometers north of the Pumphouse Creek deformation zone.

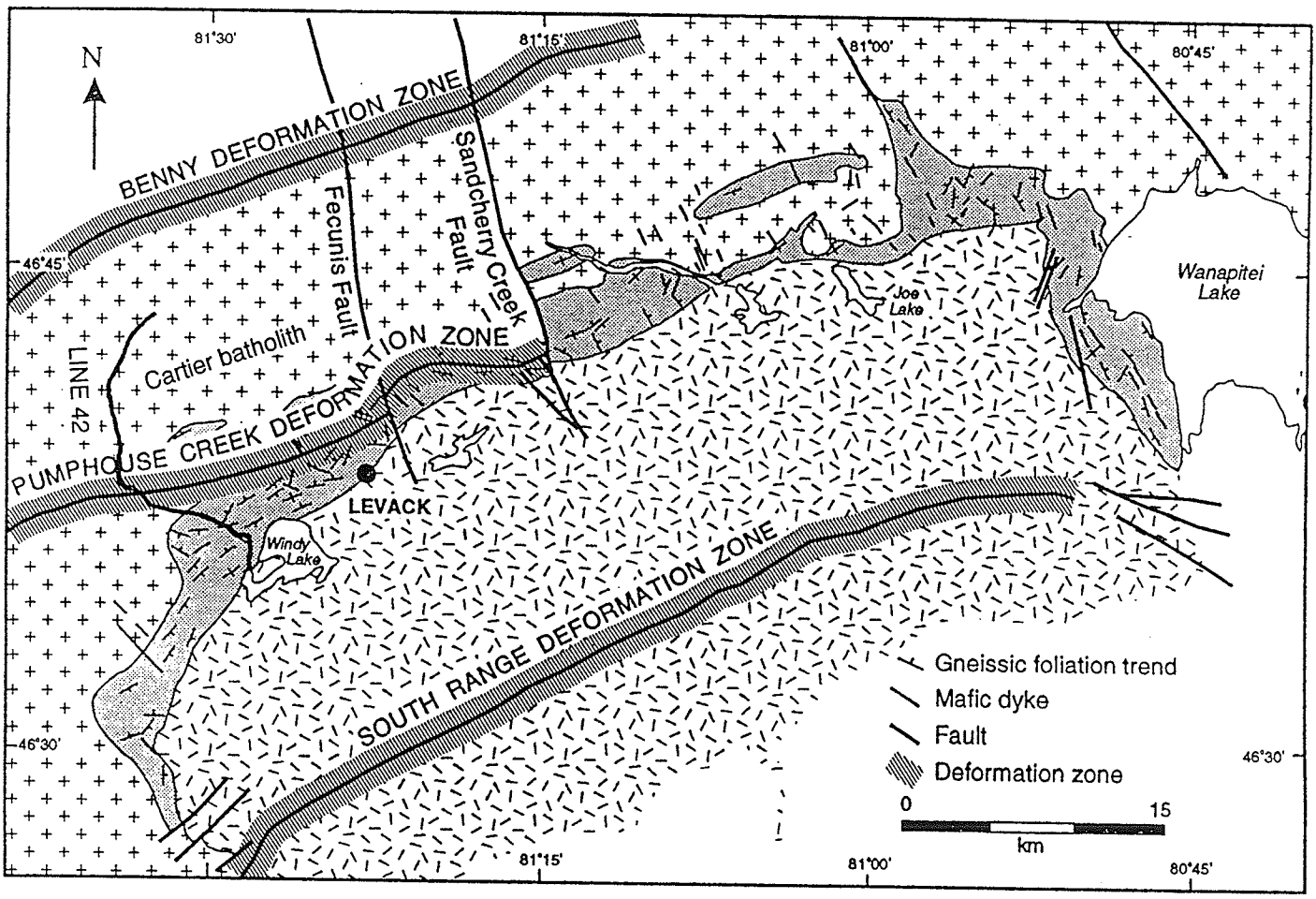

Figure 8.1: Geological map in the northwest of the Sudbury Basin after Card (1994). Three deformation zones are identified. The seismic reflection line 42 is also marked as a solid line in the figure.

8.3 Summary of the Theoretical Studies - the Wavelet Transform and the Time Varying Cross-dip Correction

To improve the quality of reflection images, two advanced seismic reflection data processing techniques were investigated theoretically and the algorithms were developed for seismic data processing applications. These new techniques were very successful with test data, and they played key roles in enhancing the reflection image of the LITHOPROBE seismic line 42 data. The results of the theoretical investigation may be summarized as follows:

1. The time varying cross-dip correction, a non-traditional processing technique, is a very effective technique for focusing reflection energy, especially for crooked line with complicated structures. By means of the cross-dip ray parameter analysis through slant stack scans, the optimum cross-dip ray parameters can be estimated and applied to the data for subsequent cross-dip corrections. The technique is flexible and applicable to data sets from various complex geological structures with consistent and/or inconsistent cross-dips at varying depths. It not only greatly enhances the seismic image, but also provides additional cross-dip information on the dipping reflectors for the final interpretation.

2. The wavelet transform (WT) is an advanced signal processing technique developed recently. By localizing information in the time and frequency spaces simultaneously, the WT provides a potentially powerful technique for seismic data analysis and processing. Successful application of the WT very much depends on the selection of the mother wavelet, from which a basis function can be constructed for

signal decomposition. There are two types of wavelet functions: orthogonal and non-orthogonal wavelet functions, thus the algorithms of the wavelet transform vary. The popularly developed wavelet functions are orthonormal and compactly supported, but do not have a finite impulse response and linear phase. For applications in exploration seismology, these properties are undesirable, especially when subsequent complex processing is required. Compactly supported non-orthogonal wavelets do not cause phase distortion after the transform, and thus provide a better choice for seismic data processing application.

3. Test application of the new WT approach in seismic data processing has proved that the WT technique is an effective method for removing coherent noise, such as ground roll. Since the ground roll noise has time and frequency characteristics that are distinct from the desired signals, it can be suppressed effectively through weighting of information content during the inverse WT. The method has also proved superior to the conventional $f - k$ filtering method (Figures 7.11 and 7.12). The WT can also be applied to detect hidden reflectors which are not discernible easily due to its capability of localizing information in both time and frequency spaces.

8.4 Regional Structure from the High Resolution Refraction

Since the number of available seismic profiles across the Sudbury Structure is very limited, the high resolution refraction data were preliminarily processed and described in the appendix B. Based on the ray tracing modeling of the high-resolution refraction data, a preliminary regional subsurface structure for the Sudbury Basin and the

surrounding area was obtained. It can be summarized as follows:

1. The refraction data interpretation being presented here is a preliminary result from the forward modeling, and no attempts were made for detailed velocity inversion processing.

2. Preliminary structural and velocity models along a northwest-southeast direction (line AB) and approximately west-east direction (line XY) crossing the the Sudbury Structure and the surrounding area were obtained by using Červený's two point dynamic ray tracing algorithm, which can handle both 2-D and 3-D laterally varying structures. The major structural units and velocity distribution in the area are outlined in the models shown in Figures B.11 and B.15. The computed travel times based on the preliminary models fit well with most observed refraction sections, which indicates that the preliminary model represents the major geological structures of the study area.

3. The first arrivals from the Moho discontinuity can be clearly identified from the refraction sections for the shots on the south side of the line AB, but they appear to be interrupted by dipping structures of the GFTZ and Britt domain for the shots on the north side of the line. However, the clearly observable wide-angle reflections from the Moho provide additional information. The results of modeling indicate that the Moho discontinuity is located at a depth of approximately 37 km in the Superior Province, north of the Sudbury Structure, and it is slightly dipping towards the southeast. When approaching the Grenville Province the Moho becomes as deep as 44 km. The velocity at the Moho discontinuity gradually varies from 8.06 to 8.24 km/s. The intermediate crustal discontinuity which produces pronounced refraction

waves is located at the depth of approximately 17-19 km.

4. There are a large numbers of shallow wide-angle reflections in the southern portion of the refraction sections. Four such events are interpreted as arising from the GFTZ and Britt domain dipping structures with approximate dip angles of 22.0^o for the Grenville Front and $8^o - 15^o$ for the remaining three reflectors. This is similar to the structural model obtained from the GLIMPCE refraction line J (Epili and Mereu, 1991). The GLIMPCE line J crosses the eastern boundary between the Southern and Grenville Provinces, which is shown in Figure B.1 and the crustal model of Epili and Mereu (1991) is shown in Figure B.3. The width of the GFTZ ranges from 34 to 40 km (at the surface it is 34 km) when projected onto the line AB.

5. The Sudbury Structure, located at the center of the Sudbury cross-array refraction lines, was modeled with a high velocity rhomboid-like block underlying near-surface slightly lower velocity media. The high velocity block was invoked by the near surface shallow strong reflections observed in several shots of line AB data (see Figures B.5a, B.6a, B.7a, B.8a), despite the shallow reflections appear not obviously observable in every shot of line XY data (without this high velocity block, the in advance arrivals of the near surface event can not be interpretated). The high velocity block has a length of about 35 km in the northwest-southeast direction and a width of approximately 80 km in the west-east direction. The block is dipping slightly toward southeast and lies at a depth range of approximately 4.5 km to 11.0 km (see Figures B.11 and B.15). Above the high velocity block the velocity varies from 5.9 km/s at the surface to 6.2 km/s at the top of the high velocity block boundary. This velocity is lower than in the surrounding area, which has the velocity of about 6.1 km/s near the surface. The average velocity within the Sudbury high velocity block

is 6.45 km/s. For the shot points located on both sides of this Sudbury high velocity block, the results of ray tracing fit very well with the observed travel times in each refraction section (see Figures B.6a, B.7a and B.8a).

The seismic velocity values for the new crustal model are compatible with the velocity and density measurement reported by Salisbury et al. (1994), who indicated that the SIC norite has a velocity value as high as 6.47 km/s and the LGC is as high as 6.5 km/s. Considering the average effect of the SIC (granophyre with 6.2 km/s and gabbro with 6.3 km/s) and the underlying LGC, an average velocity of 6.45 km/s of the Sudbury high velocity block can reasonably represents the velocity feature of the structure. The near surface slightly lower velocity distribution in the preliminary model is also supported by the velocity measurements, which report velocity values of 5.91 km/s for the Chelmsford greywacke and 5.16 km/s for the Onwatin shale (Salisbury et al., 1994). The new crustal model is also in agreement with the results from Sudbury LITHOPROBE reflection lines 41 and 42 (Milkereit et al., 1992; Miao and Moon, 1993), which suggested that the SIC and the underlying LGC are dipping southeast, and that the bottom boundary of the LGC is located at a depth range of 6-12 km. This is in the same depth range as the Sudbury high velocity block.

The results obtained in this thesis research are based on the ray tracing forward modeling approach and optimum traveltime matching between the observed and computed seismic sections for multiple shot data with other geophysical information obtained from previous studies being incorporated as constraints. The results, therefore, reflect the observed seismic data and are compatible with the geological and geophysical setting defined by the previous studies. However, for a refraction profile with multiple shots, it is difficult to obtain a perfect match between the calculated and

observed values using only the forward modeling method. The results are only for presenting a gross picture of the regional structures in the Sudbury area as it was initially intented.

Further detailed interpretation has to be carried out with finer structural units such as observable wide-angle reflection in the northern part of the line AB. A velocity inversion should be carried out to provide a more accurate velocity model. A 3-D model can also be derived by combining the present results with the fan shooting sections.

8.5 An Interpretation Model for the Sudbury Structure and Surrounding Area.

Based on the information obtained from the high-resolution refraction lines AB and XY and the reprocessed reflection line 42 along with the interpretation of the preliminarily processed reflection lines 40 and 41, a more complete structural model for the Sudbury Structure and the surrounding area can be derived.

Figure 8.2 shows such a model. The Sudbury Structure is located approximately 10 km north of the Grenville Front. A rhomboid-like high velocity zone ("Sudbury high velocity block") (90×60 km in the model) dipping slightly southeast is located at 4.5 - 11 km depth range and has an average velocity of approximately 6.45 km/s. The high velocity norite and gabbro in the SIC and the high density and velocity LGC underlying the SIC appears to be responsible for this anomalous block. Near the surface the velocity of the Sudbury Structure, in general, is slightly lower than the surrounding area, which is probably caused by the sediments of the Whitewater group

above the SIC. Beneath the Sudbury Structure, the intermediate crustal boundary is located at an approximately 17-19 km depth range. The depth of the Moho boundary is about 37 km in the Superior Province, however it increases to 44 km under the Grenville Province. The Grenville Front is a major intracrustal tectonic boundary and it has an attitude of about 22^o southeast dip along line AB profile. The structural trends below the GFTZ and the Britt domain dip southeast with dip angles varying from $8^o - 15^o$. The seismic velocity values in the GFTZ are generally higher than in the neighboring area to the north.

The detailed structure under the Sudbury Structure can be extended further north after inclusion of the information from line 42 (see Figure 8.3). The boundary between the LGC and Cartier Batholith is actually located a couple of kilometers north of the current location in the compilation map (The exact surface location of this contact must be verified by detailed field mapping). Unlike the interpretation in the recent gravity model (McGrath and Broome, 1994) the interface is dipping southeast at about $32^o - 35^o$. Immediately north of the LGC/Cartier Batholith boundary is probably a major fault or shear zone, which is located at approximately 7-9 km north of the boundary and also has an attitude of southeast dip. Further to the north, no structural trend can be traced from the available data.

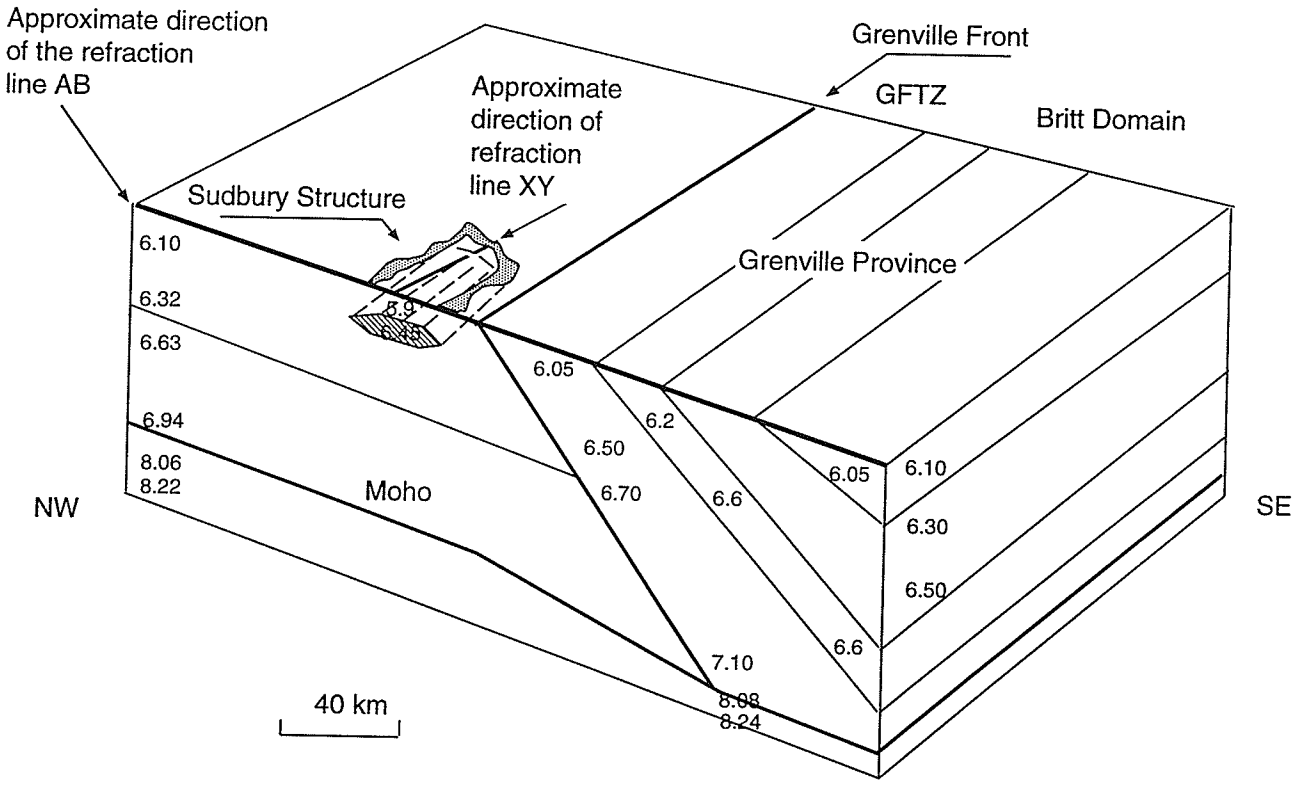

Figure 8.2: A schematic diagram of the velocity structure model for the Sudbury area based on interpretation of the LITHOPROBE seismic refraction and reflection data. The numbers represent $P-$ wave velocities (km/s).

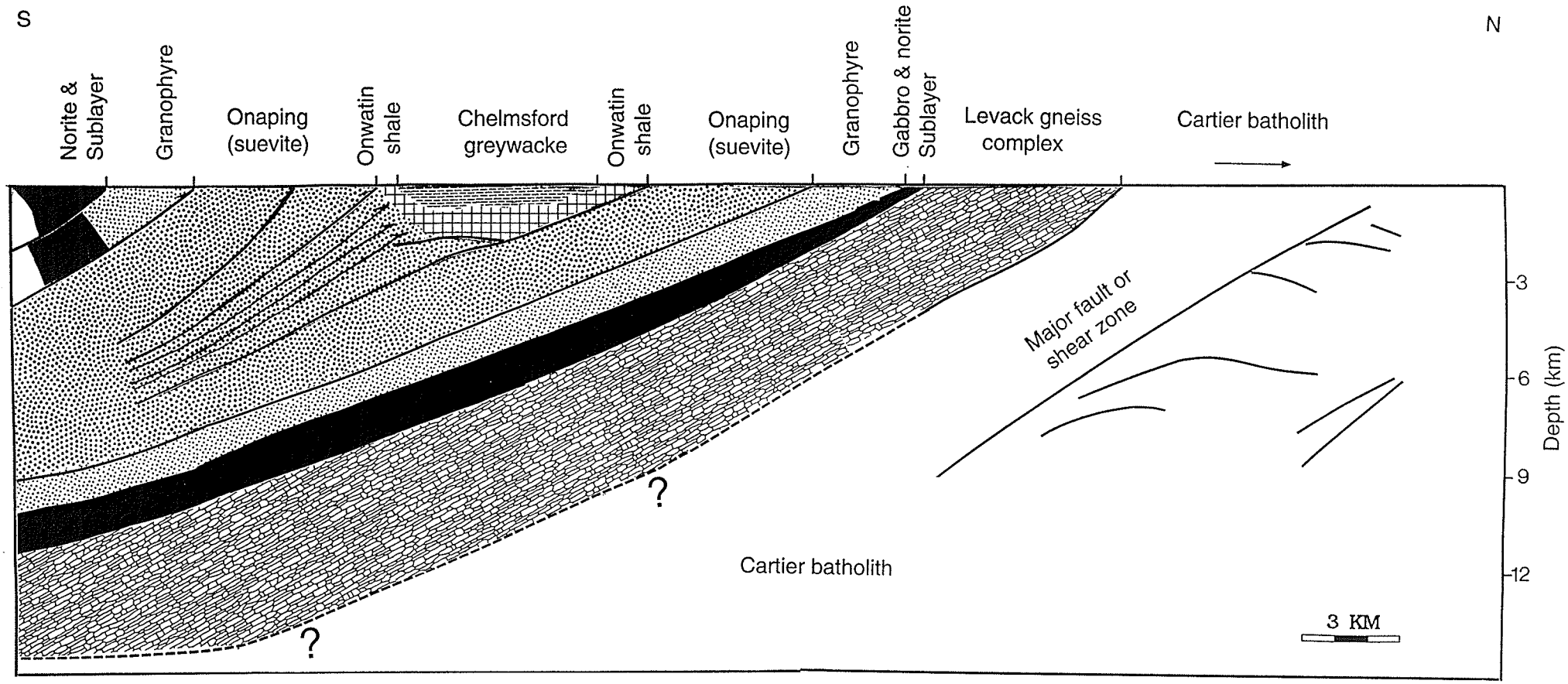

Figure 8.3: A cross-section of the interpreted structural model for the Sudbury Structure based on the LITHOPROBE seismic reflection and the multi-offset VSP results. The geometry in the south of the LGC is adapted from Wu et al. (1994).

8.6 Implication of the Seismic Results Related to the Origin of the Sudbury Structure

The semi-elliptical map pattern and the original size of the Sudbury Structure have been the focus of the debate with respect to the origin of the Sudbury Structure for many years. Advocates of the volcanic origin argue that the Sudbury Basin was never circular and no corresponding amount of impact melt sheet has been found in the Sudbury area which can satisfactorily explain the original size of impact crater (Muir, 1984; Peredery, 1984). The SIC was rejected as an impact melt sheet on the grounds that its volume relative to the size of the crater was in excess of that expected in the impact event (Dence, 1972; French, 1970).

Recently, Grieve (1991) indicated that by analogy with other terrestrial impact structures, the spatial distribution of shock features and Huronian cover rocks at the Sudbury Structure suggest that the transient cavity was in the range of 100 km in diameter. This places the original diameter of the final structure rim in the range of the 150-200 km with more circular shape. Theoretical calculation and empirical relationships indicate that the formation of an impact structure of this size will result in -$10^4 km^3$ of impact melt, more than sufficient to produce a melt body the size of the present SIC ($4 - 8 \times 10^3 km^3$) and the Onaping basal member. Thus a self-consistent argument was proposed which suggests an impact origin for both the Sudbury Structure and SIC. In reviewing the results from the LITHOPROBE Sudbury project and other recent studies, Deutsch and Grieve (1994) also concluded that the SIC is a coherent impact melt.

Nevertheless, by examination of the ERS-1 C-band radar imagery of the Sudbury

area along with follow-up fieldwork, Lowman (1992) pointed that the North Range and adjacent Superior Province show no evidence of pervasive compression directed to the northwest, as would be expected if the structure's present shape in plan view resulted from regional deformation. It was therefore concluded that the outline of the North Range is original (the original final structure rim of the impact crater? even though he did not directly indicate that), supporting the elliptical crater interpretation (Rousell, 1972). Lowman also suggested that the elliptical shape of the present structure may be understandable if an obliquely impacting body hit an active orogenic belt. Its unusual shape should no longer be cited as an argument against an impact origin (Lowman, 1992).

The line 42 reflection profile extends the subsurface structural image of the Sudbury area to an additional 20 km northwest. The results provide further evidence on the issue of the original dimensions. The reprocessed line 42 profile and interpreted seismic model (Figures 6.20 and 8.3) show that in spite of weak surface deformation as mentioned by Lowman (1992), there appears to be significant subsurface structural deformation outside the North Range, even in Levack township, including the reflection event R2 (a major fault or shear zone ?) and the adjacent reflection patterns (Figure 6.20). This reflection event has the same southeast dipping attitude as the main Sudbury structural trends. The surface intersection is fairly close to the location of final outer rim pointed by Gold (1980) (Figure 8.4). It is about 12-15 km from the north shore of the Windy Lake, where the line 42 survey line starts (Figures 4.1 and 6.20), and 7-9 km from the LGC/Cartier Batholith contact. This structural feature might have been caused by an impact event or the Penokean Orogeny. If the deformation outside the North Range including the newly imaged reflection features

is impact related, the original size of the impact should be considerably larger than the present size. Thus the result from this study supports a much larger dimension of the original crater proposed by Grieve and Deutsch (1991 and 1994).

However, the line 42 seismic profile is not sufficiently long and the geometrical construction alone can not resolve the problem. The original final outer rim and shape of the original impact crater are still open for debate. An extension of the reflection survey across the Cartier Batholith - Benny Greenstone deformation zone may help to determine the original size of the impact crater. A 3-D tomographic inversion with fan shots of the refraction lines AB and XY will also be useful and may provide important information on the subsurface structure in the northwest of the Sudbury Basin and the surrounding area.

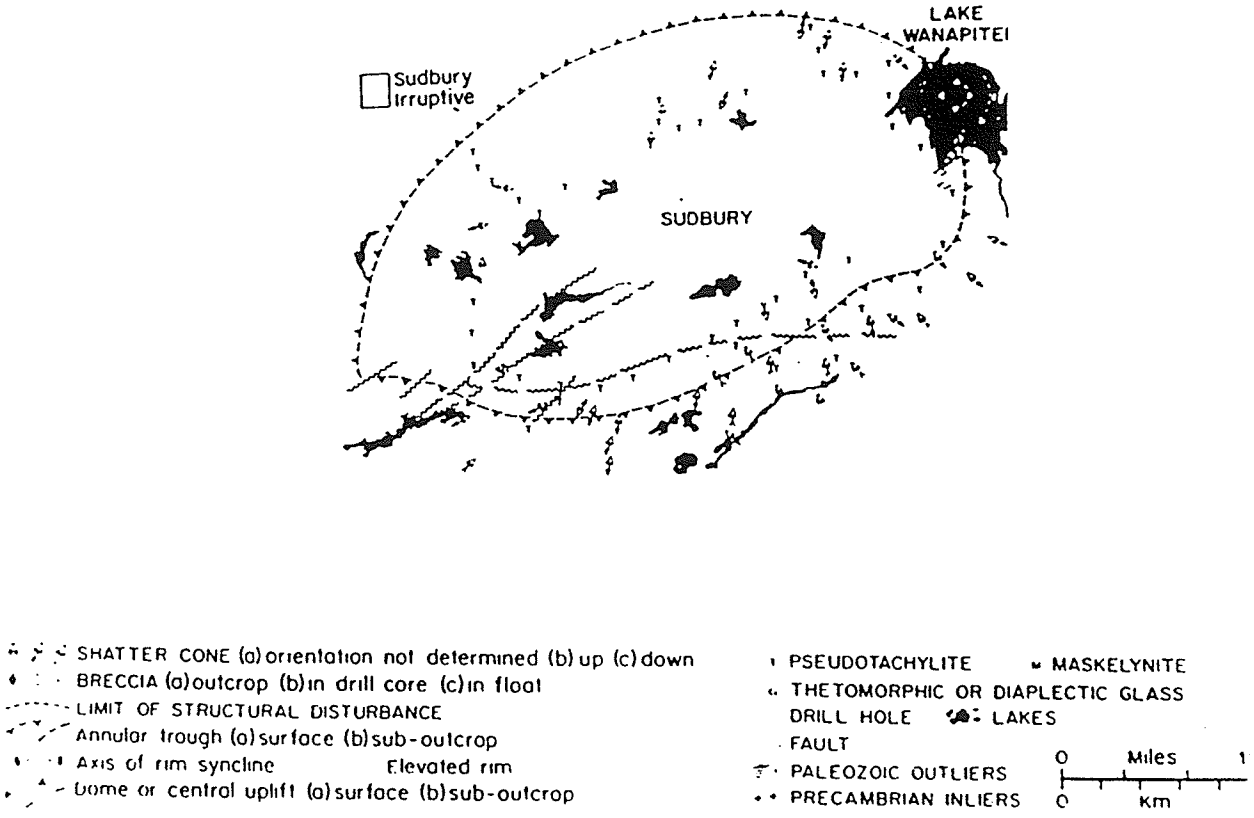

Figure 8.4: Shape, relative size, and distribution of shock deformation features of Sudbury Basin. Note that Sudbury irruptive diagram shows outline of inferred outer ring, not the Sudbury Igneous Complex, from Gold (1980).

Chapter 9

Conclusions

Since the discovery of extensive massive sulfide deposits in the Sudbury area in the late 1800's, continuous effort has been expended to determine the origin and configuration of this unique geological structure and associated unusually rich mineral deposits. Even though mapping and extensive drilling at many strategic sites have provided a much better understanding of the surface geology and stratigraphy of the structure, the origin of the structure remains enigmatic. Because the geometry of the Sudbury Structure can be closely tied to its origin, an integrated seismic study including seismic refraction, reflection and VSP experiments were carried out and interpreted in this thesis research, which provides valuable information for understanding this unique structure.

The high resolution refraction experiment, carried out in 1992 as a part of the LITHOPROBE AGT Sudbury Transect, explores a cross-array of two profiles that are approximately 285 km long in NW-SE direction and 170 km long in W-E direction, which provide major subsurface regional structures for the Sudbury Structure and the surrounding area. The preliminary results suggest that there exists a "Sudbury high

velocity block" with an average velocity of 6.45 km/s underlying a slightly low velocity media with respect to the surrounding regional velocity structures. The SIC norite and gabbro and the LGC appear to be responsible for this high velocity block, and the Whitewater sediments may be responsible for the overlying low velocity structure. The depth of the Moho boundary is about 37 km in the Superior Province but is as deep as 44 km under the Grenville Province. There is geological evidence that the Grenville Front overthrusted onto the Southern and Superior Provinces with a southeast dip of about 22^o near the Sudbury Structure. Further to the southeast, in the Grenville Front Tectonic Zone and Britt Domain of the Grenville Province, three southeast dipping structures are founded which appear to be responsible for the wide angle reflections (Figures B.9 and B.10).

Carefully designed traditional processing steps combined with advanced data processing techniques developed in this research has dramatically enhanced the seismic image of the Sudbury Transect line 42 regional reflection profile. With application of the time varying cross-dip correction, which greatly focuses reflection energy in complicated geological environments and the new wavelet transform approach, which effectively removed the ground roll noise, the reprocessed Sudbury regional reflection line 42 data successfully extends the reflection image of the Sudbury area to about 20 km further northwest. The profile has revealed the subsurface structural relationship between the LGC and the adjacent Cartier Batholith. The results indicate that the contact between the LGC and Cartier Batholith is actually a couple of kilometers north of the current position in the geological compilation map. It dips southeast in parallel with the general structural trend of the main Sudbury Structure. The LGC is about 5-8 km thick and has a relatively high velocity and density. Immediately

north of the LGC is the Cartier granite, which has a lower seismic velocity and is interrupted by a major fault or shear zone dipping southeast. The major fault or shear zone imaged in the north of LGC suggests that the structural deformation in the subsurface is stronger than the surface expressions, thus it partially supports a much larger original diameter of the final structure rim proposed by Grieve et al. (1991).

The time-varying cross-dip correction technique developed here is a very efficient method for focusing the seismic reflection energy in the complicated geological structures and crooked survey lines. It not only greatly enhances the seismic image, but also provides additional cross-dip information on the dipping reflectors for the final interpretation. The new signal processing technique, the wavelet transform, has proven to be a specially powerful technique for time-frequency analysis. The development carried out in the research for this thesis on the application of the wavelet transform should find wide applications in the future in seismic data processing and other signal processing fields. Further work on application of the wavelet transform, such as detection of nonstationary signals and laminate structures and suppression of coherent noises etc, should be continued in the future.

The VSP technique can play an important and complementary role in bridging the observational gap between surface seismic reflections and well-log surveys. The multi-offset VSP experiment carried out as part of this research has demonstrated that the integrated seismic study is useful not only in the interpretation of the shallow structural geological attitudes but also in accurate correlation of the reflecting interfaces with local lithological formations. The results indicate that the contacts between the Chelmsford and Onwatin formations and between the Onwatin and Onaping forma-

tions are respectively located at 380 m and 1240 m depths in the center of the basin. The hodogram analysis of the VSP data provides independent evidence for the dipping attitude of the Chelmsford/Onwatin contact. Correlation of the VSP velocity analysis with the well-log data suggests an average $P-$ wave velocity of 5.99 km/s for the Chelmsford greywacke, which is consistent with the velocity measurement in the laboratory from the drill core samples.

Most of the VSP data processing and interpretation techniques developed and implemented in this thesis research, such as the horizontal component rotation, travel time inversion for velocity analysis, combination of the hyperbolic filter with the Radon transform for wavefield separation the VSP-CDP transform, and particle motion hodogram analysis for estimating reflector dips are very effective. They should be very useful for processings of other VSP data sets from the crystalline rock terranes.

The results from this integrated seismic investigation of the Sudbury Structure have been very encouraging, and suggest that integrated seismic experiments can be very useful in exploring complicated geological structures such as the Sudbury Basin. It can provide both regional and detailed subsurface structures and help one to understand the origin and paleo-setting of the structures. The results of this thesis research suggest that application of seismic techniques in the mining area can be as effective and useful as in petroleum exploration.

References

Aki, I and Richards, P. G., 1980, Quantitative seismology Vol. I: W. H. Freeman and Co.

Asudeth, I., Spencer, C., Wetmiller, R., 1993, LithoSEIS user manual, Geological Survey of Canada open file report.

Avermann, M., Bischoff, L., Brockmeyer, P., Buhl, D., Deutsch, A., Dressler, B., Grieve, R.A.F., Lakomy, R., Müller-Mohr, V. and Stöffler, D., 1994, The Sudbury impact structure, Canada. (personal communication).

Barazangi, M. and Brown, L., 1986, Reflection seismology, A global prospective: AGU, Geodyn. Ser., 13.

Behrendt, J. C., Green, A. G., Cannon, W. F., Hutchinson, R. D., Lee, M. W., Milkereit, B., Agena, W. F., and Spencer, 1988, C., Crustal extension in the Midcontinuent Rift System: Results from GLIMPCE deep seismic reflection profiles: Geology, 16, 81-85.

Behrendt, J. C., Green, A. G., Cannon, W. F., Hutchinson, R. D., Lee, M. W., Milkereit, B., Agena, W. F., and Spencer, C., 1989, Crustal extension in the Midcontinuent Rift System: Results from GLIMPCE deep seismic reflection profiles over Lakes Superior and Michigan, *in* Properties and processes of earth's lower crust: Geophys. Monogr. Ser., 51, edited by Mereu, R. F., Mueller, S., and Fountain, D. M., 81-89, AGU, Washington D. C..

Behrendt, J. C., Hutchinson, D. R., Lee, M., Thornber, C. R., Trehu, A., Cannon, W. and Green, A., 1990, GLIMPCE seismic reflection evidence of deep crustal and upper-

mantle intrusions and magmatic underplating associated with the Midcontinuent Rift System of North America, Tectonophysics, 173, 595-615.

Berry, M. J. and Fuchs, K., 1973, Crustal structure of the Superior and Grenville Provinces of the northeastern Canadian Shield, Bull. Seismol. Soc. Am., 63, 1393-1432.

Boerner, D. E. and Milkereit, B., 1994, Introduction to the special section on the Lithoprobe Sudbury project: Geophys. Res. Lett., 21, 919-922.

Brysk, H. and McCowan, D. W., 1986, A slant stack procedure for point source data: Geophysics 51, 1370-1386.

Calvert, A. J. and Clowes R. M., 1990, Deep, high-amplitude reflections from a major shear zone above the subducting Juan de Fuca plate: Geology, 18, 1091-1094.

Card, K. D. and Hutchinson, R. W., 1972, The Sudbury Structure: its regional setting, *in* New developments in Sudbury geology, ed. Guy-Bray, J. V.: Geol. Assoc. Canada, special paper #10, 67-78.

Card, K.D., 1982. Progress report on regional geological synthesis, central Superior Province, *in* Current research, Part A.: Geological Survey of Canada, Paper 82-1A, 23-28.

Card, K. D., Gupta, V. K., McGrath, P.H., and Grant, F. S., 1984, The Sudbury Structure: its regional geological and geophysical setting, *in* The geology and ore deposits of the Sudbury Structure, in: Ontario Geological Survey, Special Volume 1, eds Pye, E. G., Naldrett, A. J., and Giblin, P. E., 26-41.

Card, K. D. 1994, Geology of the Levack Gneiss Complex, the northern footwall of the Sudbury Structure, Ontario, *in* Current Research (in press).

Červený, V., 1985, Ray synthetic seismograms for complex two-dimensional and three-dimensional structures: J. Geophys., 58, 2-26.

Červený, V., 1989, Synthetic body wave seismograms for laterally varying media containing thin transition layers: Geophys. J, Int., 99, 331-349.

Červený, V. and Pšenčik, I., 1984, SEIS83-Numerical modelling of seismic wave fields in 2-D laterally varying layered structures by the ray method, *in* Documentation of earthquake algorithms, Report SE-35, 36-40, ed. Engdahl, E. R.: World Data Center for Solid Earth Geophysics, Boulder.

Červený, V. and Ravindra, R., 1971, Theory of seismic head waves: University of Toronto Press, Toronto.

Chapman, C. H., 1978, A new method for computing synthetic seismogram: Geophys. J. Royal Astro. Soc., 54, 481-518.

Chapman, C. H. , 1981, Generalized Radon transform and slant stack: Geophys. J. Roy. Astr. Soc., 66, 445-453.

Chui, C. K., 1992, An introduction to wavelets: Wavelet analysis and its applications, Vol. 1: Academic Press, Inc, 54-60.

Claerbout, J. F., 1978, Snell waves: Stanford Exploration Project Report #15: Stanford University, 57-72.

Clowes, R. M., 1989, LITHOPROBE Phase III proposal, Submitted to NSERC and Geological Survey of Canada, 2-69–3-21.

Dahl-Jensen, T., 1989, Static corrections on crystalline rocks: Geophysical Prospecting, 37, 467-478.

Daubechies, I., Grossmann, and A., Meyer, Y., 1986, Painless nonorthogonal expansions: J. Math. Phys., 27, 1271-1283.

Daubechies, I., 1988, Orthonormal bases of wavelets: Communication on pure and Applied mathematics, XLI 909-996.

Daubechies, I., 1990, The wavelet transform, time-frequency localization and signal analysis: IEEE Transactions on Information Theory, 36, 961-1005.

Davies, J.F., M.V. Leroux, R.E. Whitehead, and W.D. Goodfellow, Oxygen-isotope composition and temperature of fluids involved in deposition of Proterozoic sedex deposits, Sudbury Basin, Ontario, Can. J. Earth. Sci., 27, 1299-1303, 1991.

Dence, M. R., , 1972, Meteorite impact craters and the structure of the Sudbury Basin, Special Paper Geol. Assoc. Can., 10, 7-18.

Dietz, R. S., 1964. Sudbury Structure as an astrobleme. J. Geology, 72: 412-434.

DiSiena, J. P., Gaiser, J. E., and Corrigan, D., 1981, Three-component vertical seismic profiles - orientation of horizontal components for shear wave analysis: 51st Ann. Internat. Mtg., Soc. Expl. Geophys., Tech. Paper S5.4, 1990-2011.

Dressler, B. O., 1984, Sudbury geological compilation; Ontario geological survey map 2491, Precambrian geology series. Scale 1:50000, geological compilation 1982-1983.

Dressler, B. O., 1984a, The effects of the Sudbury event and the intrusion of the Sudbury Igneous Complex on the footwall rocks of the Sudbury Structure, *in* The geology and ore deposits of the Sudbury Structure, eds. by Pye, E. G., Naldrett, A. J., and Giblin, P. E., Ontario Geological Survey, Special Volume 1, 97-136.

Dressler, B. O., 1984b, General geology of the Sudbury area, *in* The geology and ore

deposits of the Sudbury Structure, eds. by Pye, E. G., Naldrett, A. J., and Giblin, P. E.: Ontario Geological Survey, Special Volume 1, 58-82.

Deutsch, A. and Grieve, R. A. F., 1994, The Sudbury Structure: constraints on its genesis from Lithoprobe results.: Geophys. Res. Lett., 21, 963-966.

Embree, P., Burg, J. P., and Backus, M. M., 1963, Wide-band velocity filtering - the pie slice process: Geophysics, 28, 948-974.

Epili, D. and Mereu, R. F., 1991, The Grenville Front Tectonic Zone: Results from the 1986 Great Lakes onshore seismic wide-angle reflection and refraction experiment: J.G.R., 96, 16335-16348.

Farrell, R. C. and Euwema, R. N., 1984, Refraction statics: Proc. IEEE, 72, 1316-1329.

Farrart, B. E., Basu, A. R., and Tatsumoto, M., 1985, Origin of the Sudbury complex by meteoritic impact: Neodymium isotopic evidence: Science, 230, 436-439.

Feauveau, J., 1992, Non-orthogonal multiresolution analysis: *in* Wavelet analysis and its applications, ed. by Chui, C. K., New York.

French, B. M., 1970, Possible relations between meteorite impact and igneous petrogenesis, as indicated by the Sudbury Structure, Ontario, Canada, Bull. Volcanol., 34(2), 466-517.

French, B. M., 1972, Shock-metamorphic features in the Sudbury Structure, Ontario: *in* New developments in Sudbury geology, ed. by Guy-Bray, J. V., Geological Association of Canada, Special paper 10, 19-28.

Fueten, F., Seabright, R. and Morris, B., 1992. A structural transect across the

Levack Gneisses - Cartier Batholith Complex, northwest of the Sudbury Structure: LITHOPROBE Abitibi-Grenville project workshop, Montreal, Canada.

Gibb, R. A., Thomas, M. D. Lapointe, P. L. and Mukhopadhyay, M., 1983, Geophysics of proposed Proterozoic sutures in Canada, Precambrian Res., 19, 349-384.

Gold, D. P., 1980, Structure geology, *in* Remote Sensing in Geology, eds. by Siegal B. S. and Gillespie, A. R., 419-484, John Wiley, New York.

Goupillaud, P., Grossmann, A. and Morlet J., 1984, Cycle-Octave and related transforms in seismic signal analysis: Geoexploration, 23, 85-102.

Grant, F. S., and West, G. F., 1965, Interpretation theory in applied geophysics, McGraw-Hill Press, 134-138.

Green, A. et al., 1988, Crustal Structure of the Grenville front and adjacent terranes, Geology, 16, 788-792.

Green, A., Cannon, W. F., Milkereit, B., Hutchinson, D. R., Davison, A., Behrendt, J. C., Spencer, C., Lee, M. W., Morel-a-l'Huissier, and Agena, W. F., 1989, A "GLIMPCE" of the deep crust beneath the Great Lakes, *in* Properties and processes of earth's lower crust, Geophys. Monogr. Ser., 51, eds. by Mereu, R. F., Mueller, S., and Fountain, D. M., 81-89, AGU, Washington D. C..

Green, A. G., Milkereit, B., Percival J., Davison, A., Parrish, R., Cook, F., Geis, W., Cannon, W., Hutchinson, D., West, G., and Clowes, R., 1990, Origin of deep crustal reflections: seismic profiling across high-grade metamorphic terranes in Canada: Tectonophysics, 173, 627-638.

Grieve, R. A. F., Stöffler, D. and Deutsch, A., 1991. The Sudbury Structure: controversial or misunderstood? J. Geophys. Res., 96, 22753-22764.

Gupta, V. K., Grant, F. S. and Card, K. D., Gravity and Magnetic characteristics of the Sudbury Structure: *in* The Geology of Ore Deposits of the Sudbury Structure, eds. by Pye, E. G., Naldrett, A. J., and Giblin, P. E.: Ontario Geological Survey, Special Vol. 1, 381-410

Hardage, B. A., 1983, Vertical seismic profiling, part A, principles: Geophysical Press, London–Amsterdam, 307-315.

Head, J. W., 1977, Origin of outer rings in lunar multi-ringed basins, *in* Impact and explosion cratering, eds. by Roddy, D. J., Pepin, R. O. and Merrill, R. B., Pergamon Press, 563-574.

Hearst, R., Morris, W. and Thomas, M., 1994, Magnetic interpretation along the Sudbury Structure Lithoprobe Transect: Geophys. Res. Lett., 21, 951-954.

Irving, R. et al., 1993, 1992 LITHOPROBE Abitibi-Grenville seismic refraction survey: acquisition and processing report: LITHOPROBE report #30.

IT&A, 1992, INSIGHT-4.0 processing package: Calgary.

Jackson, S. L., Sutcliffe, R. H., Ludden, J. N., Hubert, C., Green, A. G., Milkereit, B., Mayrand, L., West, G. F., and Verpaelst, P., 1990, Southern Abitibi greenstone belt: Archean crustal structure from seismic-reflection profiles: Geology, 18, 1086-1090.

James, R. S. and Dressler, B. O., 1992. Nature and significance of the Levack Gneisses Complex - Footwall rocks of the North and East Ranges of the Sudbury Igneous Complex: The Canadian Mineralogist, 30, 487-488.

Kappus, M. E., Harding, A. J. and Orcutt, J. A., 1990, A comparison of tau-p transform methods: Geophysics, 55, 1202-1215.

Kelamis, P. G.and Mitchell, A. R., 1989, Slant stack processing: First Break, 7, 21-24.

Kim, J., Moon, W. M., Percival, J. A. and West, F. G., 1992, Seismic imaging of shallow reflectors in the eastern Kapuskasing structural zone with correction of crossdip attitudes: Geophys. Res. Lett., 19, 2035-2038.

Klemperer, S. L., and the BIRPS group, 1987, Reflectivity of the crystalline crust: hypotheses and tests: Geophys. Int. Res. Astro. Soc., 89, 217-222.

Larner, K. L., Gibson, B. R., Chambers, R., and Wiggins, R. A., 1979, Simultaneous estimation of residual static and crossdip correction: Geophysics, 44, 1175-1192.

Li, X.-Y. and Crampin, S., 1993, Linear-transform techniques for processing shear wave anisotropy in four component seismic data: Geophysics, 58, 240-256.

Lowman, P. D. Jr., 1992, The Sudbury Structure as a terrestrial mare basin: Reviews of Geophysics, 30, 227-243.

Lowman, P. D. Jr., Masuoka, P. M. and Singhroy, V. H., 1993. Original dimension of the Sudbury Structure, Ontario: New evidence from ERS-1 radar images and supporting field work, submited for proceedings of international conference on large meteorite impacts and planetary evolution, Sudbury, Ontario.

Lumbers, S. B., 1978, Geology of the Grenville Front Tectonic zone in Ontario, *in* Toronto'78, Field trips guide book, ed. by Currie, A. L. and Mackasey, W. O., Geol. Asso. Canada, St. John's Newfoundland, 347-361.

Lűschen, E., Sőllner, W., and Hohrath, A., 1991, Integrated P- and S- wave borehole experiments at the KTB-deep drilling site in the Oberpfalz area: Geodynamics Series, 22.

Mallat, S. G., 1989, A theory of multiresolution signal decomposition: the wavelet representation: IEEE pattern Anal. Machine Intell., 11, 674-693.

Mallat, S. G. and Zhong S., 1992, Characterization of signals from multiscale edges: IEEE pattern Anal. Machine Intell., 14, 710-732.

McGrath, P. H. and Broome, H. J, 1994, A gravity model for the Sudbury Structure along the LITHOPROBE seismic line: Geophys. Res. Lett., 21.

Mereu, R. F. and Jobidon, G., 1971, A seismic investigation of the crust and Moho on a line perpendicular to the Grenville Front, Can. J. Earth, Sci., 8, 1553-1583

Mereu, R. F., Wang, D. , Kuhn, O., Forsyth, A., Green, A. G., 1986, The 1982 COCRUST seismic experiment across the Ottawa-Bonnechere graden and Grenville Front in Ontario and Quebec, Geophys. J. R. Astro. Soc., 84, 491-514.

Messfin, D. and Moon, W. M., 1984, Seismic approaches for structural studies of the Sudbury Basin: Geophysics, 49, 1675-1689.

Meyer, Y., 1985-1986, Principe d'incertitude, bases hilbertieness et algèbres d'opérateurs, Séminaire Bourbaki, 662.

Miao, X. and Moon, W. M., 1993, Improvement of signal/noise ratio using the wavelet transform: the Can. Soc. Expl. Geophys., ann. Convention, Calgary, Canada.

Miao, X., Moon, W. M. and Milkereit, B., 1994, Three component vertical seismic profiling (VSP) experiment in the Sudbury basin: Geophys. Res. Lett., 21, 939-942.

Miao, X., Moon, W. M. and Milkereit, B., 1994a, Application of the multi-offset Vertical Seismic Profiling (VSP) experiment in the Sudbury basin: Geophysics, (in press).

Miao, X., Moon, W. M. and Milkereit, B., 1994b, Seismic imaging of the Levack Gneiss Complex, in the northwest of the Sudbury: Can. Geophys. Union, Ann. Convention, Banff, Canada.

Mike, W., 1990, Basalts, water, or shear zones in the lower continental crust? Tectonophysics, 173, 163-174.

Milkereit, B., Green A. G. and the Sudbury working group, 1992. Deep geometry of the Sudbury Structure from seismic reflection profiling. Geology, 20: 807-811.

Milkereit, B., Percival, J. A., White, D., Green. A. and Salisbury, M. H., 1991, Seismic reflectors in the high-grade metamorphic rocks of the Kapuskasing uplift: results of preliminary drill site surveys: Geodynamics, 22, 39-45.

Milkereit, B., Epili, D., Green, A., and Morel-a-l'Huissier, P., 1990, Migration of wide-angle seismic reflection data from the Grenville Front in Lake Huron: J.Geophys. Res., 95, 10987-10988.

Milkereit, B., Green, A., Morel-a-l'Huissier, P., Lee, M. W., Agena, W. F., 1988, Great Lakes seismic reflection survey migrated data: Geol. Surv. of Can., Open File Report, 1592, 33, Ottawa, Ont.

Moeckel, G. P., 1986, Moveout correction, bin and stack of offset VSP reflection data: 56th ann. internat. Mtg., Soc. Expl. Geophys., Expanded Abstracts, 568-572.

Moon, W. M., Carswell, A. and Owusu, J., 1985, A Final report on the Use of Vertical Seismic Profiling (VSP) in Detecting Subsurface Fracture Zones within a Granite Batholith. Publication No. 107, Center for Precambrian Studies, University of Manitoba.

Moon, W. M., Carswell, A., Tang, R., and Dilliston, C., 1986, Radon transform wave field separation for vertical seismic profiling data: Geophysics, 51, 940-947.

Moon, W. M., Serzu. M., and Krause, B., 1989, High resolution reflection seismic experiment in the North Range of Sudbury Basin: Geophysics Technical Report, #11, the University of Manitoba, 1-125.

Morlet, J., Arens, G., Fourgeau, E., and Giard, D., 1982, Wave propagation and sampling theory - Part II: Sampling theory and complex waves: Geophysics, 47, 222-236.

Muir, T. L., 1984, The Sudbury Structure: considerations and models for an endogenic origin, *in* The geology and ore deposits of the Sudbury Structure, eds. by Pye, E. G., Naldrett, A. J., and Giblin, P. E.: Ontario Geological Survey, Special Volume 1, 234-251.

Naldrett, A. J., Rao, B. V., and Evensen, N. M., 1986, Contamination at Sudbury and its role in ore formation, *in* Metallogeny of basic and ultrabasic rocks: London, Institute of Mining and Metallogeny, 75-91.

Papoulis, A., 1962, The Fourier integral and its applications: McGraw-Hill, New York.

Peredery, W. V. and Morrison, G. G., 1984, Discussion of the origin of the Sudbury Structure, *in* The geology and ore deposits of the Sudbury Structure, eds. by Pye, E. G., Naldrett, A. J., and Giblin, P. E.: Ontario Geological Survey, Special Vol. 1, 490-512.

Popelar, J., 1972, Gravity interpretation of the Sudbury area, *in* New development in Sudbury geology, ed. by Guy-Bray, J. V.: Geol. Assoc. Can., Special paper, 11,

103-115.

Pye, E. G., Naldrett, A. J., and Giblin, P. E., eds, 1984. The Geology and ore deposits of the Sudbury Structure: Ontario Geological Survey, Special Vol 1: 25-37.

Rector III, J. W., 1988, Acquisition and preliminary analysis of oriented multi-component multioffset VSP data: Dosecc Cajon pass deep scientific drillhole: Geophys. Res. Lett., 15, 1061-1064.

Roest, W. R. and Pilkington, M., 1994, Restoring post-impact deformation at Sudbury: A circular argument: Geophys. Res. Lett., 21, 959-962.

Ronen, J. and Claerbout, J. F., 1985, Surface-consistent residual statics estimation by stack-power maximization: Geophysics, 50, 2759-2767.

Rousell, D. H., 1972, The Chelmsford formation of the Sudbury Basin-a Precambrian turbidite, *in* New developments in Sudbury Geology, ed. by Guy-Bray, J. V.: Geological Association of Canada, Special Paper 10, 79-91.

Rousell, D.H., 1984, Onwatin and Chelmsford formation, *in* The geology and ore deposits of the Sudbury Structure, eds. by Pye, E. G., Naldrett, A. J., and Giblin, P. E.: Ontario Geological Survey, Special Volume 1, 213-217.

Salisbury, M. H., Iuliucci, R., and Long, C., 1994, Velocity and reflection structure of the Sudbury Structure from laboratory measurements: Geophys. Res. Lett., 21, 923-926.

Seeman, B. and Horowicz, L., 1983, Vertical seismic profiling: Separation of upgoing and downgoing acoustic waves in a stratified medium: Geophysics, 48, 555-568.

Shanks, W. S. and Schwerdtner, W. M., 1991a. Structural analysis of the central and

southwestern Sudbury Structure, Southern Province, Canadian shield: Can. J. Earth Sci., 28, 411-430.

Shanks, W. S. and Schwerdtner, W. M., 1991b. Crude quantitative estimates of the original northwest-southeast dimension of the Sudbury Structure, south-central Canadian shield: Can. J. Earth Sci., 28, 1677-1686.

Sheng, Y. and Szu, H. H., 1992, Optical wavelet transform: Optical Engineering, 31, 1840-1845.

Sheriff, R. E. and Geldart, L. P., 1986, Data-Processing and interpretation, in Exploration seismology, Vol. 2: Cambridge University Press, New York.

Singh, V., Moon, W. M., Singhroy, V., and Slaney, R. V., 1993. Preliminary studies of airborne multi-sensor geophysical data from Sudbury, Ontario: Can. J. Remote Sensing, 19, 160-169.

Stevenson, J. S. and Stevenson, L. S., 1980, Sudbury, Ontario, and the Meteorite theory: Geosciece Canada, 7, 103-109.

Stewart, R. R., 1984, VSP interval velocities from traveltime inversion: Geophys. Prospecting, 32, 608-628.

Walker, R. J., Morgan, J. W., Naldrett, A. J., Li, C., and Fassett, J. D., 1991, Re-Os isotope systematics of Ni-Cu sulfide ores, Sudbury igneous complex, Ontario: Evidence for a major crustal component: Earth and Planetary Science Lett., 105, 416-429.

White, D., Milkereit, B., Wu, J. J., Salisbury, M., Mwenifeembo, J., Berer, E. K., Moon, W. M., and Lodha, G., 1994, Seismic reflectivity of the Sudbury Structure North Range from borehole logs: Geophys. Res. Lett., 935-938.

Wu, J. and Milkereit, B., 1994, Sudbury impact structure: poster presented in 1994 Lithoprobe seismic group meeting (May, 1994).

Yilmaz,O. 1987, Seismic Data Processing, Investigations in Geophysics No.2, Soc. of Expl. Geophys., Tulsa, Oklahoma.

Zolnai, A. I., Price, R. A. and Helmstaedt, H., 1984. Regional Cross Section of the Southern province adjacent to Lake Huron, Ontario: Implications for the tectonic significance of the Murray Fault Zone: Can. J. of Earth Sci., 21: 447-456.

Appendix A

Logistic Lay-out of the Seismic Data Processing System

The VSP data were processed utilizing mostly the main frame computer IBM 3090-200E. The reflection line 42 data were processed using the *IT&A*'s INSIGHT software along with the in-house developed software at the University of Manitoba (see Chapter 6 and 7) and plotted utilizing the LSPF plotting facilities. The refraction data were processed at University of Manitoba using the in-house developed software and the programs provided by Dr. Bob Mereu at the University of West Ontario (see Chapter 4 and Appendix B).

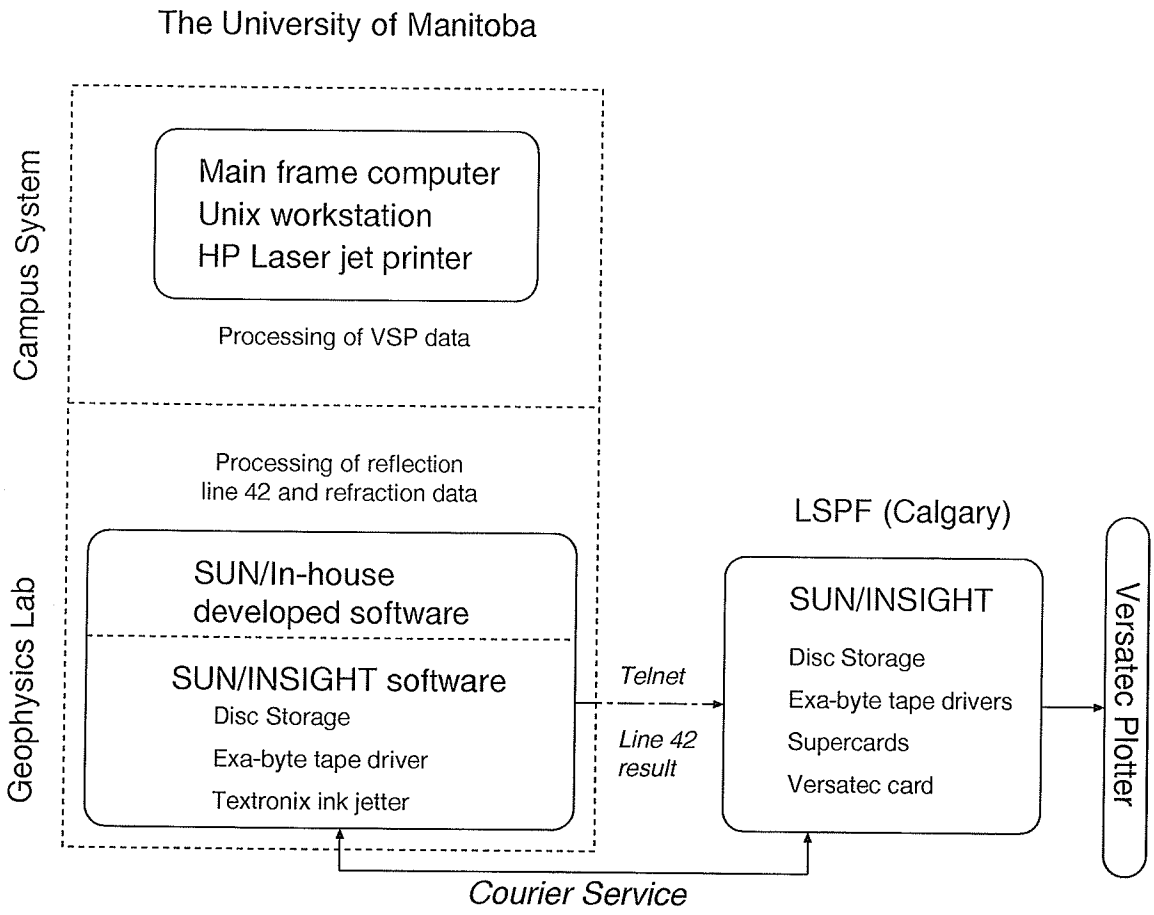

Figure A.1: Seismic data processing system lay-out.

Appendix B

High Resolution Seismic Refraction Data Processing and Ray Tracing Modeling.

Even though the author has fully participated in all the phases of refraction experiment including line scouting, GPS surveying, and field data acquisition, processing and interpretation of the refraction data carried out here are limited to preliminary level because there is already a large amount of research work involved in this thesis research and limited time. The purpose of including the preliminary results in this appendix is to provide a complementally picture of the Sudbury Structure along with other seismic data interpretation. Only the in-line shot data will be discussed and preliminary models will be presented based on the forward ray tracing seismic modeling and interpreted with other results.

B.1 Objectives, Target Refractors and Reflectors of the Experiment

The high resolution refraction seismic experiment conducted in the Sudbury region (lines AB and XY see Figure 4.5) was planned and aimed at exploration of the crustal structure of the Sudbury Basin and the surrounding area and study of the structural relationship between the Sudbury Structure and the Grenville Front.

The 1992 LITHOPROBE Sudbury refraction line AB, from northwest to southeast, traverses the Abitibi subprovince in the Superior Province, the Sudbury Structure, the Huronian group in the Southern Province, and the Grenville Front Tectonic Zone (GFTZ) and Britt Domain in the Grenville Province. The refraction line XY traverses the Sudbury Structure and the Huronian group in an approximate west-east direction. In the northwest, the Abitibi subprovince represents the latest and youngest of the late Archean plutonic granite-greenstone terranes to be accreted in the Superior Province. The Sudbury Structure, in the center of the refraction survey lines (Sudbury cross), is one of the primary targets of the survey (Figure 4.5). It produced significant reflection events in the earlier 1990's LITHOPROBE Sudbury reflection profiles (Milkereit et al., 1992; Miao and Moon 1993 and 1994). The SIC, which contains high velocity rocks such as the gabbro and norite, and the Levack Gneiss Complex (LGC), which has relatively high density and velocity values (Salisbury el. at., 1994; McGrath, 1994), can be good reflectors and refractors. The structural relationship between the SIC and the intermediate crustal boundary can also be investigated by means of the high resolution refraction survey.

To the southeast of the Sudbury Basin, the GFTZ is approximately 30 km wide

and superimposed upon earlier structures such as the Southern, Superior, and Nain provinces (Lumbers, 1978). It separates the high-grade metamorphic rocks of the Grenville Province from the low-grade metamorphic rocks of the Superior Province to the northwest and the Southern Province to the southwest. The region is in general characterized by ductile deformation and mylonite zones with foliation and layering aligned parallel to the GF. In other words, it is represented by a series of southeast dipping stacked crustal sheets (Gibb et al., 1983). The Britt domain of the Central Gneiss Belt in the Grenville Province (Davidson and Morgan, 1980; Davidson, 1984) is characterized by quartz feldspathic gneisses of both supracructal and plutonic origin, deformed together and metamorphosed to middle and upper amphibolite facies along with local migmatite formation.

The GFTZ appears to have a profound effect on the nature of the reflector patterns according to the GLIMPCE (Great Lakes International Multidisciplinary Program) seismic reflection and refraction studies (Behrendt et al., 1988, 1989, and 1990; Green et al. 1988, 1989, 1990, Milkereit et al., 1990) (see Figure B.1 for locations of the GLIMPCE reflection and refraction lines). These reflectors are also well imaged in the wide-angle migrated reflection profiles (Figure B.2). The line J refraction sections of the GLIMPCE experiments show that the GFTZ is composed of bands of reflectors dipping with angles of 20^o - 35^o extending to the lower crust. The Britt domain is generally represented as shallow southeast dipping reflectors (Epili and Mereu, 1991). Figure B.3 shows the velocity structure model obtained from the line J refraction survey. Seismic data from other lines crossing the GF to the east in Quebec provide evidence for a 5 to 10 km depression in the Moho along the GFTZ (Mereu and Jobidon, 1971; Berry and Fuchs, 1973; Mereu et al., 1986). All these reflectors and refractors

and their extensions were the potential targets of the 1992 refraction seismic survey.

B.2 Seismic Refraction Data Processing

The original data received at the University of Manitoba were stored in a SEG-Y formatted tape. They were extracted from an exabyte tape and copied on the hard disk by using a FORTRAN program kindly provided by Professor B. Mereu of the University of Western Ontario. The data were converted to the *IT&A* INSIGHT format by a program developed in this research. The INSIGHT software was then utilized for screen display, trace edit, and time domain filtering. Other processing steps including time correction, offset and azimuth information manipulation, and reduced time plotting were all implemented using the programs developed in this thesis research.

B.2.1 Time Correction and Filtering

The time errors of the seismic field data come mainly from two sources. One is shot time errors, which were corrected before the data were distributed. Another is the seismograph clock errors. The information about these errors was stored in the SEG-Y header files. Hence the clock service errors were corrected on all the traces after the data sets were received.

The raw data traces were contaminated with various types of noise. In order to interpret the observed data effectively, a series of processing steps were applied to improve the S/N ratio. The following steps were carried out in order to create the

final recording sections for interpretation, which include bandpass filtering, automatic gain control (AGC), median filtering, and spectral balance. A bandpass filter with a pass band from 8 to 35 Hz was applied to the data and a median filter was used for the data to remove high-frequency electric-storm noise. The gain-control processing with a 0.8 s time window effectively suppressed the strong air-wave noise in the near shot traces and enhanced the subsequent reflection events which were often overwhelmed in the coda phases of the air wave noise. Subsequently spectral balance with a sliding window of 0.5 s was applied to the data to further enhance refraction and reflection signals. Figure B.4 shows a comparison of the data before and after the processings. It is obvious that the strong air-waves and electric storm noises are suppressed after the processing.

B.2.2 Data Display

The original data were recorded in a -5 to 55 s time window and were reduced to the $t - x/8.0$ time section. To observe both intermediate and Moho boundary refractions more clearly, the data were converted to the reduced time sections of $t - x/6.8$. The offset distances and azimuthes between the sources and receivers were calculated from the latitude and longitude information stored in the original SEG-Y header files. The plotting routine was developed for a SUN Sparc workstation and the data were plotted on a 400*600 resolution HP laser printer. The processed, trace-equalized, seismic refraction sections are plotted and shown in the Appendix C.

The data from line AB shows significant Moho reflections (see the hyperbola-like curves in Figures C.1 and C.3. There are also clearly observable reflections, mostly

very shallow events, which intersect the surface (Figures C.4 and C.6). They are probably related to the Sudbury Structure and the dipping structures associated with the GFTZ. The head wave arrivals from the Moho boundary can be identified from the shots in the southern part of the line (see shots ab9 and ab10 sections (Figures C.9 and C.10)). However, they are not sufficiently clear to be identified from the shots in the northern part of the profile, which have been probably disturbed by the GFTZ's dipping interfaces.

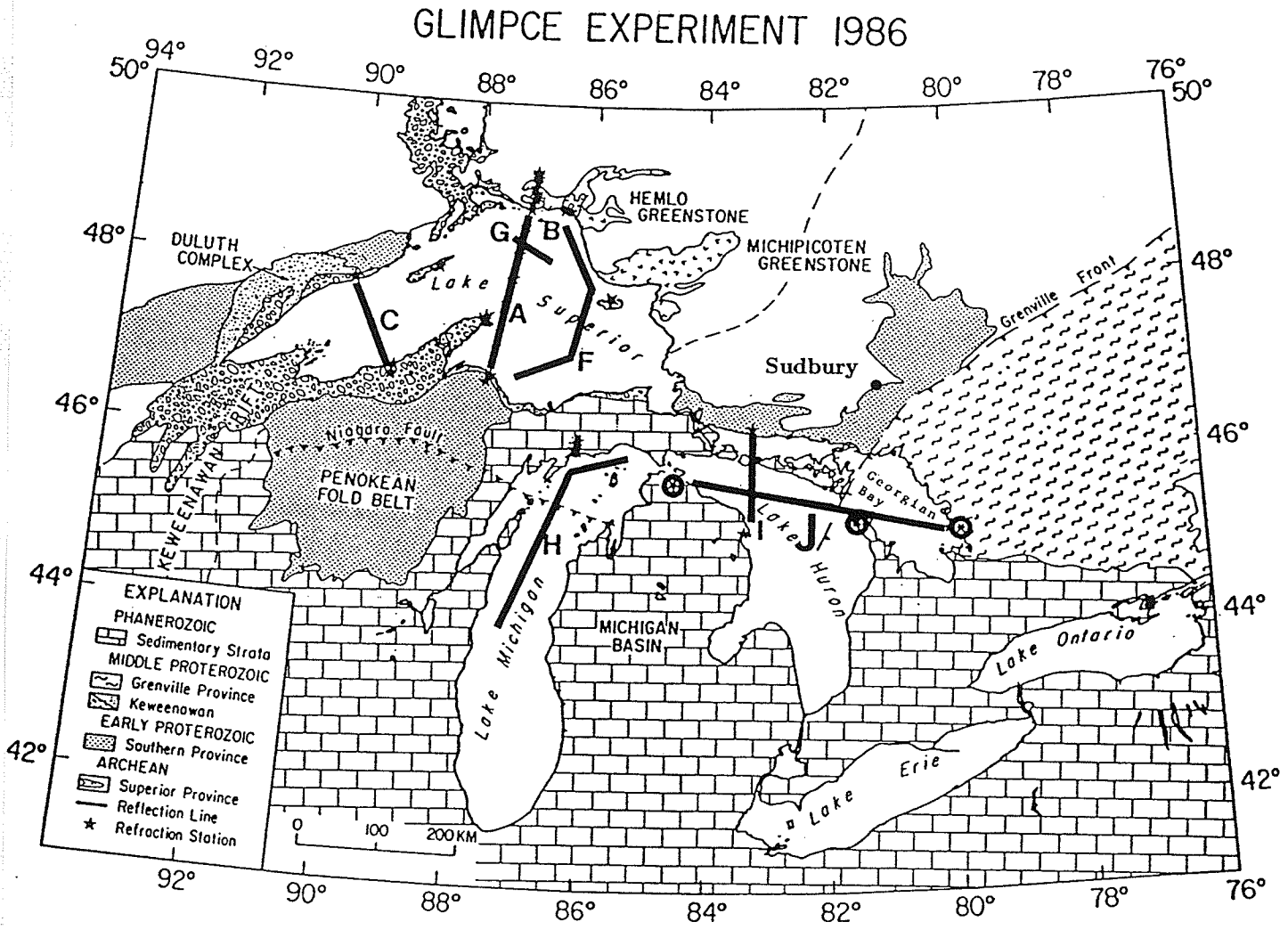

Figure B.1: Location of the 1986 GLIMPCE refraction seismic experiment. Line J traverses from the Britt domain, the GFTZ, and to the Southern Province (Epili and Mereu, 1991). The relative location of the Sudbury Structure is shown with respect to the regional tectonic setting.

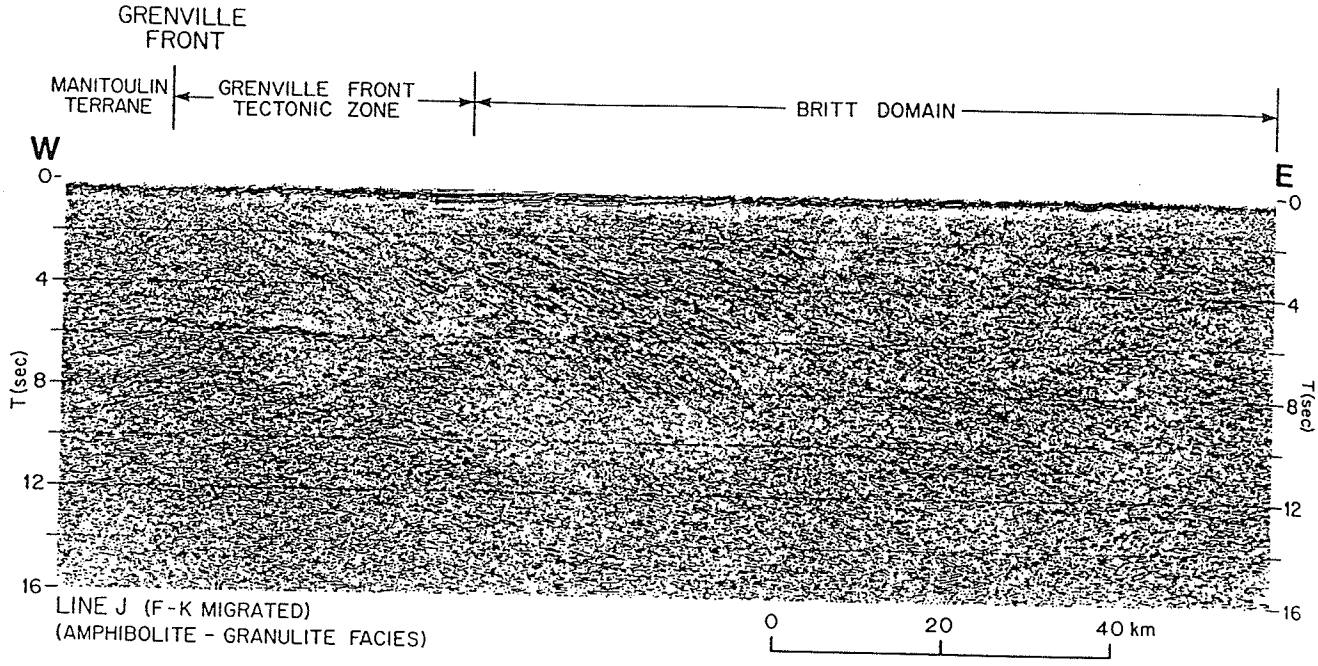

Figure B.2: The $f - k$ migrated seismic wide-angle reflection data of the eastern part of the GLIMPCE seismic marine profile J across the Grenville Front Tectonic Zone (GFTZ) and interior of the Grenville Orogen in Lake Huron/Georgian Bay. After Green et al. (1990). Note the steep dipping reflectors in the GFTZ and Britt Domain.

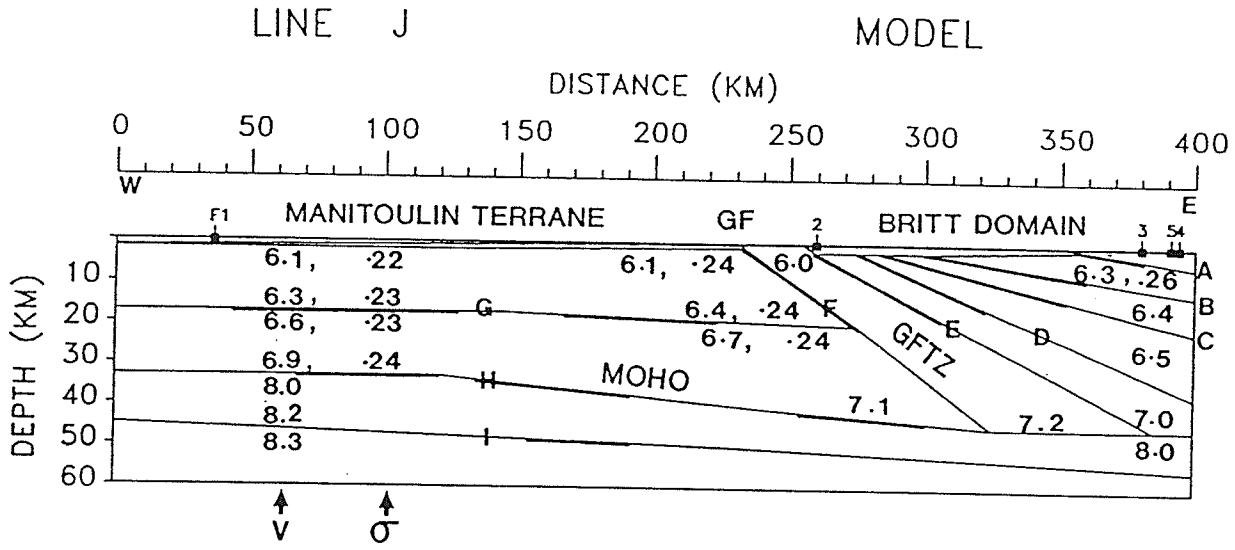

Figure B.3: Seismic $P-$ wave velocity model showing the schematic geological structure below the GLIMPCE line J (Epili and Mereu, 1991). V represents velocity and σ represents Poisson's ratio.

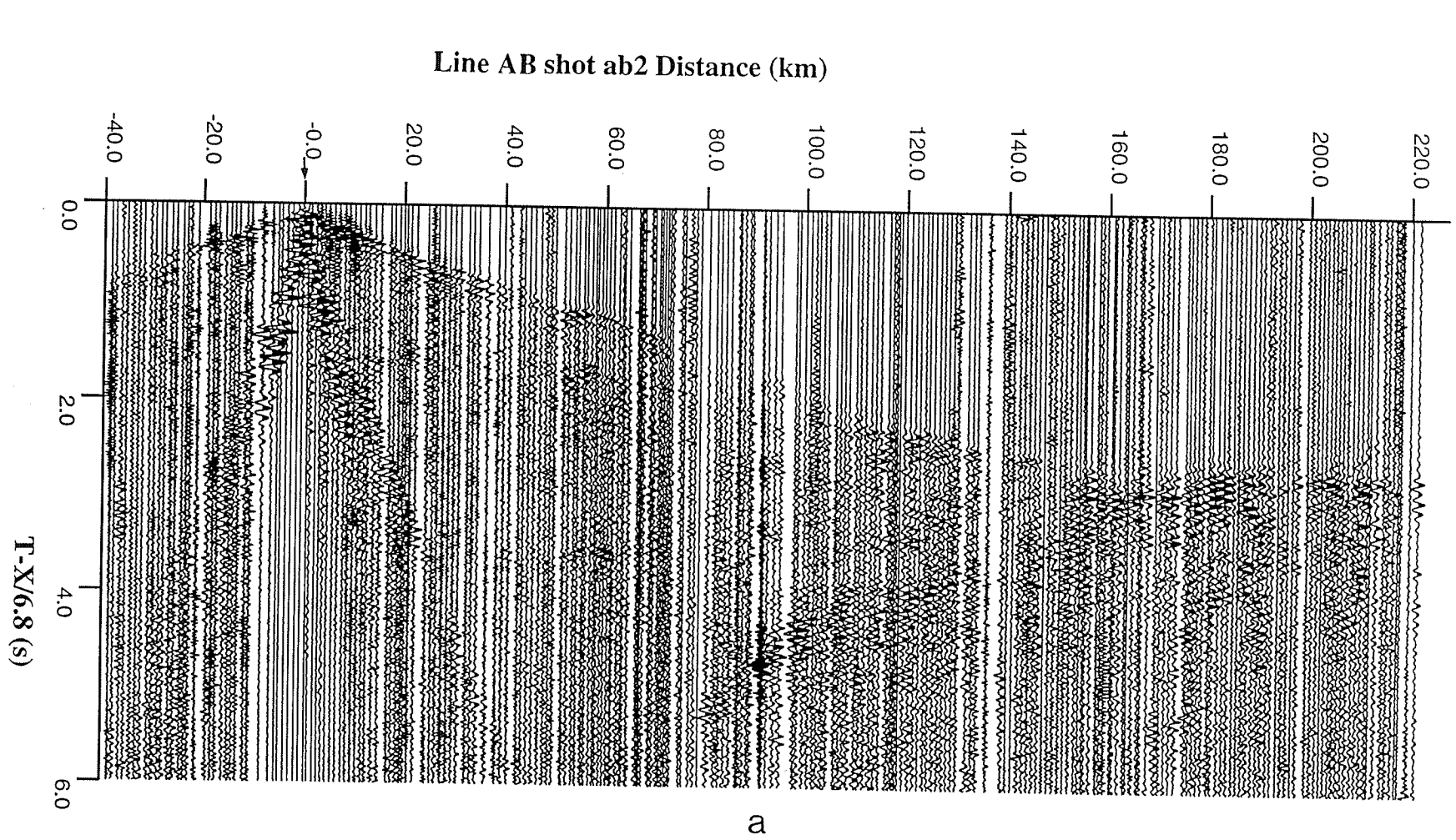

Figure B.4: LITHOPROBE Sudbury Transect line AB refraction section with shot ab2: (a) the raw data section, (b) the refraction section after application of the band-pass filtering, automatic gain control (AGC), median filtering, and spectral balance.

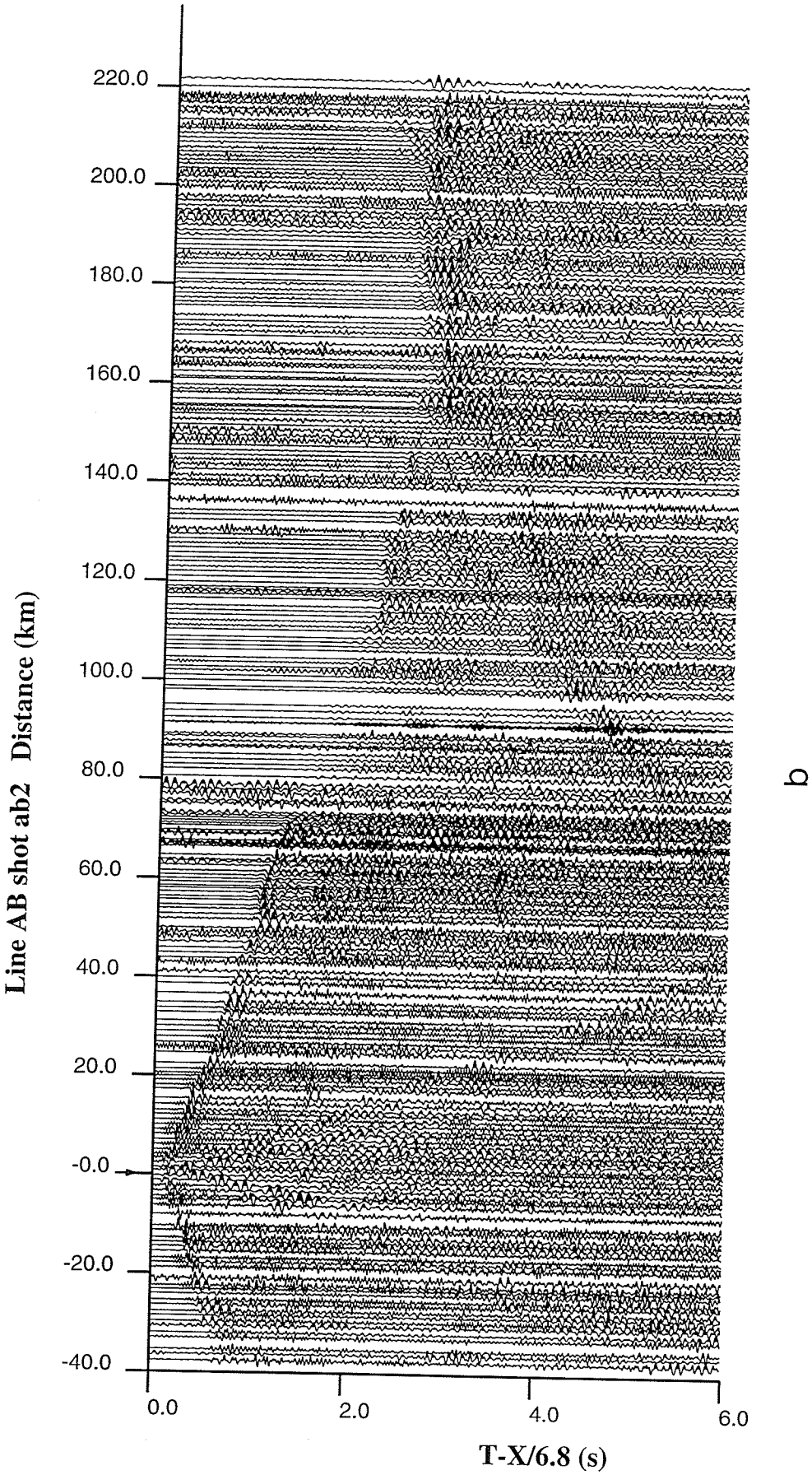
220.0
200.0
180.0
160.0
140.0
120.0
100.0
80.0
60.0
40.0
20.0
-0.0
-20.0
-40.0
Line AB shot ab2 Distance (km)
0.0
2.0
4.0
6.0
T-X/6.8 (s)
b

Line XY is not long enough to record Moho refraction events as the first arrival signals. However, refractions from the intermediate crustal discontinuity are observable. There are also significant reflections at shallow depths in the line XY records, which are probably related to the Sudbury Structure (Figures C.13 and C.15).

B.3 Ray Tracing and Seismic Modeling

There are several published ray tracing programs. The Červený's ray tracing program (Červený 1985 and 1989; Červený and Pšenčik, 1984; Červený and Ravindra, 1971) is one of the most effective programs and can handle both 2-D and 3-D inhomogeneous media and generate realistic ray tracing as well as synthetic seismograms. It was thus utilized in this thesis for ray tracing and seismic modeling for interpretation of the Sudbury refraction data.

B.3.1 Červený's Ray Tracing Algorithm

Červený's ray tracing algorithm is a two-point dynamic ray tracing approach (Červený and Pšenčik, 1984). The wave field generated by a line or a point source situated in a 2-D laterally varying layered structure is computed as a superposition of elementary waves (reflected, refracted, converted, etc), which correspond to the zero-order approximation of the ray method. The source time function has a form of a harmonic carrier modulated by a Gaussian envelope:

$$f(t) = exp(-(\omega t/\gamma)^2)cos(\omega t + \eta),$$

where t is time, ω is angular frequency, γ and η denote the parameters of the source-time function. With a proper choice of these parameters it is possible to simulate

a broad variety of wavelets which are close to the observed data in seismology and seismic prospecting. The two-point ray tracing (i.e. determination of rays which arrive at specified receiver positions along the Earth's surface) is performed by a modified shooting method and the rays are determined by the initial value (Cauchy) ray tracing. The ray tracing equations have the forms:

$$dx_j/d\tau = v^2 p_j, dp_j/d\tau = -v^{-1}\partial v/\partial x_j,$$

where τ is the travel time along the ray, x_j and p_j are the Cartesian coordinates and the components of the slowness vector along the ray respectively, v is the propagation velocity. The equation system is solved using the Runge-Kutta method. The geometrical spreading is determined by solving a system of two linear ordinary differential equations of the first order (so called dynamic ray tracing) by a modified Euler's method.

The algorithm can deal with various interfaces and laterally varying velocity structures, which include vanishing layers, block structures, fractures, and isolated bodies. The interfaces and velocity distribution are approximated by a cubic spline interpolation.

B.3.2 A Preliminary Model for the Line AB Shots

Using Červený's program, ray tracing was performed for lines AB and XY refraction data. For line AB data, a starting model consistent with the geology of the area was first determined from analysis of the first arrivals and the information from other refraction line studies across the area (GLIMPCE line J (Epili and Mereu, 1991)). For a modeling procedure, rays were traced from the source to the surface, and a

comparison was made between the computed and observed travel times. Adjustments were then made to the velocity values and/or the boundary positions until a good fit was achieved between all the computed and observed data. The results of the ray tracing are shown in Figures B.5, B.6, B.7, B.8, B.9, and B.10 for the shots ab0, ab2, ab3, ab6, ab9, and ab10 respectively. The computed travel times were overlaid on the processed sections to show how well the computed values match with the observed data, which are shown in Figures B.5a, B.6a, B.7a, B.8a, B.9a, and B.10a. The corresponding seismic rays and the model interfaces are shown respectively in Figures B.5b, B.6b, B.7b, B.8b, B.9b and B.10b.

Shots ab0, ab2, ab3 were located at the northern side of the Sudbury Structure (see Figure 3.2), the Sudbury Structure appears to produce clear effects in these refraction sections. By inspecting the recorded data section of the shot ab0 (Figure C.1), one may notice there is a strong near surface reflection at receiving distance of approximately 100 km. This event can also be traced in the adjacent shots, the shots ab2 and ab3, in which case the strong events appears at receiving distances of approximately 60 km and 40 km respectively (Figures C.3 and C.4). For the records with the shots on the south side of the Sudbury Structure (see Figure C.6), this strong near surface reflection can also be traced. It appears in the right side of the shot ab6 data section at an approximate receiving distance of 20-45 km. This strong amplitude event can be generated by the near surface high velocity structure. In the preliminary model (Figure B.11) for the line AB, a rhombus block with a slight higher velocity (v=6.45 km/s) was used to simulate this structure. The computed travel times fit well with the observed data (see Figures B.5a, B.6a, B.7a, and B.8a). This structure may be related to the SIC rocks of the norite or gabbro and/or the high density LGC

which underlies the SIC and has a density of 2.77 g/cm^3 and velocity of 6.5 km/s based on the most recent result of gravity modeling (McGrath, 1994) and velocity measurement (Salisbury et al., 1994).

For the shots at the southern end of the line (shots ab9 and ab10), the p_g phases are very complex and appear to have a 'shingle-like' pattern (Mereu, 1990) up to a distance of 110 km (Figures C.9 and C.10). A large number of hyperbola-like curves in the record sections show that the wide-angle reflections dominate these sections. The dipping structure of the GFTZ and Britt domain must be responsible for 'shingle-like' patterns. In the preliminary model (Figure B.11), four dipping reflectors with dipping angles ranging from approximately 8^o to 22^o simulate the GFTZ and Britt domain with a very good fit corresponding between the computed and observed travel times. The results are shown in Figures B.9a and B.10a. The reflections with 'shinge-like' patterns were also observed in the eastern stations of the GLIMPCE refraction line J where they were interpreted as arising from the dipping reflectors below the GFTZ and Britt domain (Epili and Mereu, 1991).

Thus a preliminary model with velocity parameters and structural boundaries was finally obtained for line AB profile and shown in Figure B.11. The results show that the Moho boundary is about 37 km deep at the northern end of the line, and it reaches a depth of 44 km at the southern end of the line. The intermediate crustal interface is about 17 to 19 km deep and it is interrupted at the GFTZ. The shallow high velocity structure related to the Sudbury Structure is located at about 4.5 to 7 km depths with a velocity contrast to the surrounding medium of approximately 0.25 km/s. The velocity above the Sudbury high velocity lens is slightly lower than the surrounding medium.

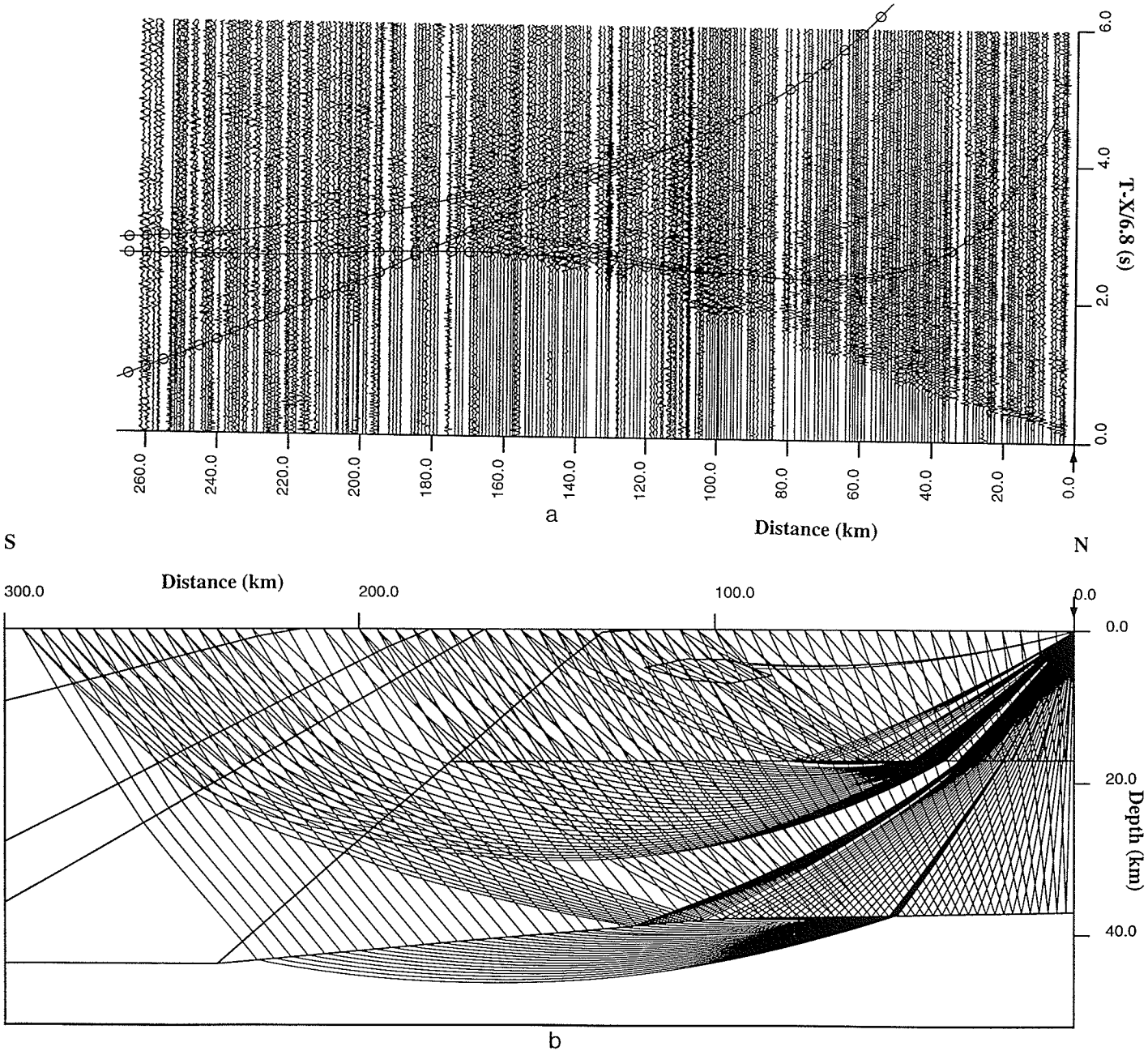

Figure B.5: (a) Sudbury line AB refraction section from the shot ab0, overlaid with the theoretically computed travel times represented by the open circles; (b) the corresponding structural interfaces and the seismic ray plots.

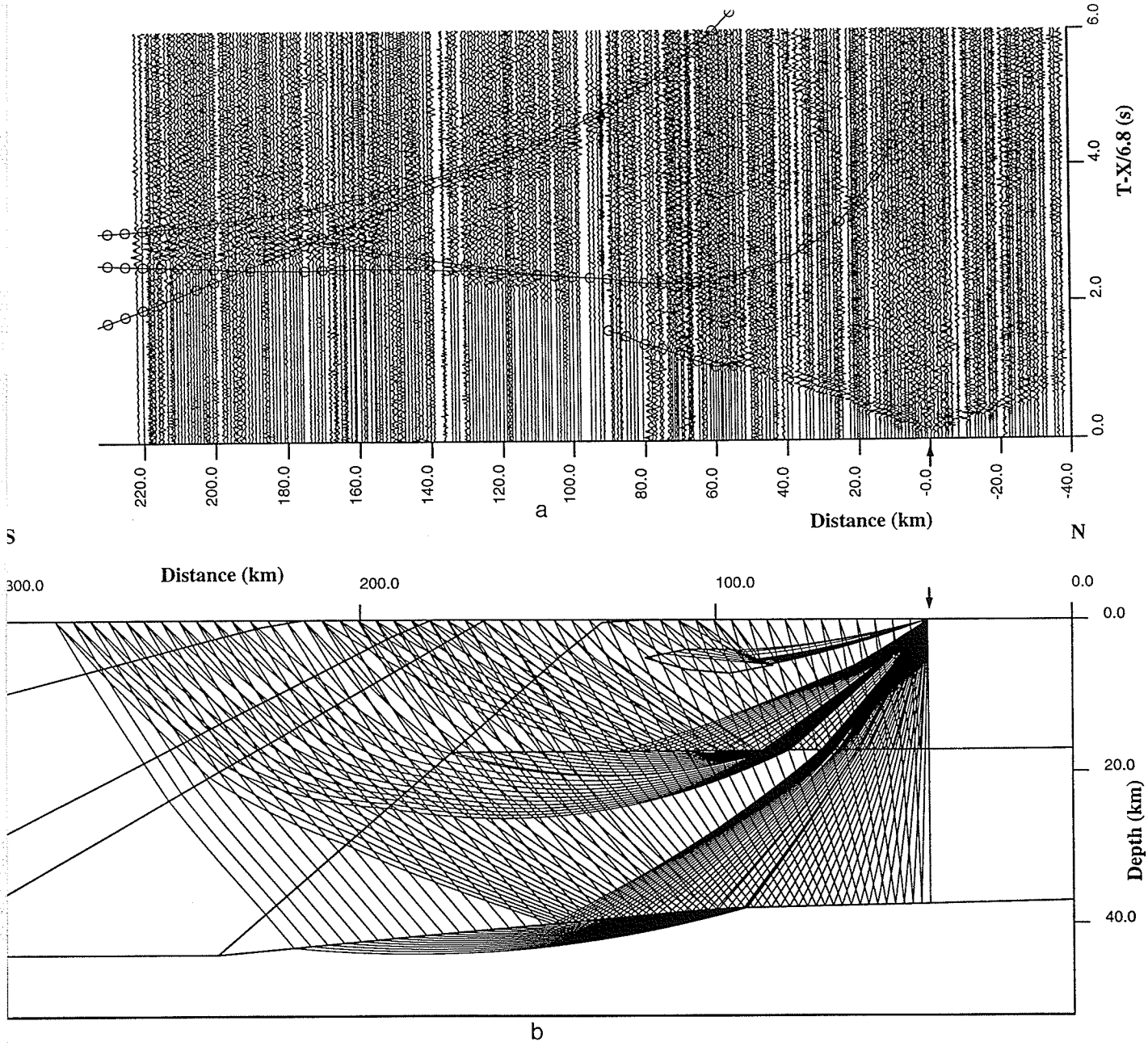

Figure B.6: (a) Sudbury line AB refraction section from the shot ab2, overlaid with the theoretically computed travel times represented by the open circles; (b) the corresponding structural interfaces and the seismic ray plots.

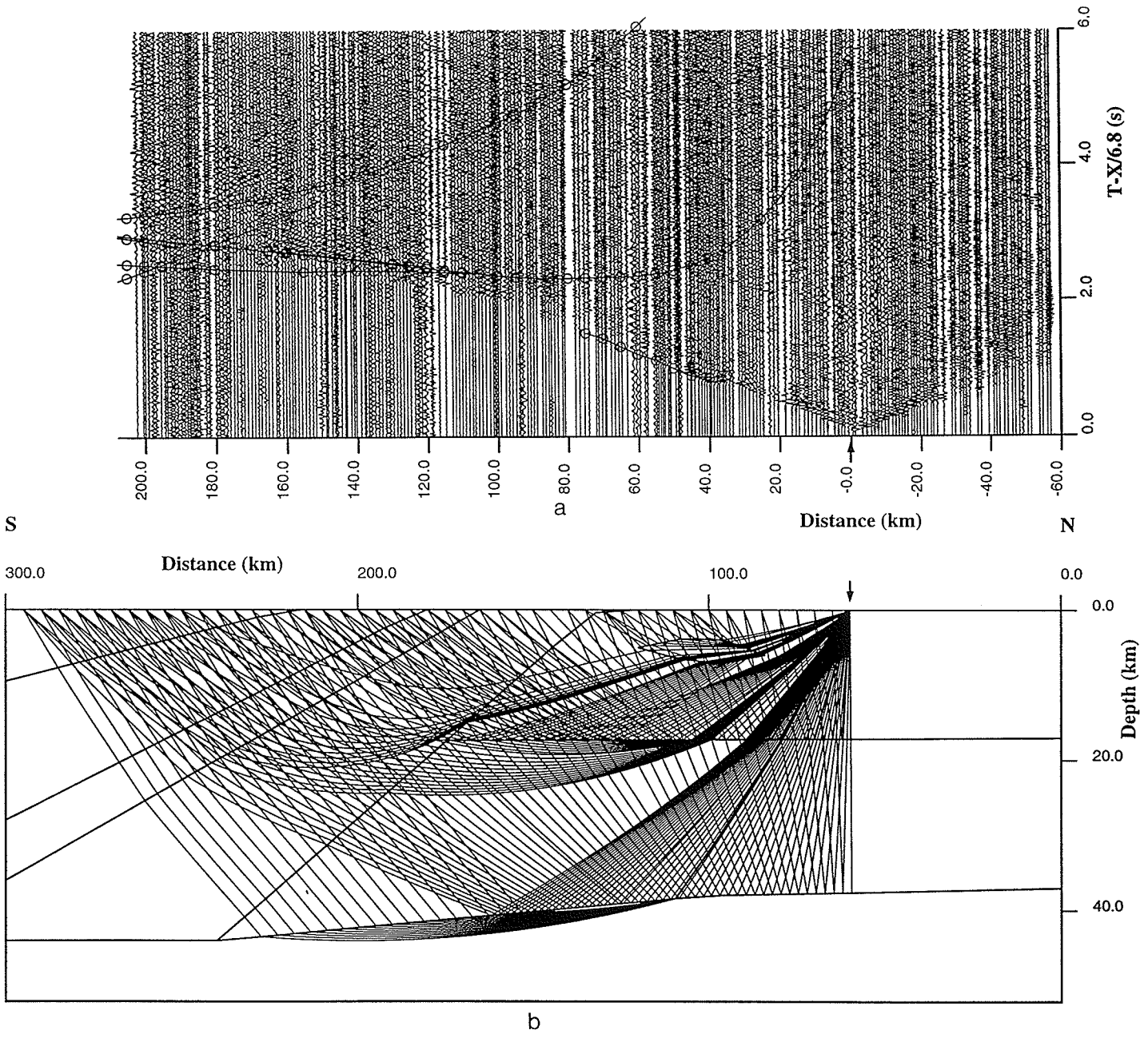

Figure B.7: (a) Sudbury line AB refraction section from the shot ab3, overlaid with the theoretically computed travel times represented by the open circles; (b) the corresponding structural interfaces and the seismic ray plots.

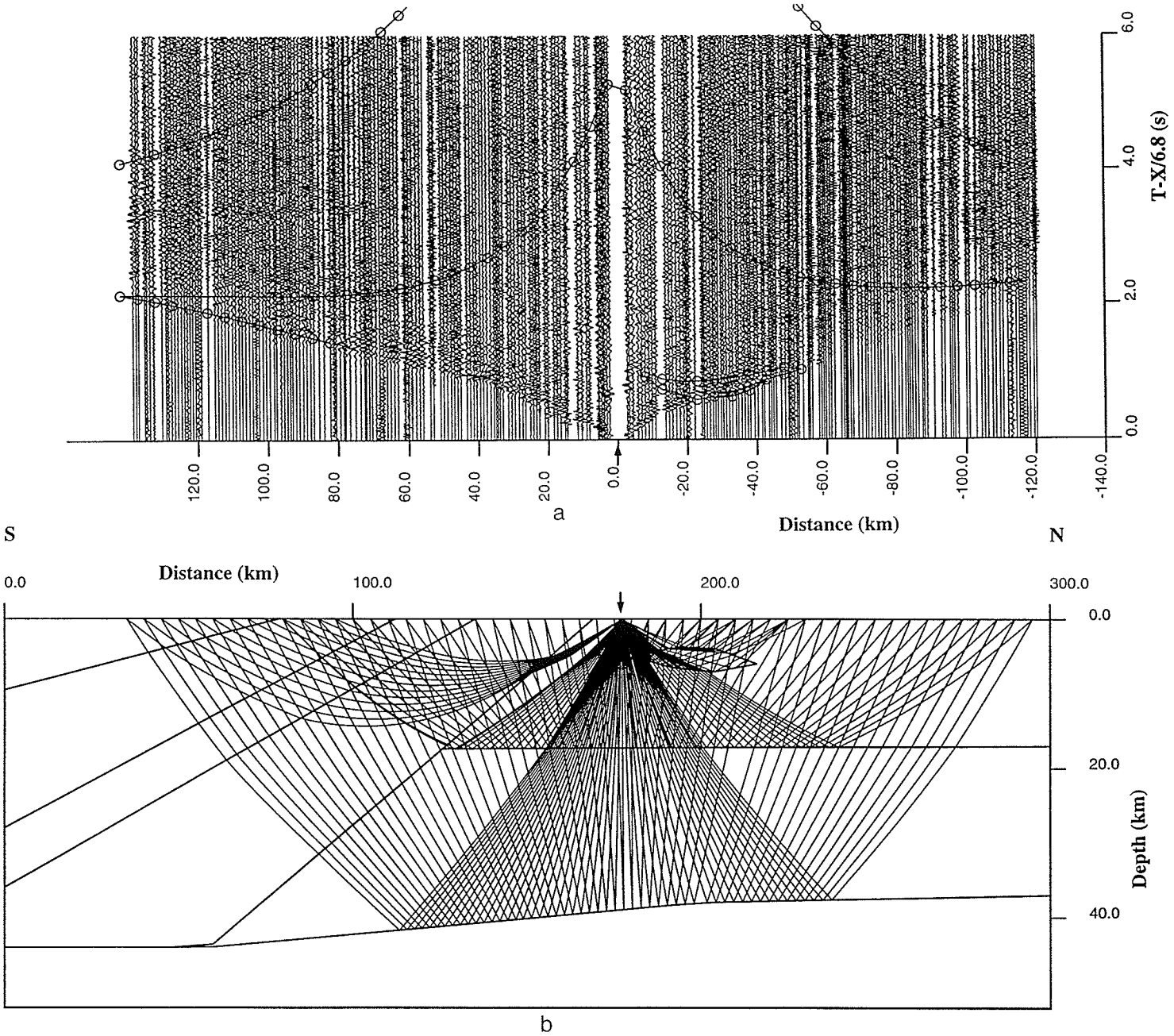

Figure B.8: (a) Sudbury line AB refraction section from the shot ab6, overlaid with the theoretically computed travel times represented by the open circles; (b) the corresponding structural interfaces and the seismic ray plots.

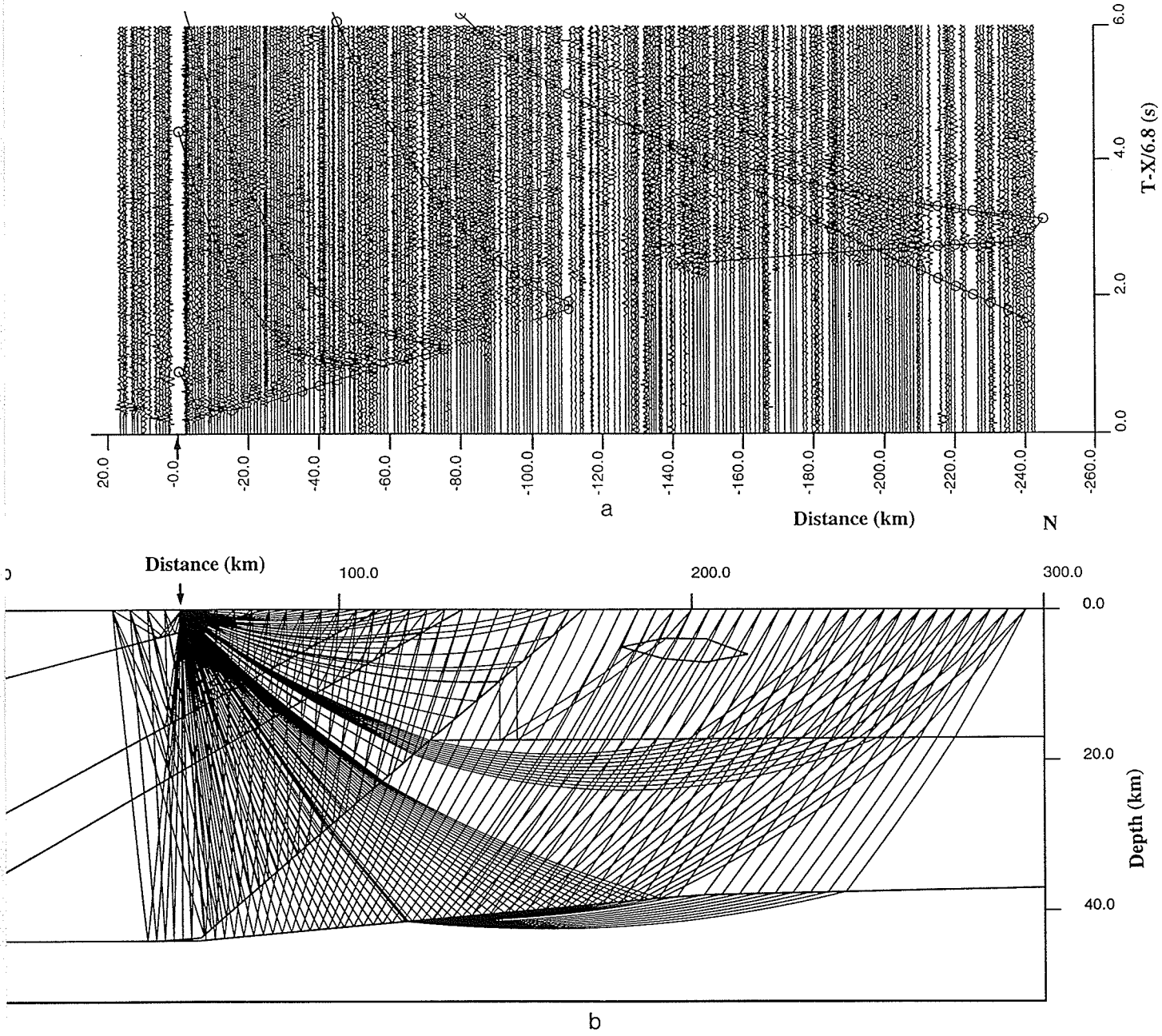

Figure B.9: (a) Sudbury line AB refraction section from the shot ab9, overlaid with the theoretically computed travel times represented by the open circles; (b) the corresponding structural interfaces and the seismic ray plots.

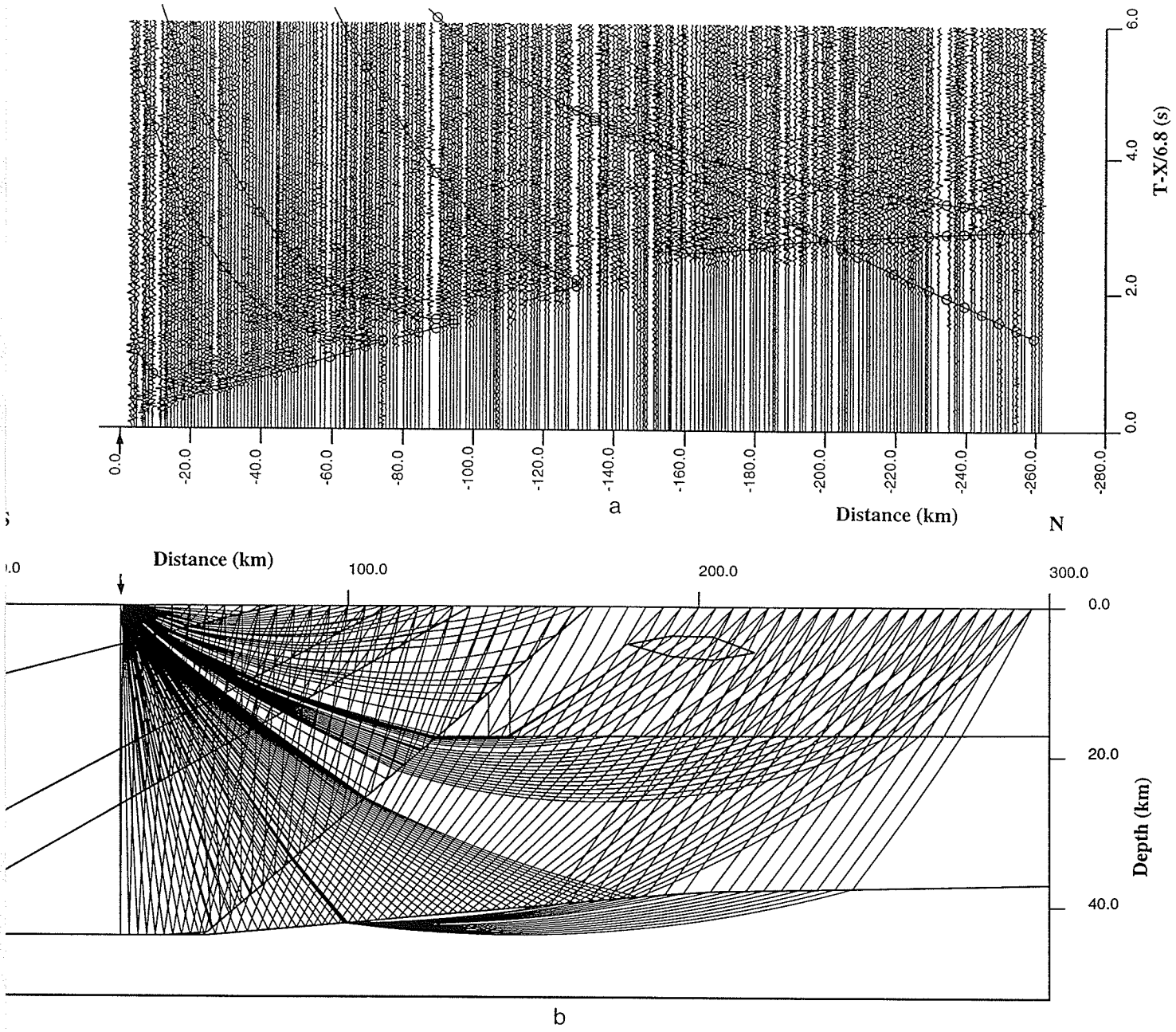

Figure B.10: (a) Sudbury line AB refraction section from the shot ab10, overlaid with the theoretically computed travel times represented by the open circles; (b) the corresponding structural interfaces and the seismic ray plots.

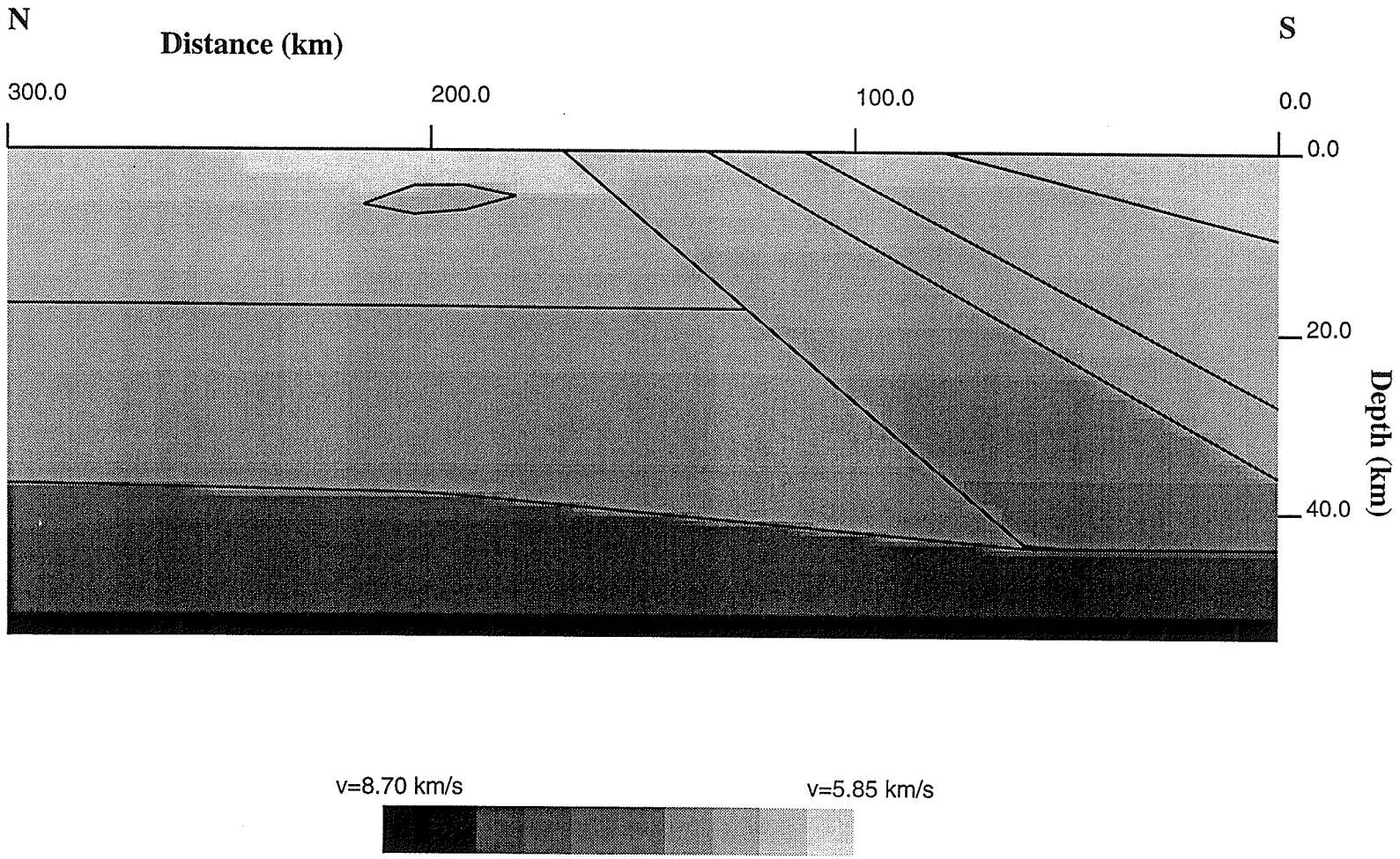

Figure B.11: Preliminary crustal model beneath the Sudbury Structure along the refraction profile line AB. V represents velocity.

It is not surprising that the average effect of the SIC and the LGC is similar to a high velocity block, since the structures are bounded to the south and east by the Huronain sedimentary group rocks, which have a lower density of about 2.70 g/cm^3, and to the north and northwest by the Archean granite-greenstone belt with an even lower density of 2.65 g/cm^3. The GFTZ and the Britt domain were modeled as four southeast dipping reflectors in this preliminary interpretation model.

B.3.3 A Preliminary Model for the Line XY Shots

The starting model for line XY profile was generated by analyzing the first arrivals and the information obtained from line AB. The same ray tracing method was used to model the structural profile along line XY. The geological cross-section along the line XY is parallel to the GFTZ and the starting model is simpler than that of the line AB. The results of the theoretically computed travel times are also overlaid on the observed refraction data sections and shown in Figures B.12a, B.13a and B.14a respectively for shots xy1, xy2, and xy5. The corresponding seismic ray plots are shown in Figures B.12b, B.13b, and B.14b. A shallow strong reflection event can again be clearly seen in the shot xy2 records (Figure B.13a), and it can also be traced in the shot xy5 records (Figure B.14a). This event is probably related to the high velocity structures associated with the SIC norite and/or the LGC underlying the SIC, as mentioned in the previous section.

The preliminary model is finally obtained based on the results of ray tracing modeling and is shown in Figures B.11 and B.15. It shows that the Moho discontinuity is about 37 km deep along the line. The intermediate crustal interface has depth

ranging approximately from 17 to 19 km (Figures B.11 and B.15). A lenticular block of about 70 km length along the line with a high velocity of 6.45 km/s located at the depth ranging 7-11 km simulates the shallow reflection event with a good fit between the computed and observed travel times (see Figure B.12a and B.14a). Overlaying on this high velocity block is a slightly lower velocity zone with a velocity variation from 5.9 to 6.2 km. This lenticular sheet like block appears to be related to the Sudbury Structure as mentioned in the interpretation of line AB data, but it requires further investigation. Geological interpretation of this velocity block will have significant impact on the formation hypothesis of the Sudbury Structure.

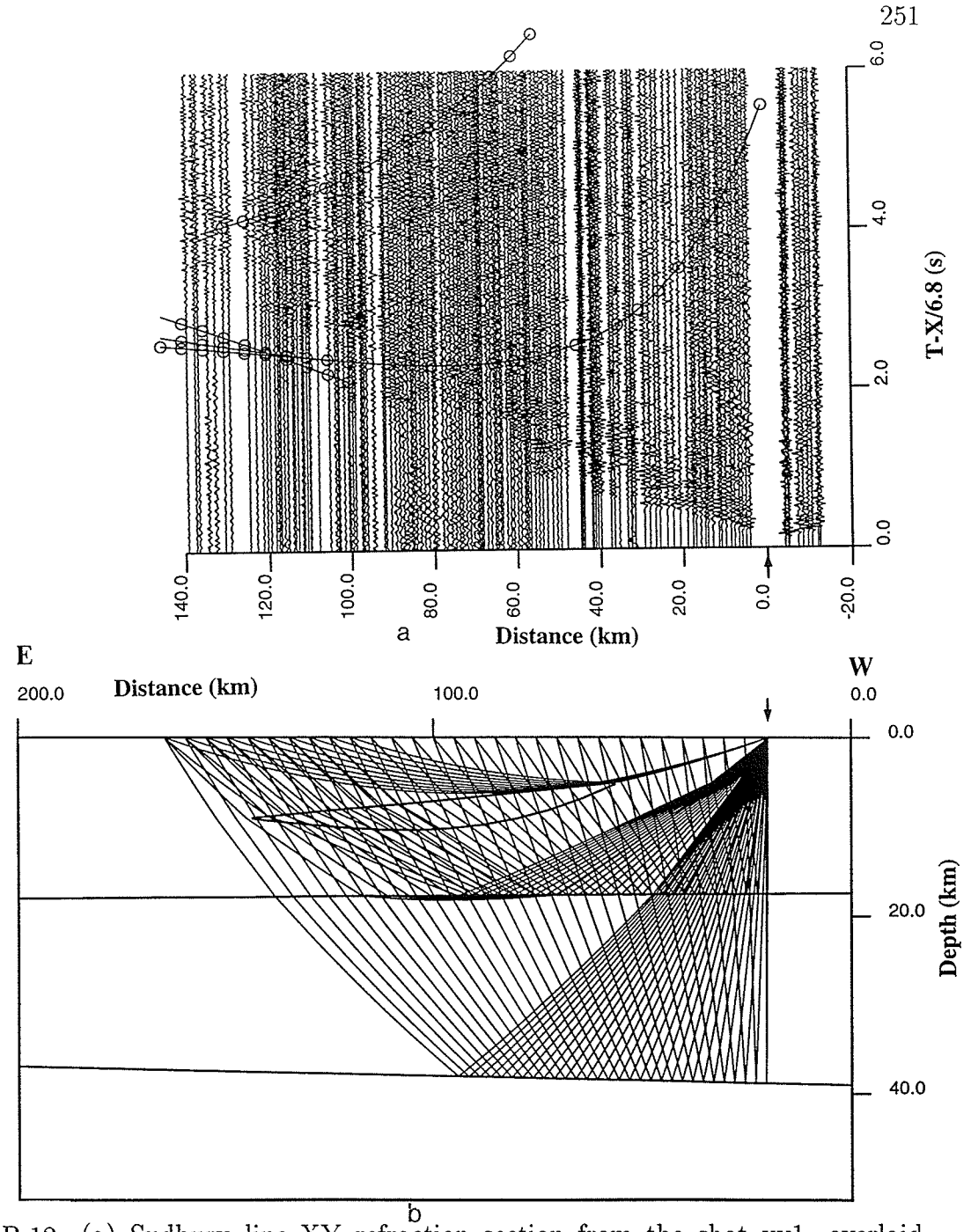

Figure B.12: (a) Sudbury line XY refraction section from the shot xy1, overlaid with the theoretically computed travel times represented by the open circles; (b) the corresponding structural interfaces and the seismic ray plots.

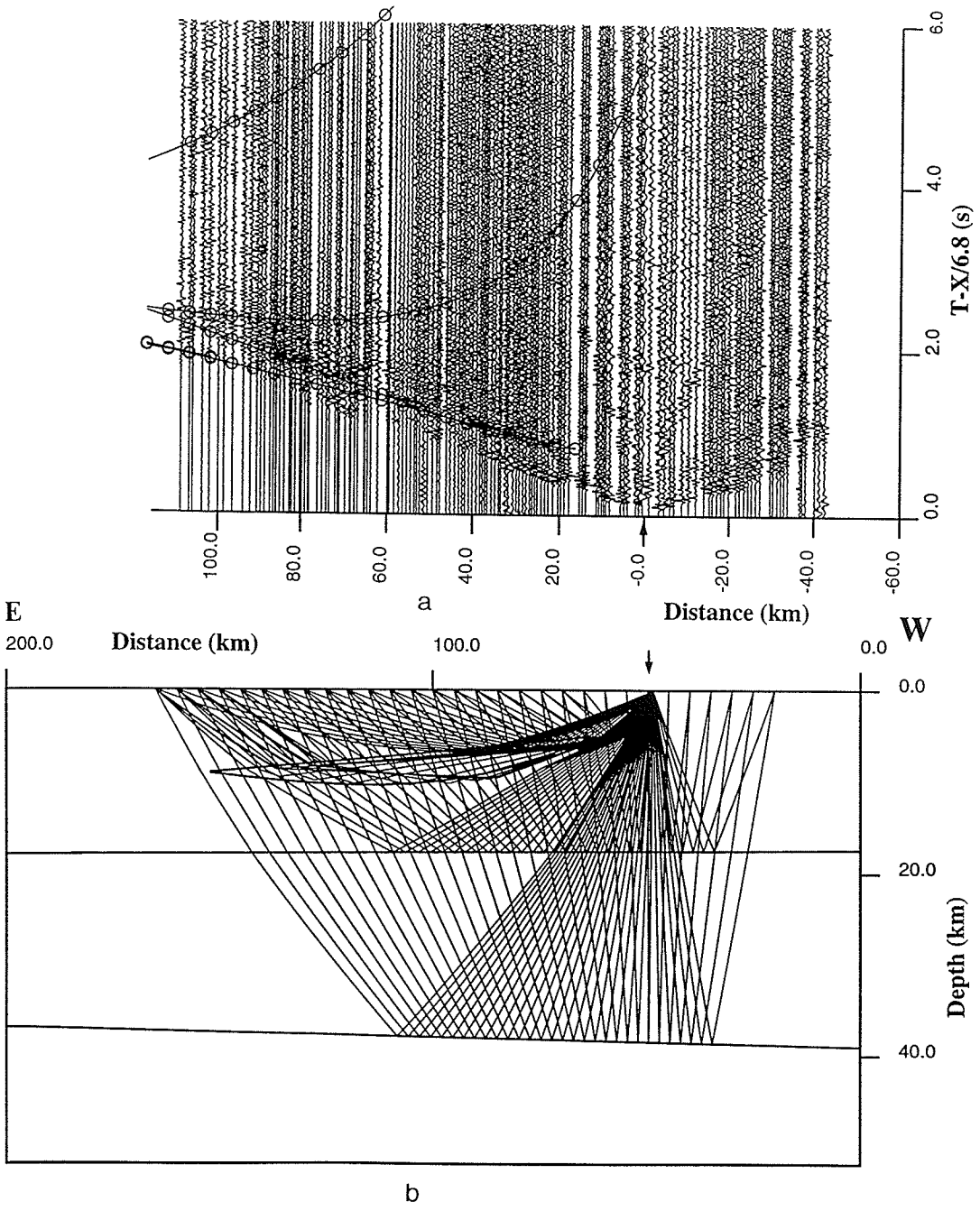

Figure B.13: (a) Sudbury line XY refraction section from the shot xy2, overlaid with the theoretically computed travel times represented by the open circles; (b) the corresponding structural interfaces and the seismic ray plots.

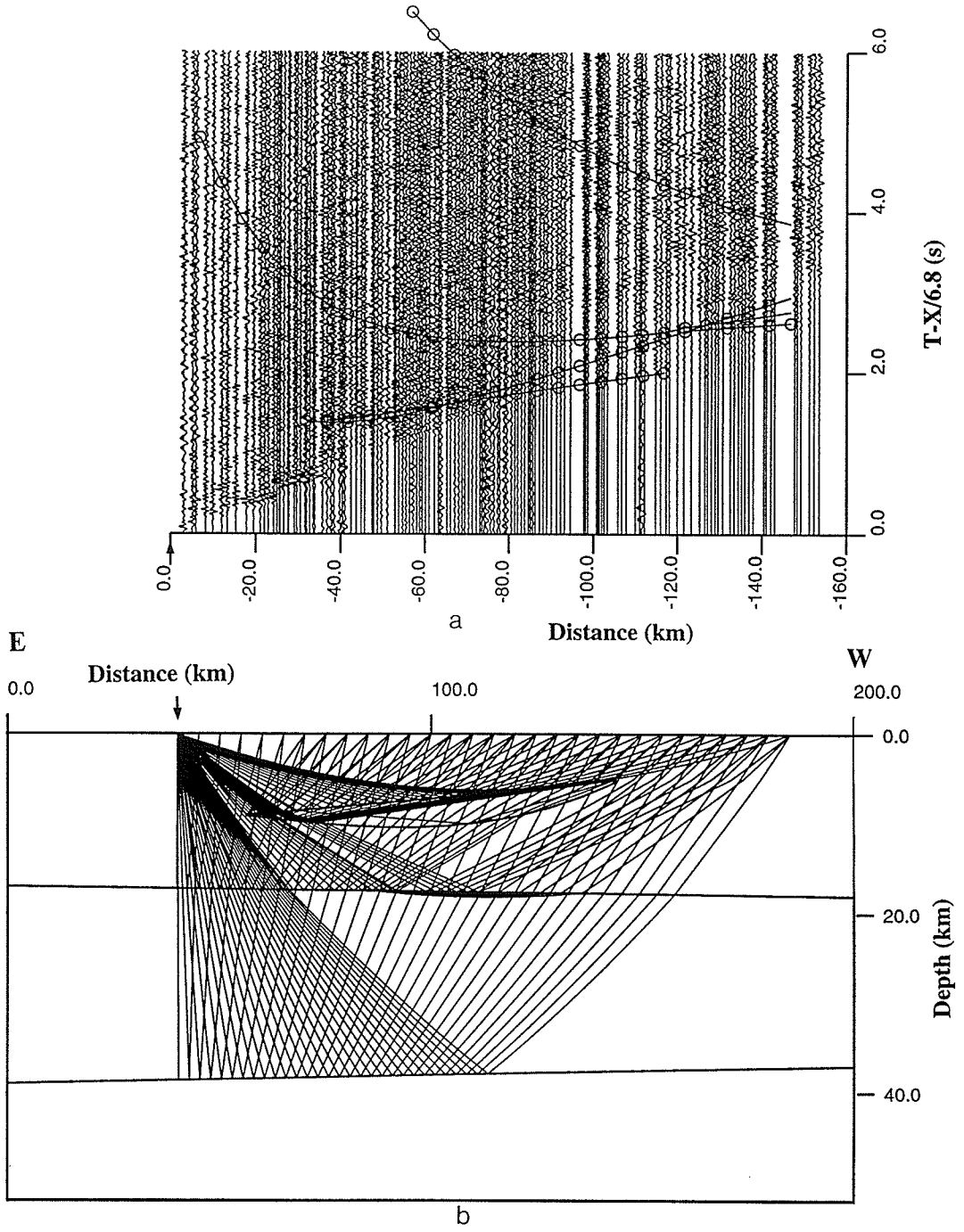

Figure B.14: (a) Sudbury line XY refraction section from the shot xy5, overlaid with the theoretically computed travel times represented by the open circles; (b) the corresponding structural interfaces and the seismic ray plots.

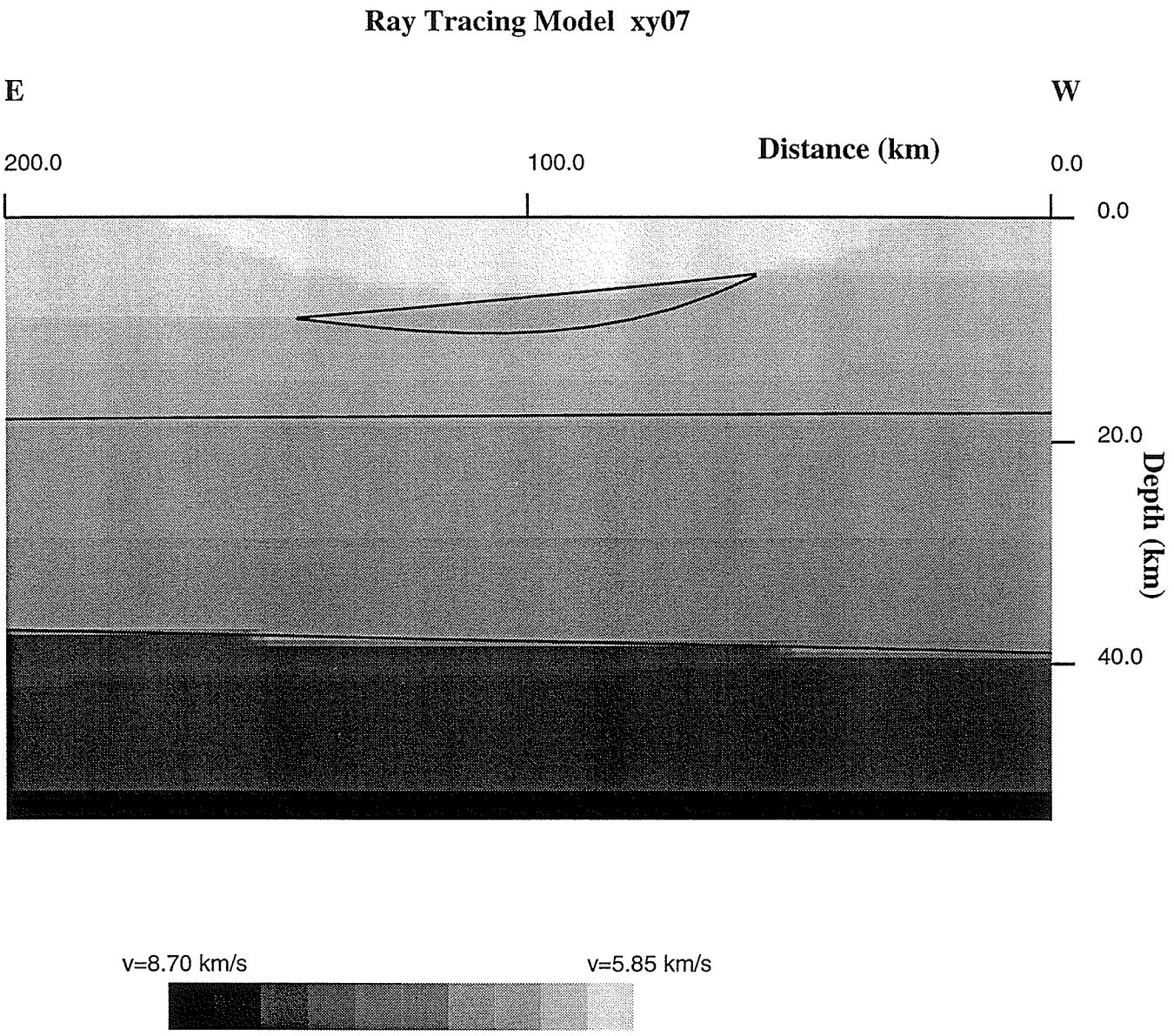

Figure B.15: Preliminary crustal model beneath the Sudbury Structure along the refraction profile line XY. V represents velocity.

Appendix C

Preliminarily Processed 1992 AGT Refraction Seismic Sections

Plots of the preliminarily processed 1992 LITHOPROBE Abitibi-Grenville Transect Sudbury sub-transect high resolution refraction in-line data are presented in the following pages. These plots were created with a reducing velocity of 6.8 km/s after bad-trace editing, bandpass filtering, AGC, median filtering, and spectral balance processings. The coincident shots ab5 and xy3 were canceled prior to actual recording due to local safety concerns.

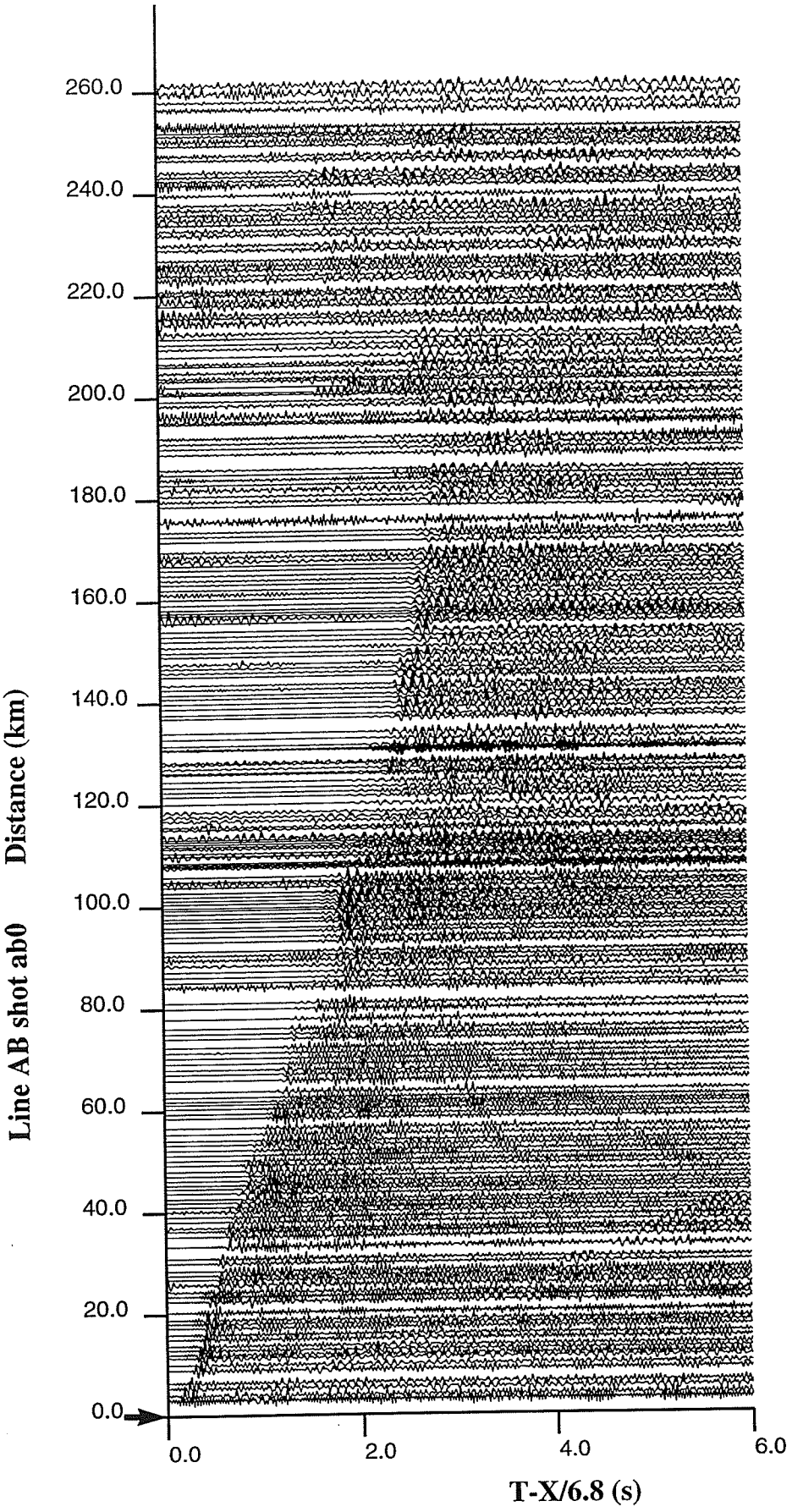

Figure C.1 Refraction section for the shot ab0 of the line AB.

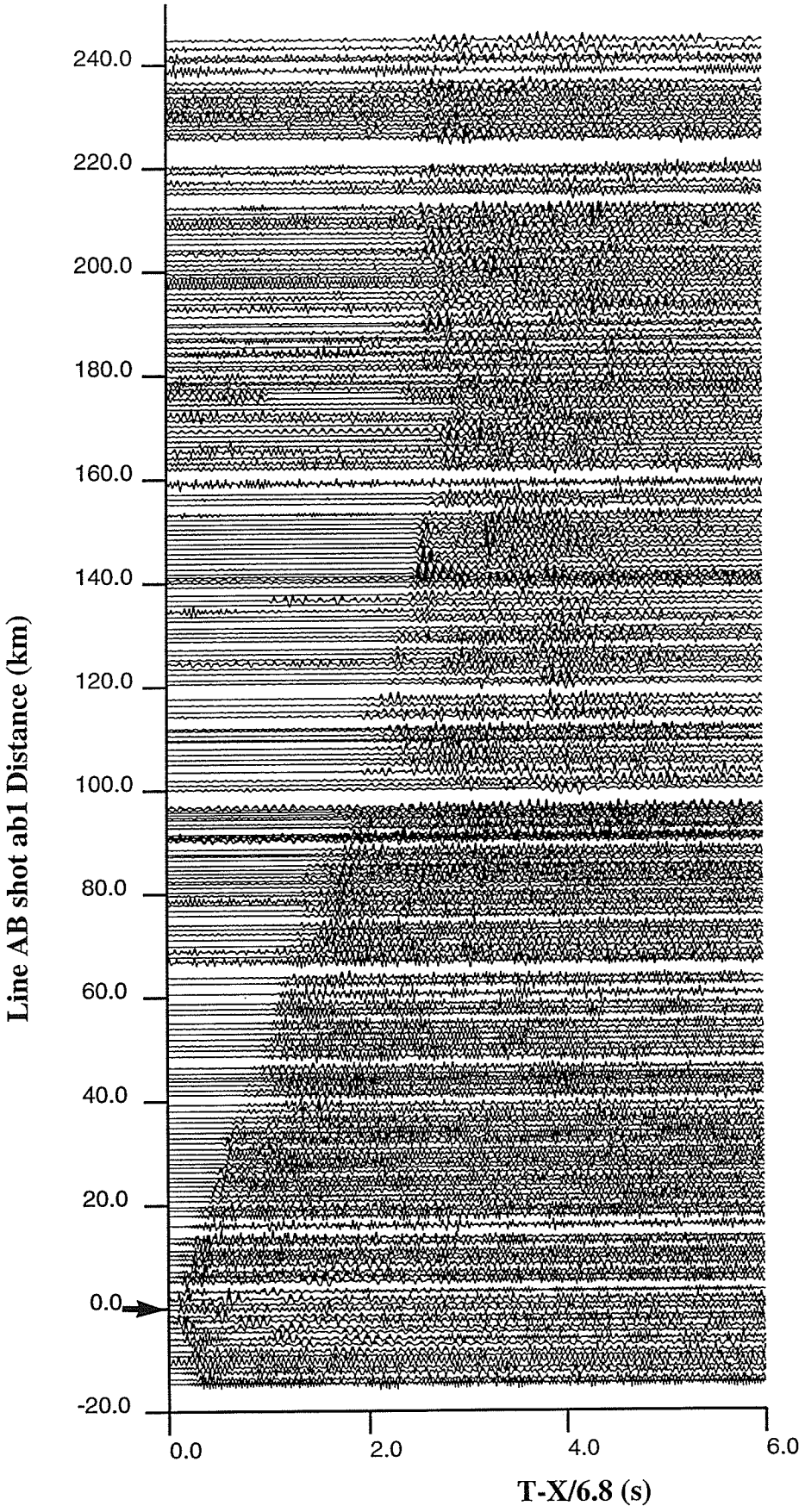

Figure C.2 Refraction section for the shot ab1 of the line AB.

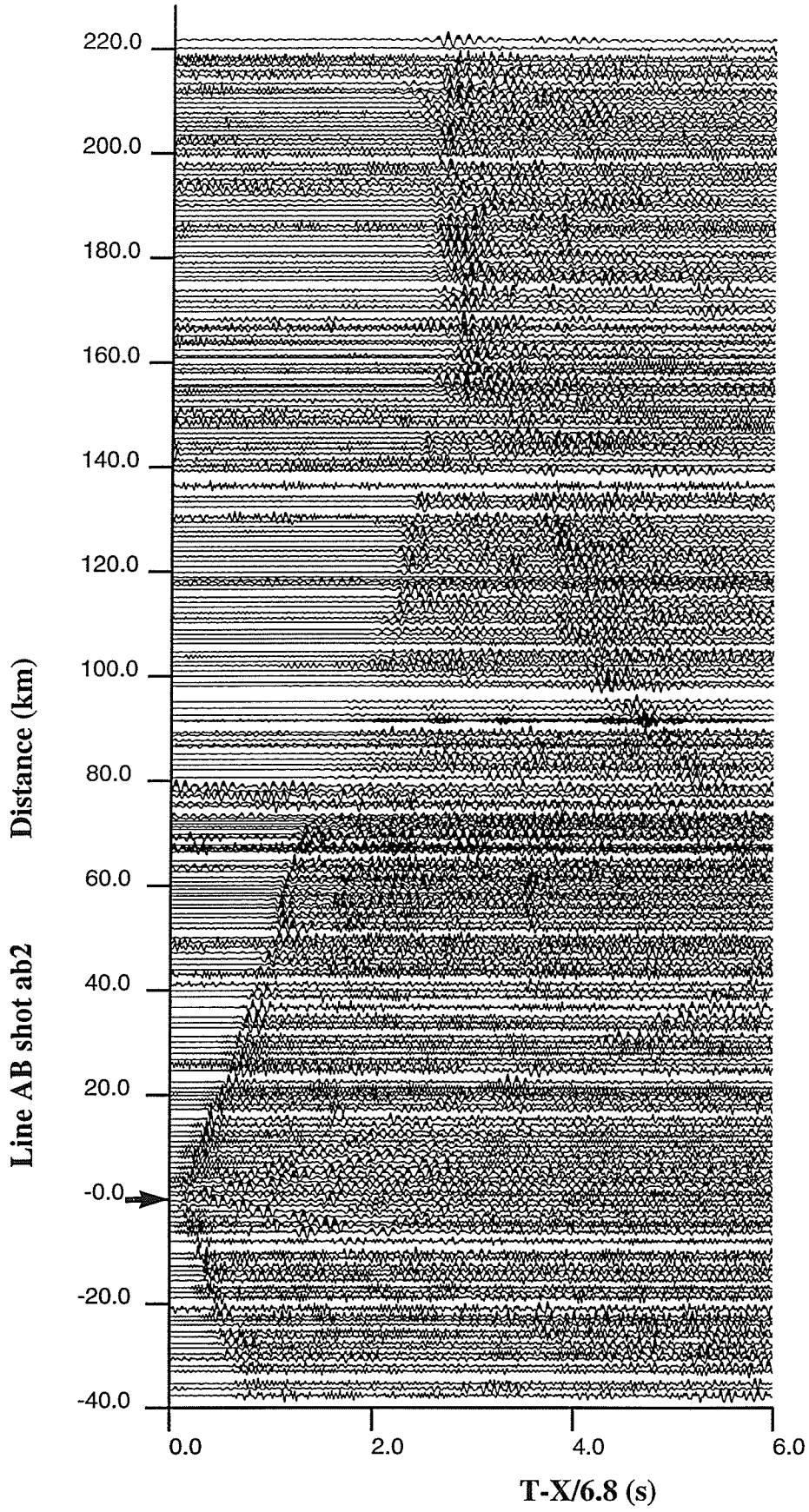

Figure C.3 Refraction section for the shot ab2 of the line AB.

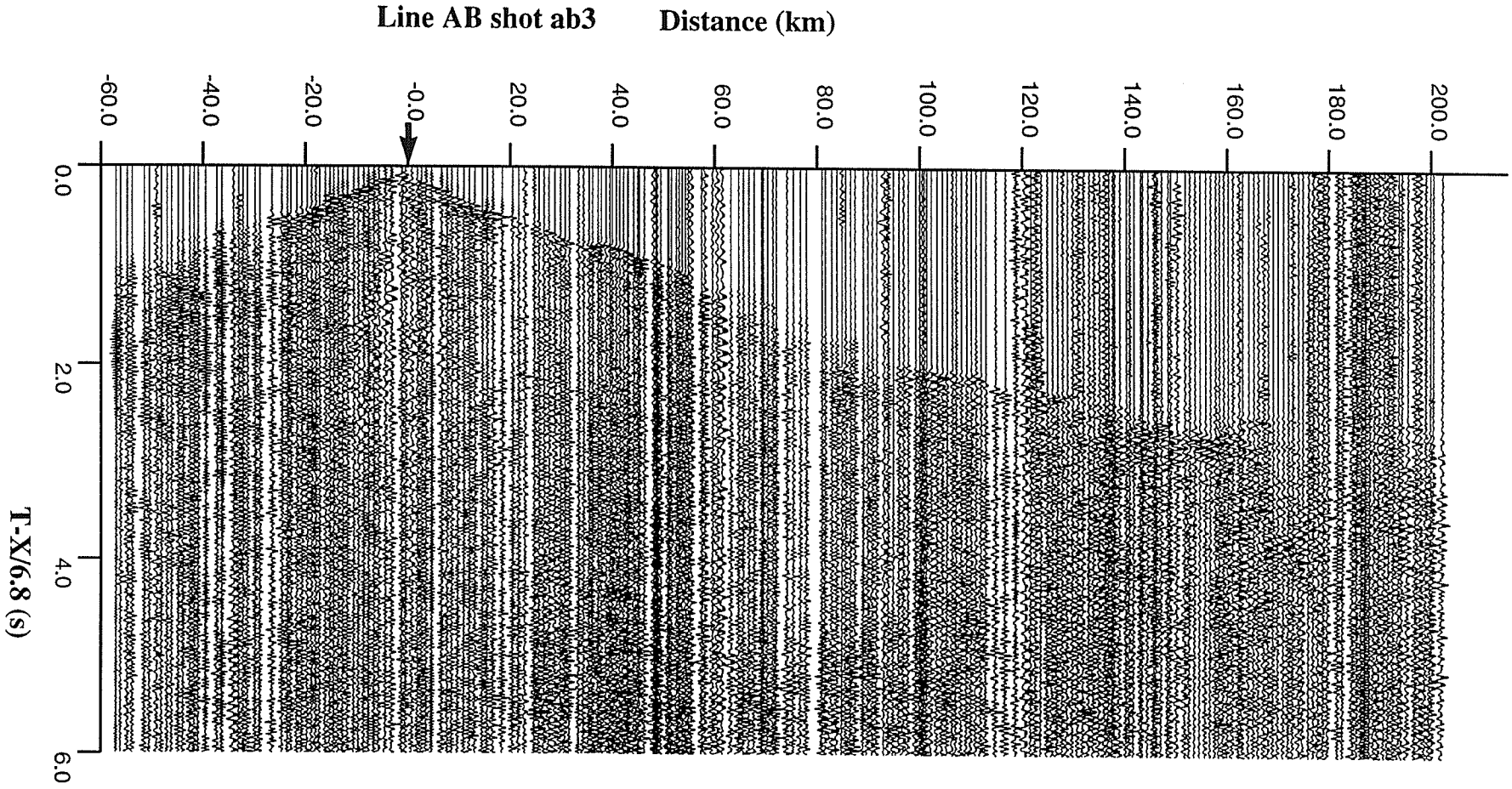

Figure C.4 Refraction section for the shot ab3 of the line AB.

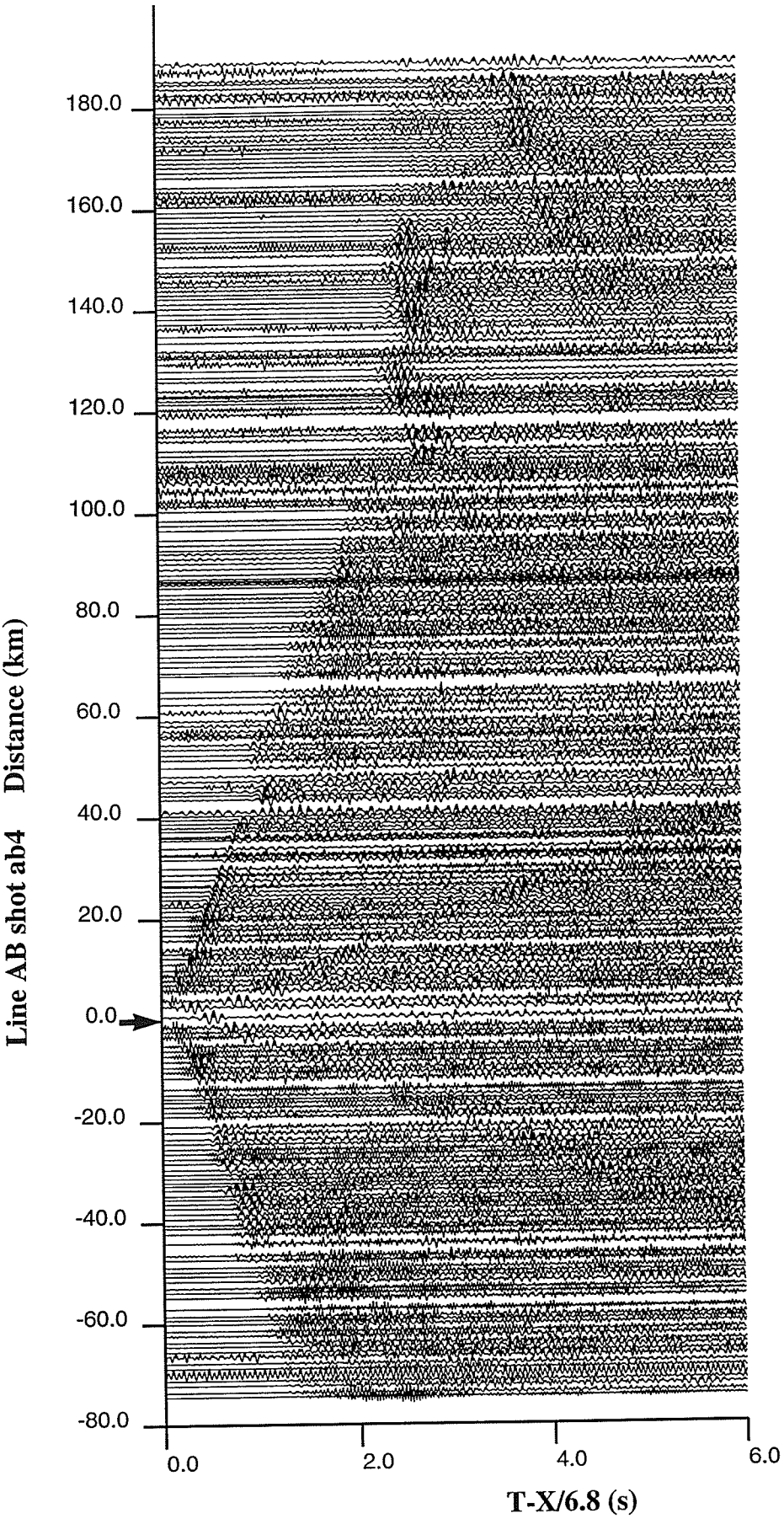

Figure C.5 Refraction section for the shot ab4 of the line AB

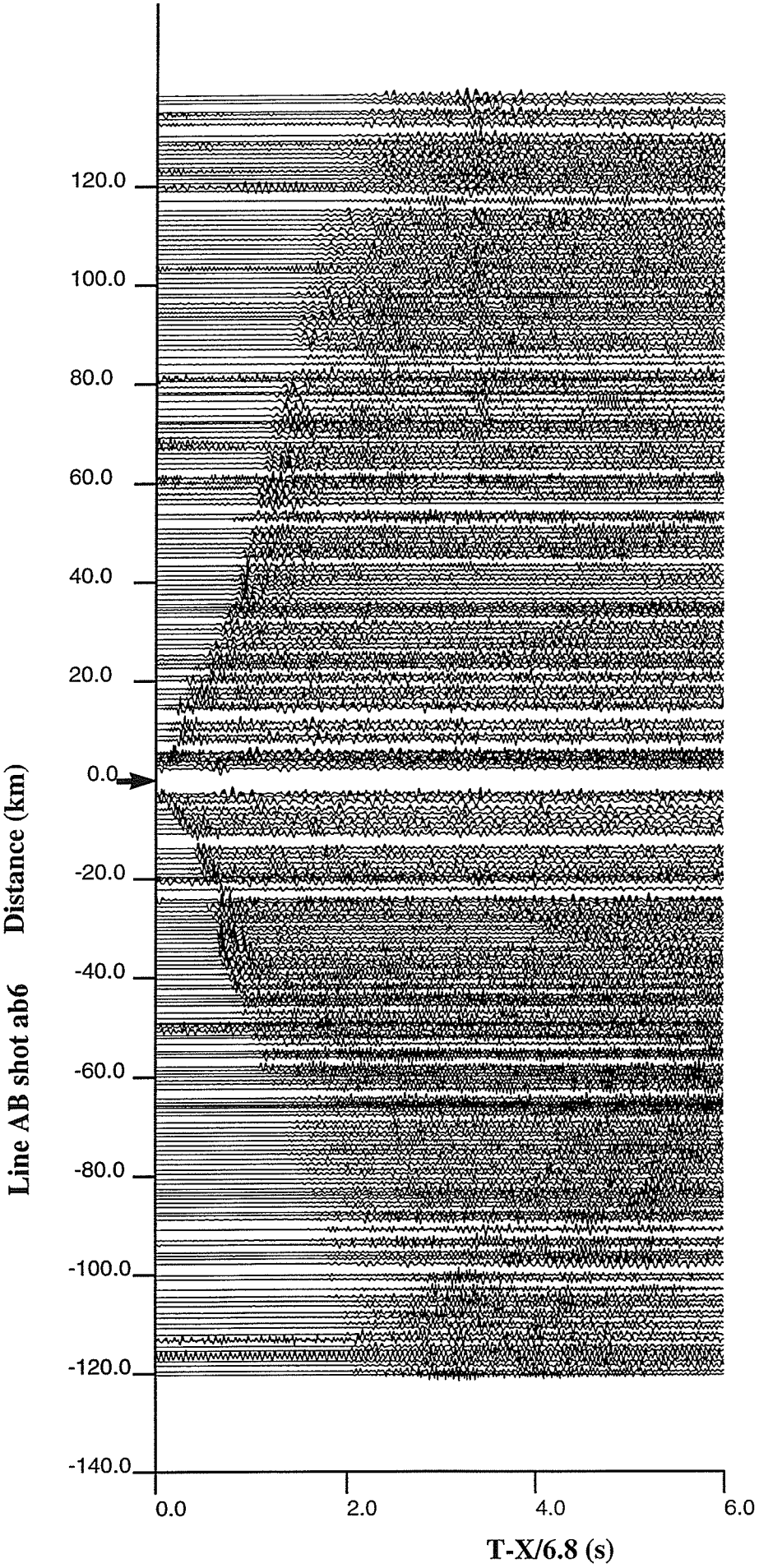

Figure C.6 Refraction section for the shot ab6 of the line AB.

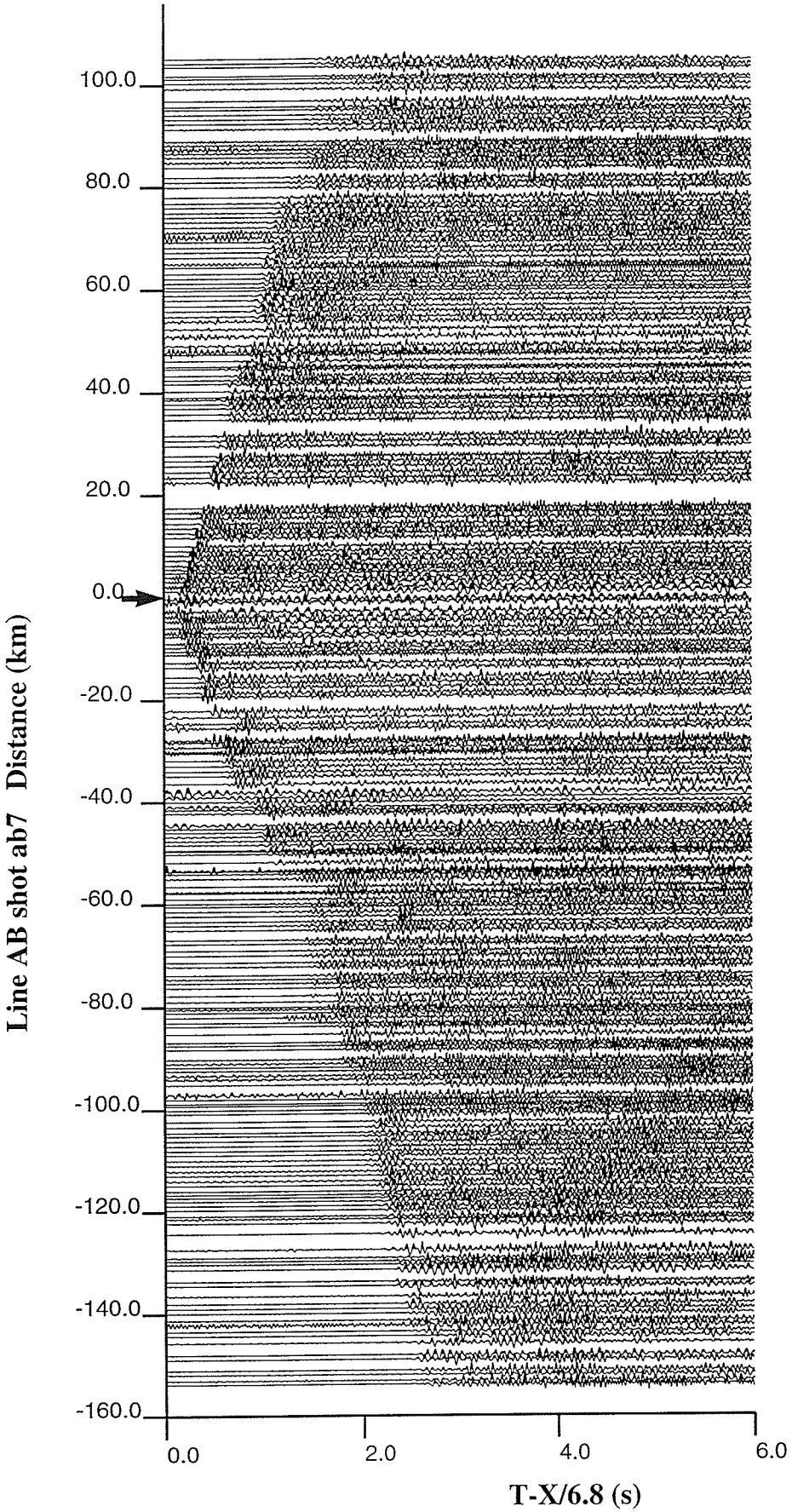

Figure C.7 Refraction section for the shot ab7 of the line AB.

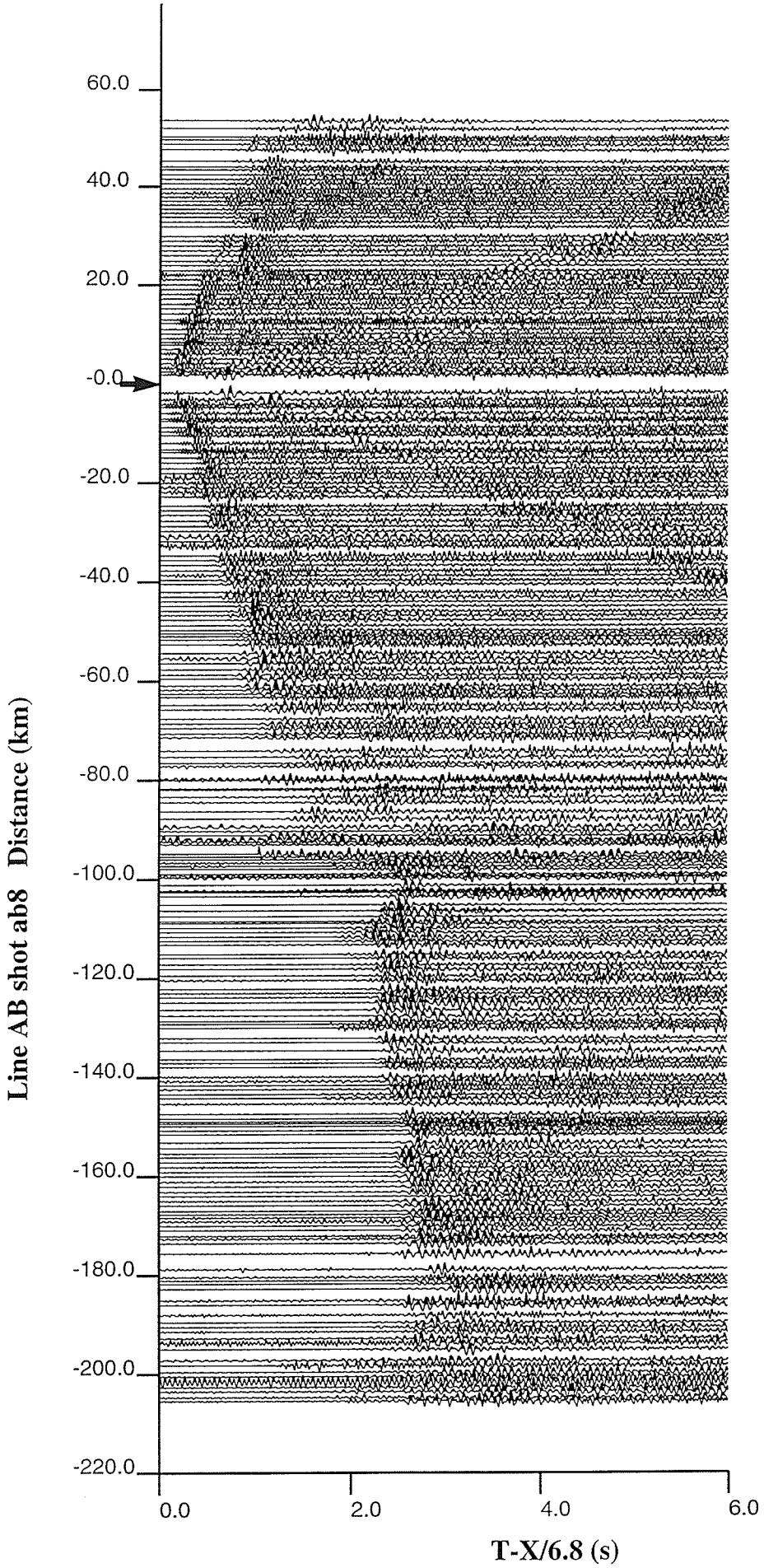

Figure C.8 Refraction section for the shot ab8 of the line AB

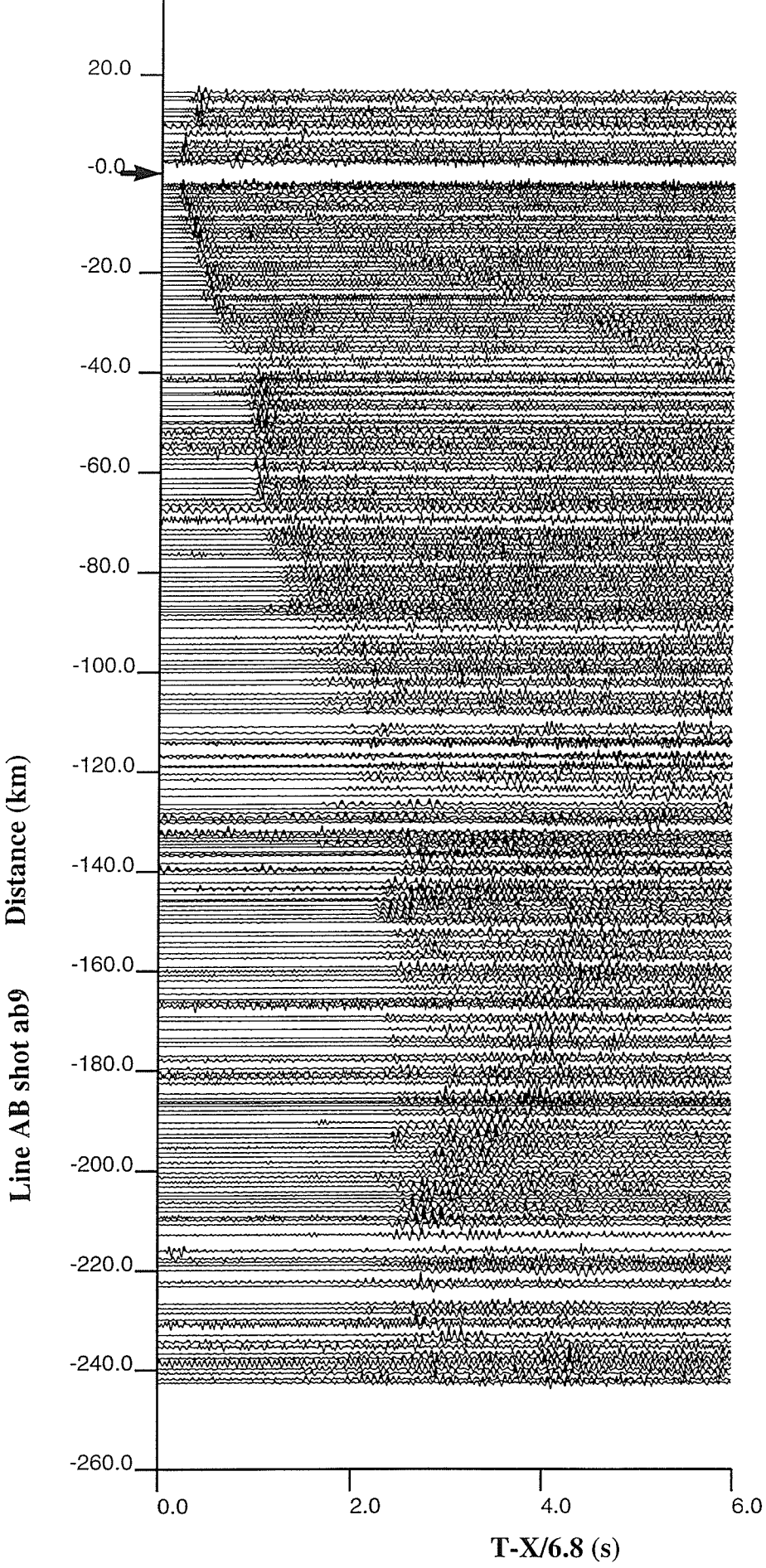

Figure C.9 Refraction section for the shot ab9 of the line AB

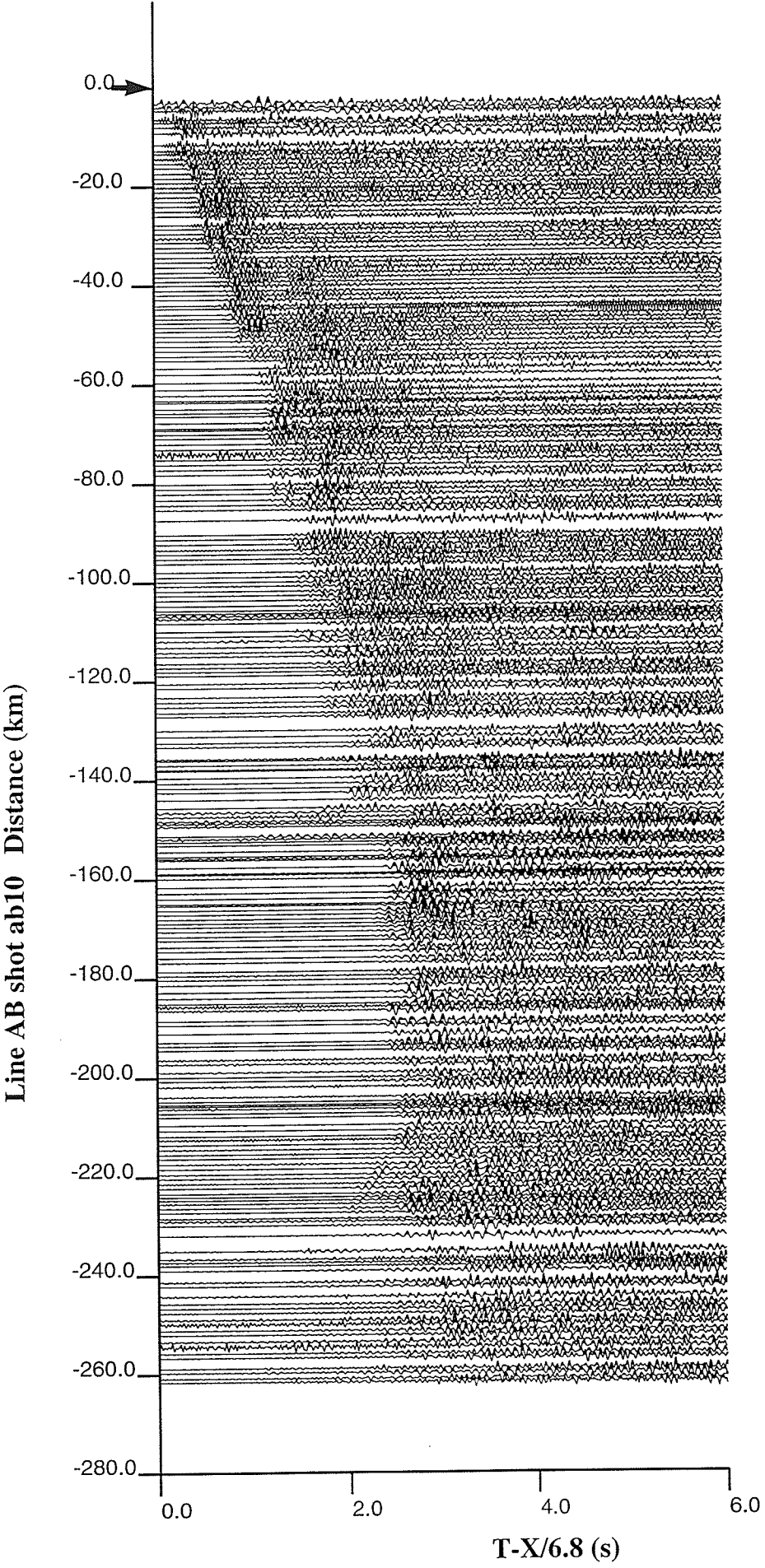

Figure C.10 Refraction section for the shot ab10 of the line AB

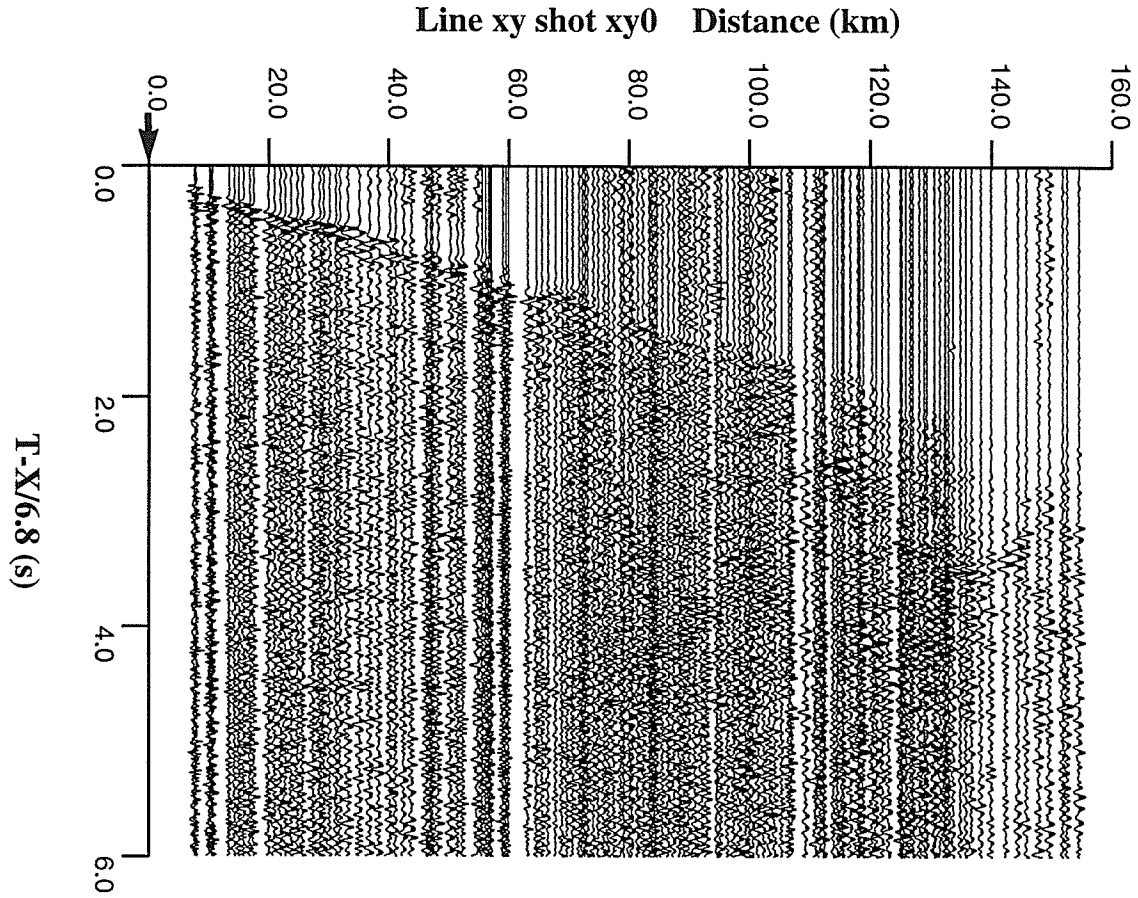

Figure C.11 Refraction section for the shot xy0 of the line XY.

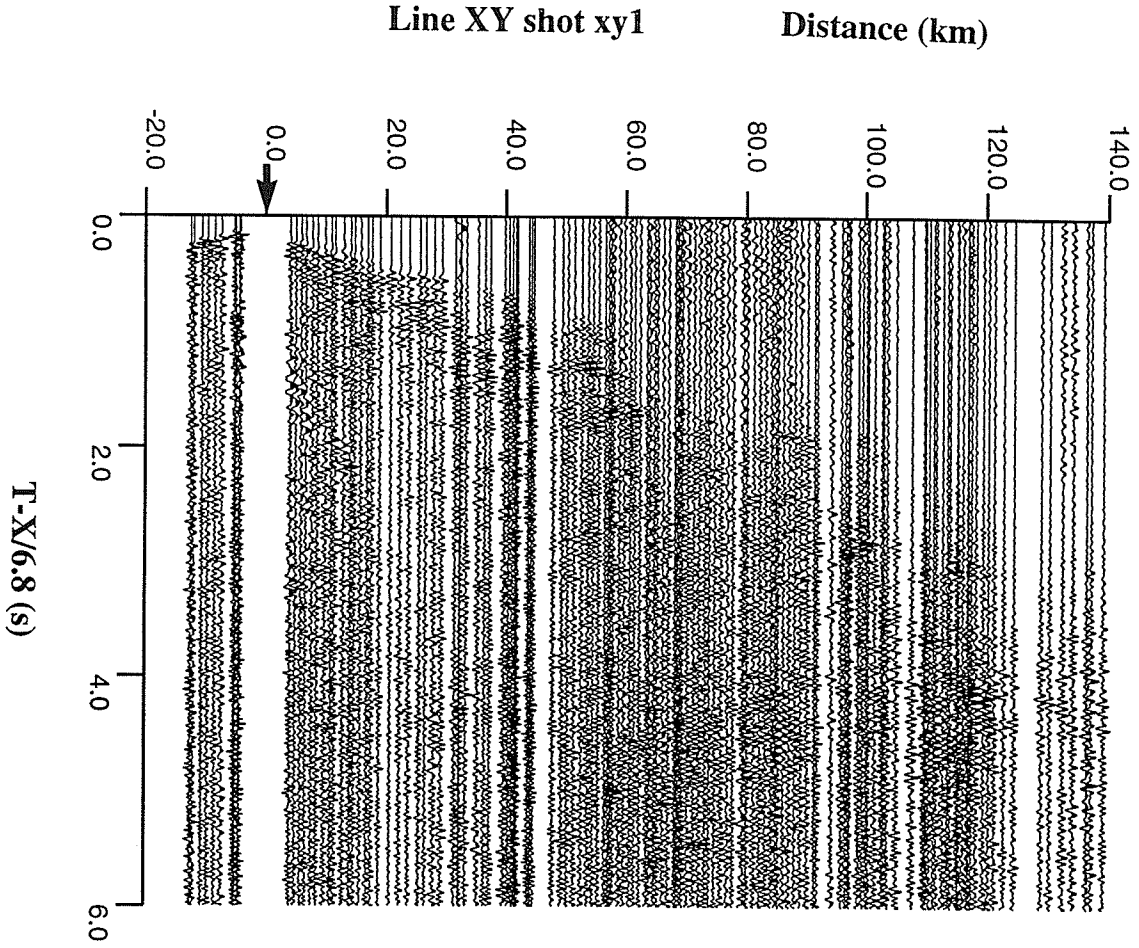

Figure C.12 Refraction section for the shot xy1 of the line XY.

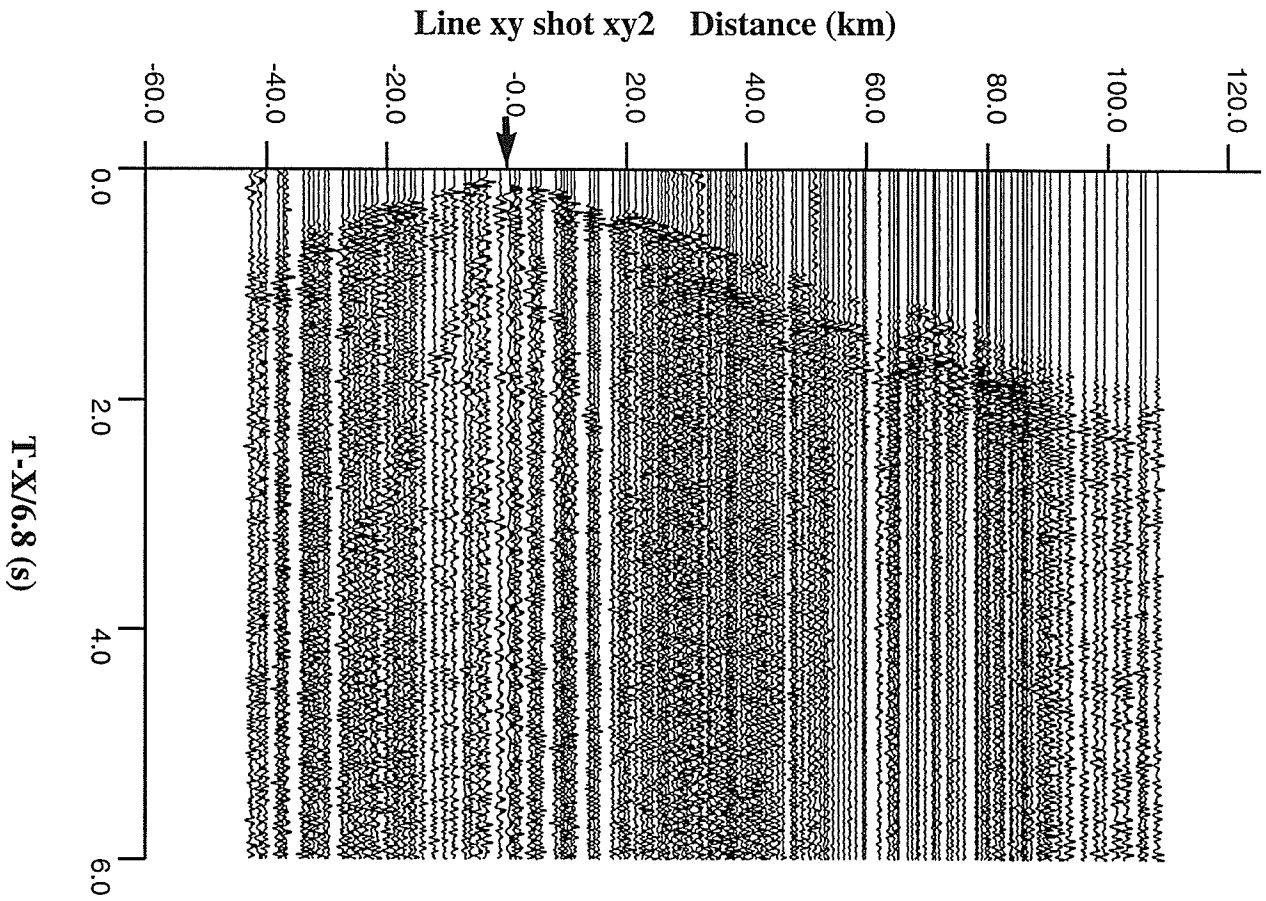

Figure C.13 Refraction section for the shot xy2 of the line XY.

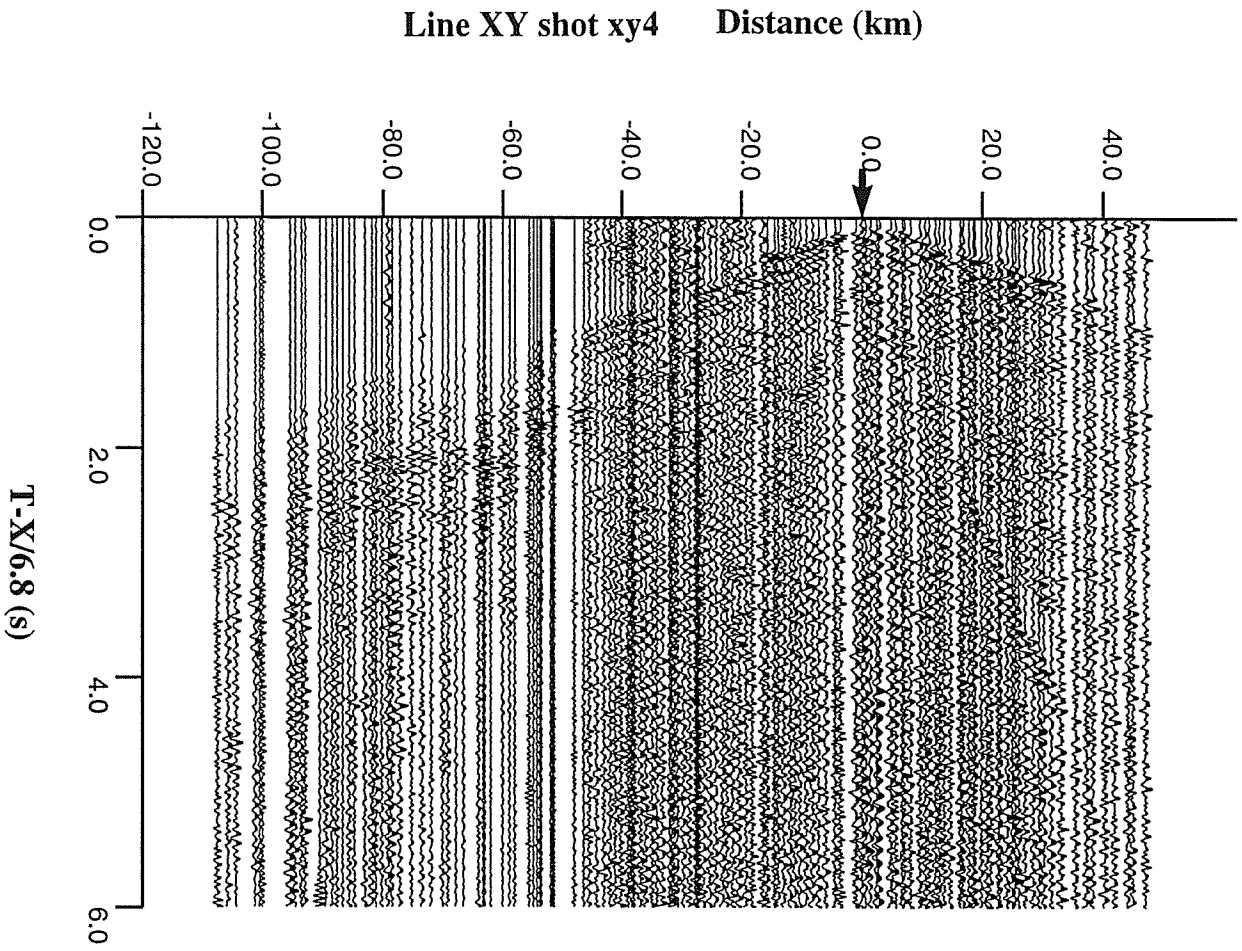

Figure C.14 Refraction section for the shot xy4 of the line XY.

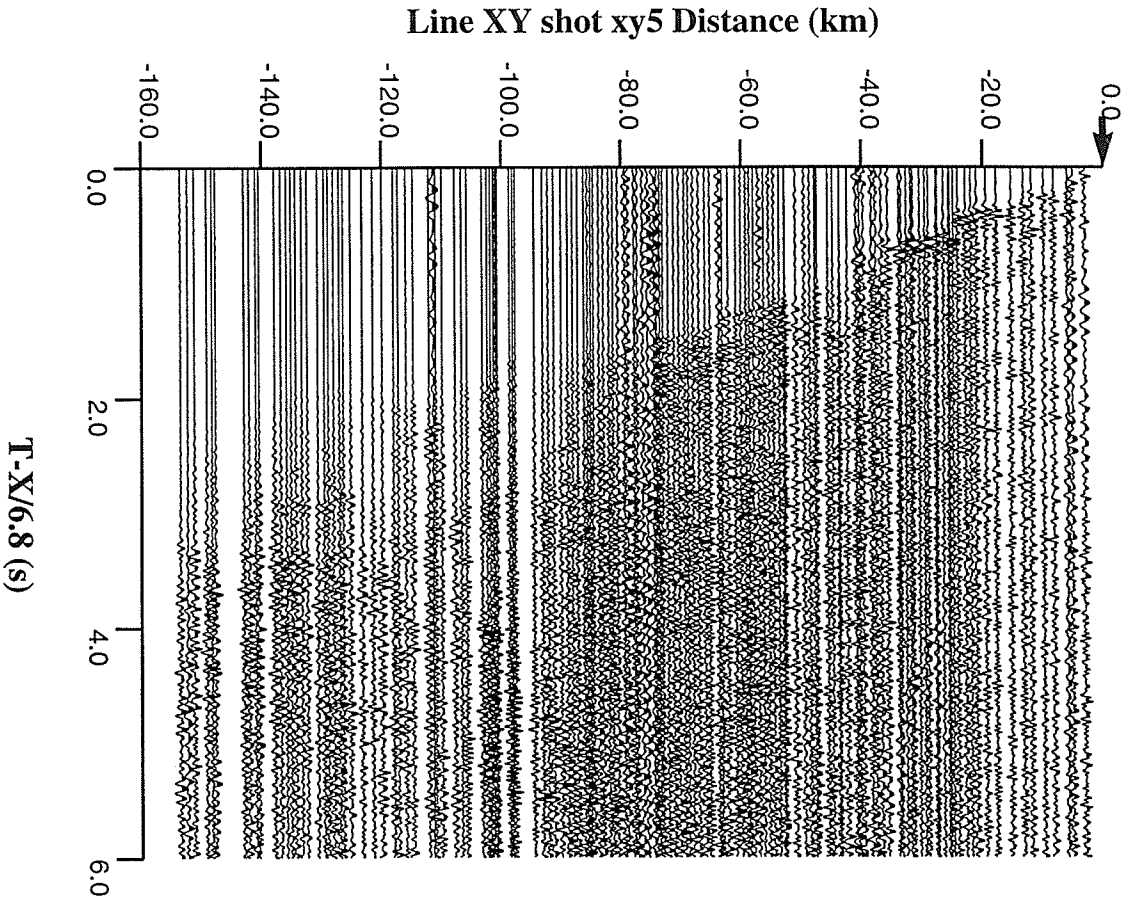

Figure C.15 Refraction section for the shot xy5 of the line XY.

Appendix D

Notes on the ERS-1 C-SAR Image Processing

The Synthetic Aperture Radar (SAR) C-band data collected on board the Earth Resource Satellite (ERS-1) were obtained from Canada Center for Remote Sensing. The ERS-1 was launched in 1991 by the European Space Agency for earth observation purposes. The Sudbury Basin was chosen as one of the scientific verification sites by the European Space Agency and a number of airborne and ground truth surveys were carried out. The VV polarized SAR antenna orbit the Earth at an altitude of 785 km with an inclination of 20^0 SW. Its look direction is right and the ground resolution is approximately 30 m.

The resolution of the ERS-1 SAR image is much higher than that of many available airborne geophysical data. When interpreting them together, the space-borne SAR data has to be processed including resampling, enhancing through histogram equalization, and geometrical registration to corrected airborne geophysical data. The detailed processing steps are described in the following.

D.1 Preliminary Processing of the SAR

The processing of the SAR image includes geometric correction and histogram enhancement. To register the SAR image to the airborne geophysical images, the control points have to be selected from both images. Since there may be distortions and vagueness of geographic symbols in the geophysical data images, the UTM topographic map with which the airborne geophysical images were registered was used as the master image for the geometric correction.

The control points were selected from three lakes with reasonable distribution. After standard deviation analysis, 10 out of 12 sample points were used to establish a second order polynomial transform.

The form of polynomial transform is:

$$x' = a_0 + a_1 x + a_2 y + a_3 x^2 + a_4 xy + a_5 y^2$$

$$y' = b_0 + b_1 x + b_2 y + b_3 x^2 + b_4 xy + b_5 y^2$$

where the parameters of transform are listed in Table D.1.

Table D.1: Parameters of the Polynomial Transform

a_0	0.4991×10^3	b_0	0.1611×10^3
a_1	0.5448×10^0	b_1	0.1286×10^0
a_2	-0.3103×10^0	b_2	0.1161×10^0
a_3	0.2093×10^{-3}	b_3	-0.6091×10^{-4}
a_4	$0.2176 \times 10{-}3$	b_4	-0.2227×10^{-3}
a_5	$0.2182 \times 10{-}3$	b_5	-0.3636×10^{-3}

Based on the above polynomial coordinate transform, the SAR data was tied to the airborne data with exact spatial locations.

The SAR image was also histogram equalized and stretched to adjust the brightness of the image in order to overlay it with the other airborne geophysical images for later interpretation (Figure D.1). The image processing task was carried out using the image processing software KHOROS which was installed in a SUN workstation.

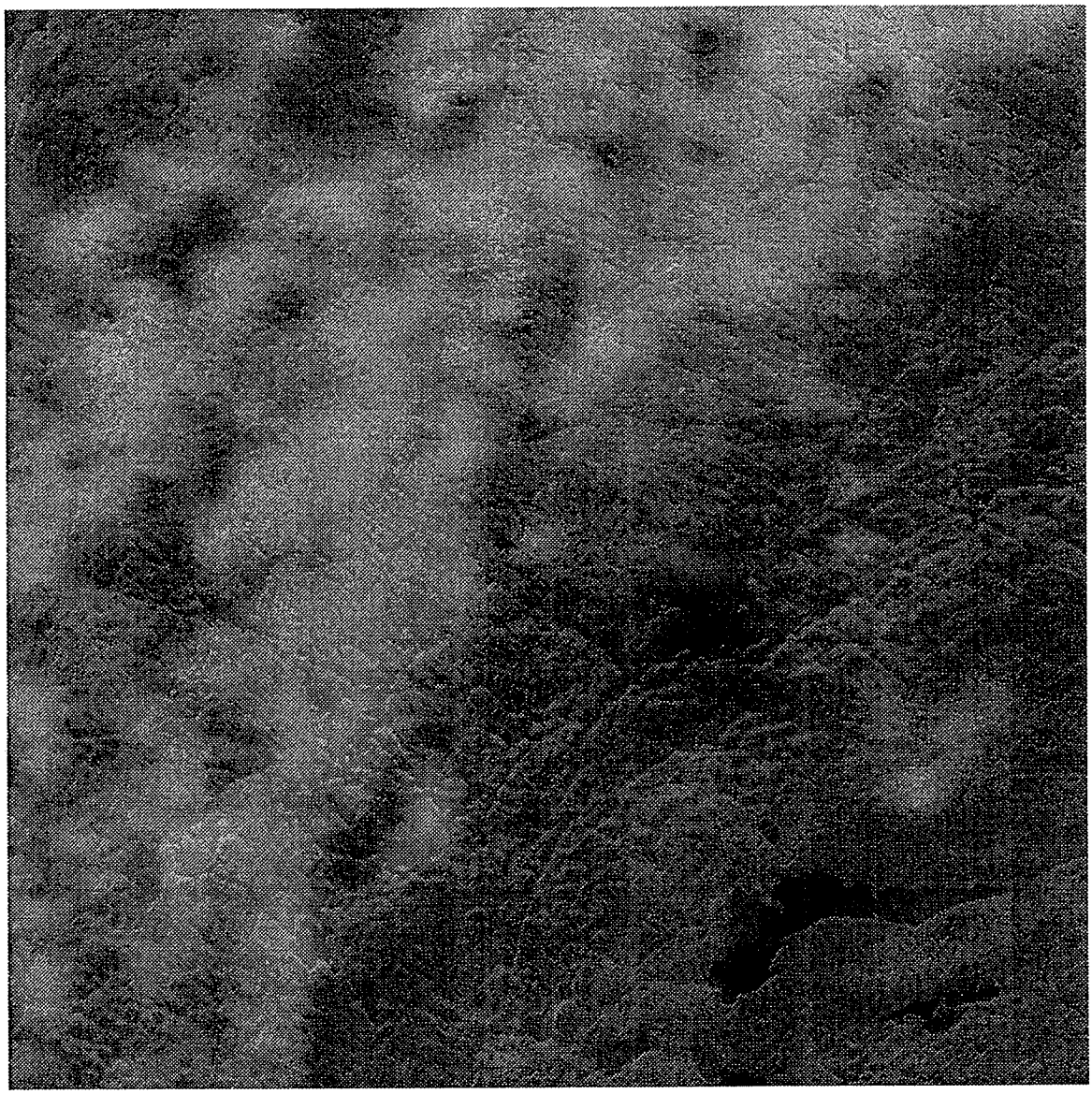

Figure D.1: The overlaid image of the airborne EM quadrature and magnetic data (see Table 1.1) with the ERS-1 SAR data over the northwest portion of the Sudbury Basin.

Appendix E

Notes on Removal of the Man-made Noise from the Airborne EM Data

A set of multi-parameter airborne geophysical data were provided by the Geological Survey of Canada, and include VLF (very low frequency) EM total field and quadrature data, γ ray spectrometer data, and total field magnetic data. The airborne VLF data provides good reliable information for mapping mafic dikes and they were utilized in this research. For this particular airborne survey, the receiver coils were tuned to the station NAA at Culter, Maine, U.S.A., which transmits radio signals at 24.0 KHz. The airborne radiometric measurements were made using a 256 channel spectrometer with twelve $102 \times 102 \times 406$ mm NaI (T1) detectors. The actual airborne surveys were flown in 1989 at an elevation of 125 m at 190 km/h speed and a flight line spacing of 1000 m. The data were sampled at one second intervals with a ground cell resolution of approximately 100 m.

The airborne data were all compiled, registered, and geometrically corrected to the UTM topographic base map (Singh et al., 1993). However, the airborne EM

raw data contained numerous linear features (see Figure E.1), some of which are associated with the subsurface geological conductors. Some of them are, however, associated with surface or near surface man-made conductors such as power lines and railroads, which contaminates the original images. Thus preliminary processing steps were taken to verify and remove man-made noise.

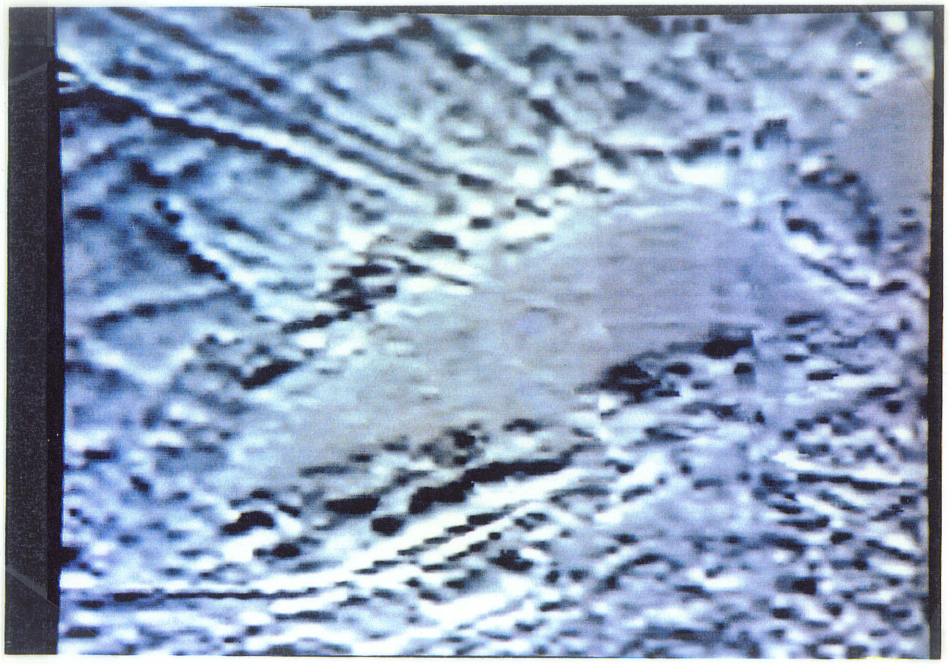

Figure E.1: The original image of the EM quadrature data.

The following image processing techniques were employed to remove man-made power line and railroad noise:

(1) Identification of the power line and railroad images and geometrically registration to the EM Quadrature image;

(2) Feature enhancement of the power lines and railroads on the EM image.

(3) Smoothing process to remove the noise.

The ARIES-II image analysis system, which was connected with VAX−11/750 computer system was utilized for this steps.

E.1 Geometric Correction and Registration

As mentioned earlier, some of the linear features may created by the man-made structures such as power lines and railroads. To verify this the power lines and railroads were digitized from a $1 : 500,000$ geological map (Dressler, 1984). Part of three lakes in the area were also digitized in order to use them as tie points for later correlation. The geometric correction was carried out as described in the SAR image processing section (Appendix D). Then the coordinate transformed power lines and railroads were overlaid on the EM Quadrature data, which is shown in Figure E.2.

E.1.1 Feature Enhancement of Power Lines

The objectives of image enhancement is to extract those features possibly caused by the power lines. Inspection of the EM Quadrature image of the Sudbury area indicates that the Sudbury central basin was electrically quiet and nearly free of anomalies. The Whitewater sedimentary formations have very low magnetic susceptibility and electrical conductivity. However the central basin was surrounded by complicated linear structures. It was thus relatively easy to identify the linear features in the central ellipsoidal basin. Therefore the main target of enhancement was focused on extraction of the linear features in the central basin.

(a) Directional line detection

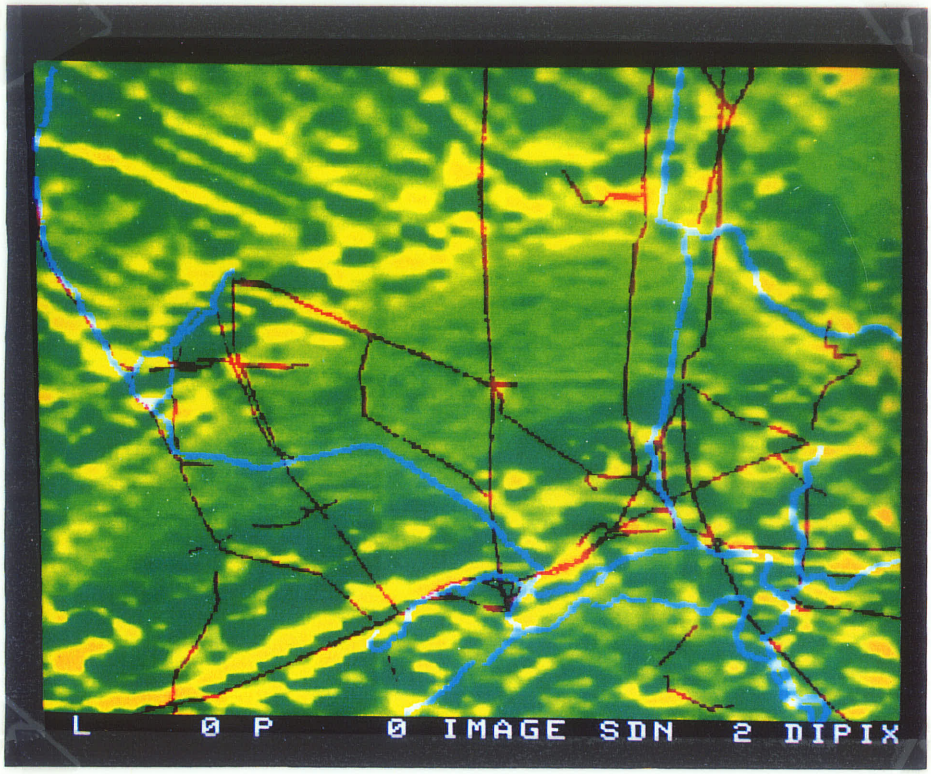

Figure E.2: The overlaid image of the geometric correction power lines and railroads on the EM Quadrature data. Power line is black, and railroad is blue.

Two 5×5 directional gradient filters were designed and applied to the data. One is for detection of the north-south oriented lines and other is for the northwesterly oriented lines:

$$G^1_{vertical} = \begin{pmatrix} 1 & 1 & 0 & -1 & -1 \\ 1 & 5 & 0 & -5 & -1 \\ 5 & 5 & 0 & -5 & -5 \\ 1 & 5 & 0 & -5 & -1 \\ 1 & 1 & 0 & -1 & -1 \end{pmatrix}$$

$$G^1_{northwest} = \begin{pmatrix} 0 & -1 & -1 & -1 & -1 \\ 1 & 0 & -5 & -5 & -1 \\ 1 & 5 & 0 & -5 & -1 \\ 1 & 5 & 5 & 0 & -1 \\ 1 & 5 & 5 & 5 & 0 \end{pmatrix}$$

(b) Thresholding

Following the direction detection thresholding operation was implemented through an intensity conversion of the grey levels to a binary image in order to strengthen the effect of the power lines and railroads.

The power lines were then overlaid on the thresholded image to see whether some of the linear features are related to the power line and railroad noises. The results have shown that the enhanced linear features in central basin in the EM image were consistent with the power lines, and the only exception was a horizontal line which could be a new power line that was not shown in the 1984 geological map. Thus removal of these linear features related to man-made noise was conducted in steps.

E.1.2 Removal of the Power Line and Railroad Noises

The steps designed to remove the noises consist of three steps: first thinning the image of power lines and railroads, encoding these lines, and then following the chain codes to smooth out the noises.

(a) Thinning

Encoding a line with several pixel width in a raster image can lead to either a wrong direction chain code or an algorithmic trap. Thinning is thus a necessary preprocessing step prior to the encoding steps.

Before carrying out thinning, conversion of the grey level values to binary numbers has to be done. The basic rules for a contour point P_1 (see the matrix below) to be flagged to delete is equivalent to a step of verifying if it satisfys:

$$\begin{pmatrix} P_9 & P_2 & P_3 \\ P_8 & P_1 & P_4 \\ P_7 & P_6 & P_5 \end{pmatrix}$$

(1). $2 \leq N(P_1) \leq 6$, where N(P_1) is the number of neighborhood points of P_1 with value of 1 among the 8 neighbors.

(2). $S(p) = 1$, where S(p) is the number of transition points from 0 to 1 in the sequence of $P_2 \rightarrow P_3 \rightarrow P_4 \rightarrow P_5 \rightarrow P_6 \rightarrow P_7 \rightarrow P_8 \rightarrow P_9 \rightarrow P_2$.

(3).

$$Prod(P_2P_8P_6) = 0$$

$$Prod(P_4P_6P_8) = 0$$

Apply the above procedure over the whole image, then replace the principal (3) by (3'),

(3')

$$Prod(P_2P_4P_8) = 0$$

$$Prod(P_2P_4P_6) = 0$$

and repeat these steps for the whole image.

(b) Encoding

The orientation of a curve described in terms of a sequence or "chain" of discrete descriptors is called curve encoding. The code chain is derived from a neighborhood matrix with each neighbor coded to correspond to the primitives in the image and the matrix described below:

$$\begin{pmatrix} 3 & 2 & 1 \\ 4 & * & 0 \\ 5 & 6 & 7 \end{pmatrix}.$$

To avoid to fall into an algorithmic trap, the encoding was implemented in four steps depending on the orientation of the power lines. The first set of lines to be

encoded was oriented north-south and north-west, The direction code 1234 with a sequence of 2341 was used to make chain codes. The code 4567 with sequence of 4567 was used for second set of lines, the third set of the code with 6701, and the fourth set 1234 with a sequence of 3421. The method is, however, sensitive to the starting points. When all of the power lines were encoded, they were saved for subsequent processing.

(c) Decoding and smoothing

Smoothing was done by a neighborhood averaging method along the chain codes and a median filter was tested for this propose. Considering the fact that the EM field generated by the power lines was a symmetric variant field with respect to the power lines and the visible effects were extend from several pixels to a dozen of pixels. For each direction code, a $1 \times m$ removal window was selected, and for each removed point, a $n \times n$ basic smoothing window was applied.

A 9×9 smoothing window with a 1×9 and a 1×11 removal window was tested. It was found that the global smoothing window size may cause either over-smoothing or under-smoothing. The size of smoothing window then was adjusted by comparing the local average value averaging over a convolution range of 1×15 removal window and a $N \times N$ basic smoothing window with the pixel average value averaging over a $N \times N$ smooth window. When the difference between the two values exceeded a threshold value, the smoothing window was enlarged. The threshold value was thus determined by trial and error.

Figure E.3 is the final image obtained after applying the adjusted smoothing window. Comparing the original EM image (Figure E.1) with Figure E.3, some improve-

Figure E.3: The EM quadrature data after smoothing out the power line and railroad noises

ments are visible. The leftmost and the third power lines in central basin are almost smoothed.